Distinguishing cyanobacteria from algae using bio-optical remote sensing

A DISSERTATION PRESENTED
BY
MARK WILLIAM MATTHEWS
IN
THE OCEANOGRAPHY DEPARTMENT

FOR THE DEGREE OF
DOCTOR OF PHILOSOPHY

UNIVERSITY OF CAPE TOWN
CAPE TOWN, SOUTH AFRICA
JANUARY 2014

Thesis advisors: Stewart Bernard
with Trevor Probyn and Frank Shillington
Mark William Matthews, January 2014

Distinguishing cyanobacteria from algae using bio-optical remote sensing

Abstract

This study advances the use of remote sensing for eutrophication and cyanobacterial bloom detection in inland and near-coastal waters. The hypothesis that prokaryotic cyanobacteria can be systematically differentiated from algae (or eukaryotic species) on the basis of their distinctive bio-optical features is tested using a novel *in situ* bio-optical dataset and remotely sensed data from the Medium Resolution Imaging Spectrometer (MERIS). The *in situ* dataset was collected between 2010 and 2012 from three optically-diverse South African inland waters. An empirical algorithm, called the maximum peak-height (MPH) algorithm, was developed for operational determinations of trophic status (chlorophyll-*a*), cyanobacterial blooms and surface scum from MERIS. The algorithm uses top-of-atmosphere data to avoid the large uncertainties associated with atmospherically corrected water leaving reflectance data in optically-complex and turbid waters. The detailed analysis of the variability of the optical properties of the three diverse reservoirs provides new knowledge of the inherent optical properties of South African inland waters which have previously not been described. The study also provides the first detailed investigation of the effects of intracellular gas vacuoles on the optics of phytoplankton using a two-layered sphere model. The results demonstrate how gas vacuoles impart distinctive bio-optical features to cyanobacteria and cause backscattering to be enhanced. An advanced inversion algorithm is developed for detecting phytoplankton assemblage type and size from water leaving reflectance data. The algorithm, based on a direct solution of the equation of radiative transfer using Ecolight-S radiative transfer model, successfully distinguishes between phytoplankton assemblages dominated by small-celled cyanobacteria and those dominated by large-celled dinoflagellate species. It also provides reliable estimates of phytoplankton biomass (chl-*a*), and the absorption coefficients of phytoplankton and combined non-phytoplankton particulate and dissolved matter. Finally, the application of the MPH algorithm to a time series of MERIS data from 2002 to 2012 in South Africa's 50 largest reservoirs is likely to be the most comprehensive assessment of eutrophication and cyanobacteria occurrence from earth observation data yet performed. The results confirm that widespread cyanobacterial blooms and eutrophication remain issues of critical concern for water quality in South Africa.

Contents

1 INTRODUCTION **1**

1.1 Rationale and problem statement 2

1.2 Hypothesis, aims and objectives 4

1.3 Thesis structure 5

2 AN ALGORITHM FOR DETECTING TROPHIC STATUS (CHLOROPHYLL-A), CYANOBACTERIAL-DOMINANCE, SURFACE SCUMS AND FLOATING VEGETATION IN INLAND AND COASTAL WATERS **7**

2.1 Introduction 8

2.2 Methods 10

2.3 The MPH algorithm 15

2.4 Results and discussion 20

2.5 Application and conclusions 27

3 CHARACTERISING THE ABSORPTION PROPERTIES FOR REMOTE SENSING OF THREE SMALL OPTICALLY-DIVERSE SOUTH AFRICAN RESERVOIRS **37**

3.1 Introduction 38

3.2 Methods 39

3.3 Results and discussion 44

3.4 Conclusion 65

4 USING A TWO-LAYERED SPHERE MODEL TO INVESTIGATE THE IMPACT OF GAS VACUOLES ON THE INHERENT OPTICAL PROPERTIES OF *MICROCYSTIS AERUGINOSA* **67**

4.1 Introduction 68

4.2 Methods 74

4.3 Results and discussion 80

4.4 Applications 93

4.5 Conclusion 95

5 DISTINGUISHING CYANOBACTERIA FROM ALGAE IN OPTICALLY-COMPLEX INLAND WATERS USING A RADIATIVE TRANSFER INVERSION ALGORITHM **97**

5.1 Introduction 98

5.2 Methods 104

5.3 Results and discussion 113

5.4 Applications 120

5.5 Conclusion 130

6 EUTROPHICATION, CYANOBACTERIAL BLOOMS AND SURFACE SCUM IN SOUTH AFRICAN RESERVOIRS: 10 YEARS OF MERIS OBSERVATIONS **133**

6.1 Introduction 134

6.2 Methods 137

6.3 Results and discussion 143

6.4 Applications 163

6.5 Conclusions 173

7 CONCLUSION **175**

REFERENCES **179**

To Lauren, Liam and Josh.

Acknowledgments

My deepest gratitude goes to Stewart Bernard. Thanks for dreaming big together, the many long conversations discussing the intricacies of this work, for friendship and often buying the beer (and lunch). Your input has been invaluable to this research. To Trevor Probyn for generously allowing me to utilise your equipment, lab space and expertise, and to Frank Shillington for much lively discussion and sound council.

To my wife Lauren for being my greatest supporter and confident. You have been a great source of strength and encouragement to me without which this work would probably not have been completed.

My dad for calling me Dr. Mark before I had a PhD.

My mom for encouraging me to become a young achiever.

To Andy Rabagliati for downloading and processing huge amounts of data and programming assistance which made Chapter 6 possible. The many people who assisted in the field: Paul Oberholster, Nobuhle Majozi, Heidi van Deventer, Marie Smith, Hayley Evers-King, the Theewaterskloof Sports Club, the Department of Water Affairs, Jannie and the Loskop Dam Nature Reserve team, Renaud Mathieu. Those at the CSIR who contributed to the Safe Waters Earth Observation Systems project, which funded most of the field work. Michael Silberbauer and DWA for data of various kinds. Lisl Robertson for generously sharing your expertise related to all things Hydrolight and Fortran. The following scientists: Antonio Ruiz-Verdu, Arnold Dekker, Dani Odermatt, Grant Pitcher, Luis Guanter, Stefan Simis, Dariusz Stramski, Tiit Kutser, Julie Deshayes. To the anonymous referees who reviewed some of the work published here. The European Space Agency and Carsten Brockmann for MERIS FR data.

My office mates in room 214; the bio-optics group at UCT and CSIR: Marjolaine, Sandy and Christo; and my fellow PhD students and colleagues in the Oceanography Department with whom I enjoyed many tea time conversations.

For funding: The CSIR/UCT scholarship. The PhD Package Award from UCT. ACCESS. The University of the Western Cape for employment during the last six months of this research.

Finally, I want to thank my God and Father and the Lord Jesus Christ for these ideas, the strength to carry them out, and his providence over all aspects of this research.

"The challenge for operational remote sensing of optical water quality... is seen to have two components. One is to provide an effective characterization of the target inland and adjacent coastal waters and the other is to streamline the data analysis to provide maps of water properties in the time and cost frameworks required for operational use."

Jupp, D.L.B, Kirk, J.T.O., Harris, G.P., 1994, Aust. J. Mar. Freshwater Res., 45, 801-828

1

Introduction

1.1 RATIONALE AND PROBLEM STATEMENT

THE SCIENCE OF WHAT IS CALLED ocean colour radiometry has advanced well beyond its initial scope to include coastal and inland waters. The optical properties of these waters differ vastly from open-ocean waters and therefore the requirements for remote sensing also differ substantially. Given signals from at least three optically significant constituents besides water itself, often present at considerably higher concentrations than open-ocean waters, these waters are complex from an optical perspective. This requires that algorithms used for retrieval of optical and biogeochemical variables must account for all the various water constituents. This has led to the development of more advanced algorithms based on direct or approximate solutions to the radiative transfer equation (RTE), which relates the inherent optical properties (IOPs) to the observed apparent optical properties (AOPs) such as the remotely sensed reflectance (R_{rs}). Simultaneously to the development of advanced procedures, there has been a growing body of research using more simple empirical algorithms to derive biogeochemical variables, most often the concentration of chlorophyll-*a* (chl-*a*), directly from the AOPs (see review by Matthews, 2011). Such empirical approaches have considerable value alongside more advanced algorithms due to their simplicity and robustness, the physical basis for which can be shown to be based on the IOPs (*ibid.*).

The optical complexity of these waters also makes atmospheric correction of satellite radiances more challenging and leads to substantial uncertainties and errors in water leaving reflectance and biogeochemical products. Bright water pixels with non-negligible water leaving reflectance in the red and near-infra red (NIR), as well as contamination of top-of-atmosphere (TOA) signals with stray light caused by the contrast between dark water targets and the brighter adjacent land, means that algorithms used for open-ocean applications most often fail. Correcting for the effects of continental aerosols such as dust and smoke which are highly variable in space and time is particularly challenging. While substantial progress has been made (e.g. Guanter et al., 2010), there exists at this time no routine or standard atmospheric correction providing reliable water leaving reflectances in complex inland waters. The use of empirical algorithms targeting closely clustered spectral features in the red and NIR of top-of-atmosphere data types offer the ability to bypass the need for aerosol corrections which are typically associated with large errors.

The requirements in terms of sensor resolution also substantially differ with regards to inland waters. From a spatial perspective, high resolution in the order of tens to hundreds of meters is required to sufficiently detect smaller inland water targets. Due to the optical complexity of the water, the spectral resolution and sensor sensitivity requirements are higher in order to sufficiently resolve the signal from various confounding constituents. In particular, bands targeting specific phytoplankton pigment absorption, backscattering and fluorescence features are needed in order to derive quantitative information products related to biomass (chl-*a*). Furthermore, due to the dynamic nature of smaller inland systems, sufficient temporal resolution is required to resolve changes occurring on daily–weekly time scales. The only recently past systematic space-borne sensor that meets these demanding requirements is the Medium Resolution Imaging Spectrometer (MERIS) on board the European Space Agency's (ESA) Envisat platform (Matthews et al., 2010). Envisat was operational from 2002 until 8 April 2012 and overlapped two years of this study which began in 2010. Therefore, at the time of writing, there are no space-born instruments systematically acquiring global data that might be used for frequent near real-time observations of surface water quality in spatially constrained inland and near-coastal waters. Furthermore the only mission with global systematic acquisitions planned in the next decade that meets these requirements is the Ocean and Land Colour Instrument (OLCI) on board the ESA Sentinel-3 platform scheduled for launch in 2014–2015.

The global concern related to eutrophication and cyanobacterial blooms is based on the increasing occurrence of nuisance blooms which contaminate water supply systems and rivers, and represent a health risk to humans and animals through toxins produced by cyanobacteria and other algal species (Codd, 2000, Downing et al., 2001, Smith et al., 1999). In particular *Microcystis* is a severe problem species, with a truly global distribution, and which is capable of producing *Microcystin* toxin which can lead to human and animal fatalities if ingested in large quantities (de Figueiredo et al., 2004, Visser et al., 2005). The incidence of such cases and its apparent relationship to liver cancer occurrence (Fleming et al., 2002), make the monitoring and assessment of *Microcystis* in freshwater systems a matter of global health concern (WHO, 1999). Rising global temperatures are furthermore likely to exacerbate cyanobacterial blooms (Johnk et al., 2008, Michalak et al., 2013). Furthermore the negative economic, ecological and social impacts of eutrophication related to increased water treatment costs, negatively affected ecological function of sensitive systems, and deteriorated quality of the resource for recreation and conservation, make eutrophication a global environmental concern. Up till the present study however, there exists no quantitative and validated remote sensing technique for the detection of *Microcystis* cyanobacteria or any other freshwater cyanobacteria species from remotely sensed data. Furthermore, there exists no standard remotely sensed water quality products for inland waters, including chl-*a* which is the foremost indicator for eutrophication.

The quotation from Jupp et al. (1994) on the title page of this Chapter identifies two challenges related to the use of satellite-derived optical water quality information in operational monitoring systems. The first relates to the characterisation of the optical properties of optically complex inland and near-coastal waters, which also includes the availability of suitable algorithms. This remains an ongoing area of study, and significant progress has been made since the 1990s in this regard. The second challenge relates to the processing and handling of large quantities of data, which have become more feasible given the considerable advancement of computational ability during this time. Despite the advances in both of these areas, operational use of satellite-derived water quality information products remains scarce. It is the author's opinion that this can be attributed to the same problems identified in the 1990s by Jupp et al. (1994) which have generally received inadequate attention from the scientific community, as well as policies surrounding data access and limited non-proprietary data sources that meet the demanding resolution requirements.

Given the concerns briefly re-laid above, the present challenge for remote sensing in inland waters might be summarised as follows:

1. There is a need for the advancement of both simple empirical and advanced inversion radiative transfer based techniques for retrieving IOPs and biogeochemical variables in inland waters, whilst accounting for the challenges associated with atmospheric correction, and the optical characterisation of complex waters.

2. There is a need for techniques aimed at the detection of cyanobacteria species including *Microcystis* from remotely sensed data.

3. There is a need for standard chl-*a* products that can be broadly applied in inland waters for monitoring the occurrence and severity of eutrophication.

4. There is a need for the development of suitable techniques that can be applied for systematic and near real-time monitoring of smaller inland waters in order to manage risks associated with eutrophication and cyanobacterial blooms.

1.2 Hypothesis, aims and objectives

This thesis aims to contribute towards solving the challenges identified above. The main aim of the thesis is to test the hypothesis that prokaryotic cyanobacteria (predominantly consisting of *Microcystis*) can be differentiated from eukaryotic phytoplankton (or algae) using remotely sensed data on the basis that cyanobacteria possess unique features related to pigmentation and internal cellular structure in the form of gas vacuoles. The hypothesis is tested using both simple empirical and advanced inversion algorithms. Whilst testing this hypothesis the thesis also aims to: develop a simple empirical algorithm that bypasses the demanding atmospheric aerosol correction and provides trophic status estimates in the form of a standard chl-*a* product for inland waters; to add to the knowledge of the optical properties of diverse inland waters; and to develop techniques that can be used for systematic near real-time monitoring of surface water quality in small inland waters on sub-continental scales (e.g. South Africa).

These aims are achieved through the following objectives:

1. Develop a simple empirical algorithm for differentiating cyanobacteria from algae and for the retrieval of chl-*a* in inland waters without the need for an aerosol atmospheric correction.

2. Characterise the variability of absorption properties and biogeochemical variables of three optically diverse South African inland reservoirs.

3. Perform a detailed analysis of the impact of intracellular gas on the IOPs of *Microcystis*.

4. Develop an advanced radiative transfer based inversion algorithm for detecting IOPs, size and differentiating cyanobacteria from algae in inland waters.
5. Perform an analysis of the status and trends of eutrophication and cyanobacterial blooms in 50 of the largest South African reservoirs using the full archive of MERIS data from 2002 to 2012.

1.3 THESIS STRUCTURE

Each of the thesis objectives are addressed in a separate chapter which together comprise an extensive bio-optical study testing the overall hypothesis. Each chapter is in the form of a self-contained published or publishable study which includes a review of relevant literature, and addresses an aspect of the overall hypothesis. In the case of published studies, the co-authors are included due to their contribution in an advisory and editorial capacity only. The thesis is broadly structured to address the two approaches, namely the empirical and advanced inversion approaches. Chapters 2 and 6 present the derivation and application of the empirical approach, respectively, which frame the overall study. The three middle chapters focus on the advanced analytical approach. Chapters 3 and 4 present empirical and modelled IOPs which are then applied with respect to the inverse problem in Chapter 5. The content of each of these chapters is briefly summarised as follows:

Chapter 2 presents a novel empirical algorithm which may be used to differentiate between cyanobacteria and algae in complex inland waters, whilst also providing an indicator of trophic status through chl-*a*. The algorithm, called the maximum peak-height (MPH) algorithm, uses a baseline subtraction procedure with Rayleigh corrected TOA reflectances to normalise for atmospheric effects, avoiding a complicated aerosol correction.

Chapter 3 is a data-rich chapter which gives a detailed analysis of the absorption and biogeochemical properties of the three study areas based on a large *in situ* data set collected between 2010 and 2012.

Chapter 4 presents an investigation of the optical effects of gas vacuoles on the IOPs of *M. aeruginosa* through using a two-layered sphere model and *in situ* bio-optical data.

Chapter 5 presents a hyperspectral radiative transfer based inversion algorithm for the detection of phytoplankton assemblage type and size, as well providing estimates of IOPs and biogeochemical variables, using the data from Chapters 3 and 4.

Chapter 6 then presents the application of the MPH algorithm to the full archive (2002 to 2012) of MERIS data in order to determined the phenology, extent and severity of eutrophication and cyanobacteria occurrence in South Africa's 50 largest reservoirs.

Finally, the main findings and recommendations for future research arising from the study are discussed in Chapter 7.

This chapter is based on work published as:
Matthews, M. W., Bernard, S., and Robertson, L. (2012). An algorithm for detecting trophic status (chlorophyll-a), cyanobacterial-dominance, surface scums and floating vegetation in inland and coastal waters. Remote Sensing of Environment, 124, 637–652.

2

An algorithm for detecting trophic status (chlorophyll-a), cyanobacterial-dominance, surface scums and floating vegetation in inland and coastal waters

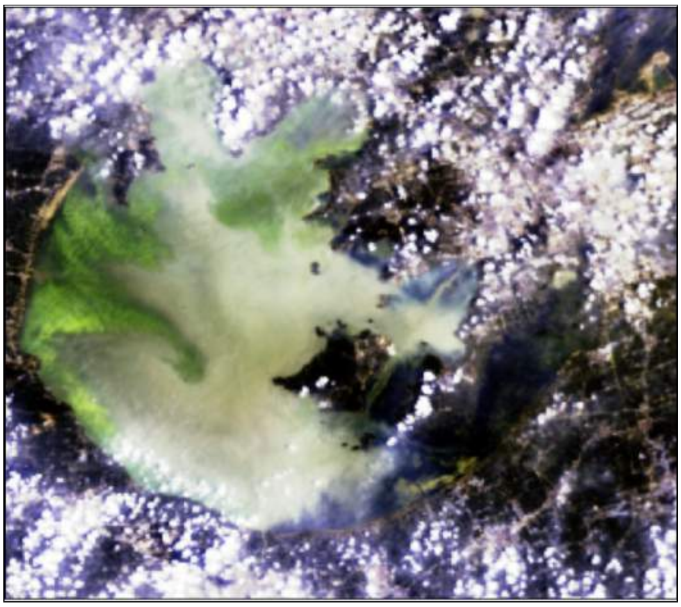

A massive cyanobacterial bloom on Lake Taihu, China, as seen by MERIS on 14th August 2007.

Abstract

A novel algorithm is presented for detecting trophic status (chlorophyll-*a*), cyanobacterial blooms, surface scum and floating vegetation in coastal and inland waters using top-of-atmosphere data from the Medium Resolution Imaging Spectrometer. The maximum peak-height algorithm uses a baseline subtraction procedure to calculate the height of the dominant peak across the red and near-infrared MERIS bands between 664 and 885 nm caused by sun-induced chlorophyll fluorescence (SICF) and particulate backscatter. Atmospheric correction of the MERIS TOA reflectance data for gaseous absorption and Rayleigh scattering proved adequate given the spectral proximity of the relevant bands and the sufficiently large differential spectral signal. This avoided the need to correct for atmospheric aerosols, a procedure which is typically prone to large errors in turbid and high-biomass waters. A combination of switching algorithms for estimating chl-*a* were derived from coincident *in situ* chl-*a* and MERIS bottom-of-Rayleigh reflectance measurements. These algorithms are designed to cover a wide trophic range, from oligotrophic/mesotrophic waters (chl-$a < 20$ mg m^{-3}), to eutrophic/hypertrophic waters (chl-$a > 20$ mg m^{-3}) and surface scums or 'dry' floating algae or vegetation. Cyanobacteria-dominant waters were differentiated from those dominated by eukaryote algal species (dinoflagellates/diatoms) on the basis of the magnitude of the MPH variable. This is supported by evidence that vacuolate cyanobacteria (*Microcystis aeruginosa*) possess enhanced chl-*a* specific backscatter which is an important bio-optical distinguishing feature. This enables these phytoplankton groups to be distinguished from space. An algorithm derived from cyanobacteria-dominant waters had a r^2 value of 0.58 for chl-*a* between 33 and 362 mg m^{-3} and an error of 33.7% (N=17). The operational algorithm for eukaryote-dominant algal assemblages gave a coefficient of determination of 0.71 and a mean absolute percentage error of 60% for chl-*a* in the range 0.5 to 350 mg m^{-3} (N=48). A flag based on cyanobacteria-specific spectral pigmentation and fluorescence features was used to identify cyanobacterial-dominance in eutrophic waters. Examples demonstrate how the MPH algorithm can offer rapid and effective assessment of trophic status, cyanobacterial-dominance, surface scums and floating vegetation in inland and coastal waters.

2.1 INTRODUCTION

THE NEEDS OF NEAR-COASTAL AND INLAND USERS are generally not addressed by global ocean colour algorithms. These algorithms primarily have an open-ocean focus and are not designed for the predominance of case II (Morel and Prieur, 1977) and eutrophic conditions encountered in close proximity to land. The optical complexity and sometimes extreme concentration of constituents in these coastal and inland waters calls for new atmospheric and bio-optical scientific capabilities. Furthermore, user needs for such waters are typically focused on water quality rather than biogeochemistry, and a greater emphasis is placed on the use of earth observation data for sustainable resource management, operational detection of trophic state, and phenological characterisation of eutrophication over time. The shift in scientific application also calls for new and more applied product types such as eutrophication indices.

The European space agency's Envisat-1 Medium Resolution Imaging Spectrometer (MERIS) and the planned Sentinel-3 Ocean Land Colour Instrument (OLCI) are likely the optimal past and planned sensors for near real-time frequent monitoring applications for spatially constrained inland and transitional coastal waters (Guanter et al., 2010, Matthews, 2011). Chl-*a* algorithms for MERIS in turbid, high-biomass inland and coastal waters have historically been based on the water-leaving reflectance (Gitelson et al., 2008, 2009, Gons, 2005, Gons et al., 2002, Moses et al., 2009a,b). However, the limited ability of routinely implemented atmospheric corrections for accurately resolving the shape of the water-leaving reflectance in the red-NIR MERIS bands in high biomass 'bright-pixel' waters, has hampered these efforts (Guanter et al., 2010, Matthews et al., 2010, Schiller and Doerffer, 2005). Here, for the first time, a red-edge baseline-subtraction algorithm is presented for retrieving phytoplankton biomass estimates (chl-*a*) from MERIS bottom-of-Rayleigh reflectance (BRR) in low and high biomass phytoplankton-abundant inland and coastal waters. The algorithm is named the maximum peak-height or MPH algorithm, because it uses the position and magnitude of the chl-*a* fluorescence and particulate backscatter/absorption related peaks in the MERIS red/NIR bands. The top-of-atmosphere (TOA) approach used by the MPH algorithm avoids error-prone aerosol atmospheric correction procedures used to derive the water leaving reflectance, while the baseline-subtraction between red and NIR bands minimizes the atmospheric effects from the aerosol particles.

A series of switching algorithms is derived using a two-step process. First the MPH variable is calculated using the MERIS BRR data. Then empirical relationships are identified between the MPH variable and coincident *in situ* chl-*a* measurements. Eukaryote and cyano-dominant assemblages are distinguished based on the magnitude of the MPH variable and using a flag based on reflectance features related to chl-*a* and cyanobacterial phycobiliprotein absorption and fluorescence. The dataset comprises measurements made in four diverse phytoplankton-abundant southern African systems: the southern Benguela marine coastal upwelling system; and the three inland freshwater reservoirs of Zeekoevlei, Hartbeespoort dam and Loskop dam. The MPH algorithm is designed to provide a quantitative measure of trophic status through chl-*a* estimates. It covers a wide trophic range while also offering the ability to identify surface scums and floating vegetation. The MPH algorithm is intended for operational trophic status determination, and for providing warning indicators for cyanobacteria and HABs in phytoplankton-dominant coastal and inland systems. The study provides a thorough description and error assessment of the dataset, then gives details of the MPH algorithm, and concludes with example applications from various southern African and global systems.

2.2 METHODS

2.2.1 DESCRIPTION OF STUDY AREAS

The MPH algorithm was derived using datasets collected from four diverse study areas. The four systems are similar with regard to the occurrence of HABs, but differ considerably in their phytoplankton community structure, biochemistry and ecological drivers. The southern Benguela is an extremely dynamic and productive upwelling system off the west coast of southern Africa that is affected by frequent HAB events (Pitcher and Calder, 2000). In bloom conditions, the phytoplankton assemblage is typically composed of a variety of dinoflagellate or diatom species varying in toxicity, or autotrophic ciliates including *Mesodinium rubrum* (Fawcett et al., 2007). The optical water type can be described as an extreme 'Case 1', with phytoplankton being the dominant causal IOP, and minerals and chromophoric dissolved organic matter (here referred to as *gelbstoff*) playing lesser roles (Bernard et al., 2001). In the inshore waters of the Benguela, the concentration of chl-*a* is extremely variable, and may range from less than one mg m^{-3} in non-bloom conditions, to greater than 500 mg m^{-3} in peak bloom conditions (Pitcher and Weeks, 2006). Therefore, the southern Benguela represents an extremely variable coastal upwelling system, and a challenging environment for ocean colour remote sensing.

Loskop dam is the most similar of the three inland waters to the Benguela with regards to water type and algal assemblage composition. Located at about 1000 m altitude in South Africa's Mpumalanga province, 150 km north east of Johannesburg, the lake shows pronounced longitudinal zonation with riverine, transitional and lacustrine zones that range from hypertrophic to oligotrophic, respectively (Oberholster et al., 2010). During winter sampling in July/August of 2011, the riverine zone was dominated by a dense bloom of the large-celled dinoflagellate, *Ceratium hirundinella*, which turned the water a chocolate brown colour. Chl-*a* values of up to 500 mg m^{-3} were recorded in this bloom. In the transitional and lacustrine zones further downstream, lower biomass blooms of chlorophytes and diatoms were present. Chl-*a* values were near 20 mg m^{-3} in the mesotrophic transitional zone, and less than 1 mg m^{-3} in the oligotrophic main basin representing the lacustrine zone. Importantly, dense blooms of the cyanobacterium *M. aeruginosa* become dominant in the riverine and transitional zones in summer months as the water temperature increases. These are present alongside eukaryote species during these months. Additional measurements found that there were also significant contributions from *gelbstoff* and minerals (see Chapter 3).

The final two study areas, Zeekoevlei lake and Hartbeespoort dam, represent two of the most productive freshwater reservoirs in southern Africa, and indeed the world (Harding, 1997, Robarts, 1984). Their phytoplankton assemblages are near-permanently dominated by the colonial cyanobacterium *M. aeruginosa* and regularly exhibit dense surface blooms called 'hyperscums' (Zohary, 1985). Chl-*a* values in these systems average around 200 mg m^{-3}, with values in excess of 1000 mg m^{-3} being frequently recorded. Despite the similar trophic status and phytoplankton assemblages, the two systems differ considerably in their morphology and limnology. Zeekoevlei Lake, located just above sea level in the urban center of Cape Town, is a small (2.5 km^2), shallow (average depth of 2 m) and continuously mixed (hypermictic) natural freshwater pan (for details see Matthews et al., 2010). Hartbeespoort dam at an altitude of 1005 mamsl is by comparison larger (20 km^2), deeper (average depth of 10 m), monomictic and stratified. The bulk IOPs of both lakes are overwhelmingly dominated by phytoplankton and associated detrital material, but there are also significant contributions by *gelbstoff* and minerals dependent on the season and meteorological conditions.

2.2.2 CHL-*A* MEASUREMENTS

DESCRIPTION OF COMBINED *IN SITU* CHL-*A* DATASET

The combined data set consists of 74 *in situ* surface chl-a measurements with corresponding simultaneously acquired MERIS full resolution (FR) or reduced resolution (RR) radiometry as follows: Benguela (N=37), Loskop (N=20), Zeekoevlei (N=9) and Hartbeespoort (N=8). The chl-*a* data from the four systems were acquired through numerous fieldwork campaigns spanning a period of 9 years from 2003 to 2011. The data from the Benguela were acquired by the Department of Agriculture Fisheries and Forestry, and is used with due acknowledgment. In all circumstances, surface water samples were collected using a well-rinsed bucket from a small boat with care being taken to minimise disturbance of the delicate surface blooms (if present). The dominant phytoplankton group was determined by microscopy. Chl-*a* was determined using a different analytical technique in each of the study areas. For the Benguela chl-*a* was measured by fluorometric analysis using 90% acetone (Holm-Hansen et al., 1965) in accordance with accepted marine protocols (Ducklow and Dickson, 1994). For inland waters, spectrophotometric analyses with 90% or 95% boiling ethanol were used due to the improved extraction efficiency of ethanol with cyanobacteria dominated assemblages (Sartory and Grobbelaar, 1984). Inevitably there will be differences between the extraction efficiencies of the solvents, and between the detection limits of the fluorometric and spectrophotometric techniques. However, no attempt was made to quantify these errors and they are likely to be small compared to the relative standard error of measurement. With the exception of the Benguela dataset, all chl-*a* analyses were performed in triplicate, using the mean as the representative value. The mean relative standard error (mrse) for chl-*a* was calculated as the standard deviation of triplicate results divided by the mean of the triplicate results. In this way, the mrse was determined as 17.1% (N = 31) for Zeekoevlei, 6.5% (N=38) for Hartbeespoort and 29.7% (N=54) for Loskop. It is important to consider the high frequency ($> 50\%$) of low chl-*a* values (< 10 mg m^{-3}) for the Loskop dataset, leading to larger relative errors.

Error in chl-a due to bloom patchiness: discreet-point sampling error

Several authors have questioned the usefulness of discreet-point samples for validating remotely sensed chl-*a* due to bloom patchiness (Galat and Verdin, 1989, Kutser, 2004, 2009). Discreet-point surface samples that neglect the horizontal and vertical components may lead to mis-representative biomass estimates especially in high biomass waters exhibiting patchy blooms, such as in this dataset. There are also significant dilution effects associated with the disturbance of delicate buoyant surface blooms during sampling. Previous estimates of the horizontal patchiness in cyano-blooms in Hartbeespoort (Robarts and Zohary, 1992) and the Gulf of Finland (Kutser, 2004) show that these errors can exceed two orders of magnitude. This leads to substantial within-pixel variability in chl-*a* values making it difficult to validate chl-*a* values retrieved from remote sensing data using discreet-point samples.

In order to gauge the likely relative magnitude of the error due to horizontal patchiness for the dataset, coincident measurements from a Hyperspectral Tethered Spectral Radiometer Buoy (Satlantic Inc.) were used. The TSRB measures the upwelling spectral radiance at a depth of 0.66 m, Lu(0.66), and the downwelling irradiance above the surface, Ed(0+), in the spectral range 400 to 800 nm with a frame rate of 1 Hz, a resolution of 3.3 nm and an accuracy of 0.3 nm. During sampling, the TSRB was allowed to drift freely in the sample area and acquire data for no less than three min. The relative standard error of the 710 nm band, known to be significantly correlated with chl-*a* values in high phytoplankton biomass waters (Gitelson, 1992, Schalles et al., 1998), was calculated from the typical three minute burst sampling time and was used as an approximate index for biomass patchiness. The results indicated that for Hartbeespoort, a highly stratified system with severely patchy cyano-blooms, the error due to bloom patchiness had a mean of 14.8% and a maximum of 44.8% (N=17). For the Benguela, a more mixed system with occasional surface blooms, the mean error is 10.8% (N = 44). For the hypermictic Zeekoevlei the mean error is reduced to only 8.6% (N=18). These mean errors were used as the typical expected error to discreet-point chl-*a* measurements resulting from bloom patchiness for the dataset. However, in the case of surface blooms, the error is likely to be substantially larger (see Robarts and Zohary, 1992).

The total uncertainty of *in situ* chl-*a* measurements was calculated by adding the mrse of measurement and the discreet-point sampling error estimates (if available). The total mean expected error for chl-*a* values from discreet-point surface samples for the four systems are 29.7% for Loskop, 10.8% for the Benguela, 25.7% for Zeekoevlei and 21.3% for Hartbeespoort. These errors are shown as error bars in figs. 2.4.2 and 2.4.3.

2.2.3 MERIS reflectance data

Data processing and atmospheric correction

MERIS data were processed using the Basic ENVISAT Toolbox for (A)ATSR and MERIS (BEAM) V. 4.9.0.1. The L1b data were first corrected for small spectral variations in spectral wavelengths between pixels, detector-to-detector systematic radiometric differences, and re-calibrated using the Level 1 Radiometry Processor V. 1.0.1 (Bouvet and Ramoino, 2009). An improved cloud product was calculated using the Cloud Processor V. 1.5.203 (© ESA, FUB, and Brockmann Consult, 2004). In order to account for the effects of gaseous absorption in the red bands from water-vapour (H_2O), ozone (O_3) and molecular Rayleigh scattering, the bottom-of-Rayleigh reflectance processor V. 2.3 was then used to compute ρ_{BR} (ACRI, 2006, Santer et al., 1999). ρ_{BR} is the dimensionless (*dl*) reflectance above the aerosol and ground system and is corrected for gaseous absorption using climatological values for the gas content in the atmospheric column, and Rayleigh scattering which relies on barometric pressure. This simplified atmospheric correction procedure is a first attempt to correct the TOA signal for gaseous and Rayleigh effects, whilst ignoring the more complicated and variable effects of absorbing aerosols (particles like smoke and dust). Importantly, the procedure corrects for the significant absorption by water vapour in the band centered at 709 nm. For comparison, and to assess the impact of the adjacency effect, the Improve Contrast between Ocean and Land (ICOL+) processor V. 2.6 was also implemented to give the adjacency effect corrected (AEC) BRR reflectance, or ρ_{AECBR} (Santer, 2010). The adjacency effect from Rayleigh scattering and aerosols was computed by ICOL while taking into account the aerosol type over water as well as the occurrence of case II waters.

The limited geographical extent of the inland water bodies in this study necessitates the use of MERIS full resolution (FR) data, whereas in the Benguela FR data are not systematically acquired and reduced resolution (RR) data are more frequently available for routine processing. As a result, a combination of FR (inland) and RR (Benguela) data are used in this study. The systematic bias in TOA radiance determined through on-board calibration has been estimated at less than 2% (Sotis, 2007). Taking account of error propagation, the error from intrinsic MERIS radiometry in the algorithm was estimated as no greater than 4%. The overall error associated with the reflectance based independent variables was determined through error propagation analysis.

MERIS BOTTOM-OF-RAYLEIGH REFLECTANCE DATA

MERIS reflectance spectra from single pixels were extracted from processed scenes corresponding to *in situ* match-up stations. The time difference between the *in situ* surface sample collection and the MERIS overpasses is less than 2 hours (but often less than 30 minutes) for the entire marine and freshwater dataset. Fig. 2.2.1 shows the bottom-of-Rayleigh reflectance data for the match-up dataset. The spectra have been arranged to aid comparison of the spectral shapes associated with the different waters, with spectra with fluorescence effects (681 nm) and absorption/backscatter (709 nm) maximum peak positions displayed separately. Fig. 2.2.1A shows spectra from the Benguela with small 681 nm fluorescence peaks that are otherwise relatively flat at longer wavelengths towards the NIR. The spectra from Loskop in fig. 2.2.1B have less obvious fluorescence peaks and are noisier towards the NIR, although the magnitudes are very similar to those in fig. 2.2.1A. The spectra in fig. 2.2.1C from Loskop and Benguela have clearly distinguishable peaks at 709 nm and belong to the backscatter/absorption domain. However, there is a clear difference between spectra from the Benguela, which typically slope downwards toward the NIR, and those from Loskop which have a continuous upward slope. The increased NIR reflectance values from Loskop are most likely caused by the adjacency effect in the small inland water body, or even partial contamination of the pixels from nearby land. This effect is also apparent in fig. 2.2.1B.

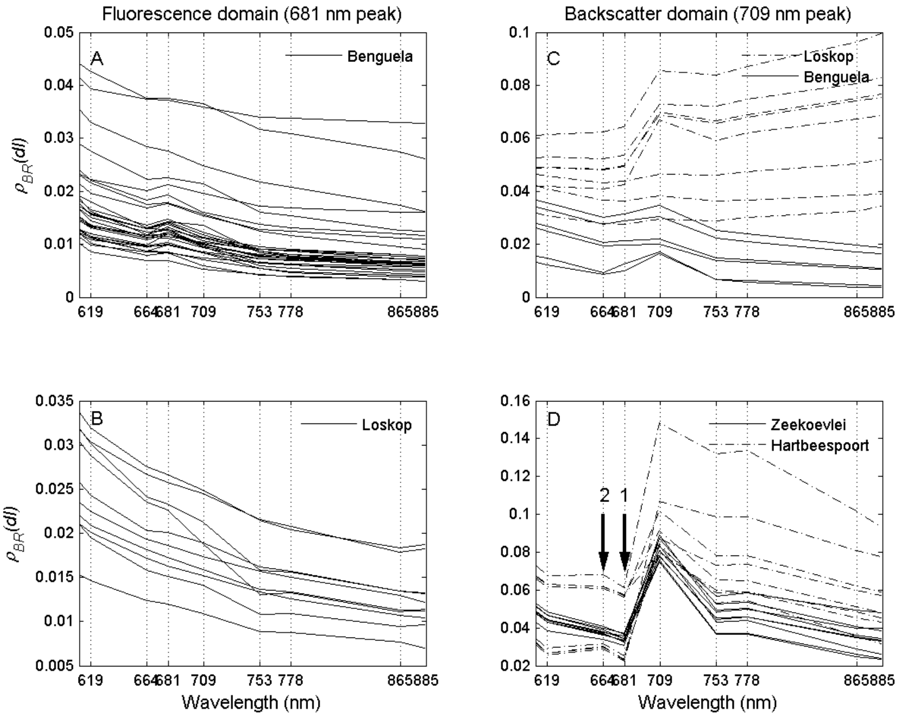

Figure 2.2.1: Bottom-of-Rayleigh reflectance spectra from single pixels corresponding to coincident chl-*a* measurements from each of the four study areas as indicated. The left hand side panels (A, B) display spectra possessing a 681 nm fluorescence related maximum peak position, while the right hand side (C, D) those with a 709 nm backscatter related maximum peak position. For more detail see section 2.3.2. *dl* = dimensionless.

Finally, fig. 2.2.1D presents spectra from the cyano-dominant waters of Hartbeespoort and Zeekoevlei. Three features specific to fig. 2.2.1D are worth noting: the larger magnitudes of the 709 nm peak relative to fig. 2.2.1C; a marked trough at 681 nm (arrow 1); and a small peak at 664 nm (arrow 2). These features make these spectra unique from those in the other panels. The increased magnitude of the 709 peak is thought to be due to cyanobacterial internal structure and is examined in detail in section 4.2.3 and in Chapter 4. The 681 nm trough (arrow 1) is likely the result of a combination of biomass related fluorescence re-absorption, reduced SICF related to the fact that the bulk of chl-*a* in cyanobacteria is located in photosystem I (Seppälä et al., 2007), and state transition associated with high light adaptation in cyanobacteria (pers. comm. Stefan Simis, 2012). Therefore a fluorescence signal at 681 nm is generally not suitable for providing chl-*a* estimates in cyano-dominant waters. This feature was used to identify *Microcystis* blooms in the Great Lakes (Stumpf et al., 2012, Wynne et al., 2008). Arrow 2 showing the elevated reflectance in the 664 nm band, overlaps the fluorescence emission domains of the phycobilipigments allophycocyanin (APC) and phycocyanin (PC). PC is the main light harvesting pigment in cyanobacteria (Bogorad, 1975), but the fluorescence likely originates from APC. The role that sun-induced phycobilipigment fluorescence (SIPF) plays in the peak formation is speculative at present since it has not been conclusively shown in other published works. This peak has also been observed in model-based studies which neglect fluorescence suggesting that sparse spectral cyanobacterial pigment absorption also plays a critical role in the peak formation (Kutser et al., 2006). This SIPF and absorption feature will be shown later to be critical in identifying cyano-dominant waters (see section 2.3.3), used in conjunction with the absorption maximum of PC near 620 nm.

2.3 THE MPH ALGORITHM

The baseline-subtraction MPH algorithm is similar in form to the fluorescence line height (FLH) algorithm (Gower et al., 1999). However, instead of having a fixed peak position, the MPH algorithm searches for the position and magnitude of the maximum peak in the red/NIR MERIS bands at 681, 709 and 753 nm (bands 8, 9 and 10). The MPH algorithm uses a baseline between MERIS bands 7 (664 nm) and 14 (885 nm) to measure the height of the red peak: this baseline was found to give more robust results than a spectrally shifting baseline. The MPH variable is calculated as follows:

$$MPH = \rho_{BRmax} - \rho_{BR664} - (\rho_{BR885} - \rho_{BR664}) \times \frac{\lambda_{max} - 664}{885 - 664} \tag{2.1}$$

where ρ_{BRmax} and λ_{max} are respectively the magnitude and position of the highest value from MERIS bands at 681, 709 and 753 nm.

The MPH algorithm is designed to handle three cases, each with two sub-cases, commonly occurring in phytoplankton-dominant and HAB affected waters. These can be summarised as follows, and are discussed in detail in the following sections:

1. Mixed oligotrophic/mesotrophic low-medium biomass waters (chl-$a <$ approx. 20 mg m^{-3})
    a) Eukaryote-dominant assemblages with SICF signal (predominantly diatoms/dinoflagellates)
    b) Special case: low biomass cyano-blooms (no observable SICF)
2. High biomass eutrophic/hypertrophic waters (chl-$a >$ approx. 20 mg m^{-3})
    a) Eukaryote-dominant assemblages
    b) Cyano-dominant assemblages

3. Extremely high biomass (chl-*a* $>$ approx. 350 mg m^{-3}) with surface scums (hyperscums) or 'dry' floating algae or vegetation
    a) Eukaryote blooms and floating aquatic macrophytes
    b) Cyanobacterial surface scums

2.3.1 FLUORESCENCE DOMAIN: MIXED OLIGOTROPHIC/MESOTROPHIC LOW-MEDIUM BIOMASS WATERS

The first case relates to mixed oligotrophic/mesotrophic low to medium biomass conditions with chl-*a* less than approx. 20 mg m^{-3}. In these waters where phytoplankton is optically dominant, the concentration of chl-*a* is known to be correlated with the line height of the SICF peak at 681 nm (Giardino et al., 2005, Gitelson et al., 1994, Gower, 1980, Hoge et al., 2003, Letelier and Abbott, 1996, Neville and Gower, 1977, Zhao et al., 2008), which is typically larger than the peaks at 709 and 753 nm due to strong absorption by water. In these conditions, the MPH algorithm emulates the FLH algorithm, calculating the line height of the fluorescence peak using the MERIS bands 7, 8 and 14. Available validation studies in inland and coastal waters using an FLH type algorithm with MERIS have shown the significant potential of this approach (Binding and Greenberg, 2011, Gons et al., 2008, Gower and King, 2007, Lee et al., 2007). An important distinction between previous studies and the present one is the ability to detect SICF using a type of TOA reflectance, rather than water-leaving reflectance data. The possibility to detect chl-*a* fluorescence at high altitudes despite atmospheric effects was demonstrated by Neville and Gower (1977) and is further confirmed here. Any phytoplankton assemblage possessing observable SICF is theoretically detectable using this approach, while not taking into account complications introduced through variable fluorescence quantum yields between species, diel and other photo-physiological variations (e.g. Suggett et al., 2009).

A special case is encountered with low-medium biomass cyanobacteria-dominated phytoplankton assemblages, which often occur in summer in the Baltic Sea. These blooms are generally not detectable using a SICF approach. An alternative approach is to take advantage of the phycobiliprotein fluorescence/absorption features visible in MERIS bands at 619 and 664 nm (see fig. 1.D). However, model studies show these features only become clearly distinguishable at chl-*a* concentrations larger than 8-10 mg m^{-3}, assuming a SNR of 1000 or greater for the satellite sensor (Metsamaa et al., 2006). In this case, with a MERIS SNR of approx. 600 - 700 in the relevant bands and using ρ_{BR}, these phycobiliprotein related features are probably only distinguishable at chl-*a* values larger than 20 to 30 mg m^{-3} (representing medium-high biomass) (Kutser et al., 2006). The ratio of PC:chl-*a* is also highly variable due to assemblage composition and intracellular and physiological processes (Simis et al., 2005, 2007), rendering unsound chl-*a* estimates from PC related features. Therefore detection of cyano-bloom initiation may not be feasible with current instruments.

For example, PC concentrations less than 50 mg m^{-3} may not even be detected with confidence using *in situ* spectroradiometric data (Simis et al., 2007). It is also important to consider how frequently this special case scenario of low biomass cyano-blooms might occur in nature, without taking into account exceptions. Given that cyanobacteria have a strong tendency to become dominant in eutrophic high-biomass conditions, the risk of cyanobacterial dominance at chl-*a* $<$ 20-30 mg m^{-3} is small (Downing et al., 2001). Statistically, at chl-*a* concentrations $<$ 10 mg m^{-3}, the risk of cyanobacterial dominance is $<$ 10%. Furthermore, the WHO alert level two gives a cyanobacterial chl-*a* concentration equal to or larger than 50 mg m^{-3} for the issuing of cyanobacteria health warnings; however, this may drop to between 12 and 25 mg m^{-3} for more toxic species (WHO, 1999). Given the above considerations, it is probably only possible, and arguably only necessary, to detect cyano-blooms of high biomass from an operational risk identification perspective (ignoring special cases such as the Baltic Sea). Therefore we can assume that the signal from backscatter/absorption related effects becomes apparent which, as now discussed, is the second case handled by the MPH algorithm.

2.3.2 The backscatter/absorption domain: high biomass eutrophic/hypertrophic waters

The second case for the MPH algorithm concerns high biomass eutrophic/hypertrophic water with chl-*a* concentrations greater than approx. 20 mg m^{-3} (incidentally 20 mg m^{-3} is the WHO classification threshold for eutrophic fresh water). These conditions are typically encountered in HAB affected systems during bloom periods. In this case, the red peak shifts towards longer wavelengths from a fluorescence peak at 681 nm (if present) which becomes masked by increasing chl-*a* absorption, to a peak near 700 nm induced by increased particulate backscatter and the offset by pure water absorption. In high biomass phytoplankton dominant waters, chl-*a* is known to be significantly correlated with the height (and position) of the 709 nm peak (Gitelson, 1992). Various ratio-type algorithms exploiting the 665 nm chl-*a* absorption and the 709 nm peak reflectance features have been used to provide accurate chl-*a* estimates (e.g. Dall'Olmo and Gitelson, 2005, Gitelson et al., 1993, 2009, Gons, 1999, Le et al., 2011, Zimba and Gitelson, 2006). When the backscatter/absorption peak becomes more distinct than the fluorescence peak, the MPH variable is calculated using the 709 nm band. This is similar to the scattered/reflectance line height algorithms (Dierberg and Carriker, 1994, Yacobi et al., 1995), and also the maximum chlorophyll index or MCI (Gower et al., 2005). Unfortunately, MERIS and OLCI are the only current and planned ocean colour sensors with an appropriate band at 709 nm able to utilise these types of algorithms.

2.3.3 A method for the discrimination of cyano-dominant waters

A simple but robust method for distinguishing high-biomass cyano-dominant waters from eukaryote dominant blooms is also implemented. The method is based on two theoretical and observable suppositions related to the unique pigment complement of cyanobacteria (see fig. 2.2.1.D, section 2.2.3):

1. Cyano-dominant waters possess no observable SICF peak at 681 nm (arrow 1, fig. 2.2.1D)
2. Cyano-dominant waters possess an observable absorption/SIPF induced peak at 664 nm (arrow 2, 2.2.1D)

Based on these observable features, it is possible to distinguish waters dominated by cyanobacteria (fig. 2.2.1D) from those dominated by eukaryote chl-*a* fluorescing species (fig. 2.2.1C). This presents itself in the MERIS waveband configuration by an observable trough at the 681 nm band (Wynne et al., 2008), and an observable sun-induced phycobiliprotein absorption/fluorescence (SIPAF) peak in the 664 nm band, respectively. A previous model-based study by Kutser et al. (2006) showed that a peak near 664 nm is a distinguishing feature of cyanobacteria blooms and is caused by the effect of phycocyanin absorption at 620 nm and sparse pigment absorption near 664 nm (their bio-optical model did not account for fluorescence). Using the baseline subtraction technique, these two features are used to identify high biomass cyano-dominant waters (see Wynne et al., 2008). The two baseline subtraction variables may be calculated as follows:

$$SICF_{peak} = \rho_{BR681} - \rho_{BR664} - (\rho_{BR709} - \rho_{BR664}) \times \frac{681 - 664}{709 - 664} \tag{2.2}$$

$$SIPAF_{peak} = \rho_{BR664} - \rho_{BR619} - (\rho_{BR681} - \rho_{BR619}) \times \frac{664 - 619}{681 - 619} \tag{2.3}$$

The following condition, most easily expressed as a logical statement, is then used to raise a flag for the presence of cyano-dominance:

$$If\ SICF_{peak} < 0\ and\ SIPAF_{peak} > 0,\ cyanoflag = TRUE \tag{2.4}$$

The cyanoflag correctly distinguished cyano-dominant water from those dominated by eukaryote species in the dataset (fig. 2.2.1).

2.3.4 HANDLING OF CYANOBACTERIAL SURFACE SCUMS AND FLOATING VEGETATION

The third case handled by the MPH algorithm is extremely high biomass conditions associated with surface scums, or hyperscums, and 'dry' floating algae or vegetation. Surface scums form during calm conditions as upwardly-buoyant phytoplankton (often cyanobacteria) accumulate on the water surface in dense mats or rafts. This is commonly observed, for example, in the waters of the Gulf of Finland (Kutser, 2004), and in cyano-dominant lakes (Hu et al., 2010b, Zohary, 1985). In these extreme conditions, the red peak shifts towards 750 nm or higher wavelengths, because the absorbing effect of water is excluded or minimised. Consequently, the water leaving reflectance resembles dry vegetation rather than water (Kutser, 2004, Kutser et al., 2009, Richardson, 1996). It is difficult to identify a threshold value for chl-*a* where a transition might occur between a maximum peak position of 709 (band 9) and that of 754 nm (band 10). For example, Kutser (2004) showed using a bio-optical model that this transition occurred at chl-*a* values close to or larger than 500 mg m^{-3}, provided the phytoplankton are in suspension and the concentration of suspended solids is held constant at 2 mg L^{-1}. However, terrestrial type reflectance has been observed for chl-*a* concentrations as low as 350 mg m^{-3} (Jupp et al., 1994). Furthermore, it is possible that surface scum conditions possessing terrestrial type reflectance can contain almost no chl-*a* due to photodegredation and chlorosis (pigment bleaching). Therefore the MPH algorithm does not attempt to provide quantitative chl-*a* estimates for MERIS spectra possessing terrestrial type reflectance as these are practically not yet quantified. Instead, a flag is raised for surface scum conditions when the 754 nm peak overwhelms the 709 nm peak. A more general flag is raised for potential surface scums for pixels with chl-$a > 500$ mg m^{-3}, however this can be specified according to requirements of the region of interest.

Cyanobacterial scums and eukaryotic surface blooms were distinguished from one another using the cyano-flag from section 2.3.3. This is based on the assumption that the optical properties of the scums are not too different from cells in suspension. For pixels identified as cyano-dominant and having either a chl-*a* value > 500 mg m^{-3}, or a maximum peak position of 754 nm, a flag is raised for cyanobacterial scum (cyano-scum) .

Floating aquatic macrophytes, such as the notoriously invasive water hyacinth *Eichhornia crassipes*, represent a substantial problem for lake and estuarine environments. For example, water hyacinth is often present in Hartbeespoort dam in relatively small quantities, but can rapidly become widespread if not manually controlled using costly mitigation measures (van Wyk and van Wilgen, 2002). Floating macrophytes have reflectance spectra resembling terrestrial dry vegetation (see Cavalli et al., 2009) and may be detected by enlarged reflectance in the 754 nm band. In these instances where a maximum peak position of 754 nm is detected, a flag is raised for floating vegetation. For these cases, the MPH algorithm resembles the floating algae index (FAI) algorithm used to detect floating surface scums in Lake Taihu, China with MODIS (Hu et al., 2010b). Quantitative chl-*a* estimation for floating vegetation detected by the MPH algorithm is not currently accounted for, although might be feasible following correct parameterisation on a species basis. Since reflectance signatures from floating macrophytes do not possess the distinctive reflectance features of cyanobacteria, it is rather simple to distinguish between these and cyano-scum, using equation 2.4. The separation of land and water pixels also becomes more challenging when dealing with highly enlarged reflectance data in the NIR caused by floating macrophytes.

Each BRR spectrum was assigned to one of the following classes or MPH domains: the fluorescence domain (681 nm peak), the backscatter domain (709 nm peak), and the 'dry' domain (753 nm peak). For each domain, a series of least squares fitting procedures correlated the observed matching *in situ* chl-*a* concentration with the MPH variable. In each case, the following functions were tested: exponential growth function of form $y = a\exp(bx)$, quadratic function of form $y = ax^2 + bx + c$, power law function $y = ax^b$, and linear fit $y = a + bx$. The goodness of fit was in each case judged by the value of the root mean square error (rmse). The results of the analysis are presented in section 2.4.2.

2.4 RESULTS AND DISCUSSION

2.4.1 AN ANALYSIS OF ADJACENCY EFFECT CORRECTIONS USING ICOL+

To assess the effect of the ICOL correction, a comparison between adjacency effect corrected bottom-of-Rayleigh reflectances and uncorrected bottom-of-Rayleigh reflectances was performed (fig. 2.4.1). Some unusual and unexpected spectral shapes were obtained following correction with ICOL and these are illustrated using a few selected spectra (fig. 2.4.1A). Against expectations, many of the corrected spectra showed elevated values at 885 nm and unusual shapes in the $753 - 778$ nm region (compare to fig. 2.2.1). To gauge the overall effect of ICOL on the red bands, the mean percentage difference between uncorrected and corrected spectra was calculated (fig. 2.4.1B). As expected, the effect of ICOL was to decrease the overall magnitude of the bands in the red. The mean percentage difference was -12.6% at 664 nm, -12.2% at 681 nm, -13.5% in at 709 nm, -10.7% at 753 nm and -5.2% at 885nm. ICOL had the greatest relative effect on the 709 nm band, while the effect further in the NIR is roughly half that. This result appears to be against expectations, given that other studies suggest that the adjacency effect is relatively larger in bands further towards the NIR (e.g. Odermatt et al., 2008). There is an expectation that bands further towards the NIR would have relatively larger adjacency correction factors. Therefore, there appears to be an overcorrection at smaller wavelengths (<709 nm) and an under-correction at larger wavelengths. Fig. 2.4.1C and 2.4.1D illustrate the effects of ICOL on the MPH variable. It was found that the height of the maximum peak in the red was reduced following ICOL by mean value of 12.0%, which had a significant effect on the value of the MPH variable. The MPH variable generally became smaller and there were more negative values (fig. 2.4.1C). The mean percentage difference between the corrected/uncorrected MPH variable values was -47.2%, which was heavily influenced by a small number of large outliers.

Evidently, ICOL has a large influence on the MPH variable and significant effects on the red bands. ICOL was implemented in a way that calculates the aerosol type (that is the *Ångström* coefficient, α) and the aerosol optical thickness (AOT) over water while taking into account case I or case II water (based on the BRR at 709 nm). This means that the retrieval of the AOT and the aerosol type (α) is determined simultaneously from NIR bands and extrapolated to smaller MERIS bands (Santer, 2010). Therefore, the selection of an incorrect aerosol type could lead to the unusual effects (bias) observed in the ρ_{AECBR}. Therefore, the unexpected effects appear to be

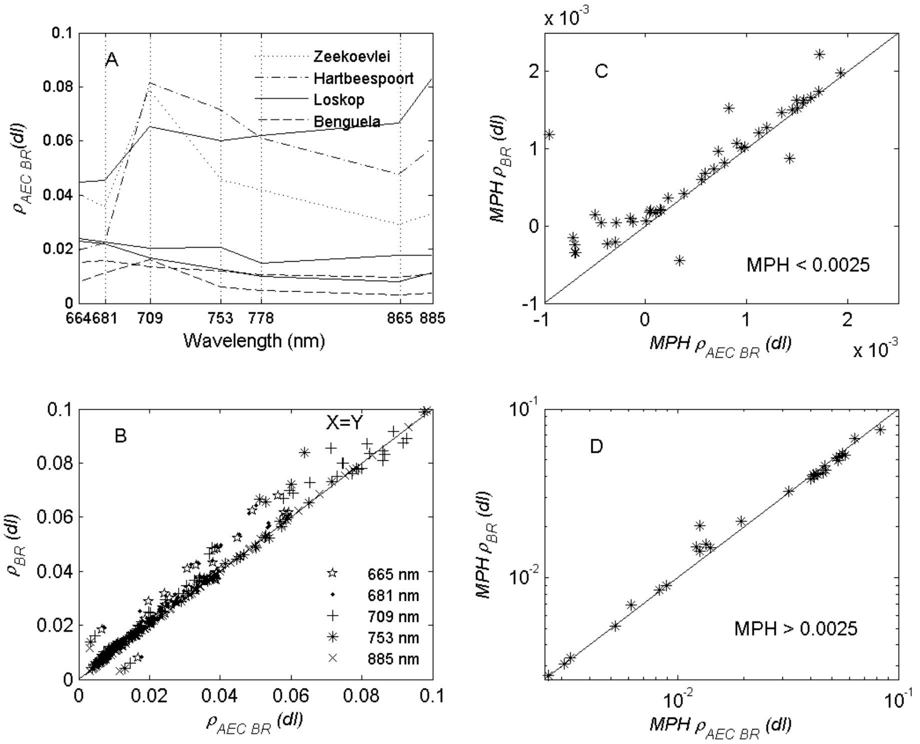

Figure 2.4.1: Comparison between uncorrected bottom-of-Rayleigh reflectances (ρ_{BR}) and those corrected for the adjacency effect using the ICOL+ processor (ρ_{AECBR}). Panel A shows selected spectra identified because of their unusual shapes following correction with ICOL. The change in the MERIS red bands following correction with ICOL is show in panel B. Similarly, panels C and D show the change in the MPH variable after application of ICOL, for low (C) and high ranges (D). dl = dimensionless.

associated with the retrieval of the AOT and aerosol type selection. Based on these findings, an adjacency correction only taking into account Rayleigh effects is preferable, based on the recommendation of Santer and Schmechtig (2000) for operational adjacency effect corrections. The main reason for this is due to the large influence that the vertical aerosol distribution has on the aerosol adjacency effect, which is unknown (*ibid.*). It seems that an adjacency effect correction including aerosol effects over these targets is currently not well performed and introduces artifacts in the data that cause more negative and erratic MPH variable values. Due to the sensitivity of the MPH variable to relative changes in the red/NIR bands and based on these initial analyses, ICOL+ is not recommended for application with the MPH algorithm at this stage. Undoubtedly, the small size and eutrophic conditions of the water targets makes them extremely challenging targets for any atmospheric or adjacency effect correction procedure.

2.4.2 PARAMETERISATION OF THE MPH ALGORITHM

THE FLUORESCENCE 681 NM DOMAIN

Separate fits were used to best describe the fluorescence and backscatter/absorption domains. In the fluorescence domain the best fit was given as (fig. 2.4.2):

$$Chl\ a = 2.7 + 6903 \times MPH \tag{2.5}$$

The rmse is 3.5 mg chl-*a* m^{-3} and the mape is 69% for chl-*a* in the range $0.5 - 30$ mg m^{-3} (r^2 = 0.71, p = 0.00, F=83, N=36). Therefore the algorithm is sensitive to a minimum chl-*a* value of approximately 3.5 mg m^{-3}. To improve the goodness of fit, the algorithm is constrained to data points with maximum peak positions at 681 nm and corresponding chl-*a* values < 30 mg m^{-3}. This resulted in several outliers being excluded that had chl-*a* values > 30 mg m^{-3} (N=3). The rationale for excluding these data is due to the difficulty in quantifying the fluorescence signal in waters with chl-*a* values > 30 mg m^{-3} (Babin, 1996), and in order to improve the algorithm's sensitivity at lower values. Further to this, outliers (show in grey on fig. 2.4.2) were also excluded from the regression, on the basis of a 95% confidence interval for studentised residuals (N=2). This also served to improve the goodness of fit.

Fig. 2.4.2 includes several data points with negative MPH values, all of which are from Loskop. These negative values are within the 95% confidence interval and occupy an expected region of low chl-*a* concentrations. For these reasons the data are not excluded. In determining an explanation for the negative MPH values, the specific conditions related to the target (Loskop), and the mechanisms whereby the MPH variable becomes inverted must be considered. Firstly, the data points are from the very dark oligotrophic main basin in Loskop lake. Atmospheric correction over similar, dark, oligotrophic lakes is extremely challenging due to stray light adjacency effects and the dark nature of the target (for the impact of the adjacency effect in subalpine lakes see Guanter et al., 2010, Odermatt et al., 2010). Such effects would cause reflectances in the red and NIR bands to be enlarged resulting in an inverted (negative) MPH variable. This seems to be the most plausible explanation for the negative values and highlights the difficulty associated with handling small, oligotrophic inland waters.

Despite this finding, the algorithm's performance in the florescence domain seems to be very robust given that it is capable of detecting chl-*a* with a sensitivity of less than 4 mg m^{-3} from bottom-of-Rayleigh reflectance data. As fig. 2.4.2 shows, there were no data points from cyano-dominant waters (Zeekoevlei/Hartbeespoort) belonging to the fluorescence domain. Table 2.4.1 shows statistics associated with the MPH variable in the fluorescence domain.

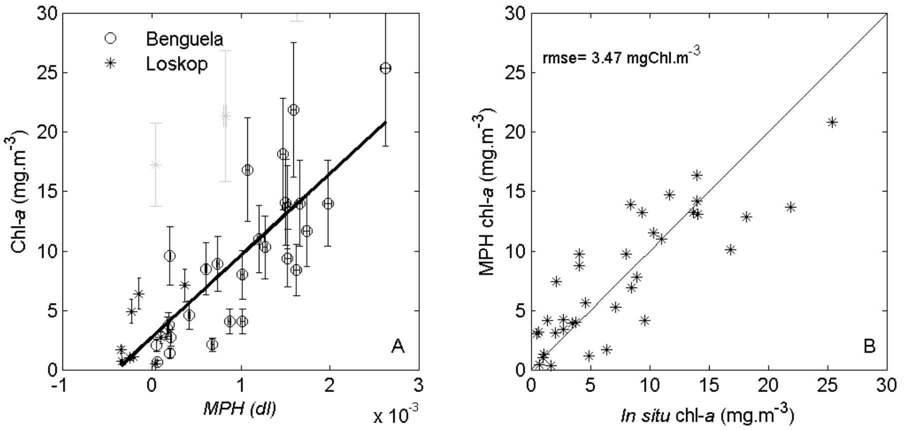

Figure 2.4.2: Chl-*a* versus the MPH variable for the fluorescence domain calculated using a maximum peak-height position of 681 nm (panel A). Only data from Loskop and Benguela study areas belonged to this domain. Outliers are shown in grey. The observed chl-*a* versus that estimated by the MPH algorithm is shown in panel B. *dl* = dimensionless.

THE BACKSCATTER/ABSORPTION 709 NM DOMAIN

There was a large offset in MPH values between data points from *Microcystis* cyano-dominant waters (Zeekoevlei and Hartbeespoort) and those from eukaryote dominant waters (Loskop/Benguela) (fig. 2.4.3). Concurrently, there was significant overlap between the data for each of these water types. Therefore, separate fits were used for *Microcystis* cyano-dominant waters (prokaryotes) and for waters with phytoplankton assemblages made up predominately of dinoflagellates or diatoms (eukaryotes) (fig. 2.4.3A). For dinoflagellate/diatom dominant waters, the best fit was given as:

$$Chl\ a = 37.2 + 11228.4 \times MPH \tag{2.6}$$

The rmse is 88.8 mg m^{-3} which equates to a mean percentage error (mpe) of 104% (r^2=0.384, p=0.042, F=5.6). According to studentised residual values, there were no outliers. The algorithm was not constrained further due to the small sample number (N=11). The relatively low statistical significance and large mpe must be taken into account given the small sample size and the large range of chl-*a* values over which the algorithm is expected to perform (a range of 343 mg m^{-3}). An

Table 2.4.1: Statistics for the MPH variable grouped by the position of the maximum peak-height.

Domain	Mean	Min.	Max.	Range	St. dev.	Chl-a min.	Chl-a max.
Fluorescence	0.00073	-0.00034	0.0026	0.00029	0.00078	0.5	26.85
Backscatter (dino/diatom)	0.0105	0.0022	0.0203	0.0180	0.0059	7.7	350.4
Backscatter (cyano)	0.0465	0.0217	0.0752	0.0536	0.0124	33.0	362.5

exponential fit was obtained for *Microcystis* cyano-dominant waters:

$$Chl\ a = 22.4 \times exp(35.8 \times MPH) \tag{2.7}$$

The robust nonlinear least squares estimation gave an rmse of 46.6 mg m^{-3} corresponding to a mape of 33.7% (r^2=0.58, N=17). All of the data from cyano-dominant waters had a 709 peak position and MPH values > 0.02 (see 2.4.1). Based on the intercept of the algorithm, only chl-*a* values greater than 22.4 mg m^{-3} can be estimated using the algorithm.

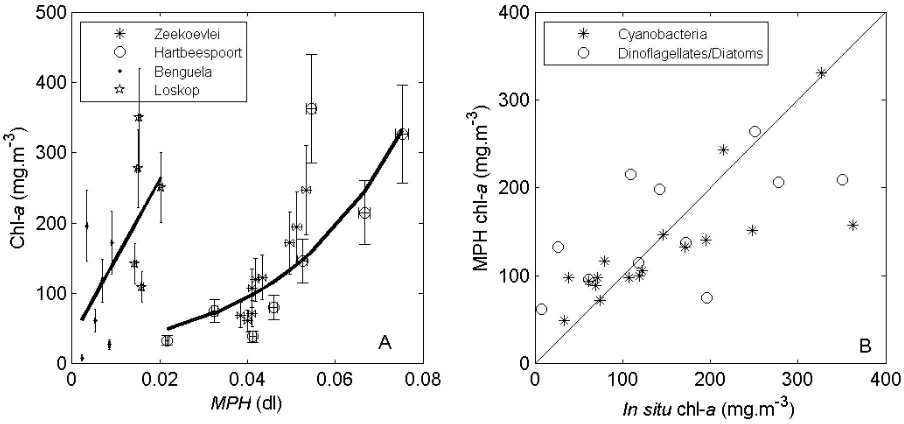

Figure 2.4.3: Performance of the MPH algorithm for the backscatter/absorption domain (panel A). Separate fits were used for cyano-dominant waters (Hartbeesport/Zeekoevlei) and eukaryote dominant waters (Loskop/Benguela). The observed vs. predicted chl-*a* is shown in panel B.

THEORETICAL CONSIDERATIONS RELATED TO CYANO-DOMINANT WATERS

The large discontinuity in fig. 2.4.3 enables us to distinguish *Microcystis* dominant cyano-blooms purely on the basis of the magnitude of the MPH variable. These large and quantifiable differences in the red-NIR reflectance between *Microcystis* and textitDinoflagellate/Diatom dominant waters requires closer examination. Assuming phytoplankton is the dominant constituent with regards to causal IOPs, the magnitude of the 709 nm peak will predominantly be dependent upon the specific backscattering coefficient (b_b^*) of the dominant phytoplankton species, which is known to vary by several orders of magnitude between different cultured species/classes (Stramski et al., 2001, Whitmire et al., 2010). Therefore, the large observed discontinuity could be explained on the basis that *Microcystis* spp. cyanobacteria have significantly greater backscattering per unit chl-*a* (chl-*a* specific backscatter coefficients, b_b^*) in the red than the dinoflagellate/diatom species in our dataset. This would lead to larger MPH values such as observed in *Microcystis* cyano-dominant waters since remote sensing reflectance is directly proportional to backscatter ($R_{rs} \approx b_b/(a + b_b)$), while also providing a robust theoretical explanation for the observations. However, is there any evidence for this hypothesis?

Firstly, there is a significant amount of evidence that gas vacuoles found in certain cyanobacterial species (incl. *M. aeruginosa*) are very efficient light scatterers in the forward and backward direction (Walsby, 1994). For example, in a turbid reservoir dominated by *Microcystis* spp., Ganf et al. (1989) found that 80% of light scatter could be attributed to the intracellular gas vacuoles. Further evidence can be found in the findings of Volten et al. (1998) who showed that the presence of gas vacuoles altered the scattering properties of phytoplankton considerably, in agreement with the earlier findings of Dubelaar et al. (1987) who found anomalous light scatter in vacuolate *M. aeruginosa*. Because morphological differences and intracellular structure has been shown to have a large influence on backscattering (Svensen et al., 2007, Whitmire et al., 2010), the effect of gas vesicles contained in cells on backscattering is likely to be substantial. Secondly, phytoplankton with small diameters (d) possess larger backscatter per unit chl-*a* (b_b^*) than intermediate and large celled species (Ahn et al., 1992, Bernard et al., 2009). Consequently, per unit chl-*a*, small-celled vacuolate *Microcystis* cyanobacteria may backscatter up to two orders of magnitude greater than larger and non-vacuolate species. Therefore, based on the presence of vacuoles, and on theoretical explanations and experimental observations related to cell size, *Microcystis* cyanobacteria in many instances posses larger b_b^* than eukaryote and non-vacuolate species. This is examined in detail in Chapter 4 with respect to the effects of intracellular gas vacuoles.

To verify whether this can be observed in natural waters, ancillary measurements of spectral backscattering collected using a Hydroscat 2 meter (Hobilabs Inc.) in *M. aeruginosa* dominant blooms in Hartbeespoort and in a dense (chl-*a* > 500 mg m^{-3}) dinoflagellate *Ceratium balechii* bloom in the southern Benguela (see Pitcher and Probyn, 2011) were used. The Hydroscat was configured to measure the backscattering coefficient at 420 and 700 nm. The conversion between the measured volume scattering function at 120 ° (minus pure water) to backscattering was based on a single conversion factor (χ) obtained from instrument calibration (Maffione and Dana, 1997). A single conversion factor is known to be generally sufficient for use with various phytoplankton classes (e.g. Whitmire et al., 2010). From co-incident backscatter and chl-*a* measurements, a mean chl-*a* specific particulate backscatter (b_{bp}^*) in Hartbeespoort was calculated as 0.4×10^{-3} m^{-1} at 420 nm and 1.98×10^{-3} m^{-1} at 700 nm (N = 13). In contrast, b_{bp}^* in the marine *Ceratium* bloom was 0.116×10^{-3} m^{-1} at 420 nm and 0.141×10^{-3} m^{-1} at 700 nm, an order or magnitude smaller than for *Microcystis*. These measurements, made in blooms when phytoplankton was demonstrably the dominant contributor to bulk IOPs, are within the range of those presented in Ahn et al. (1992) and Whitmire et al. (2010). If anything, the value for *Microcystis* is underestimated given that the measurements were made at a depth of 0.68 m and the blooms were floating. Nevertheless, the measurements reveal that for *M. aeruginosa*, backscatter is slanted towards the red and is at least an order-of magnitude larger in the red than for the dinoflagellate *C. balechii*. A detailed comparison of the backscattering properties of dinoflagellates and vacuolate cyanobacteria is presented in Chapter

5.

Further supporting evidence is found in Whitmire et al. (2010) who showed that for single species of cultured marine phytoplankton, there is a significant linear relationship between chl-*a* and b_{bp}, and that the magnitude and slope of b_{bp} is distinctive enough to distinguish between different species (see Fig. 5 in Whitmire et al., 2010). Substantial experimental and theoretical grounds therefore exist for the result in fig. 2.4.3. This might offer significant justification for the finding that *Microcystis* dominant cyano-blooms are distinguishable from non-cyanobacterial blooms based on the magnitude of the backscatter/absorption-induced 709 nm peak, and on the observation of accessory pigment related reflectance features (such as those of phycocyanin). Given that the phytoplankton assemblages in our study areas were made up of comparative species, either *M. aeruginosa* or *Ceratium* spp., the relationship between chl-*a* and b_{bp} was maintained between the systems, allowing derivation of algorithms specific for each of these phytoplankton classes.

2.4.3 An operational switching MPH algorithm

In order to obtain an algorithm suitable for operational use, separate algorithms for eukaryote algal assemblages and for waters identified as cyano-dominant were developed. Table 2.4.1 shows the descriptive statistics for the MPH variable obtained from the statistical fits in figs. 2.4.2 and 2.4.3. The continuity between the fluorescence domain and the backscatter domain for eukaryotes is good, with some overlap. Therefore, in order to obtain a single continuous algorithm for chl-*a* estimation in eukaryote dominant waters, a 4th order polynomial was fitted after sorting the data (fig. 2.4.4) to obtain the following equation:

$$Chl\,a(Eukaryotes) = 5.24 \times 10^{9} mph^{4} - 1.95 \times 10^{8} mph^{3} + 2.46 \times 10^{6} mph^{2} + 4.02 \times 10^{3} mph + 1.97 \tag{2.8}$$

The mean absolute percentage error between the derived function and the unsorted data is 59.9% and the r^2 value is 0.71. The operational algorithm is designed to operate seamlessly between the fluorescence and backscatter/absorption domains for eukaryote SICF possessing algae. Similar 4th order polynomials are also used for the operational empirical algorithms for MODIS (OC3M) (Campbell and Feng, 2005) and SeaWiFS (OC4) (O'Reilly et al., 1998), which use the maximum value of several band ratios, similar to the maximum peak selection of the MPH algorithm. The polynomial fit is advantageous because it provides good continuity between the different domains of the algorithm, shown in fig. 2.4.4A. It is important to consider that the algorithm here is not a 'best fit' for the data - the data has been sorted to give this fit - but rather the polynomial function was used as to obtain the smallest difference between predicted and observed chl-*a*. For waters identified as cyano-dominant based on the flag in section 2.3.3, eq. 2.7 was used (fig. 2.4.4B). The combined performance of the algorithms (fig. 2.4.4 C and D) in each of the trophic status classes is:

oligotrophic, mape=71%, N=26; mesotrophic, mape=19%, N=9; eutrophic, mape= 131%, N=3; hypertrophic, mape=37%, N = 10.

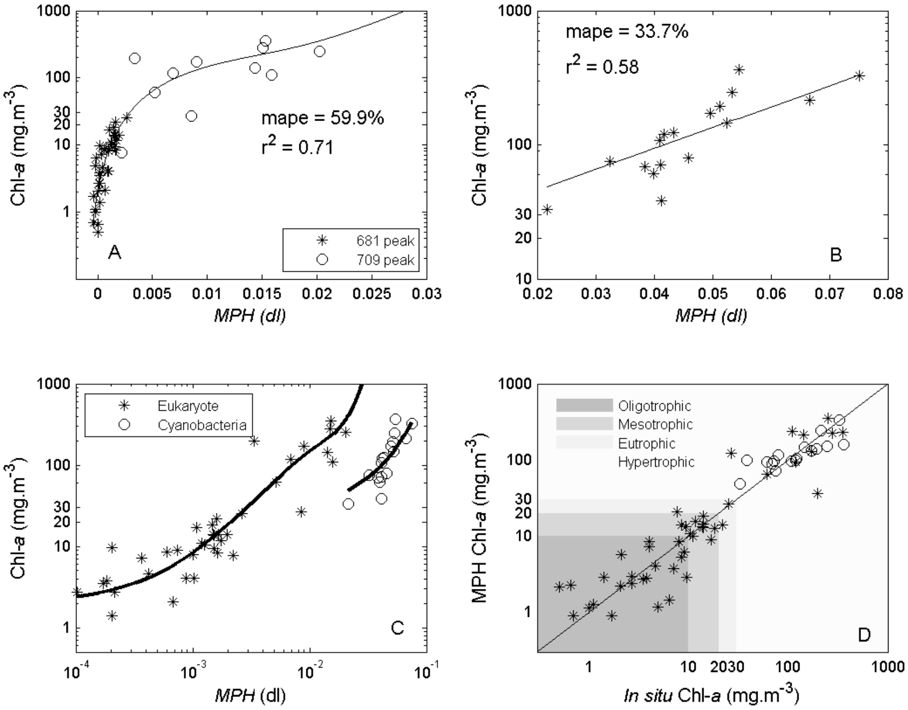

Figure 2.4.4: The switching operational MPH algorithm for eukaryote-dominant waters showing class membership (panel A). The MPH algorithm for cyano-dominant waters (panel B). The combined algorithms scope and performance is shown in panels C and D. Panel D shows the algorithms performance relative to trophic status classification.

2.5 APPLICATION AND CONCLUSIONS

2.5.1 APPLICATION TO STUDY AREAS

The operational MPH algorithm (section 2.4.3) was applied to imagery from the study areas in order to test its performance (fig. 2.5.1). The following cases were used to assess different aspects of the algorithm:

1. Identification of cyano-scums and cyano-dominant water in the hypertrophic waters of Hartbeespoort Dam.

2. Trophic status detection over a wide range of trophic states from oligotrophic to hypertrophic in eukaryotic-dominated assemblages in Loskop Dam.

3. High biomass HAB event detection in the waters of the southern Benguela and comparison of standard MERIS L2 algal products.

For the first test case, the cyano-flag correctly identified cyano-dominant water as well as cyano-scums that were observed at Hartbeespoort *in situ* during October 2010 (fig. 2.5.1B). Cyano-scum presents a substantial risk for significant levels of toxin production (more than 50% of cyano-scums analysed in a sample of 50 scums in the U.K. were found to be toxic Codd, 2000). As a control, the algorithm was also applied to a scene from winter of the same year, before the onset of the spring cyano-bloom (fig. 2.5.1A). In this case the algorithm did not detect the presence of cyanobacteria in the lake, although this may be a result of chl-*a* concentrations below the detection limits of the cyano-flag ($< 30\,\mathrm{mg\,m^{-3}}$). Nevertheless, the example illustrates how the algorithm might be used for cyano-detection in small hypertrophic inland waters, and serve as a warning product for both commercial and recreational users. The cyano-flag also appeared robust when applied to a time series of the data (see Chapter 6).

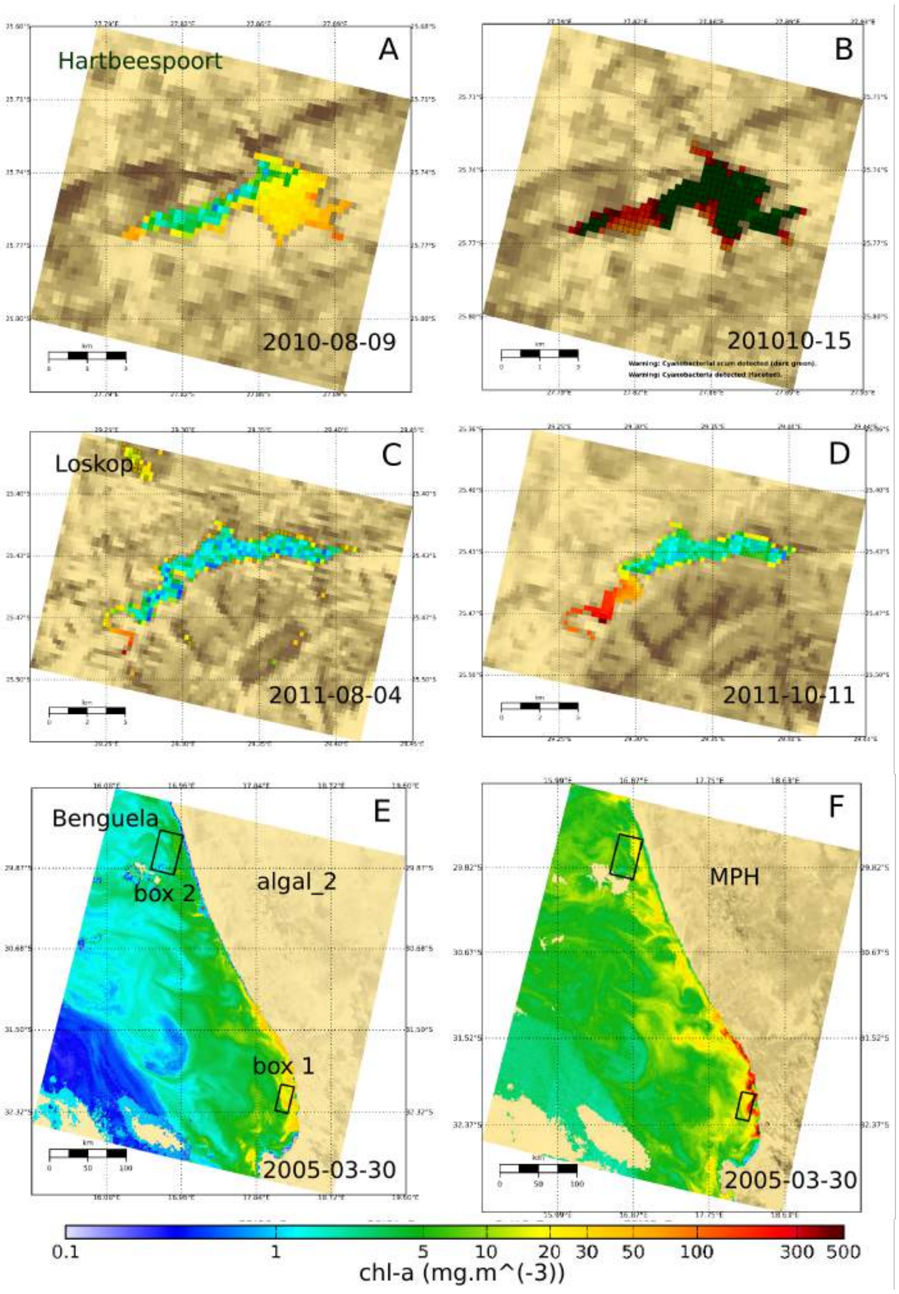

Figure 2.5.1: Example applications of MPH algorithm to Hartbeespoort Dam (A, B) Loskop Dam (C, D) and the southern Benguela (F). The MERIS standard L2 algal2 product is shown in panel E. Shaded and faceted pixels indicate where the cyano-flag has been raised, while dark green pixels indicate surface scum (chl-*a* > 500 mg m^{-3}). Box 1 shows the pixels extracted for comparison with the algal2 product, while box 2 shows those extracted for comparison with algal1.

For the second test case, the MPH algorithm reproduced the strong longitudinal chl-*a* gradient observed *in situ* in Loskop during August of 2011 (fig 2.5.1C). The hypertrophic water towards the riverine zone in the south west corner shows the presence of a persistent *Ceratium* dinoflagellate bloom, which was correctly identified as eukaryote-dominated water (not cyanobacteria) by the algorithm. Towards the north east and the main basin of the lake, the algorithm reproduced the gradual trophic gradient until oligotrophic water was detected in the main basin (chl-*a* < 3 mg m^{-3}). This demonstrates the algorithm's ability to operate over a large trophic range, switching smoothly between the 681 nm fluorescence and 709 nm backscatter/absorption-induced peaks as the optimal signal source. A second image from October 2011 shows that the bloom has moved further downstream towards the main basin of the lake most likely in response to the first spring rainfall (fig 2.5.1D). This example illustrates the capability of the MPH algorithm to operate across a wide range of trophic states in a small lake with some confidence and shows how the MPH algorithm might be used as a trophic status indicator in small inland waters.

The final test case is a high-biomass *Prorocentrum triestinum* bloom that occurred in the southern Benguela during March 2005 (fig. 2.5.1 E and F). Chl-*a* derived from the MPH algorithm correctly estimated the extremely high concentrations (> 500 mg m^{-3}) that were observed *in situ* towards the coastline, and which occurred occasionally in dense patches (fig. 2.5.1F). However, the standard MERIS L2 algal1 and the case II algal2 product (fig. 2.5.1E) severely underestimated the bloom biomass near the coast. To achieve a more detailed understanding of the performance of the standard MERIS L2 algal products for the region relative to the MPH algorithm, pixels were extracted from the rectangular boxes drawn in fig. 2.5.1E, and scatter plots made (fig. 2.5.2). The two areas were selected on the basis of the validity flags of the algal1 and algal2 products and on biomass: the area for algal2 had higher biomass and covered the peak bloom area, while the area for algal1 generally had chl-*a* < 25 mg m^{-3}. For waters with chl-*a* < 25 mg m^{-3}, the algal1 product was found to be highly covariant ($r^2 = 0.93$) with the MPH algorithm estimates. However, algal1 was consistently and significantly smaller than chl-*a* estimates from the MPH algorithm (fig. 2.5.2A). This either is a result of underestimates from the algal1 product, or due to limit of detection of the MPH algorithm, which is likely near 3.5 mg m^{-3}. The findings suggests that algal1 may underestimate chl-*a* in oligo/mesotrophic waters in the Benguela region.

In waters surrounding the peak area of the bloom, chl-*a* estimates from algal2 were highly covariant with those from the MPH algorithm (r^2=0.88) when constrained to an upper range of 45 mg m^{-3} (fig. 2.5.2B). Although the algal2 product is generally smaller, the values estimated in the range between 15 and 30 mg m^{-3} are quite similar. For chl-*a* > 45 mg m^{-3}, there was no correlation, since algal2 has an upper training range of around 30 mg m^{-3} (Schiller and Doerffer, 2005). For chl-*a* concentrations above the upper limits of algal2, the estimates neatly occupied an expected position on the plot. Therefore the preliminary comparison results indicate that the standard MERIS L2 products generally underestimate biomass in the southern Benguela during bloom conditions.

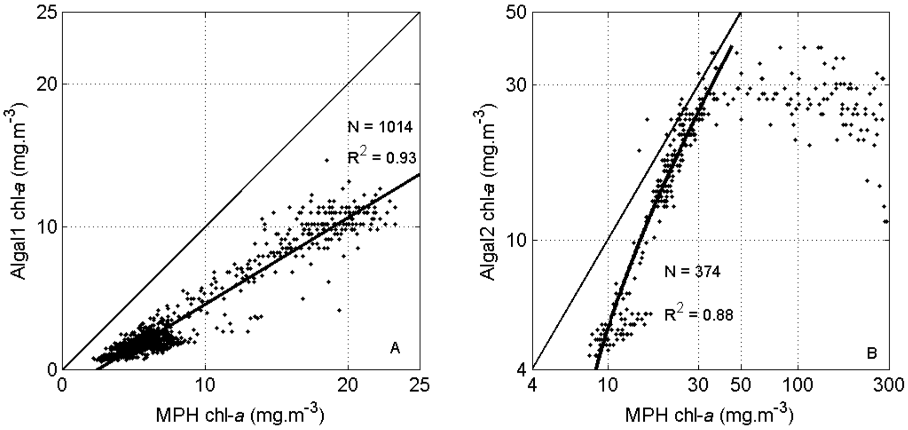

Figure 2.5.2: Comparison between MERIS standard level 2 products, algal1 (panel A) and algal2 (panel B) and chl-*a* derived from the MPH algorithm in the southern Benguela in a large dinoflagellate bloom on 30 March 2005. The boxes in fig. 6 show where the data was taken from within the MERIS scene.

These standard products may however be useful for providing estimates below the detection limits of the MPH algorithm, which is around 3.5 mg m^{-3}. An independent validation of the MPH product in inland waters is presented in Chapter 6.

Further comparison between the MPH algorithm and other ocean colour algorithms was not performed for the Benguela primarily because the algorithms are constrained to an upper limit near 30 mg chl-*a* m^{-3} which is generally too low for the region. Further testing of the MPH algorithm using *in situ* data sets (such as NOMAD) is not feasible as these currently lack sufficiently high chl-*a* data and the appropriate red/NIR reflectance data.

2.5.2 GLOBAL APPLICATION EXAMPLES

The MPH algorithm was applied to various well-known study areas in order to demonstrate its cross-applicability for both cyanobacteria and floating algae detection in diverse environments. The Baltic sea is frequently affected by very large cyano-blooms in summer months that form surface scums, and these have often been observed using remote sensing (e.g. Reinart and Kutser, 2006). Fig 2.5.3A. shows the MPH algorithm applied to a MERIS RR scene on 17 July 2002 (note cyano-mask alongside for comparison). The MPH algorithm correctly identifies the cyanobacterial bloom which according to Reinart and Kutser (2006) are most likely *Aphanizomenon flos-aquae, Nodularia spumigena,* or *Dolichospermum circinale.* This demonstrates the cyano-flag correctly identifies buoyant marine species of cyanobacteria in the Baltic sea. The range of chl-*a* values estimated by the algorithm are also within the ranges of those estimated by local algorithms for blooms occurring in the same month (Reinart and Kutser, 2006). Therefore initial results from the MPH algorithm indicates that it might be well-suited for application with cyano-blooms in the Baltic Sea, where conventional algorithms most often often fail (Reinart and Kutser, 2006).

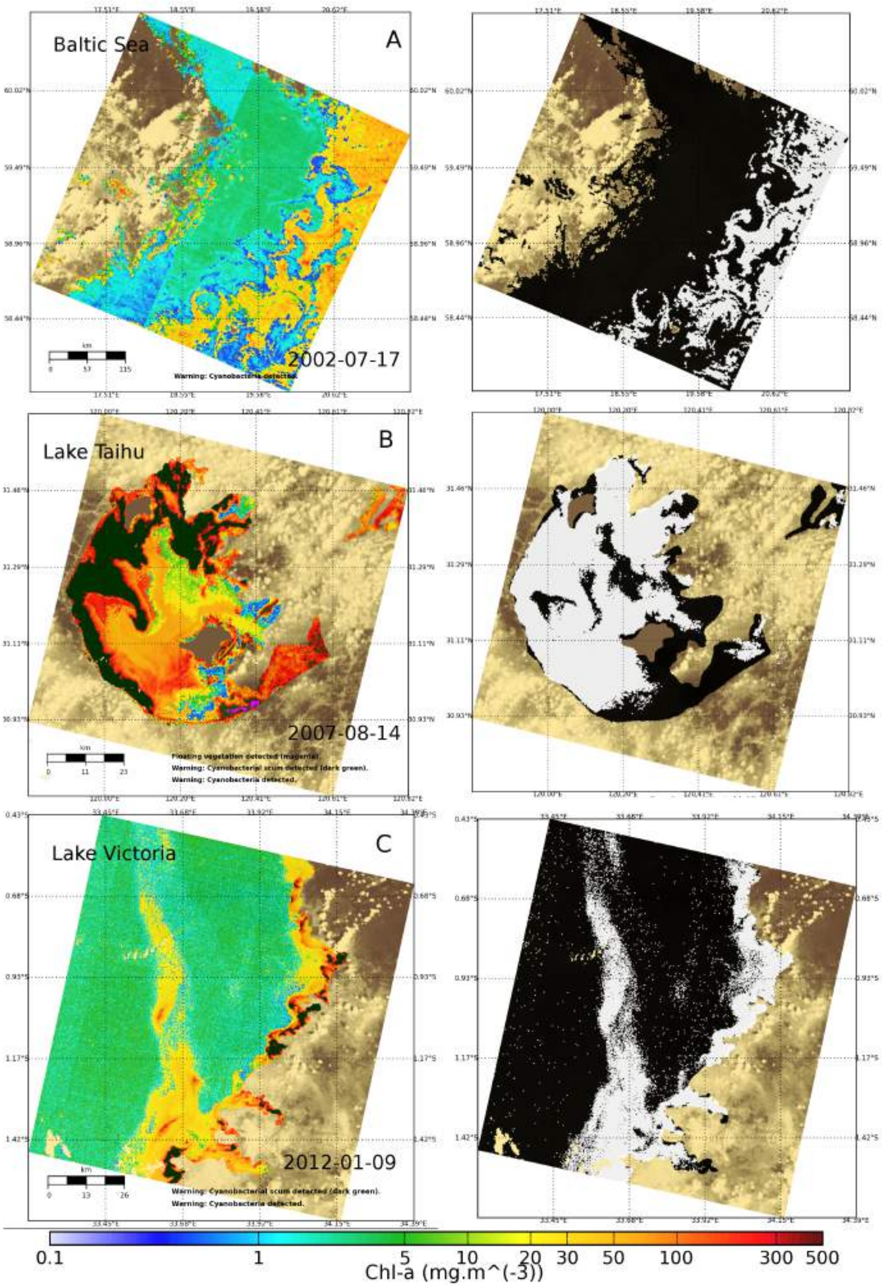

Figure 2.5.3: Global examples of the MPH algorithm in A) the Baltic sea during and intense cyanobacteria bloom (likely *Aphanizomenon flos-aquae*), B) Lake Taihu (*M. aeruginosa*), and C) Lake Victoria (unidentified species). The corresponding images alongside show the cyano-flag (white pixels equals cyanobacteria, black pixels equals other water).

Lake Taihu in China is well known for outbreaks of severe *Microcystis* spp. blooms that accumulate in dense cyano-scums on the surface. These have recently been observed in a ten year time series using MODIS and the FAI (Hu et al., 2010a). Initial results from the MPH algorithm in Lake Taihu show that it correctly identifies these cyano-blooms and scums, reproducing the observations of Hu et al. (2010a) (fig. 2.5.3B). This result is expected as the MPH algorithm is derived from lakes with *Microcystis* spp. dominated assemblages similar to Lake Taihu. As can be seen in the south eastern parts of the Lake, the MPH algorithm also detected floating macrophyte vegetation (magenta pixels). Macrophytes are known to occur in this region of the Lake and are most likely *Potamogeton maackianus* (pondweed) or *Vallisneria natans* (eelgrass) which are emergent and floating-leaf species (Qin et al., 2007). A final example is given from Lake Victoria, which experiences severe eutrophication and cyano-dominance in some regions (Lung'ayia et al., 2000). Floating vegetation such as waterhyacinth (*E. crassipes*), Nile Cabbage (*Pistia stratiotes*), and water lily (*Nymphaea caerulea*) are also present in the Lake in standing crops (Cavalli et al., 2009). Fig 2.5.3C shows a MERIS FR scene indicating a large bloom identified as cyanobacteria, most likely *Microcystis* or *Dolichospermum* (see Lung'ayia et al., 2000), extending into the central parts of the Lake, along with cyano-scum accumulations along the shoreline. This example, together with those above, demonstrate how the MPH algorithm and cyano-flag might be used for global monitoring of trophic status and cyano-blooms.

2.5.3 CONCLUSION

In conclusion, the MPH algorithm provides a new and efficient method for trophic status determination, cyano-bloom monitoring and floating vegetation detection in inland and coastal waters. The findings demonstrate that chl-*a* estimates for trophic status determination might be given with considerable accuracy using a top-of-atmosphere approach by taking advantage of fluorescence and backscatter/absorption related features in the red/NIR wavelengths of MERIS. These features are clearly discernible in the TOA MERIS reflectance data and the baseline-subtraction calculation of the MPH algorithm provides an effective normalisation of atmospheric effects, assuming that aerosol effects are relatively constant between the 664 and 885 nm bands. Therefore for broad trophic status assessment, simple Rayleigh atmospheric corrections are likely sufficient and avoid the more complicated and error-prone aerosol atmospheric corrections in turbid case II waters. The advantages of a TOA-type approach are also evident in improved processing times and simpler implementation for operational monitoring systems.

The MPH variable is suitable for distinguishing eukaryotic phytoplankton from vacuolate cyanobacteria species. Large differences were observed in MPH magnitude between assemblages dominated by prokaryotic cyanobacteria *Microcystis* spp. (Zeekoevlei/Hartbeespoort) and eukaryotic dinoflagellates/diatoms (Benguela/Loskop). These differences allow for the discrimination of these phytoplankton types/classes in high biomass circumstances based on the magnitude of the MPH variable. This is substantiated by evidence that *Microcystis* dominant cyano-dominant waters have considerably higher backscatter per unit chl-*a* leading to the increased magnitude of the MPH variable. This finding indicates the potential for 'tuning' of the MPH algorithm for detecting various phytoplankton classes on the basis of species-specific chl-*a* specific backscatter relationships as shown in Chapter 4 section 4.4.2 (*cf.* Whitmire et al., 2010). Radiative transfer modeling studies will undoubtedly be valuable in confirming and further substantiating this finding, providing that appropriate parameterisations of the the relevant phase functions and IOPs are available (see Chapters 4 and 5). In addition, a flagging method was defined which allows cyano-dominant waters to be distinguished from other blooms on the basis of cyanobacteria-specific spectral pigmentation features related to enhanced SIPF and reduced SICF. Initial results from cases with coincident *in situ* observations, and examples from global applications, suggest that this flag is a robust method for detecting high-biomass occurrences of cyano-blooms (chl-$a > 20$ mg m^{-3}). Further application of this technique, such as that presented in Chapter 6 of this study, will undoubtedly have significant implications for cyanobacteria-oriented remote sensing warning systems, as well as for frequency/risk analysis applications and bloom phenology.

The uncertainties related to the chl-*a* algorithms originate from the discreet-point sampling error, chl-*a* quantification methods, and atmospheric and sub-pixel variability. Notwithstanding the relatively small magnitudes of these errors, chl-*a* estimates are likely confident to within 3.5 mg m^{-3} for chl-$a < 30$ mg m^{-3}, and within 50 mg m^{-3} for chl-$a < 500$ mg m^{-3}. Detection of cyano-bloom initiation remains challenging due to a lack of appropriate signal caused by a relative absence of

SICF (chl-$a < 30$ mg m^{-3}). Low-biomass waters having high mineral content also present a challenge due to interference with the SICF signal (Mckee et al., 2007). Therefore, the MPH algorithm is probably best suited for application in waters where phytoplankton is the dominant contributor to the bulk IOPs.

The MPH algorithm presents a new approach for empirical algorithms used to estimate chl-*a* in inland and coastal waters. This is one of only a few studies showing that empirical chl-*a* measurements are significantly correlated with a variable derived from top-of-atmosphere MERIS reflectance data (see also Giardino et al., 2005, Matthews et al., 2010). Furthermore, this is the first study where *Microcystis* cyano-dominant blooms have conclusively been distinguished from other high biomass eukaryote-dominant waters on the basis of enhanced chl-*a* specific backscatter as observed in the 709 nm peak in MERIS band 9 and accessory phycobilipigment features (but see also Wynne et al., 2008). This finding has significant implications for empirical and model-based algorithms aimed at identifying phytoplankton type in eutrophic waters from space. A new technique presented for cyanobacteria detection based on cyanobacteria-specific spectral pigmentation and fluorescence features should provide more information on the extent and severity of cyano-dominance in affected waters. Further work is needed to assess how the MPH algorithm compares with alternative algorithms such as NIR-red band ratio algorithms designed for high-biomass waters. In conclusion, the MPH algorithm provides a substantial opportunity for water quality monitoring systems aimed at filling information gaps. The routine generation of these products will have a broad range of conservation, trend analysis, status determination, quality auditing and ecosystem analysis applications.

This chapter is based on work published as:
Matthews, M. W., and Bernard, S. (2013). Characterizing the Absorption Properties for Remote Sensing of Three Small Optically-Diverse South African Reservoirs. Remote Sensing, 5, 4370–4404.

3

Characterising the absorption properties for remote sensing of three small optically-diverse South African reservoirs

Microcystis aeruginosa surface scum photographed in Hartbeespoort Dam, October 2010.

Abstract

Characterising the specific inherent optical properties (SIOPs) of water constituents is fundamental to remote sensing applications. Therefore, this Chapter presents the absorption properties of phytoplankton, *gelbstoff*, and tripton for three small, optically-diverse South African inland waters. The three reservoirs, Hartbeespoort, Loskop and Theewaterskloof, are challenging for remote sensing due to differences in phytoplankton assemblage and the considerable range of constituent concentrations. Relationships between the absorption properties and biogeophysical parameters chlorophyll-*a* (chl-*a*), TChl (chl-*a* plus pheopigments), seston, minerals and tripton are established. The value determined for the mass-specific tripton absorption coefficient at 442 nm, $a^*_{tr}(442)$, ranged from 0.024 to 0.263 $m^2\ g^{-1}$. The value of the TChl specific phytoplankton absorption coefficient (a^*_{φ}) was strongly influenced by phytoplankton species, size, accessory pigmentation and biomass. $a^*_{\varphi}(440)$ ranged from 0.056 to 0.018 $m^2\ mg^{-1}$ in oligotrophic to hypertrophic waters. The positive relationship between cell size and trophic state observed in open-ocean waters was violated by significant small cyanobacterial populations. The phycocyanin specific phytoplankton absorption at 620 nm, $a^*_{pc}(620)$, was determined as 0.007 $m^2\ g^{-1}$ in a *M. aeruginosa* bloom. Chl-*a* was a better indicator of phytoplankton biomass than PC in surface scums due to reduced accessory pigment production. Absorption budgets demonstrate that monospecific blooms of *M. aeruginosa* and *C. hirundinella* may be treated as ”cultures”, removing some complexities for remote sensing applications. However the majority of the water is optically-complex requiring the usage of all the SIOPs derived here for remote sensing applications. These results contribute toward a better understanding of IOPs and remote sensing applications in hypertrophic inland waters. The SIOPs may be used for developing remote sensing algorithms for the detection of biogeophysical parameters including chl-*a*, suspended matter, tripton and *gelbstoff*, and in advanced remote sensing studies for phytoplankton type detection.

3.1 INTRODUCTION

KNOWLEDGE OF THE INHERENT OPTICAL PROPERTIES (IOPs) including the absorption of phytoplankton, *gelbstoff* (or chromophoric dissolved organic matter), and tripton (non-living minerals and detritus) is critical to water remote sensing. IOPs are required for remote sensing algorithm development, and for physically based bio-optical models simulating the behaviour of light in water. Physically-based water constituent retrieval remote sensing algorithms, especially those targeting specific water types or classes, rely heavily on IOPs, as do biogeochemical models. As a result, much attention has been given to determining the variability in absorption properties of coastal and open-ocean marine waters (e.g. Babin et al., 2003, Bricaud et al., 2010, 1995). Recent studies have also sought to characterise the absorption properties of optically-complex inland and estuarine waters (e.g. Belzile et al., 2004, Binding et al., 2008, Campbell et al., 2010, Le et al., 2013, Perkins et al., 2009, Zhang et al., 2009b). However, there is an ongoing need to investigate the variability that might be encountered across these diverse systems, especially those that are hypertrophic. This poses an ongoing challenge for satellite-based remote sensing applications aimed at characterizing the phenology and ecological state of earth's precious and vulnerable freshwaters.

In water-scarce South Africa, man-made reservoirs provide an essential source of potable water to a growing urban population. Widespread eutrophication and cyanobacterial blooms have degraded water quality in many of these reservoirs, posing a potential health threat to millions of consumers, as well as for industrial and commercial users (Oberholster et al., 2005). Data on the optical characteristics and variability of these reservoirs is lacking, hindering present and future monitoring efforts using remote sensing. This Chapter aims to describe the variability in absorption properties of phytoplankton, *gelbstoff* and tripton of three optically-diverse South African reservoirs. It describes the relationships between absorption and biogeophysical variables, chl-*a*, seston (total suspended solids) and mineral dry weight. The chl-*a* specific absorption coefficients (a^*_φ) are determined for the diverse phytoplankton assemblages, and discussed with reference to typical values reported in case I waters. The variability of the phycocyanin (PC) specific absorption at 620 nm, $a^*_{pc}(620)$, used in semi-analytical algorithms aimed at detection of PC (e.g. Ruizverdu et al., 2008, Simis et al., 2005), is also determined for cyanobacterial blooms and in surface scums of *Microcystis aeruginosa*. The mass-specific tripton absorption coefficients (a^*_{tr}) are determined using a modified technique and the results compared to reported values from inland and coastal waters. Finally, absorption budgets are presented for each of the reservoirs. The aims of the Chapter are to provide a thorough description of the range of variability in absorption properties that might typically be encountered in South African inland waters, and to provide IOPs for use in remote sensing radiative transfer studies and physically-based water constituent retrieval algorithms (see Chapters 4 and 5).

3.2 METHODS

3.2.1 STUDY AREAS AND SAMPLING STRATEGY

The three study areas, Hartbeespoort, Loskop and Theewaterskloof reservoirs, were chosen in order to capture some of the diverse range of water types and blooms occurring in South African inland waters (Fig. 3.2.1). Sampling campaigns were undertaken at each of the lakes for a three week period: at Hartbeespoort in October 2010, at Loskop in July/August 2011 and at Theewaterskloof in April 2012. Sample points were located so as to capture the diversity of water conditions occurring in each of the reservoirs. Surface water samples were collected in 1 l plastic containers or in 5 l opaque plastic buckets following thorough rinsing with lake water. Every effort was made to avoid disturbing the dense aggregations of cyanobacteria on the water surface (when present) by gently collecting water into containers held horizontally. Samples were kept in the dark and on ice until analysis. Water clarity was measured using a secchi disk, z_{sd}, using the mean of the depth at which the disk disappeared and then re-appeared.

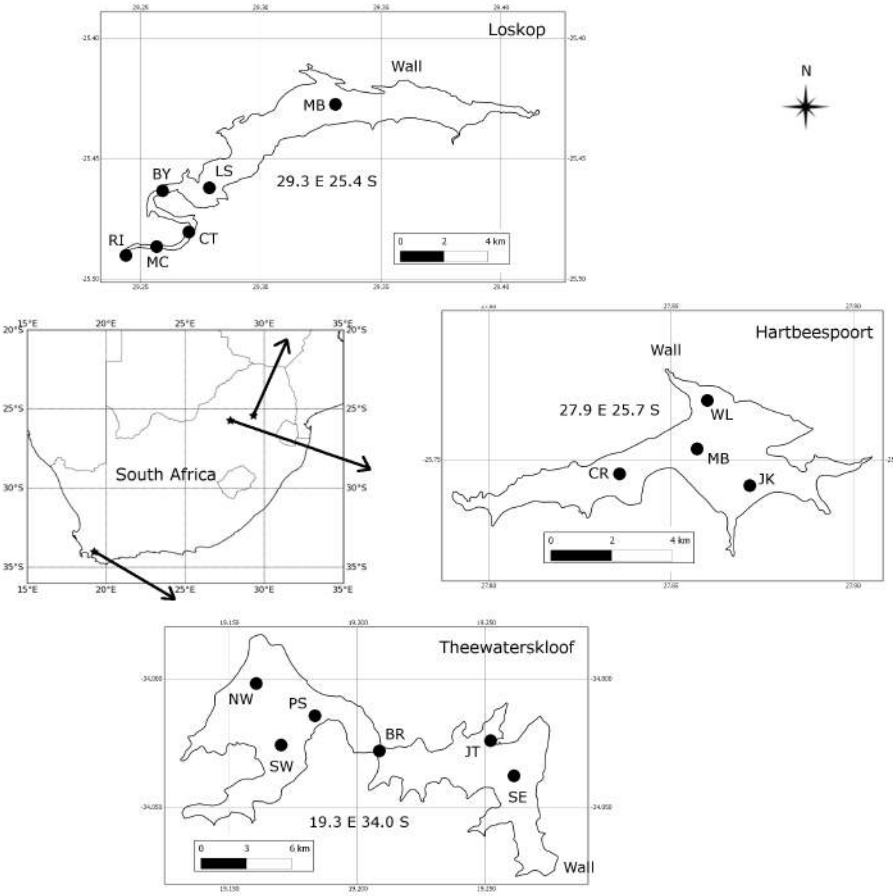

Figure 3.2.1: The geographical location and shapes of the three reservoirs Loskop, Hartbeespoort and Theewaterskloof. Sample points are indicated by labeled dots (see text for details).

Of the three study areas Hartbeespoort is the most extensively studied followed by Loskop while Theewaterskloof is almost undescribed in scientific literature. Detailed information on the limnology and phytoplankton dynamics of Hartbeespoort is available (e.g. Scott et al., 1977, van Ginkel and Silberbauer, 2007, Zohary et al., 1996). As discussed in Chapter 2, it is one of the most productive reservoirs in the world (Zohary, 1985). Measurements of its optical properties however are limited to light attenuation (Robarts, 1984, Robarts and Zohary, 1992). The water quality and phytoplankton assemblage of Loskop has previously been described (Dabrowski, 2012, Oberholster et al., 2010, Walmsley and Bruwer, 1980). Situated on the Olifants River, Loskop has very diverse water types due to its longitudinal zonation. However, information on its light environment is limited to Secchi disk. The third reservoir called Theewaterskloof is located in the western winter rainfall region of South Africa, and is one of the primary water supply reservoirs for the Cape Town region through an inter-basin transfer scheme. The reservoir is divided into two basins by a narrow channel crossed by a bridge, the western basin contains the inlet from the Sonderend River and the eastern basin the dam wall. Despite its great importance as a potable water supply, appears to be no citeable information on its limnology, phytoplankton assemblage, or light environment.

3.2.2 Phytoplankton pigments

Water samples were filtered under low pressure ($<$10 mm mercury pressure) through Whatmann GF/F filters on the same day as collection. The concentrations of chl-*a* and pheopigments were determined spectrophotometrically using an extraction solution of 90% boiling ethanol after Sartory and Grobbelaar (1984), due to the improved extraction efficiency of ethanol with freshwater phytoplankton assemblages containing cyanobacteria. TChl is defined as the sum of chl-a and pheopigments. Phycocyanin (PC) and allo-phycocyanin (APC) pigments were measured when cyanobacteria made up a significant portion of the phytoplankton assemblage. Cyanobacteria have very resistant cell walls that must be broken to release the water soluble phycobiliproteins. Various methods may be used to break the cell walls including freezing and thawing (Sarada et al., 1999), enzymatic attack (Stewart and Farmer, 1984), osmotic shock (Wyman and Fay, 1986), attack by N fixing bacteria (Zhu et al., 2007), acid, nitrogen cavitation and french press (see Viskari and Colyer, 2003, Zhu et al., 2007, for details). However the most efficient methods appear to be freeze-thaw and enzymatic attack (Zhu et al., 2007). Therefore a combination of these techniques was used after Beutler (2003) to optimise extraction efficiency and reduce the amount of time required for analysis in the field. Filter papers were frozen for at least 24 hours in 15 ml screw capped tubes. If samples were being transported, they were stored in liquid nitrogen and then at -70°. After thawing, an extraction solution of 0.25 M Trizma Base, 10 mM di-sodium EDTA and 2 mg ml^{-1} lysozyme was added. After grinding with a glass rod, the filter paper was incubated in the dark for 2 h at 37° and then stored in the cold for at least 20 h to allow for extraction. The samples were then diluted with Milli-Q water and centrifuged at 3600 g for 15 min. to reduce turbidity. The supernatant was initially filtered through a 0.2 μm pore size membrane filter, however this may interfere with the phycobiliproteins so subsequent analyses did not filter the supernatant (Simis, 2013). The sample was read in the spectrophotometer using 1 cm matched quartz cuvettes using the extraction solution as reference, and PC concentration calculated according to Bennett and Bogorad (1973). All pigment analysis were done in triplicate using the mean as the final value.

3.2.3 Seston, minerals and tripton concentrations

Seston dry mass was determined using pre-ashed Whatmann GF/F filter papers following the gravimetric technique (Environmental Protection Agency, 1983). The inorganic component (here referred to as minerals) was determined by burning the filter pads in a muffle furnace at 500° and re-weighing. All analyses were done in triplicate using the mean as the final value.

Tripton corresponds to the de-pigmented matter measured by the quantitative filter technique (QFT, see below). However, it is difficult to separate out the living phytoplankton component of seston in order to measure tripton dry mass. Determination of a^*_{tr} is useful for bio-optical models because it allows for the particulate detrital and mineral components to be handled simultaneously, and separately from living phytoplankton. Seston dry mass might be partitioned most simply into its tripton and phytoplankton components according to: $tripton = seston - \beta \times chla$, where β is a conversion factor to estimate phytoplankton dry mass from chl-*a*. Most studies using this technique assume a constant value of β most often equal to 0.07 g mg^{-1} (e.g. Dekker et al., 2001, Giardino et al., 2007, Hoogenboom et al., 1998). However, the value of β varies widely in nature according to the intracellular chl-*a* concentration which is dependent on the species, and light and nutrient environment. For cyanobacteria *P. hollandica* and *O. limnetica* cultured under a range of light and nutrient conditions, Gons et al. (1992) determined the value of β ranged between 0.02 – 0.3 g mg^{-1}, mean = 0.046 g mg^{-1}. Zhang et al. (2009a) determined a value of 0.09 g mg^{-1} for an assemblage dominated by *Microcystis* and *Scenedesmus* in lake Taihu, China. Desortová (1981) determined that the chl-*a* content per unit fresh phytoplankton biomass for various lakes was between 0.14–3.41% which corresponds to β of 0.029–0.71 g mg^{-1}. The range of variability was primarily related to seasonal variation in solar radiation, with larger values being attributed to low-light conditions (winter months). Natural populations of individual cells of various species have mean values ranging from 0.0496–0.21 g mg^{-1} (calculated from table 1.3 in Reynolds, 2006).

In this study, values of β were determined by investigating the ratio of phytoplankton to detritus, R_{pd}. In steady-state conditions (i.e. loss rate $\approx$ growth rate), R_{pd} should be constant irrespective of trophic state with a value near 0.3 (Gons et al., 1992). This is in agreement with reported values of R_{pd} in lakes which are typically between 20 and 35% (e.g. Van Valkenburg et al., 1978, Wen, 1992). In non-steady state conditions R_{pd} may vary: however its value is expected to be less than one for almost all growth conditions (Gons et al., 1992). The existence or non-existence of steady-state conditions was determined by examining variability of the chl-*a*:Seston ratio in time. For conditions deemed to be in steady-state, values for β were selected where the corresponding R_{pd} values were near to 0.3. On average, phytoplankton contain 10% mineral content (ash dry mass) (Reynolds, 2006). Therefore detrital dry weight was calculated according to: $detritus = seston - 0.9 \times minerals - \beta \times chla$. R_{pd} was calculated using the detrital and phytoplankton dry mass calculated for a range of β values. Since ash dry weight was not determined in Hartbeespoort, minerals were assumed to be zero, which is probably a reasonable assumption.

3.2.4 ABSORPTION COEFFICIENTS OF PARTICULATE, PIGMENTED AND DISSOLVED SUBSTANCES

The QFT was used to determine the absorption of total particulate matter (seston) and de-pigmented matter (tripton) after Mitchell et al. (2003). Water samples were stored in the dark and analysed on the same day as collection. The sample was filtered under low vacuum pressure ($<$ 10 mm mercury pressure) through a pre-ashed Whatman GF/F filter paper pre-washed with Milli-Q water, adjusting the volume according to the turbidity of the sample. In cases of very high biomass such as Hartbeespoort (chl-$a > 10\,000$ mg m^{-3}), as little as 2.5 ml was filtered, while for chl-$a < 1$ mg m^{-3} in Loskop, 1 l was filtered to obtain sufficient material on the filter. Blank filter papers were treated identically to the sample, by simultaneously filtering the same volume of Milli-Q water. Care was taken to not run the blank filters dry. Filter papers were kept in labeled petri dishes with a drop of water until analysis to ensure hydration.

The optical density (OD) of the particulate and blank filter paper between 350 and 850 nm was measured using a Shimadzu UV-2501 spectrophotometer using an ISR-2200 integrating sphere. The mean OD of the filter relative to the blank was near 0.5 for all samples. In the case of Hartbeespoort however, the value was unavoidably higher owing to the extremely high biomass. The mean OD of the blank measurements was subtracted from the particulate OD measurements and the absorption calculated using a pathlength amplification factor of 2 (Roesler, 1998). A null subtraction was performed at the highest wavelength of measurement (850 nm) as the assumption of no absorption from particulate matter at 750 nm does not hold in highly turbid inland waters. Duplicate particulate absorption measurements were performed for each sample, using the mean of the two spectra as the final value.

a_{tr} was determined by two methods, sodium hypochlorite (NaClO) oxidation and, in the case of Theewaterskloof, boiling methanol extraction. Both of these techniques have been used for freshwater samples (e.g. Binding et al., 2008, Zhang et al., 2008), but little information exists on what quantitative errors each of these methods might introduce. Since both methods remove non-chlorophyllous pigments (carotenoids and pheopigments), the phytoplankton absorption will tend to be overestimated. The NaClO technique has two advantages in that it bleaches the water soluble phycobilipigments and resistant cells (e.g. chlorophytes), and it may be performed more rapidly in the field (Ferrari and Tassan, 1999). However, there is some evidence to suggest that NaClO treatment of samples with high dissolved organic matter may cause bleaching of colloidal/particle-bound organic matter leading to overestimates of phytoplankton absorption in the blue (Binding et al., 2008). Furthermore, NaClO is unsuitable for waters with high abundance of heterotrophic bacteria due to the production of a yellow cytochrome byproduct deposited on the filter (Ferrari and Tassan, 1998). Techniques using organic solvents methanol or ethanol (e.g. Simis et al., 2005) might avoid these effects, although it is uncertain to what degree phycobilipigments are removed even when related absorption peaks are not visible in the absorption spectrum. Measurements were performed using both techniques in order to quantify and elucidate these errors. Complete pigment bleaching/extraction was assessed by absence of the 675 nm chl-a absorption peak. In cases of insufficient bleaching/extraction, the filter paper was gently subjected to further bleaching/extraction until the 675 nm peak disappeared. The filters were thoroughly rinsed with Milli-Q water to remove contamination by NaClO in order to perform readings < 400 nm. Blank filter papers were treated identically to samples. The mean bleached blank OD was subtracted from the bleached particulate OD to calculate the tripton absorption. The tripton absorption curves were fitted to an exponential function (Bricaud et al., 1981) and the slope coefficient, S_{tr}, was computed using a reference wavelength of 442 nm.

The phytoplankton absorption component was then computed as $a_\varphi = a_p - a_{tr}$. The specific absorption coefficients, a^*_φ and a^*_{tr}, were determined by dividing a_φ and a_{tr} by the concentration of TChl and tripton, respectively. In order to calculate the PC specific absorption coefficient, $a^*_{pc}(620)$, a correction needs to be applied to $a_\varphi(620)$ in order to remove the effect of residual chl-*a* absorption, termed $a_{chl}(620)$. Simis et al. (2005) determined the value of $a_{chl}(620)$ from $a_\varphi(665)$ using a ratio term, ε=0.24. The absorption exclusively due to PC is then calculated by $a_{pc}(620) = a_\varphi(620) - \varepsilon \times a_\varphi(665)$. $a^*_{pc}(620)$ is then calculated by $a_{pc}(620)/PC$. The value of ε determined by Simis et al. (2005) is generally suitable for use in cyanobacteria-dominated waters, and therefore is used here. No attempt was made to correct for algae containing other pigments influencing absorption near 665 and 620 nm (e.g. Simis et al., 2007). The absorbance due to *gelbstoff*, a_g, was read between 340 and 750 nm in the spectrophotometer using matched 10 cm quartz cuvettes using room temperature Milli-Q water as reference. A null-point correction at 750 nm was implemented and absorption calculated according to Mitchell et al. (2003). The curves were fitted to an exponential function (Bricaud et al., 1981) between 350 and 500 nm and the slope coefficient, S_g, was computed using a reference wavelength of 442 nm.

3.3 RESULTS AND DISCUSSION

3.3.1 BIOGEOCHEMISTRY AND PHYTOPLANKTON COMPOSITION

There was extremely large variability in biogeochemical and optical parameters between and within the three systems studied (table 3.3.1). Fig. 3.3.1 shows scatter plots illustrating this variability, and the correlation coefficients for the entire dataset are shown in table 3.3.2. Chl-*a* and seston were highly correlated ($r = 0.92$), with concentrations varying over six and five orders of magnitude, respectively (fig. 3.3.1A). The extremely high chl-a values > 1000 mg m^{-3} were measured in surface scum conditions in Hartbeespoort. The greatest trophic range was found in Loskop with chl-*a* varying from 0.5 to 500 mg m^{-3}, while Theewaterskloof was the least variable. The organic component of seston was highly correlated with chl-*a* ($r = 0.85$, fig. 3.3.1B). Weak correlations between *gelbstoff* absorption at 442 nm, $a_g(442)$, and chl-*a* and seston were apparent ($r = 0.63$ and 0.54, respectively, fig. 3.3.1C,D). However, the considerable scatter implies that the relationship is reservoir-specific and that a_g is largely controlled by catchment-related factors rather than phytoplankton biomass or seston (Kirk, 1994). Water clarity (z_{sd}) was inversely correlated to seston ($r = -0.43$) and its mineral and organic components, and phytoplankton pigments (chl-*a*, $r = -0.27$, fig. 3.3.1E,F).

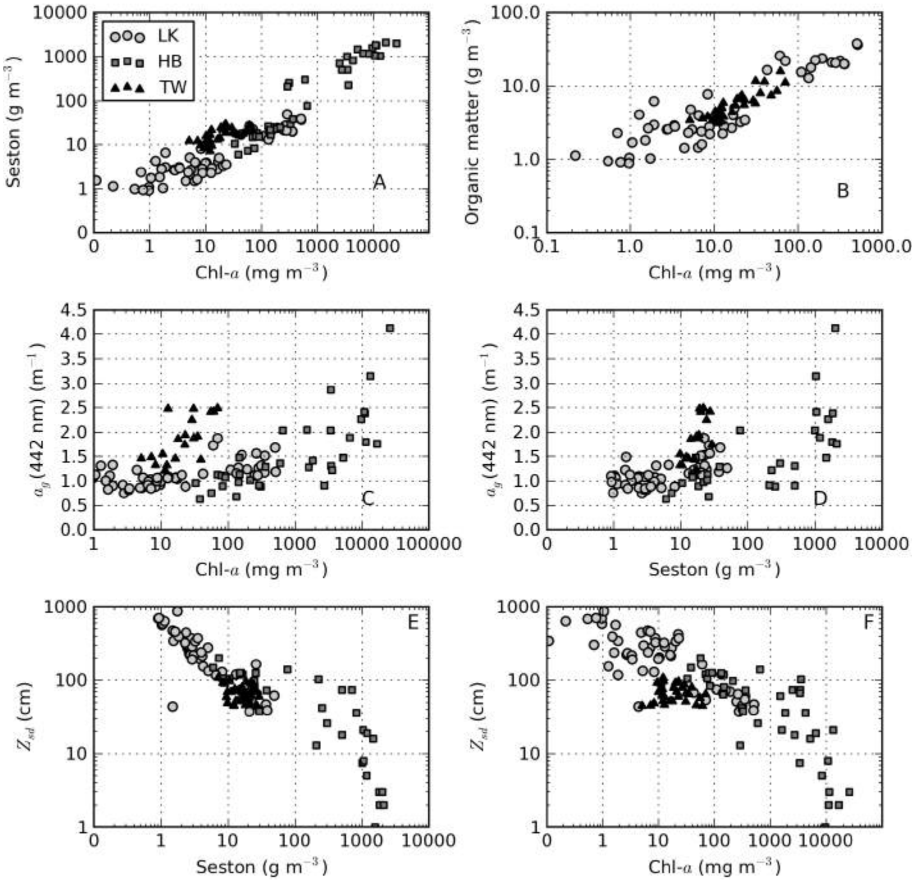

Figure 3.3.1: Scatterplots for A) seston versus chl-*a*, B) organic matter versus chl-*a*, C) $a_g(442)$ versus chl-*a*, D) $a_g(442)$ versus seston, E) z_{sd} versus seston, and F) z_{sd} versus chl-*a*. Note logarithmic scales.

Table 3.3.1: Variability in biogeophysical and optical parameters for each reservoir.

	Chl-*a* mg m^{-3}	PC mg m^{-3}	Seston g m^{-3}	Minerals g m^{-3}	z_{sd} cm	TChl mg m^{-3}	a_g(442 nm) m^{-1}	S_g nm^{-1}	a_p(442 nm) m^{-1}	a_{tr}(442 nm) m^{-1}	S_{tr} nm^{-1}	a_φ(442 nm) m^{-1}
						Hartbeespoort						
Min.	33.0	84.3	6.0	-	1.0	38.9	0.63	0.014	2.03	0.07	0.0092	1.73
Max.	25978.3	43143.9	2100.0	-	201.0	28466.6	4.13	0.021	456.24	1.74	0.0098	455.32
Mean	3872.6	4462.9	573.1	-	61.9	4260.8	1.55	0.017	87.48	0.51	0.0095	86.98
St. dev.	5703.3	8225.8	685.4	-	51.8	6208.0	0.77	0.002	133.16	0.47	0.0004	132.83
Median	1503.3	1190.7	225.0	-	61.0	1599.3	1.30	0.017	27.97	0.39	0.0095	27.61
N	39	39	35	-	39	39	34	34	19	19	2	19
						Loskop						
Min.	0.5	25.1	0.9	0.0	37.5	1.3	0.75	0.013	0.16	0.10	0.0078	0.05
Max.	512.9	73.5	48.9	5.7	870.0	856.3	1.87	0.022	12.58	1.57	0.0126	11.12
Mean	86.7	49.3	9.5	1.5	263.5	151.8	1.11	0.017	2.07	0.53	0.0103	1.56
St. dev	139.5	34.2	11.3	1.5	203.8	245.3	0.24	0.002	2.72	0.39	0.0013	2.43
Median	10.1	49.3	3.3	0.9	224.0	20.6	1.07	0.017	0.62	0.42	0.0102	0.29
N	48	2	55	55	56	49	57	57	57	57	57	56
						Theewaterskloof						
Min.	5.1	8.1	7.1	3.2	45.0	6.9	1.22	0.012	1.13	0.51	0.0084	0.41
Max.	69.7	70.3	29.1	22.8	108.0	118.4	2.49	0.015	3.65	2.26	0.0130	2.43
Mean	22.2	20.4	16.4	9.3	68.2	34.7	1.85	0.014	2.07	1.18	0.0098	0.89
St. dev.	16.3	15.1	6.0	4.6	17.7	25.5	0.45	0.001	0.72	0.44	0.0011	0.49
Median	16.3	14.9	16.4	8.0	66.0	23.0	1.86	0.014	2.18	1.05	0.0095	0.74
N	33	19	32	32	33	33	19	19	19	19	19	19

The phytoplankton species composition is shown in fig. 3.3.2 and table 3.3.3. In Hartbeespoort *M. aeruginosa* composed more than 90% of the phytoplankton assemblage. Bright green surface accumulations were present over most of the lake surface area. The concentration of chl-*a* and

Table 3.3.2: The Pearson correlation coefficient between various variables. Note that a parametric statistic was used although the variables were non-normally distributed according to the Shapiro-Wilks test.

	chl-*a*	PC	Seston	Minerals	Organic matter	z_{sd}	$a_g(440)$	TChl
chl-*a*	1							
PC	0.86	1.00						
Seston	0.92	0.68	1.00					
Minerals	-0.10	-0.21	0.57	1.00				
Organic matter	0.85	0.88	0.88	0.13	1.00			
z_{sd}	-0.27	-0.43	-0.31	-0.52	-0.47	1.00		
$a_g(440)$	0.63	0.67	0.54	0.76	0.34	-0.43	1.00	
TChl	1.00	0.87	0.92	-0.12	0.84	-0.28	0.64	1.00

phycocyanin pigments were extremely high (up to 26 000 and 43 000 mg m^{-3}, respectively). In Loskop, the dinoflagellate *Ceratium hirundinella* is dominant throughout the reservoir in terms of biovolume, although cyanobacteria (in isolated blooms) and other species were also abundant (fig. 3.3.2B, table 3.3.3). Working upstream, the main basin (point MB) is typically oligotrophic (chl-*a* < 1 mg m^{-3}) and very clear with a mixed population of diatoms, chlorophytes and dinoflagellates. The lacustrine zone (point LS) is oligotrophic (chl-*a* < 10 mg m^{-3}) with slightly decreased water clarity. The transitional zone where a bio-optical buoy was moored (point BY) is more variable due to mixing ($1 <$ chl-*a*<30 mg m^{-3}). A dense bloom of *C. hirundinella* was present at point CT turning the water dark brown, with chl-*a* values in excess of 200 mg m^{-3}. This species which commonly occurs in South African reservoirs is a nuisance for water treatment (Hart and Wragg, 2009, van Ginkel et al., 2001). A emphM. aeruginosa bloom was present further upstream at point MC. In summer, as water temperatures rise, the cyanobacteria become more abundant and blooms extend downstream towards the transitional zone (Oberholster et al., 2010). Therefore, it appears that *M. aeruginosa* and *C. hirundinella* are competing species in this reservoir.Ppoint RI at the inflow of the Olifants River is clear with chlorophytes and diatoms being present.

The water clarity in Theewaterskloof was more turbid and typically contained a phytoplankton assemblage of mixed dinoflagellate], cyanobacteria and diatom species (table 3.3.3) and a high mineralic component of dry weight (table 3.3.1). The reservoir is affected by strong prevailing SE and NW winds (gusts up to 7.5 m s^{-1} were measured) which means it is generally well-mixed. Blooms of filamentous cyanobacteria *Anabaena ucrainica* and a high abundance of diatom species, in particular *Aulacoseira ambigua* and *Asterionella formosa*, were characteristic for the reservoir. The high mineralic component of dry weight might be related to the presence of these diatom species, which may contain >40% ash weight of dry weight (Reynolds, 2006). A general pattern of increasing turbidity and phytoplankton biomass was observed from the eastern towards the western basin, near the inflow of the Sonderend River. The eastern basin was oligo/mesotrophic while the

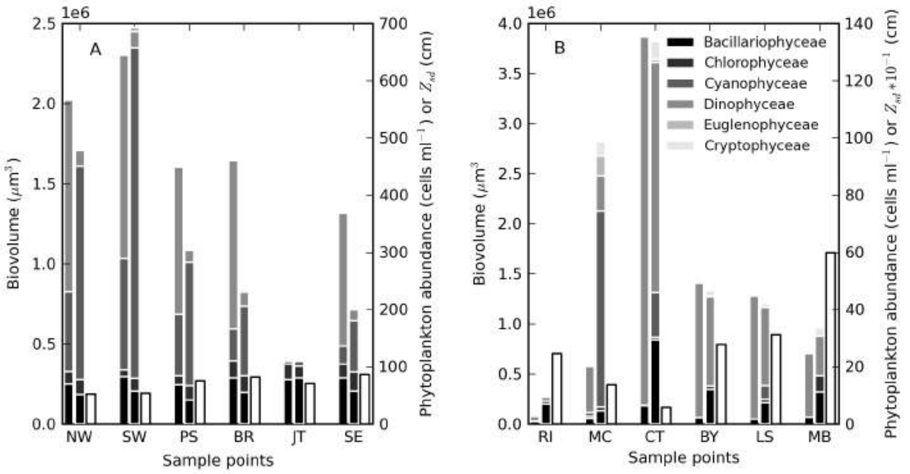

Figure 3.3.2: Mean biovolume (left bars) and abundance (center bars) of phytoplankton by group, and z_{sd} (right bars) for sample points in A) Theewaterskloof and B) Loskop. The legend is the same in A and B. Cyanophycea count for Loskop point MC has been scaled by factor of 0.1. z_{sd} is also scaled by factor 0.1 in B.

Table 3.3.3: Predominant phytoplankton species present in this study (>5000 cells l^{-1}). HB = Hartbeespoort, LK = Loskop, TW = Theewaterskloof, p = present.

	HB	LK	TW		HB	LK	TW
Bacillariophyceae				*Scenedesmus acutiformis*			p
Melosira varians		p		***Cyanophyceae***			
Fragililaria crotonensis		p		*Microcystis aeruginosa*	p	p	p
Aulacoseira granulate		p		*Anabaena ucrainica*			p
Diatoma vulgaris		p		***Dinophyceae***			
Asterionella formosa			p	*Ceratium hirundinella*		p	
Aulacoseira ambigua			p	*Peridium bipes*		p	
Navicula capitatoradiata			p	*Sphaerodinium fimbriatum*			p
Chlorophyceae				***Euglenophyceae***			
Coelastrum reticulatum		p		*Trachelomonas volvocina*		p	
Pandorina morum		p		***Cryptophyceae***			
Staurastrum paradoxum			p	*Cryptomonas ovate*		p	

western half of the reservoir was meso/eutrophic. A high biomass bloom consisting of cyanobacteria *Anabaena ucrainica* and the large-celled dinoflagellate *Sphaerodinium fimbriatum* which were co-dominant in terms of biovolume was present in the western basin.

3.3.2 Absorption by *gelbstoff*

In the three reservoirs absorption by *gelbstoff* at 442 nm varied between 0.63 to 4.13 m^{-1} (table 3.3.1). Despite its large trophic gradient, Loskop had the most narrow range from 0.75 to 1.87 m^{-1}. Therefore it appears that a_g was largely independent of trophic status. The widest range of values were found in Hartbeespoort (0.63 to 4.13 m^{-1}), which was likely associated with the extremely variable cyanobacterial biomass. Theewaterskloof had the highest average value of 1.9 m^{-1} which is consistent with brackish waters which are characteristic of rivers in the Cape region. The measured absorption curves were generally consistent with an exponential function (straight lines in fig. 3.3.3A). The values determined for of the slope coefficient, S_g, ranged between 0.012 and 0.022 nm^{-1}, within that reported in coastal (Babin et al., 2003) and other inland waters (Kirk, 1994). The mean value of 0.017 nm^{-1} was identical for Loskop and Hartbeespoort, while that for Theewaterskloof was 0.014 nm^{-1}. An inverse relationship was present between $a_g(442)$ and S_g (fig. 3.3.3B) with greater variability associated with smaller values in agreement with the findings of Babin et al. (2003).

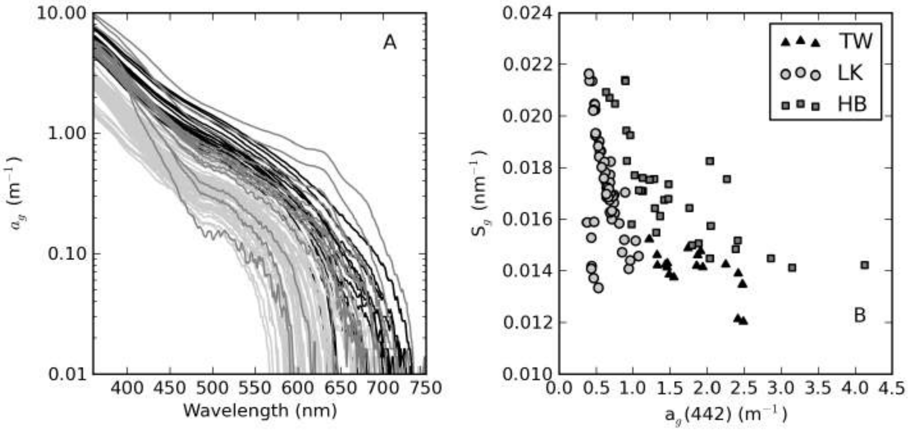

Figure 3.3.3: A) *Gelbstoff* absorption versus wavelength with log-scale y axis. B) $a_g(442)$ versus the exponential slope coefficient S_g. The legend colours are the same in A and B.

3.3.3 ABSORPTION BY SESTON

Fig. 3.3.4 shows the measured particulate absorption spectra which varied over more than four orders of magnitude. Extremely high values were measured in surface scums in Hartbeespoort (table 3.3.1, fig. 3.3.4A). The spectral shapes indicate that the contribution of phytoplankton to a_p was in these cases overwhelming. The data from Loskop were divided into two groups: those from the high biomass *C. hirundinella* bloom at sampling point CT (fig. 3.3.4B); and those from other sample points (fig. 3.3.4C). The spectra from point CT were dominated by phytoplankon absorption, while the remainder had exponential shapes which is evidence of a relatively larger influence by tripton. a_p spectra measured in Theewaterskloof (fig. 3.3.4C) appeared to be influenced by significant contributions of both tripton and phytoplankton and had exponential shapes at wavelengths < 500 nm.

Total particulate absorption was extremely variable in Hartbeespoort and Loskop (0.16 to 456.24 m^{-1}) but was more consistent in Theewaterskloof (1.13 to 3.65 m^{-1}). $a_p(442)$ was highly correlated with seston and chl-*a* (fig. 3.3.5). The data were fitted using a straight line with null point intercept ($y = ax$). The relationship $a_p(442) = 0.23 \times \text{seston}$ was determined for Loskop ($r^2 = 0.91$,

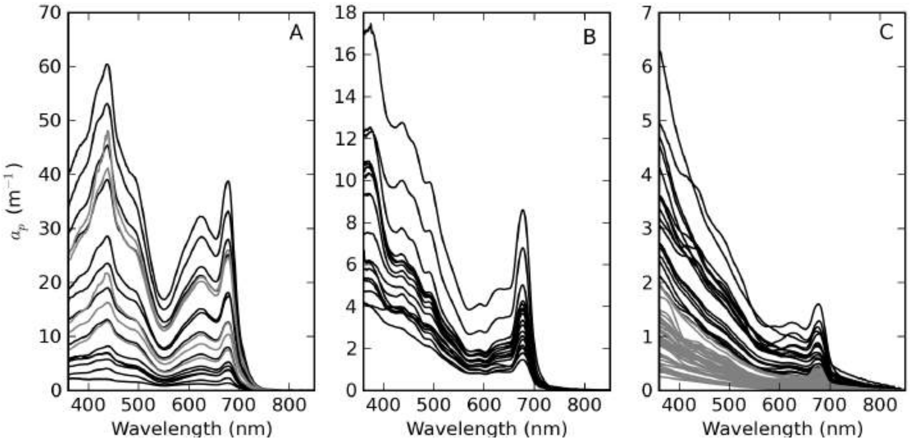

Figure 3.3.4: Seston absorption spectra measured in A) Hartbeespoort (gray lines scaled by 0.1 to facilitate comparison), B) Loskop for $a_p(442) > 2$ m^{-1}, and C) Theewaterskloof (black lines) and Loskop $a_p(442) < 2$ m^{-1} (gray lines).

Standard Error=1.03,N=56), similar to that determined for Theewaterskloof, $a_p(442) = 0.12\times$seston ($r^2 = 0.97$, SE=0.38, N=19). For combined Theewaterskloof and Loskop data the relationship was $a_p(442) = 0.19\times$seston ($r^2 = 0.85$, SE=1.22, N=75). $a_p(442)$ was more correlated with chl-*a* in Hartbeespoort according to: $a_p(442) = 0.026\times$chl-a ($r^2 = 0.82, SE = 67.9, N = 19$). The combined dataset was described by $a_p(442) = 0.15\times$seston ($r^2 = 0.68$, SE=40.25, N=91), and $a_p(442) = 0.026\times$chl-a ($r^2 = 0.82$, SE=29.9, N=94). The significance of the correlations were affected by outliers in the data mainly from Hartbeespoort.

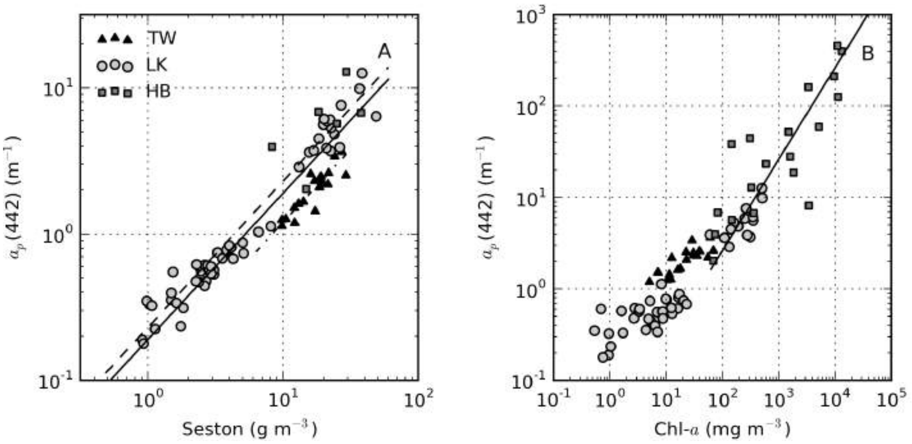

Figure 3.3.5: Seston absorption at 442 nm versus A) seston showing linear fits for Loskop (--), Theewaterskloof (-··), and the combined data (–), and B) chl-*a* showing the linear fit for Hartbeespoort (–). Note log-scales.

3.3.4 ABSORPTION BY TRIPTON

A comparison between absorption coefficients measured using hot methanol extraction and the NaClO bleaching method is shown in fig. 3.3.6. The differences in magnitude of a_p in fig. 3.3.6A were due only to the expected differences between duplicate samples. However, after normalising at 410 nm (fig. 3.3.6B) considerable spectral differences became apparent. Despite that there was no apparent residual PC absorption peak at 620 nm in the particulate absorption spectra, the ratio spectrum revealed that residual phycobilipigments were present in the 500 to 650 nm region (fig. 3.3.6C). The hot methanol method led to a 15 to 20% underestimate of a_φ (or overestimate of a_{tr}) in this region (fig. 3.3.6D). The shoulders near 420 and 650 nm are likely associated with residual chl-*b* pigment from chlorophycea which also resulted in a $\pm 4\%$ difference in the 675 nm ch-*a* absorption peak. Some evidence of bleaching of organic detritus by NaClO was visible from 700 to 750 nm (although not < 440 nm), while both methods produced roughly equivalent results from 800 nm onwards. In general the NaClO method appears to be better suited for use in inland waters as the hot methanol technique under-extracted phycobili and chlorophyte pigments.

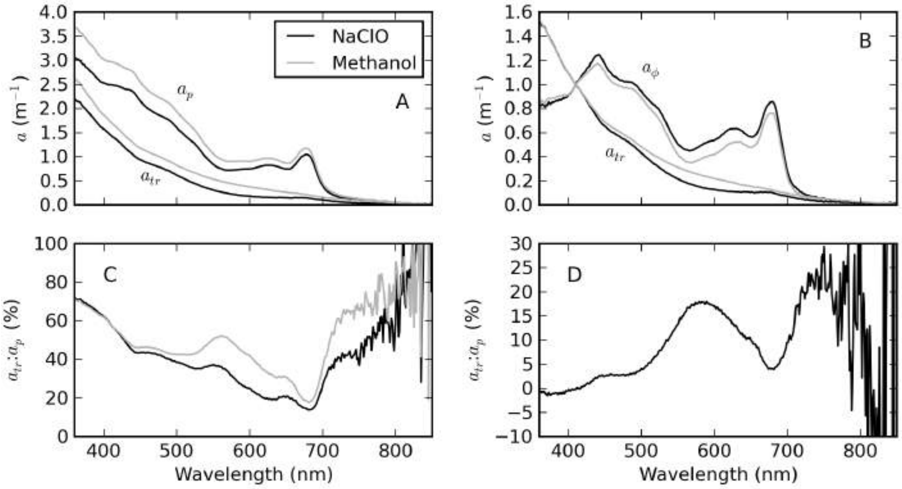

Figure 3.3.6: Comparison between NaClO and hot methanol methods for determining a_{tr}A) a_p and a_{tr} determined using both methods for a single sample from Theewaterskloof. B) a_p and a_{tr} normalised at 410 nm. C) a_{tr}:a_p ratio in percent. D) Percent difference between hot methanol and NaClO determined a_{tr}:a_p ratios shown in C.

Some examples of tripton absorption spectra are shown in fig. 3.3.7. In Theewaterskloof a strong absorption feature was visible near 450 to 550 nm which is likely to be associated with iron oxides (Estapa et al., 2012); some residual chl-*a* absorption was also apparent (fig. 3.3.7A). Residual phycobilipigment features were also clearly visible in some cases (fig. 3.3.7B). Therefore in Theewaterskloof the exponential function was fitted between 360 and 500 nm in order to avoid errors at higher wavelengths. There was an unusual flattening < 440 nm for some curves measured in Loskop at sample point MB (fig. 3.3.7C), the origin of which is unknown (see similar feature in Baltic spectra in Babin et al., 2003). For these data, an exponential function fitted between 440–600 nm was used to calculate S_{tr}. Absorption shoulders associated with iron oxide were also sometimes visible in Loskop (fig. 3.3.7D). In Hartbeespoort, bleaching of heterotrophic bacteria known to be present in in hypertrophic lakes in high abundance (Sommaruga and Robarts, 1997), caused unusually steep slopes <450 nm (fig. 3.3.7E). All but two of the measured a_{tr} spectra in Hartbeespoort were contaminated by this effect. Therefore, S_{tr} could only be computed for two uncontaminated samples in Hartbeespoort, which also displayed some iron oxide effects (fig. 3.3.7F). In order to facilitate the calculation of phytoplankton absorption in Hartbeespoort, a_{tr} spectra were estimated by extrapolating the value at 460 nm using an exponential function with a slope coefficient of 0.009 nm^{-1}. In general, the contribution of tripton to a_p was very small (see below). Obvious residual phycobilipigment features were also sometimes present as a result of inefficient NaClO bleaching. Therefore determination of a_{tr} in hypertrophic waters or surface scum, when necessary, is perhaps better performed using, for example, a numerical technique (e.g. Zhang et al., 2008).

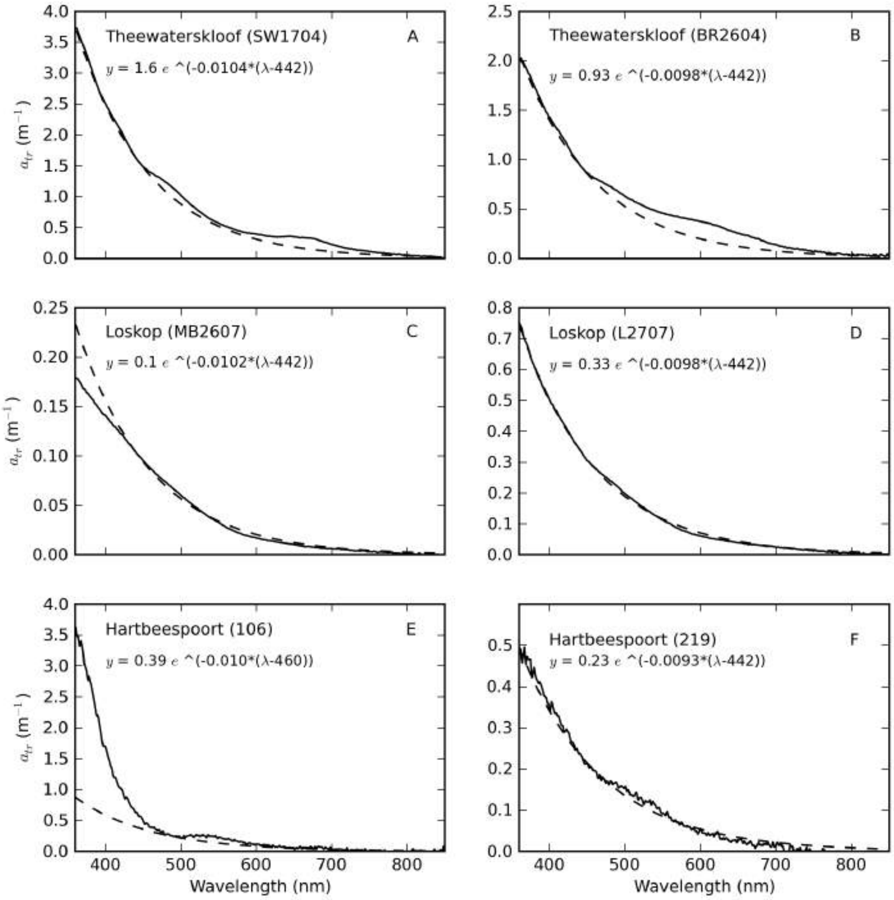

Figure 3.3.7: Selected a_{tr} examples showing measured data (solid line) and the corresponding exponential fit (dashed line). The sample point ID is shown in brackets.

The complete set of measured tripton absorption curves are shown in fig. 3.3.8 alongside histograms for the slope coefficient and $a_{tr}(442)$. In general, the exponential function closely fitted the data, evident by the straight lines on the log-linear plot (fig. 3.3.8A). The mean value of $a_{tr}(442)$ in Theewaterskloof of 1.18 m^{-1} was nearly twice that of Loskop and Hartbeespoort (see table 3.3.1). This might be related to the high mineralic component of seston and the windy climatology of the reservoir. The range of $a_{tr}(442)$ values for Hartbeespoort and Loskop were very similar (mean =

0.51 and 0.53 m^{-1} respectively), despite the extremely variable trophic conditions. The variability of $a_{tr}(442)$ was only weakly influenced by phytoplankton biomass (see below). $a_{tr}(442)$ in Hartbeespoort and Loskop were described by an inverse-Gaussian distribution (fig. 3.3.8C). Therefore there is an increased probability of encountering $a_{tr}(442)$ values < 0.5 m^{-1} in these systems, while it is also unlikely to encounter values > 2 m^{-1}. The Theewaterskloof data conforms more closely to a normal distribution with an increased likelihood of encountering $a_{tr}(442)$ values near 1.0 m^{-1}. The values determined for S_{tr} vary in a narrow range between 0.008 and 0.013 nm^{-1} with a mean of 0.010 nm^{-1} for all reservoirs (table 3.3.1, fig. 3.3.8B). These are typical of those measured in other inland and coastal waters (e.g. Babin et al., 2003, Binding et al., 2008, Zhang et al., 2009a). S_{tr} was typically normally distributed with the highest probability value being near 0.010 nm^{-1}.

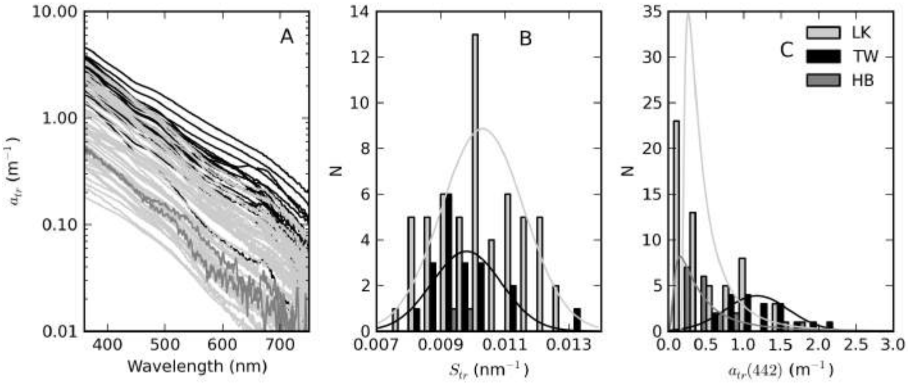

Figure 3.3.8: A) a_{tr} spectra for all reservoirs using log-scale y axis. B) Histogram of the exponential slope coefficient S_{tr} for each reservoir showing normal distributions with integrals equal to the data. C) Histogram of $a_{tr}(442)$ for each reservoir showing fitted inverse-gaussian and normal distributions with integrals equal to the data. Legend is the same in all panels.

$a_{tr}(442)$ was significantly positively correlated with seston in Theewaterskloof and Loskop. The relationship was best described by a power-law fit as $a_{tr}(442) = 0.17 \times \text{seston}^{0.62}$ ($r^2 = 0.81$, N=74) (fig. 3.3.9A). A null-point linear fit, such as those determined by Binding et al. (2008) in lake Erie (drawn in fig. 3.3.9A) and Babin et al. (2003) in European coastal waters, poorly fitted the lower range of the data. In Hartbeespoort, the relationship was poor ($r^2 = 0.32$, N=16). This could result from errors associated with a_{tr} determination in surface scum conditions. However, it may also be more simply explained by tripton making up an insignificant proportion of the dry weight, the majority of which was living cells. There was considerable scatter between $a_{tr}(442)$ and TChl which varied over 6 orders of magnitude (fig. 3.3.9B). Weak positive correlations were apparent indicating that trophic status weakly correlated with $a_{tr}(442)$. The significant offset for Hartbeespoort data indicated that in surface scum conditions the tripton:phytoplankton ratio was significantly lowered. In contrast, the grouping of Theewaterskloof data towards the left of the plot was indicative of an enlarged tripton:phytoplankton ratio, presumably resulting from a higher mineralic component. Mineral dry weight and $a_{tr}(442)$ were highly correlated with a fit of $a_{tr}(442) = 0.0.41 \times \text{minerals}^{0.51}$ ($r^2 = 0.77$, N=70, fig. 3.3.9C). The clustering of the Theewaterskloof data towards higher values was evidence of the high mineral content of seston whose mean value was 57% ,caused by the high silica content of abundant diatom species.

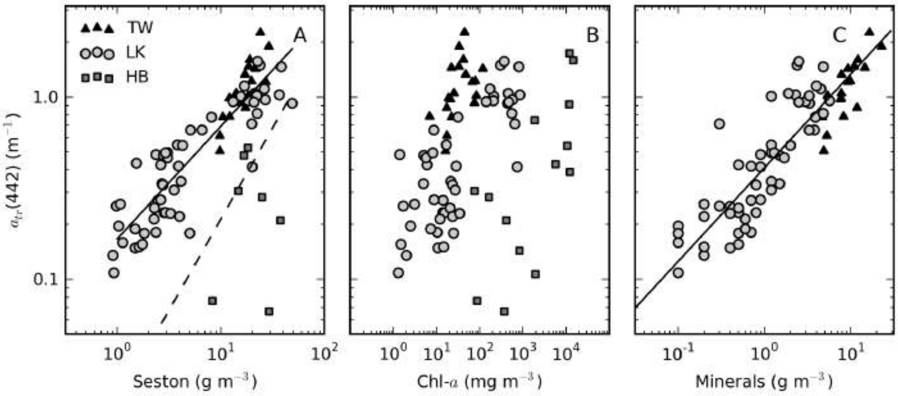

Figure 3.3.9: $a_{tr}(442)$ versus A) seston showing fit for combined Theewaterskloof and Loskop data (–) and that from Binding et al. (2008) (- -), B) chl-a, and C) minerals showing fit for combined Theewaterskloof and Loskop data (–). Legend is identical in all plots. Note log-scales.

The variability in the contribution of tripton to a_p between and within the reservoirs warrants closer investigation. For samples with $a_p(442) < 2$ m^{-1} a positive linear relationship existed: $a_{tr}(442) = 0.56 \times a_p(442)$, $r^2 = 0.94$, SE=0.2, N=58 (fig. 3.3.10A). Mean $a_{tr}(442)$:$a_p(442)$ ratios for these data were 0.65 for Theewaterskloof (range of 0.35 to 0.75) and 0.7 for Loskop (range of 0.4 to 0.9). For high biomass Loskop and Hartbeespoort waters the relationship between a_{tr} and a_p typically broke down (fig. 3.3.10B). In these waters tripton was an insignificant contributor to a_p, with $a_{tr}(442)$:$a_p(442)$ ratios of 0.1 to 0.35 in Loskop and < 0.15 in Hartbeespoort. When investigating the change in the ratio relative to phytoplankton biomass (TChl) there was a general inverse correlation (fig. 3.3.10C). In Loskop the relationship was described by $a_{tr}(442)$:$a_p(442)$=0.99×TChl$^{-0.28}$ (r^2=0.76, N = 47) while in Hartbeespoort it was $a_{tr}(442)$:$a_p(442)$ = 0.37×TChl$^{-0.50}$ (r^2=0.62, N = 14). In Theewaterskloof the relationship was much weaker (r^2=0.2 for a linear fit), signifying that phytoplankton biomass does not dictate the contribution by tripton to particulate matter. Evidently, tripton typically contributes more towards $a_p(442)$ as phytoplankton biomass decreases. Therefore phytoplankton biomass exerts a controlling influence on the contribution that tripton makes to particulate absorption (although less so in Theewaterskloof). The converse effect was visible in a weak positive correlation between minerals and the $a_{tr}(442)$:$a_p(442)$ ratio (not shown). There is no apparent relationship between the ratio and seston.

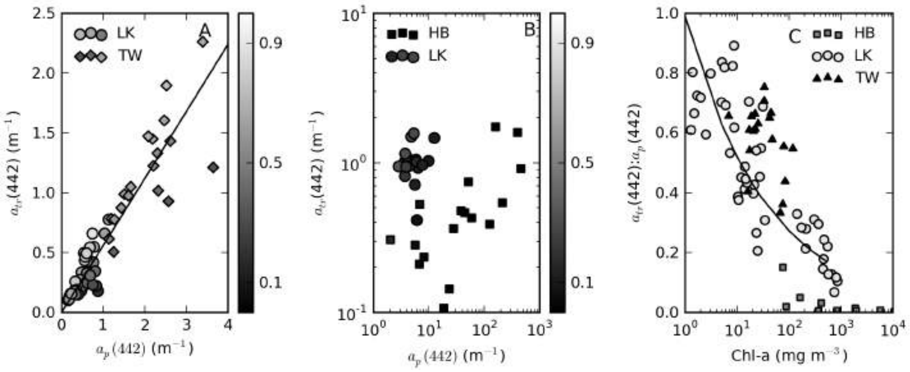

Figure 3.3.10: Scatterplots of $a_{tr}(442)$ versus $a_p(442)$ for A) Theewaterskloof and Loskop with $a_p < 2$ showing linear fit (–) and B) Hartbeespoort and Loskop with $a_p > 2$. Colorbars display the ratio of a_{tr}:a_p. C) TChl versus the ratio a_{tr}:a_p showing power-law fit for Loskop. Note log-scaled axes in B and C.

3.3.5 Mass-specific tripton absorption

Fig. 3.3.11A shows the mean chl-*a*:seston ratio used to test for steady-state conditions for various sample points in Loskop, and in Theewaterskloof and Hartbeespoort as a whole. Non-steady state conditions were indicated by widely variable ratios at point CT in Loskop (6 to 18 mg g^{-1}) and Hartbeespoort (4 to 11 mg g^{-1}). Variability elsewhere was relatively small. Therefore non-steady state conditions were associated with the high biomass blooms in Loskop and Hartbeespoort. R_{pd} is therefore expected to be larger than 0.3 in these blooms, but should be near 0.3 elsewhere, regardless of the trophic state.

R_{pd} calculated for β values ranging between 0.01 and 0.1 g mg^{-1} are shown in fig. 3.3.11B. For steady-state Loskop sample points BY, LS, and MB, values of β corresponding to a $R_{pd}of \approx 0.3$ are 0.04, 0.055 and > 0.1 g mg^{-1}, respectively. By choosing a single value of β of 0.04 g mg^{-1} for Loskop, the corresponding R_{pd} values were 0.29, 0.20 and 0.04. This is in the acceptable range of values encountered in steady-state conditions considering that chl-*a* at point MB was very small $<$ 1 mg m^{-3}. The value for β is lower than those previously determined for *C. hirundinella* of 0.079 g mg^{-1} (Reynolds, 2006) but is within the lower range previously determined for natural populations of flagellates of 0.037 to 0.714 g mg^{-1} (Desortová, 1981). Using a value for β of 0.04 g mg^{-1}, the corresponding R_{pd} for CT is 1.3. Such a high value might be acceptable since negative R_{pd} values are observed for β values > 0.05 g mg^{-1}. This occurs when phytoplankton dry mass calculated using β exceeds seston dry weight.

The value of β determined in Hartbeespoort was approx. 0.03 g mg^{-1} (fig. 3.3.11B), just under the range of 0.033 to 0.769 g mg^{-1} determined by Desortová (1981) for blue-green assemblages. However, a R_{pd} value of 0.3 is likely too low for the non steady-state bloom conditions. The average literature value of β for *M. aeruginosa* of 0.09 g mg^{-1} (Reynolds, 2006, Zhang et al., 2009a) gives a R_{pd} of 1.83 (one negative value was removed from the calculations, N=17). This R_{pd} is similar to

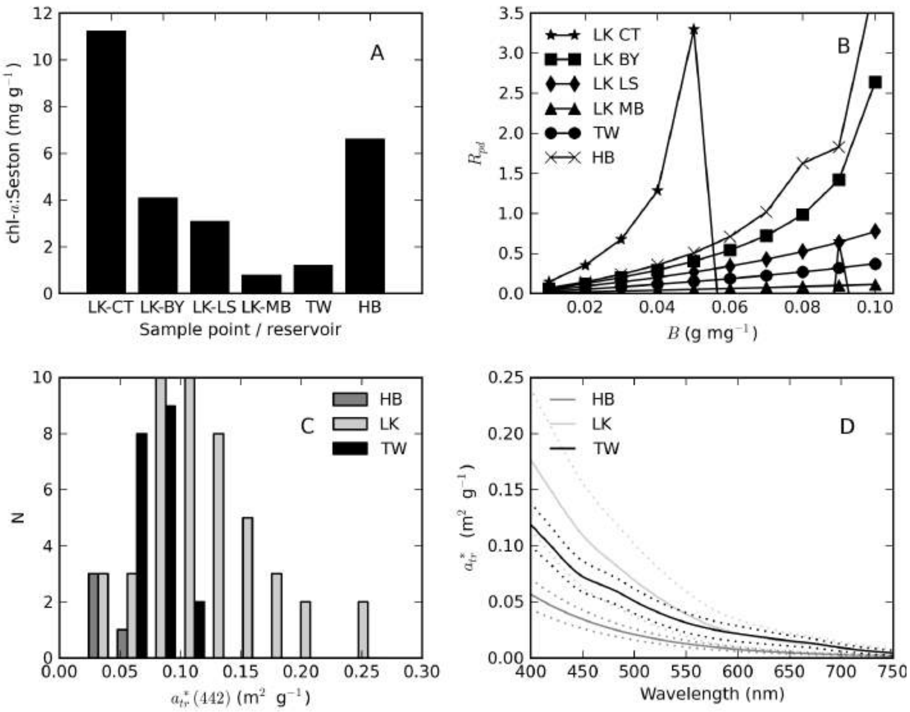

Figure 3.3.11: A) Mean chl-a:Seston ratios and B) mean R_{pd} values calculated for values of β between 0.01 and 0.10 g mg^{-1} for sample points in Loskop, Theewaterskloof and Hartbeespoort. C) Histograms of $a^*_{tr}(442)$ for each reservoir. D) The mean a^*_{tr} spectrum showing standard deviations (··) for each reservoir.

that obtained at point CT in Loskop. Theoretically however, β could lie anywhere between 0.03 and 0.09 g mg $^{-1}$ in Hartbeespoort. In Theewaterskloof a β value of 0.09 g mg^{-1} was determined. This is close to literature values for *Anabaena* of 0.063 g mg^{-1} and lower than those for diatoms *Asterionella* and *Aulacoseira* of 0.18 and 0.12 g mg^{-1}, respectively, (Reynolds, 2006) both of which were present in Theewaterskloof. In summary, β values of 0.04, 0.09 and 0.09 g mg^{-1} were finally chosen for Loskop, Hartbeespoort, and Theewaterskloof, respectively.

The $a^*_{tr}(442)$ values determined using the aforementioned β values are shown in fig. 3.3.11C. The mean a^*_{tr} spectrum for each reservoir is shown in fig. 3.3.11D. $a^*_{tr}(442)$ ranged from 0.025 to 0.263 m^2 g^{-1} in Loskop, 0.054 to 0.105 m^2 g^{-1} in Theewaterskloof, and from 0.024 to 0.048 m^2 g^{-1} in Hartbeespoort. The mean values were 0.119, 0.078 and 0.037 m^2 g^{-1}, respectively. These values compare favorably with those reported in other fresh inland waters (e.g. Campbell et al., 2010, Giardino et al., 2007, Zhang et al., 2009a). In particular values of $a^*_{tr}(550)$ for various lakes in Queensland Australia varied between 0.014 and 0.145 m^2 g^{-1} (Campbell et al., 2010). The mean spectrum for Theewaterskloof was evidently mineral-rich and affected by iron oxide absorption effects near 500 nm. The specific absorption coefficients of terrigenous mineral-rich particulate matter vary over a wide range from $<$0.1 to 1 m^2 g^{-1} (e.g. Babin and Stramski, 2004, Stramski et al., 2007). Therefore the values determined here appear to be consistent within the high variability present in the literature. A brief investigation of the sensitivity of $a^*_{tr}(442)$ to the value of β shows that in Hartbeespoort, mean $a^*_{tr}(442)$ values produced by a β of 0.03 and 0.09 g mg^{-1} were 0.0145 and 0.0374 m^2 g^{-1}, respectively. Therefore the value of β has a large influence on $a^*_{tr}(442)$ and should therefore be chosen with care, for example, using the method used here.

3.3.6 ABSORPTION BY PHYTOPLANKTON

The diversity of trophic states and phytoplankton assemblages between and within the reservoirs was evident in the variable shapes and magnitudes of a_φ (fig. 3.3.12). Extremely high a_φ values $>$ 400 m^{-1} were measured in *M. aeruginosa* surface scums in Hartbeespoort (fig. 3.3.12A). The spectral shapes had typical chl-a absorption peaks along with strong phycobilipigment features between 550 and 650 nm (phycocyanin and phycoerethrin) and shoulders associated with the carotenoids myxozanthophyll, zexanthin and echinenone (400 to 500 nm) (Ibelings et al., 1994, Schluter et al., 2006). The spectra from Loskop were much smaller in magnitude with significantly different pigmentation features associated mainly with *C. hirundinella*. These had absorption shoulders in the region 400 to 500 nm from chlorophylls c1+c2 (440 nm), the carotenoids peridinin (460 nm) and possibly fucoxanthin (440 to 460 nm) and xanthophylls (dinadinoxanthin, diatoxanthin) (Schluter et al., 2006). The presence of UV photoprotective mycosporine-like ammino acids (MAAs) typical of dinoflagellates was strikingly evident $<$ 400 nm (Laurion et al., 2002). a_φ spectra from Theewaterskloof had a mix of dinoflagellate and cyanobacterial pigment absorption features, with both kinds of species being present. a_φ for Theewaterskloof was calculated without correcting the a_{tr} spectra for residual phycobilipigment because of the strong iron oxide absorption feature. Therefore a_φ may be underestimated by max. 15 % in the region 550 to 650 nm for these data.

Five of the a_φ spectra measured in Loskop associated with low chl-a values ($<$1 mg m^{-3}) and relatively high *gelbstoff* concentrations ($a_g(440)$ = 0.94–1.5 m^{-1}) had shapes which increased exponentially towards the blue. It is possible that this affect was caused by NaClO bleaching of dissolved organic matter (DOM) in the presence of relatively high *gelbstoff* absorption (Binding et al., 2008). However, because of the presence of a strong signal from MAAs $<$ 400 nm, it is difficult to ascertain whether bleaching did in fact occur. For example, a similar effect was also visible in two spectra from Theewaterskloof. Since these were determined using boiling methanol the effect cannot be caused by NaClO bleaching and is probably better attributed to accessory pigments, methodological errors or an unknown source. There was no further evidence of DOM bleaching in the data.

TCHL-SPECIFIC PHYTOPLANKTON ABSORPTION

The relationship between $a_\varphi(440)$ and TChl is affected by pigment packaging (cell size) and accessory pigments, the former of which has the greatest affect (Bricaud et al., 1995, 2004). In so-called Case I ocean waters, where the optically dominant constituent is phytoplankton, there is a general relationship between cell size and trophic state, with larger cells occurring at higher TChl values.

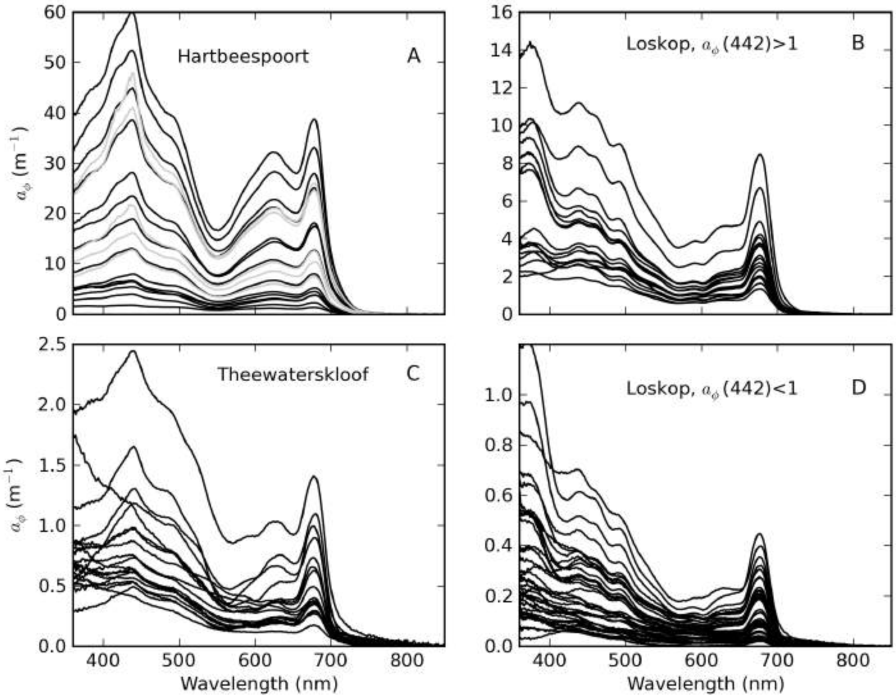

Figure 3.3.12: Spectral a_φ for A) Hartbeespoort (gray lines scaled by 0.1), B) Loskop for $a_p(442) > 1$, C) Theewaterskloof and D) Loskop for $a_p(442) < 1$.

Therefore the a_φ to TChl ratio (or the specific absorption a^*_φ) decreases with increasing TChl due to pigment packaging, which is manifest by an exponential relationship between a_φ and TChl. Similarly, the influence of non-photosynthetic pigments relative to chl-*a*, measured as the ratio of blue to red phytoplankton absorption, tends to decrease as TChl increases. However, in coastal waters accessory pigments such as pheopigments and phytoplankton size dynamics are responsible for large variations in a_φ (e.g. Babin et al., 2003, Blondeau-Patissier et al., 2009). There was significant influence of pheopigments in both Loskop and Theewaterskloof data as shown by the chl-*a*:TChl ratio which was ≈ 0.5 and 0.7, respectively (fig. 3.3.13). Therefore accessory pigments and size dynamics caused large variations in a_φ in these data.

The relationship between $a_\varphi(440)$ and TChl was best described by the power law $a_\varphi(440) = 0.031TChl^{0.89}$ (r^2=0.95, N=82, Fig. 3.3.14A). The typical relationship observed in open-ocean case I waters from Bricaud et al. (1995) is also drawn in fig. 3.3.14A). For TChl < 30 mg m^{-3} the data were in general agreement with Case I estimates (note maximum value in Bricaud et al. (1995) was approx. 25 mg m^{-3}). The reasons for the deviation at higher TChl values are most easily explained by looking at each reservoir in turn. In Loskop, the explanation is not likely related to cell size (the package effect), since the dominant species was the large-celled *C. hirundinella*. A more plausible explanation is the presence of strong accessory pigments. There was evidence of significant accessory pigment influence at high TChl values as shown by the blue:red ratio (fig. 3.3.14C, D). At 675 nm, where the influence of accessory pigments is reduced, the data were in close agreement with Bricaud et al. (1995) ($a_\varphi(675) = 0.018TChl^{0.91}$, r^2=0.97, N=82) (fig. 3.3.14B). Therefore ac-

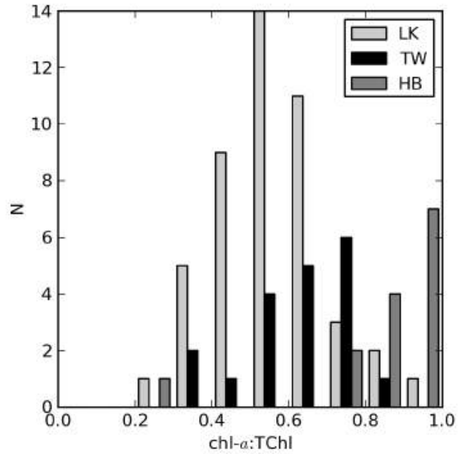

Figure 3.3.13: Frequency distribution of the chl-a to TChl (chl-a + pheo) ratio for each reservoir.

cessory pigments were determined as the cause of a noticeable deviation from Case I waters. The same explanation likely also applies to the Theewaterskloof data, which was typically dominated by a mix of intermediate and large-celled species.

The large deviation from open-ocean Case I waters observed in Hartbeespoort was more likely caused by the small cell size of *M. aeruginosa* (d of 5 μm) which reduced pigment packaging, thereby increasing absorption. Although *M. aeruginosa* existed in colonial aggregations of large size, the affect on the bulk IOPs appears to be consistent with small cells. Despite the extremely high TChl values, accessory pigments also appeared to have a significant impact in blue wavelengths (fig. 3.3.14C,D). Therefore it is apparent that the *M. aeruginosa* blooms violated both of the assumptions of Case I waters, especially that cell size increases with trophic state. This is also likely to be the case for many other freshwaters dominated by small-celled cyanobacteria, resulting in wide inter- and intra-lake variability in a^*_φ. The corresponding a^*_φ versus TChl scatter plots demonstrate this variability (fig. 3.3.14E,F). $a^*_\varphi(440)$ values were expectedly larger than those typically observed in Case I waters, however the agreement is improved for $a^*_\varphi(675)$ as a result of a smaller influence by accessory pigments at higher wavelengths. The increase in a^*_φ induced by small cell size is evident for Hartbeespoort. The wide ranging a^*_φ values for TChl > 1000 mg m^{-3} are probably caused by measurement difficulties in 'scum' conditions. The exponential fits for each reservoir are shown in table 3.3.4.

Fig. 3.3.15 provides selected examples of a^*_φ spectra arranged by trophic class as well as the mean for each reservoir. Table 3.3.5 gives statistics for $a^*_\varphi(440)$ arranged by trophic class as well as for the *M. aeruginosa* and *C. hirundinella* monospecific blooms. The statistics show that the mean value of $a^*_\varphi(440)$ decreased from oligotrophic to hypertrophic classes (from 0.056 to 0.018 m^2 mg^{-1}). The variability (indicated by the standard deviation) also decreased with TChl (excluding data for *M. aeruginosa*). The exponential shapes associated with some spectra measured in oligotrophic

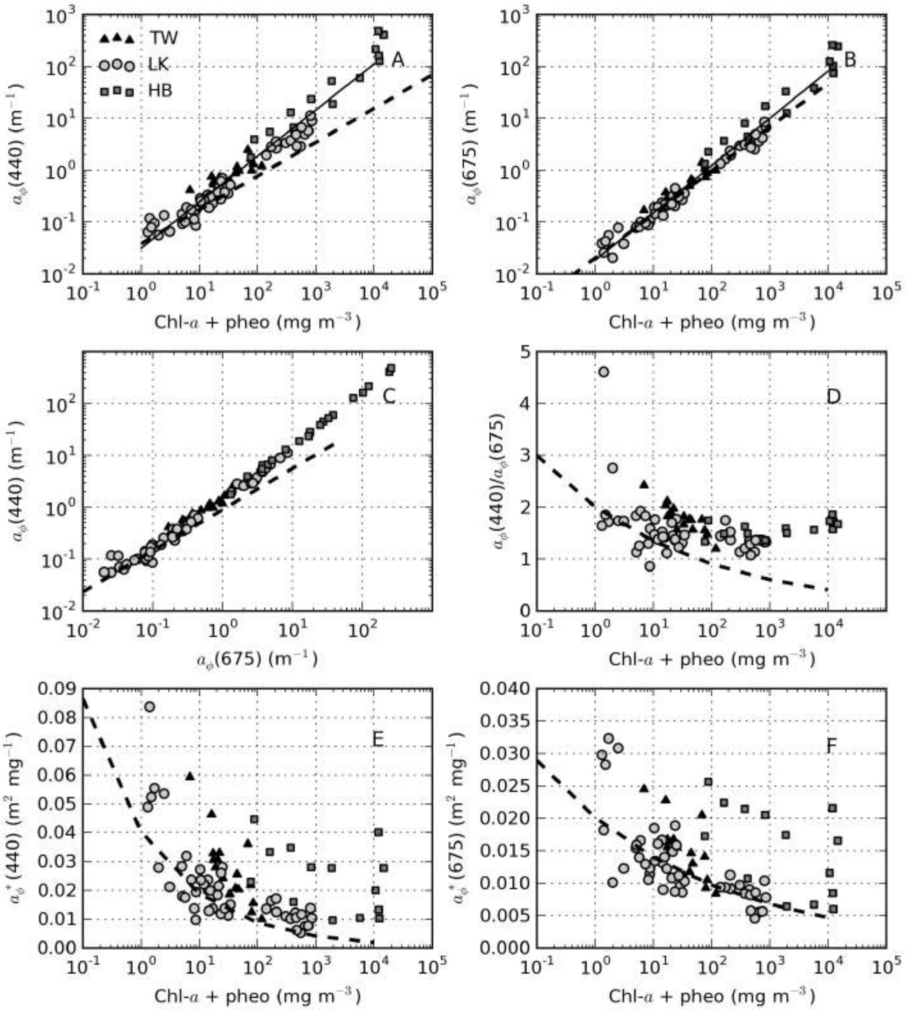

Figure 3.3.14: A) a_φ versus TChl at 440 nm and B) 675 nm showing the best fit line (–). C) $a_\varphi(442)$ versus $a_\varphi(675)$. D) $a_\varphi(442)$:$a_\varphi(675)$ versus TChl. E) a^*_φ versus TChl at 442 nm and F) 675 nm. Dotted lines show the fits from Case I marine waters (Bricaud et al., 1995). Legend is the same in all panels. Note log-scales.

Table 3.3.4: Exponential fit between a^*_φ and TChl at selected wavelengths for each reservoir.

Reservoir	Power Fit	r^2	N
TW	$a^*_\varphi(440) = 0.129TChl^{-0.48}$	0.64	19
TW	$a^*_\varphi(675) = 0.039TChl^{-0.29}$	0.52	19
LK	$a^*_\varphi(440) = 0.039TChl^{-0.23}$	0.63	49
LK	$a^*_\varphi(675) = 0.021TChl^{-0.17}$	0.62	49
HB	$a^*_\varphi(440) = 0.050TChl^{-0.11}$	0.18	14
HB	$a^*_\varphi(675) = 0.038TChl^{-0.14}$	0.28	14

waters are visible in fig. 3.3.15A. Meso-eutrophic waters in Loskop and Theewaterskloof typically had $a^*_\varphi(440)$ values near 0.02 m^2 mg^{-1} with similar spectral features from the occurrence of large-celled dinoflagellates in both reservoirs (fig. 3.3.15B). Fig. 3.3.15C and D show the large difference in magnitude and spectral pigmentation of the *C. hirundinella* and *M. aeruginosa* blooms (mean $a^*_\varphi(440)$ = 0.011 and 0.024 m^2 mg^{-1}, respectively). The wide range of $a^*_\varphi(440)$ for *M. aeruginosa* was most likely due to measurement difficulties in surface scum. Therefore the application of generalised IOP models to lakes is sub-optimal given that IOPs are specific to phytoplankton type and trophic status.

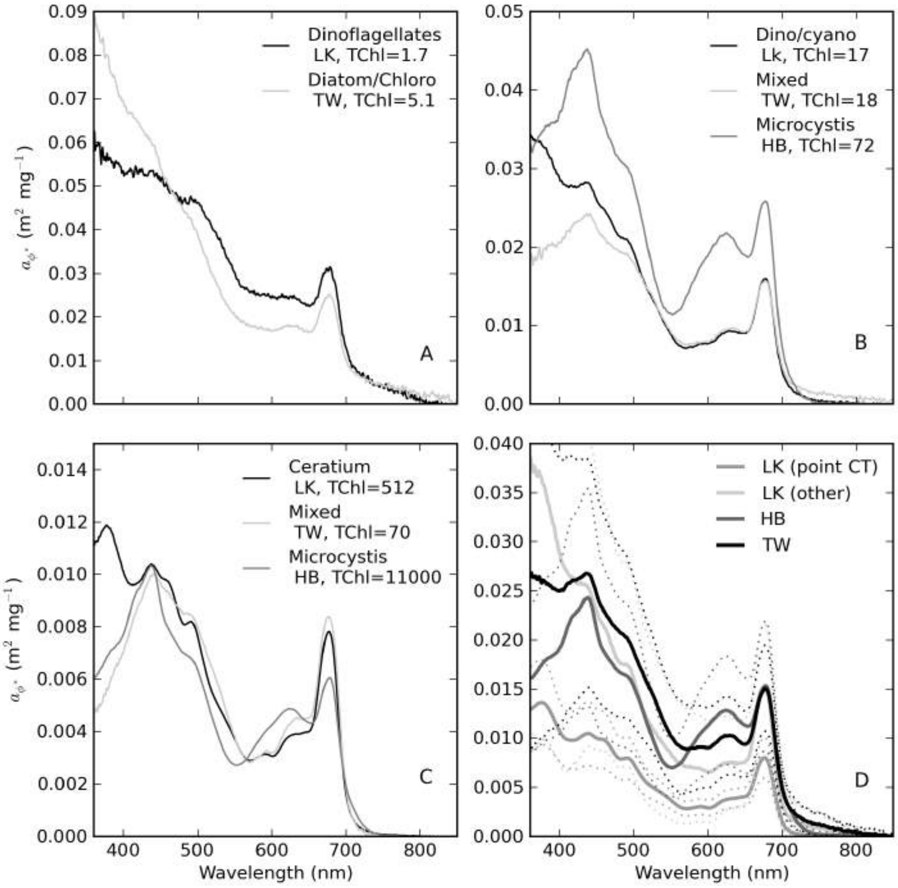

Figure 3.3.15: Selected examples of a^*_φ for A) oligotrophic, B) mesotrophic and C) hypertrophic waters. Spectra are labeled with dominant phytoplankton type(s), reservoir and TChl concentration. D) The mean and standard deviation (··) of a^*_φ for each reservoir.

Phycocyanin-specific phytoplankton absorption

Phycocyanin pigment was determined for samples where cyanobacteria made up a significant proportion of the phytoplankton population. It has been note by some authors that PC could be a better indicator of cyanobacterial biomass than chl-*a* given that it is the primary light harvesting pigment in cyanobacteria (Ahn et al., 2007). It is also a very distinctive pigment that may be used to discriminate cyanobacteria from other algal populations, as demonstrated in Chapter 2.

PC and chl-*a* were significantly correlated (fig. 3.3.16A). The relationship was best described by $PC = 8.7 \times chla^{0.74}$ in Hartbeespoort (r^2 = 0.87, N=34), and $PC = 4.70 \times chla^{0.4199}$ in Thee-

Table 3.3.5: General statistics for $a^*_\varphi(440)$ ($m^2\ mg^{-1}$) according to trophic class and monospecific blooms.

Trophic class	Min.	Max.	Range	Mean±st. dev.	Median	N
Oligotrophic (TChl<5)	0.021	0.084	0.062	0.056±0.020	0.051	8
Oligotrophic (TChl<10)	0.010	0.084	0.074	0.035±0.021	0.028	16
Mesotrophic (10<TChl<20)	0.013	0.046	0.034	0.025±0.009	0.024	12
Eutrophic (20<TChl<30)	0.012	0.033	0.021	0.022± 0.007	0.022	11
Hypertrophic (TChl>30)	0.005	0.045	0.039	0.018±0.010	0.015	42
C. hirundinella (TCh>30)	0.005	0.017	0.012	0.011±0.003	0.011	17
M. aeruginosa (TChl>30)	0.010	0.045	0.035	0.024±0.011	0.023	15

waterskloof (r^2 = 0.32, N=19). The Theewaterskloof data were from a mixed algae/cyanobacteria assemblage. Therefore chl-*a* originated from algae as well as cyanobacteria which resulted in a reduced PC:chl-*a* ratio, as observed in fig. 3.3.16A and B. In the Hartbeespoort data, reduced relative PC production was evident as cyanobacterial biomass increased. This effect was also observed for other accessory pigments such as allophycocyanin ($APC = 11.2 \times chla^{0.59}$, r^2 = 0.68, N=34) and pheophytin ($Pheo = 0.16 \times chla^{0.9522}$, r^2 = 0.95, N=38, data not shown). Therefore, these accessory pigments were modulated either by high-light, nutrient exposure,or through other physiological processes in surface scum conditions (e.g. Deblois et al., 2013).

The PC:chl-a ratio and chl-*a* were inversely related (fig. 3.3.16B). The fits were derived mathematically and are not caused by "spurious correlation" (Berges, 1997). In Hartbeespoort, the PC:chl-*a* ratio decreased from around 3 at chl-*a* of 100 mg m^{-3} to just 0.7 at chl-*a* of 10000 mg m^{-3}. This might be caused by nitrogen limitation in surface scum (Schwarz and Grossman, 1998), however nutrient data acquired simultaneously reveal no shortage of total nitrogen or other nutrients (fig. 3.3.16C). An alternative explanation is that PC production is reduced in high-light conditions (Deblois et al., 2013, Raps et al., 1985), or in fast growth scenarios, which can occur in surface scum. While a precise explanation remains somewhat unknown, the observation has some important implications for surface scum scenarios. If the production of accessory pigment PC is reduced relative to chl-*a* in surface scums, then chl-*a* might in fact be a better indicator of biomass than PC in these conditions. Secondly, when interpreting measurements made in surface scums, the reduced accessory pigment production might be used to explain some unusual effects in the PC-specific absorption, which are now discussed.

$a_{pc}(620)$ and PC were closely correlated according to $a_{pc}(620) = 0.0146 \times PC^{0.929}$ (r^2 = 0.97, N=36). Clustering in the data from 10 to 20 mg m^{-3} PC resulted in a reduced coefficient of determination for Theewaterskloof alone (r^2 = 0.61) while PC measured in Hartbeespoort varied over more than three orders of magnitude (r^2=0.93). The poor fit in Theewaterskloof is likely the result of strong influence of chl-*c* and chl-*b* pigments near 620 nm from diatoms and chlorophytes. This

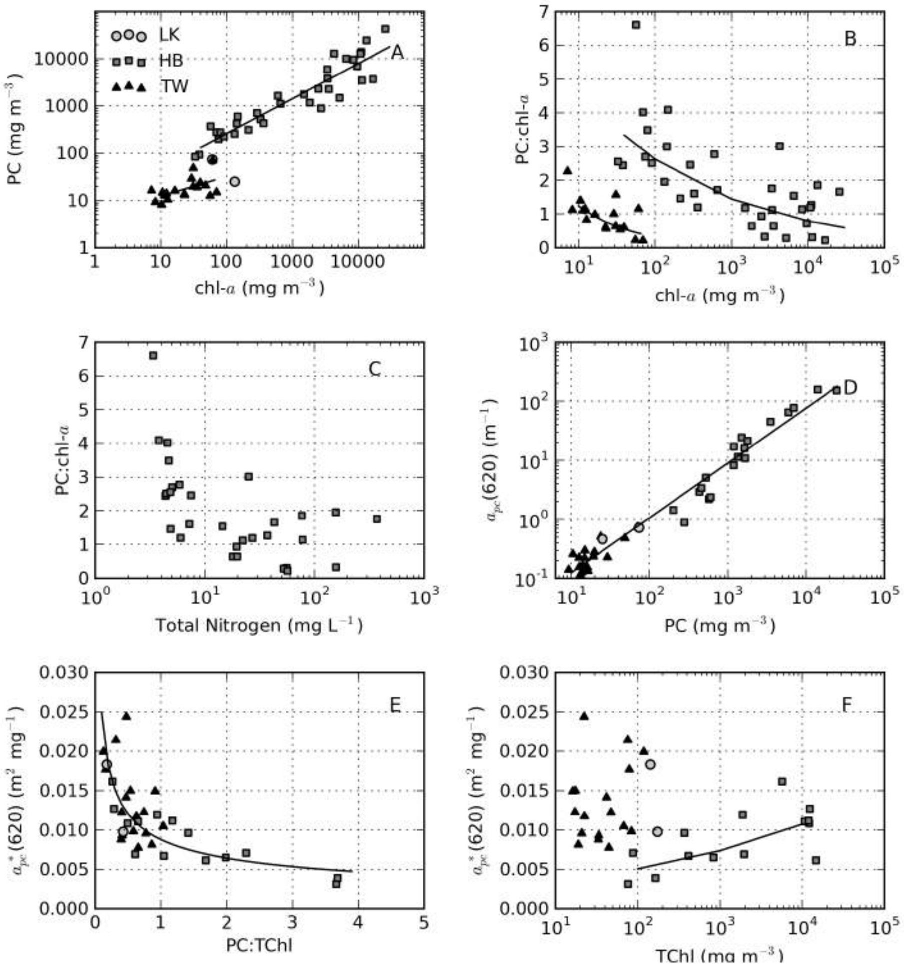

Figure 3.3.16: A) Chl-a versus PC showing best fit lines for HB and TW. B) The PC:chl-a ratio versus chl-a showing best fit lines for HB and TW. C) The PC:chl-a ratio versus total nitrogen concentration. D) $a_{pc}(620)$ versus PC showing power-law best fit line. E) The PC:chl-a ratio versus $a^*_{pc}(620)$. F) TChl-a versus $a^*_{pc}(620)$ showing power-law best fit line for HB. Legend is the same in all plots. Note log scales.

is substantiated by the relatively low PC:TChl ratios in Theewaterskloof (median value of 0.53). An inverse relationship was present between the PC:TChl ratio and $a^*_{pc}(620)$ ($y = 0.0088x^{-0.451}$, $r^2 = 0.63$, N=31, fig. 3.3.16E) similar to that observed by Simis et al. (2005). The variability in $a^*_{pc}(620)$ can typically be attributed to the contribution of cyanobacteria to the total phytoplankon population (Simis et al., 2007). While this is probably the case for Theewaterskloof, the variability observed in Hartbeespoort can only be caused by biomass related variable accessory pigment (PC) production. Therefore, $a^*_{pc}(620)$ varied not only according to the relative contributions of cyanobactieria and algae, but also with physiological processes related to biomass. Fig. 3.3.16F provides some further evidence for biomass-induced changes in $a^*_{pc}(620)$. A positive correlation was present between TChl and $a^*_{pc}(620)$ ($y = 0.0024x^{0.1627}$, r^2=0.48, N=14). Therefore the variability in $a^*_{\varphi}(620)$ in Hartbeespoort appeared to be caused at least partially by biomass-related phenomena.

The value for *in vivo* $a^*_{pc}(620)$ was recently experimentally determined as 0.007 $m^2\ mg^{-1}$ for a wide variety of cultured cyanobacteria (Simis and Kauko, 2012). The median values for $a^*_{pc}(620)$ determined in Theewaterskloof and Hartbeespoort were 0.0122 and 0.0085 $m^2\ mg^{-1}$, respectively. This is within the range of those previously measured in natural populations (Simis et al., 2005). For PC:TChl ratios > 0.5 the value in Theewaterskloof was reduced to 0.010 $m^2\ mg^{-1}$. For Hartbeespoort data not affected by large biomass effects i.e. TChl $< 1000\ mg\ m^{-3}$, the median value for $a^*_{pc}(620)$ was 0.0067 and the mean was 0.0072 $m^2\ mg^{-1}$ which is nearly identical to that of Simis et al. (2007) and Simis and Kauko (2012). This also demonstrates that the method for PC extraction used in this study was probably efficient.

3.3.7 ABSORPTION BUDGETS

The ternary plots in fig. 3.3.17 show the relative contributions by *gelbstoff*, phytoplankton and tripton towards the total absorption budget of each reservoir. At 442 nm (fig. 3.3.17A) there is a strong influence by all components. The clustering of data from Hartbeespoort towards the phytoplankton apex is indicative of an overwhelming dominance of phytoplankton absorption. Therefore Hartbeespoort waters (or the *M. aeruginosa* bloom) might strictly be classified as Case I, i.e. phytoplankton are the dominant contributor to absorption (Morel and Prieur, 1977). Similarly, the clustering of the Loskop data from the *C. hirundinella* bloom towards the phytoplankton apex might also be classified Case I: more than 80% of the absorption is attributed to phytoplankton. It should be noted however that while strictly speaking these can be classified as Case I waters, the reflectance features of Case I green waters described by Morel and Prieur (1977) will be substantially different to those described here. As the blooms of *M.aeruginosa* and *C. hirundinella* can essentially be treated as 'cultures' (i.e. minimal influence of constituents other than phytoplankton) some complexity regarding remote sensing applications are removed. This provides an opportunity for remote sensing algorithms which take advantage of a signal originating primarily from phytoplankton in eutrophic waters. One such example is the maximum peak-height algorithm derived from the data obtained from Hartbeespoort and Loskop as described in Chapter 2.

The remainder of the Loskop data were typically dominated by *gelbstoff* (40-80%) with lesser contributions from phytoplankton ($<$ 50%) and tripton (20–50%). Absorption in Theewaterskloof was generally comprised of 50% *gelbstoff*, 20% phytoplankton and 30% tripton. These fall into the classification of Case II or optically-complex waters. At 675 nm (3.3.17B) the data were expectedly clustered towards the phytoplankton apex, which resulted from the reduced influence of tripton and *gelbstoff* absorption in red wavelengths. This shift due to the spectral characteristics of the absorption components is visible at various wavebands of the upcoming Sentinal 3 and past MERIS sensors (fig. 3.3.18). The majority of the water encountered in the reservoirs was complex from an optical perspective, requiring remote sensing applications taking into account the absorption characteristics of all water constituents presented here. Chapters 4 and 5 utilise the

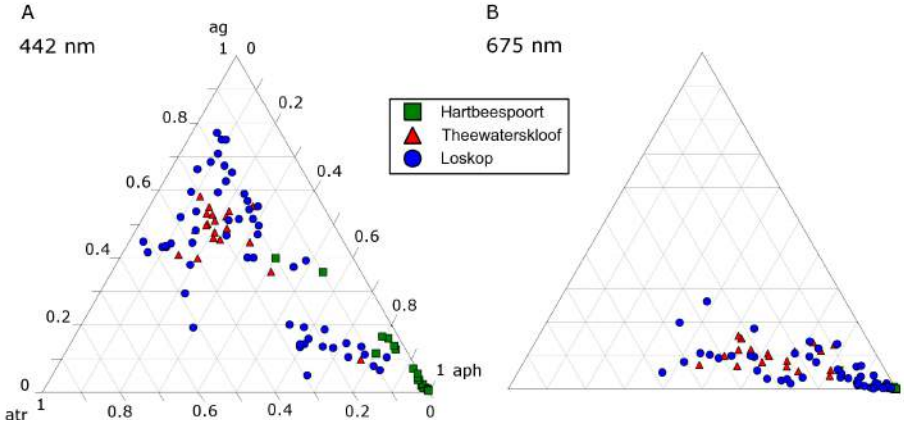

Figure 3.3.17: Ternary plots showing the relative contributions of *gelbstoff*, tripton and phytoplankton to absorption at A) 442 nm and B) 675 nm.

IOPs derived from this study for radiative transfer modeling and the derivation of remote sensing algorithms.

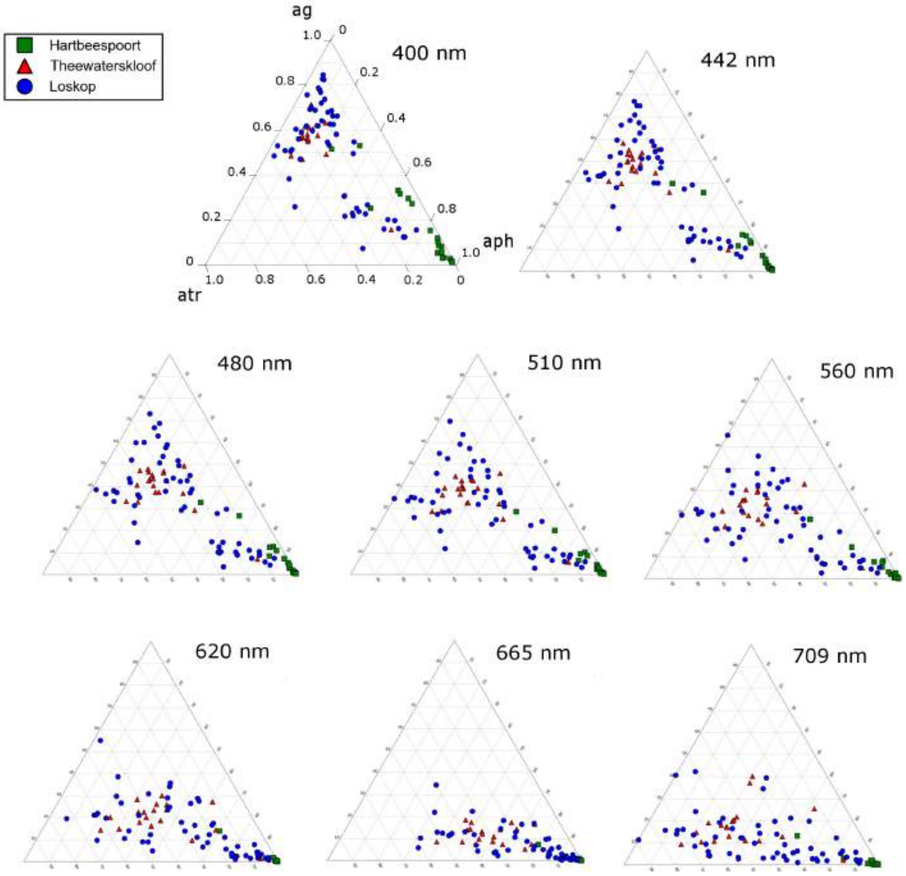

Figure 3.3.18: Ternary plots showing the relative contributions of *gelbstoff*, tripton and phytoplankton to absorption at various wavelengths of the Sentinal 3 and MERIS sensors.

The analysis conducted here is based on sampling campaigns conducted over a short time period and at various times of the year. There was significant seasonal variability in the contribution of phytoplankton towards the absorption budgets, with the maximum being reached in later summer and the minimum during winter (see phenology of phytoplankton biomass for these and other reservoirs in Chapter 6). This has large implications for remote sensing applications. For example, Hartbeespoort typically shifts from hypertrophic surface scum conditions during late summer to an oligotrophic clear-water phase during winter. The *gelbstoff* component generally has little seasonal variability but will increasingly contribute towards the absorption budget during such clear-water phases. Therefore remote sensing approaches utilising IOP models capable of simulating a wide range of water conditions are required for routine derivation of water information products. The specific IOPs derived here can be used in such models to simulate both clear water and hypertrophic phases and for training of radiative transfer based algorithms (see Chapters 4 and 5).

3.4 CONCLUSION

The inherent optical properties of phytoplankton, *gelbstoff*, and tripton have been determined for three small South African reservoirs for use in water remote sensing applications. The study adds to the limited knowledge of IOPs in diverse inland waters, especially those that are hypertrophic. The absorption properties of the reservoirs was extremely variable highlighting the need for lake, trophic class and/or species-specific IOP models. Relationships between the absorption components and biogeochemical parameters were mostly reservoir-specific. As for coastal waters, accessory pigments and variable phytoplankton size (package effect) are responsible for large variations in a_{φ}^{*} in inland waters. In particular, high biomass populations of small-celled cyanobacteria cause a breakdown in the conventional relationship between cell size and trophic state in inland waters.

The data from *M. aeruginosa* blooms provide new insight into the absorption properties and pigmentation of cyanobacterial surface scums. An observed reduction in accessory pigment production suggests that chl-*a* was a better indicator of biomass than phycocyanin (PC) in surface scums. $a_{pc}^{*}(620)$ was nearly identical to that determined experimentally by Simis and Kauko (2012) = 0.007 $\mathrm{m^2\,g^{-1}}$. The variability in $a_{pc}^{*}(620)$ could be attributed both to variable algal/cyanobacteria composition and to biomass-related effects. There was evidence that the hot methanol QFT technique leads to under extraction of PC by 15 to 20% even when no discernible absorption features are present in the tripton absorption spectrum. There were errors in the tripton absorption spectra resulting from bleaching of heterotrophic bacteria in the *M. aeruginosa* blooms. Mass specific tripton absorption determined using a new method was in general agreement with other inland and mineral-rich marine waters.

The IOPs measured here are used in Chapters 4 and 5 to advance the application of remote sensing in small, hypertrophic inland waters. Similar IOP studies should be performed in inland waters representative of other geographical regions of the world where data are lacking. The use of these and similar data in bio-optical models will contribute to the ongoing development of more globally applicable remote sensing products for inland waters.

This chapter is based on work published as:
Matthews, M. W., and Bernard, S. (2013). Using a two-layered sphere model to investigate the impact of gas vacuoles on the inherent optical properties of M. aeruginosa. Biogeosciences, 10, 8139-8157.

4

Using a two-layered sphere model to investigate the impact of gas vacuoles on the inherent optical properties of *Microcystis aeruginosa*

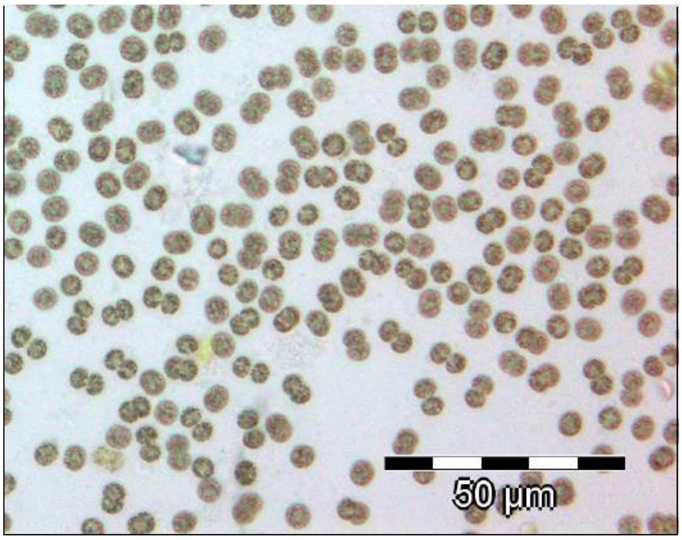

Micrograph of vacuolate Microcystis aeruginosa cells sampled from Zeekoevlei in June 2010.

Abstract

A two-layered sphere model is used to investigate the impact of gas vacuoles on the inherent optical properties (IOPs) of the cyanophyte *M. aeruginosa*. Enclosing a vacuole–like particle within a chromatoplasm shell layer significantly altered spectral scattering and increased backscattering. The two-layered sphere model reproduced features in the spectral attenuation and volume scattering function (VSF) that have previously been attributed to gas vacuoles. This suggests the model is good at least as a first approximation for investigating how gas vacuoles alter the IOPs. Measured R_{rs} was used to provide a range of values for the central value of the real refractive index, $1+\varepsilon$, for the shell layer using measured IOPs and a radiative transfer model. Sufficient optical closure was obtained for $1+\varepsilon$ between 1.1 and 1.14 which had corresponding chl-*a* specific phytoplankton backscattering, $b^*_{b\varphi}$, between 3.9 and 7.2 $\times 10^{-3}$ m^2 mg^{-1} at 510 nm. The $b^*_{b\varphi}$ values are in close agreement with literature and *in situ* particulate backscatting measurements. R_{rs} simulated for a population of vacuolate cells was greatly enlarged relative to a homogeneous population. A sensitivity analysis of empirical algorithms for estimating chl-*a* in eutrophic/hypertrophic waters suggests these are robust under variable constituent concentrations and likely to be species sensitive. The study confirms that gas vacuoles cause significant increase in backscattering and are responsible for the high R_{rs} values observed in buoyant cyanobacterial blooms. Gas vacuoles are therefore one of the most important bio-optical substructures influencing the IOPs in phytoplankton.

4.1 INTRODUCTION

4.1.1 GAS VACUOLES IN CYANOBACTERIA: IMPLICATIONS FOR LIGHT SCATTERING

Light scattering by cyanobacteria, especially those exhibiting intracellular gas vacuoles, is poorly described. Prokaryotic cyanobacteria play an important role in the functioning of freshwater and marine ecosystems alongside eukaryotic algae, although their optical properties are less well understood than the latter. These ancient organisms represent a crucial component of earth's biogeochemical cycling and are hypothesised to have contributed towards the oxygenation of the early atmosphere (Blank and Sánchez-Baracaldo, 2010). Therefore further knowledge of their optical properties will contribute towards an improved understanding of earth's biogeochmical cycle through their more comprehensive inclusion in ecological and biogeochemical ecosystem models.

Light scattering by planktonic algae and cyanobacteria is profoundly influenced by internal structure (Svensen et al., 2007, Whitmire et al., 2010). Intracellular gas vacuoles are known to have a pronounced effect on the interaction of light with cyanobacteria cells (Dubelaar et al., 1987, Ganf et al., 1989, Volten et al., 1998). Gas vacuoles in cyanobacteria are potentially one of the most important distinctive cellular structures influencing the IOPs, namely absorption (a), scattering

(b), and backscattering (b_b) (see table 4.1.1 for symbols and definitions used in this Chapter). Absorption spectra collected using an integrating sphere (which collects all of the forward scattered light) showed reduced wavelength-independent absorption following collapse of vacuoles (Dubelaar et al., 1987). This is attributed to the loss of light that is scattered in a backward direction by vacuoles which is confirmed by measurements of isolated collapsed gas vesicles which have insignificant absorption (Shear and Walsby, 1975, Waaland et al., 1971, Walsby, 1994). Therefore intracellular vacuoles probably only cause a slight increase in true cellular absorption (Ogawa et al., 1979).

Vacuoles have a far greater effect on attenuation than on absorption as a result of strong spectral scattering (see figures in Dubelaar et al., 1987, Ganf et al., 1989, Ogawa et al., 1979, Shear and Walsby, 1975, Waaland et al., 1971, Walsby, 1994). Observations of natural turbid waters dominated by *Microcystis* spp. indicate that vacuoles may contribute up to 80% of light scattering (Ganf et al., 1989). Gas vacuoles may scatter up to six times the light scattered by the cell (Fogg et al., 1973). Attenuation is generally increased by the presence of vacuoles (Shear and Walsby, 1975, van Liere and Walsby, 1982, Waaland et al., 1971, Walsby, 1994), however the results of Dubelaar et al. (1987) suggest the changes can be more complex. The difference spectra between vacuolate and non-vacuolate suspensions (which can be attributed to scattering) are typically flat with troughs corresponding to the absorption maxima of cellular pigments (Shear and Walsby, 1975, Waaland et al., 1971, Walsby, 1994). The spectral shapes of the difference curves resemble inverted absorption curves and are similar to scattering spectra of algae (e.g. Bricaud et al., 1983, Zhou et al., 2012). Therefore it appears that vacuoles contained in the cell increase the overall scattering of the cell suspensions equally across the spectrum. This is in contrast to the scattering properties of isolated gas vesicles, which scatter light as Rayleigh scatterers with a λ^{-4} shape. When vesicles are packaged within the cell wall in honeycomb-like vacuole arrangements however, their scattering properties change. This is most likely caused by the increased particle size of vacuole arrangements (Shear and Walsby, 1975).

The effect of gas vacuoles on angular light scatter was examined using flow cytometry by Dubelaar et al. (1987) and Dubelaar and van der Reijden (1995). Collapse of vacuoles in cultured *M. aeruginosa* suspensions increased forward light scatter by a factor of five while simultaneously decreasing perpendicular light scatter by a factor of ten. The reduced forward light scatter is attributed to a reduction in the real refractive index, n, of the cell as a whole as a result of the gas vacuoles. More detailed measurements of the volume scattering function (VSF) of vacuolate and non-vacuolate *M. aeruginosa* cells reveal significant changes in the shape of the VSF (Schreurs, 1996, Volten et al., 1998). Vacuolate cells consistently show a flattening of the VSF in the forward direction, which corresponds to the reduced forward light scatter measured by Dubelaar et al. (1987). This phenomenon is only reproduced by Mie modelling using homogeneous spheres with very low refractive index (=0.4) relative to water (Schreurs, 1996). This is consistent with the hypothesis that

Table 4.1.1: Symbols and definitions

Symbol	Definition	Unit
m	Complex refractive index	
n	Real refractive index	
n'	Imaginary refractive index	
n_w	Real refractive index for water	
n_m	Homogeneous real refractive index	
$1+\varepsilon$	The central value of n	
Δn	The variation of n around $1+\varepsilon$	
d	Diameter	μm
r_{eff}	Effective radius	μm
V_{eff}	Effective variance	
V_g	Gas vacuole volume	
V_c	Core layer volume	
V_s	Shell layer volume	
c_i	Intracellular chl-a concentration	$\mathrm{kg\,m^{-3}}$
a	Absorption coefficient	$\mathrm{m^{-1}}$
b	Scattering coefficient	$\mathrm{m^{-1}}$
c	Attenuation coefficient	$\mathrm{m^{-1}}$
b_b	Backscattering coefficient	$\mathrm{m^{-1}}$
a^*_φ	Chl a specific phytoplankton absorption coefficient	$\mathrm{m^2\,mg^{-1}}$
b^*_φ	Chl a specific phytoplankton scattering coefficient	$\mathrm{m^2\,mg^{-1}}$
$b^*_{b\varphi}$	Chl a specific phytoplankton backscattering coefficient	$\mathrm{m^2\,mg^{-1}}$
a^*_{tr}	Tripton mass specific absorption coefficient	$\mathrm{m^2\,g^{-1}}$
b^*_{tr}	Tripton mass specific scattering coefficient	$\mathrm{m^2\,g^{-1}}$
b^*_{btr}	Tripton mass specific backscattering coefficient	$\mathrm{m^2\,g^{-1}}$
a_g	*Gelbstoff* absorption coefficient	$\mathrm{m^{-1}}$
a_w	Water absorption coefficient	$\mathrm{m^{-1}}$
b_{bp}	Particulate backscattering coefficient	$\mathrm{m^{-1}}$
b^*_{bp}	Chl a specific particulate backscattering coefficient	$\mathrm{m^2\,mg^{-1}}$
$\tilde{b}_b$	Backscattering ratio	
$\tilde{b}_f$	Forward scattering ratio	
Qa	Optical efficiency factor for absorption	
Qb	Optical efficiency factor for scattering	
Qc	Optical efficiency factor for attenuation	
$\bar{Q}a$	The experimental mean absorption efficiency factor	
Q_c^{NAE}	The non-absorbing efficiency factor for attenuation	
R_{rs}	Remote sensing reflectance	$\mathrm{sr^{-1}}$
β	Volume scattering function or VSF	$\mathrm{m^{-1}\,sr^{-1}}$

reduced forward light scatter is caused by vacuoles which reduce the overall real refractive index of the cell.

There is also evidence that the presence of vacuoles strongly enhances spectral backscattering of cyanobacteria. In comparison with other phytoplankton, vacuolate *M. aeruginosa* is among the most efficient scatterers and is the most efficient backscatterer (Zhou et al., 2012). Matthews et al. (2012) measured a mean chl-*a* specific particulate backscatter (b_{bp}^{*}) in dense *M. aeruginosa* blooms of 0.4×10^{-3} m^{-1} at 420 nm and 1.98×10^{-3} m^{-1} at 700 nm (N = 13). These were an order of magnitude larger than similar measurements made in a high biomass dinoflagellate marine bloom and are in the upper range of values present in literature (e.g. Ahn et al., 1992, Whitmire et al., 2010). The enhanced backscatter can be partially attributed to the small cell size, but must be overwhelmingly attributed to intracellular vacuoles, since *M. aeruginosa* has no other unusual substructure or shape variation (spherical) to distinguish it from algae. Unfortunately Zhou et al. (2012) did not measure the backscatter of non-vacuolate cells. Until the present study, no detailed modeling study has been undertaken to demonstrate the effect vacuoles might have on the IOPs of cyanobacteria.

4.1.2 COMPOSITION, MORPHOLOGY AND CELLULAR ARRANGEMENT OF GAS VACUOLES

Gas vacuoles are composed of individual gas vesicles which are stacked length–wise in a hexagonal honeycomb–type arrangement within the cytoplasm (see review by Walsby, 1994). These vesicles are cylindrical membrane tubes composed entirely of proteins and capped on each end with a half-cone. In *Microcystis* individual vesicles have width and height of approx. 70 and 360 nm, respectively, while the membrane wall is approx. 2 nm thick (Jost and Jones, 1970). Waaland et al. (1971) found a peripheral cellular arrangement of vacuoles in *Nostoc* cells, as was observed in the marine cyanobacterium *Trichodesmium* (van Baalen and Brown, 1969). The peripheral arrangement of vacuoles has caused speculation of light–shielding of the photosynthetic lamella (e.g. Rajagopal et al., 2005, van Baalen and Brown, 1969) however this is somewhat disputed (Ogawa et al., 1979). Polar arrangement is observed in *Pseudanabaena* while both central and polar arrangements exist in *Oscillatoria* species (Meffert et al., 1981). In *M. aeruginosa* peripheral (Jost and Jones, 1970) and random (Jost and Zehnder, 1966, Šmarda, 2009) arrangements are observed. The main factor affecting the cellular arrangement of vacuoles appears to be the light conditions, with some evidence that high light favors a peripheral location (see Shear and Walsby, 1975, Walsby, 1994).

The ratio of gas vacuole to cell volume, V_g:V_c, also appears to be regulated by light as well as nutrient availability (Walsby, 1994). Density calculations for various cyanobacteria show that the volume occupied by vacuoles in order to make the cell neutrally buoyant varies from 3–10% (*ibid.*). However, studies show that the actual volume occupied by vacuoles is often substantially higher than this. The volume occupied by vesicles in cultured *M. aeruginosa* in logarithmic growth phase was 5.8 μm^3 per cell which equates to V_g:V_c = approx. 8% (assuming a cell radius = 2.58 μm) (Lehmann and Jost, 1971). Gas vacuoles exist throughout the life cycle of *M. aeruginosa* in variable amounts reaching >90% of the cell volume in peak summer (Šmarda, 2009). Vacuoles are even present in the benthic overwintering stage in relatively high volumes (V_g:V_c = 1.8–2.9%) (Reynolds et al., 1981).

One of the primary consequences of vacuolation is lowering of cellular density (providing buoyancy) and therefore the overall real refractive index. The refractive index of the vacuole is close to 0.825 while that of the other cellular material is close to 1.028 relative to the medium (water) (Fuhs, 1969). This change in refractive index has substantial implications for how light interacts with the cell (Dubelaar et al., 1987, Porter and Jost, 1976, Shear and Walsby, 1975). Using the concept of a significant refractive index and the Gladstone-Dale volume equivalence formulation, the overall or homogeneous refractive index, n_m, can be calculated from its parts according to $n_m = \sum_j n_j v_j$ where v is the relative volume and j is the number of components (Aas, 1996). Increasing the vacuole content leads to a concentration of cellular material as vacuoles occupy space within the cytoplasm (Raven, 1987). Calculating the homogeneous refractive index of the cell using the values of Fuhs (1969) for the gas vacuole and chromatoplasm and V_g:V_c ranging from 2 to 90% gives n_m varying over a considerable range between 1.02 and 0.84 relative to water. This demonstrates the considerable effect gas vacuolation may have on n_m. A detailed calculation of the complex refractive index, m, for the gas vacuole and chromatoplasm is performed in section 4.2.2.

4.1.3 THE TWO-LAYERED SPHERE MODEL APPROXIMATION

Lorenz-Mie modeling using a population of homogeneous spheres has been used extensively to model phytoplankton IOPs (e.g. Stramski et al., 2001). However, this approach is often criticised as being overly–simplistic since phytoplankton differ considerably in shape and internal structure from homogeneous spheres. Recent comparisons between Mie modeling and experimental results demonstrate the limitations of this approach to sufficiently simulate phytoplankton IOPs (e.g. Whitmire et al., 2010, Zhou et al., 2012). An alternative approach is therefore required to account for variation in internal structure (and shape) of phytoplankton cells. Two-layered and three–layered sphere models which simulate internal structures of the cell wall, the cytoplasm, and or the chloroplast can more adequately simulate phytoplankton IOPs (e.g. Bernard et al., 2009, Kitchen and Zaneveld, 1992, Quinby-Hunt et al., 1989). In particular the Aden–Kerker 2 layered sphere is probably the simplest geometrical arrangement capable of reproducing experimental IOPs (Quirantes and Bernard, 2006). The suitability of such a two-layered Aden–Kerker model for investigating the optical consequences of gas vacuoles is evaluated here.

The cellular arrangement of cyanobacteria and *M. aeruginosa* in particular provides a unique opportunity for the two-layered model to investigate the influence of vacuole substructure. The traditional assignment of the two spherical layers of the model to chloroplast and cytoplasm respectively (e.g. Bernard et al., 2009) is less suitable to prokaryotic cyanobacteria. The thylakoids in cyanobacteria are not arranged in strict membrane bound chloroplasts but rather occur in the intracytoplasmic membrane towards the periphery of the cell (the so-called chromatoplasm). Given this cellular arrangement, the opportunity arises for the core layer to be assigned to a vacuole–like particle, while assigning the shell layer to that containing the photosynthetic thylakoids and the cytoplasm. This is based on the assumption that the vacuole can be adequately simulated as a single homogeneous particle of spherical shape. However, the shape and organisation of the vacuole might actually lend itself to such an approximation. In comparison with isolated vesicles, the vacuole is more irregular and in some cases spherical in shape owing to vesicle stacking; organised in the cell in one or more discrete packages; and much larger than the tiny individual vesicles (up to 3.5 μm in diameter by volume calculation) (see figures in Reynolds et al., 1981, Šmarda, 2009). Therefore vacuoles behave as larger optical units (Shear and Walsby, 1975) and might be sufficiently approximated by a spherical core layer.

4.1.4 *M. AERUGINOSA*: A REPRESENTATIVE PROTOTYPE FOR MODELING

M. aeruginosa is a ubiquitous cyanophyte responsible for much of the concern related to toxin-production from cyano–blooms in freshwaters. Worldwide it represents a prolific species of great relevance to environmental monitoring and remote sensing applications. Its morphological characteristics — spherical shape, relatively small size, high vacuole content — make it well suited to modeling studies based on spherical geometries and for testing theories related to how vacuoles might affect the IOPs. Previous IOP modeling studies of cyanophytes have mainly been restricted to small marine species (picoplankton) (e.g. *Synechococcus*), useful because they are assumed to generally obey the assumptions of Mie theory (e.g. Morel et al., 1993, Morel and Bricaud, 1986, Stramski et al., 2001). However, these are not representative of the genera. There therefore seems to be a paucity in detailed IOP studies of the cyanobacteria, especially for larger ubiquitous freshwater species e.g. *Microcystis* or *Dolichospermum*. The prolific occurrence of *M. aeruginosa* blooms in South African reservoirs make it a convenient species for studies using natural populations. It therefore represents a convenient prototype for optical modeling while simultaneously being of great relevance to environmental applications owing to its abundance.

The existence of *M. aeruginosa* in nature in colonial arrangements undoubtedly has significant implications for its IOPs, especially when considering absorption effects related to the package effect (Agusti and Phlips, 1992, Kirk, 1975). Microcystis cells form colonies with great variability in size and shape, and cell densities can be as high as 3 to 5 cells per 1000 μm^3 (Reynolds et al., 1981). Analysing colony size using flow cytometry, Dubelaar and van der Reijden (1995) found that colonies appear to behave as a collection of individual cells, rather than as larger discrete optical units (see Fig. 1 therein). While the geometries used in flow cytometry are appreciably different from nature, for the purposes of this study it is assumed that *M. aeruginosa* blooms can be modelled as a population of single cells.

The aim of this paper is to test the hypothesis that gas vacuoles significantly alter the IOPs of *M. aeruginosa* by causing large changes in scattering. The study begins by investigating the effects of containing a gas vacuole–like particle within a two-layered sphere on the optical efficiency factors, chl-*a* specific IOPs, and VSF of *M. aeruginosa*. The potential influence and contribution of gas vacuoles to the higher than usual R_{rs} signals observed in blooms of vacuolate cyanophytes is then investigated using a suite of *in situ* experimental data of the IOPs and R_{rs}, and a radiative transfer model. A range of plausible n values for the shell chromatoplasm layer are therefore determined, along with the corresponding chl-*a* specific backscattering for *M. aeruginosa*.

4.2 METHODS

4.2.1 STUDY AREA AND *IN SITU* DATA

In situ measurements were performed at Hartbeespoort Dam, South Africa, in October 2010 on spring blooms of *M. aeruginosa* which made up more than 90% of the population as percentage as determined by microscopy. Background information on Hartbeespoort as well as details of sampling strategy, locations and methods can be found in Chapter 3. The *M. aeruginosa* blooms existed at very high biomass as aggregated colonial surface accumulations (scum) with chl a ranging from 70 to 1503 mg m^{-3} with a mean value of 404 mg m^{-3}. Given the extremely high biomass, the water might effectively be treated as a "culture", eliminating some of the complexity as far as optical modelling is concerned (Matthews and Bernard, 2013a).

Chl-*a* was determined in triplicate spectrophotometrically by extraction in boiling ethanol (Sartory and Grobbelaar, 1984). The quantitative filterpad technique was used to determine the spectral absorption coefficients of particulate matter between 350 and 850 nm using a Shimadzu UV-2501 spectrometer fitted with an integrating sphere (Mitchell et al., 2003). The pigmented component was determined by sodium hypochlorite bleaching. The Whatman GF/F filterpad was assumed to be completely diffuse (Roesler, 1998). The integrating sphere collects almost all of the forwards scattered light, however it does not account for the loss by backscatter which may be caused by vacuoles (Dubelaar et al., 1987). However, no attempt was made to correct the absorption measurements for backscatter by vacuoles but its effects are investigated (section 4.3.1). The chl-*a* specific phytoplankton absorption coefficient (a^*_φ) was calculated as the pigmented component divided by chl-*a*. The concentration and absorption properties of tripton (TR) and *gelbstoff* were determined as described in Chapter 3. TR ranged from 1.7 to 19.8 g m^{-3} while $a_g(442)$ ranged between 0.17 and 2.04 m^{-1}, with a mean exponential slope coefficient of 0.017 m^{-1}.

R_{rs} was measured using an ASD FieldSpec3 (ASD Inc.) using the measurement geometry of Mueller et al. (2003), see Chapter 5 for details. Briefly, 10 radiance spectra were collected in sequence for Spectralon^{TM}, sky and water targets. Taking care to exclude contaminated or outlying spectra, the mean of the radiance spectra for each target was computed, from which an R_{rs} spectrum was calculated. This procedure was performed in triplicate at each site, with the final R_{rs} spectrum determined as the mean. Measurements were made under mostly clear sky conditions (cloud cover $<$ 20%) to avoid errors from shadows and diffuse sky light (Doxaran et al., 2004).

The depth-dependent particulate backscattering coefficient, $b_{bp}(z)$, was measured at 440 and 700 nm using a Hydroscat 2 (Hobilabs Inc.). Depth profiles ranging from the surface to a depth of approx. 5 m were binned, median filtered to reduce noise, re-sampled and interpolated to 10 log-spaced depth bins between 0.8 m and the maximum depth using nearest neighbour interpolation. The profiles were measured simultaneous to R_{rs} and chl-*a* measurements, and the chl-*a* specific particulate backscattering coefficients, b^*_{bp}, calculated using b_{bp} at $z = 0.8$ m and surface chl-*a* measurements. Profiles measured in chl-*a* > 1500 mg m^{-3} were excluded.

4.2.2 COMPLEX REFRACTIVE INDEX OF *M. AERUGINOSA*

The details of Mie and Aden-Kerker theory of light scattering with small particles may be found in Morel and Bricaud (1986) and Bernard et al. (2009). Briefly, the complex refractive index (m) is composed of real (n) and imaginary parts (n') according to $m = n - in'$. n is said to vary according to $1 + \varepsilon + \Delta n$ where $1+\varepsilon$ is the central value around which n varies and Δn is the spectral variation as predicted by the Kramers-Kronig or Ketteler-Helmholtz theories. In this text n is presented relative to water where $n = n/n_w$ where n_w is 1.334. m for phytoplankton may be determined from spectral absorption and particle size distribution (PSD) measurements using an inverse anomalous diffraction approximation (ADA) model (Ahn et al., 1992, Bricaud and Morel, 1986). This is based on the ADA assumption that the value of $1 + \varepsilon$ is close to the the value of n_w (i.e. $1 + \varepsilon \approx 1.334$). This assumption is generally valid for phytoplankton (Aas, 1996). While heavily vacuolate cells violate this assumption, it should be valid for non-vacuolate cells. Since vacuoles have an insignificant effect on true cellular absorption used by the method, an initial value for the refractive index of a homogeneous *M. aeruginosa* cell consisting of chromatoplasm and centroplasm (minus effects of gas vacuoles) was determined using the method of Bricaud and Morel (1986) as modified by Bernard et al. (2001).

The particle size distributions of *M. aeruiginosa* were not measured due to difficulties associated with the colonial arrangement of the cells and their existence at extremely high biomass in a surface scum layer. Therefore, a log-normal distribution of cells with diameters ranging from 3.2 to 8 μm was used to estimate the PSD for *M. aeruginosa*. The size range is based in measurements of individual *M. aeruginosa* cells previously made in Hartbeespoort Dam (Robarts, 1984). The distribution was expressed in terms of the effective variance (V_{eff}) and radius (r_{eff}) (Bernard et al., 2007) which were set to 0.02 and 2.58 μm respectively. The log-normal distribution is generally suitable for representing mono–specific phytoplankton blooms (Ahn et al., 1992, Bricaud and Morel, 1986). The size distribution was scaled to give 1 mg chl-*a* for the phytoplankton population (or the chl-*a* specific PSD) using an intracellular chlorophyll density (c_i). The c_i value has large implications for n', the absorption and scattering efficiencies (Q_a, Q_b) and the chl-*a* specific volume coefficients (Morel and Bricaud, 1986). Therefore an appropriate value for c_i must be chosen with care. Values for c_i for *M. aeruginosa* previously measured are 2.1 kg m^{-3} (Zhou et al., 2012), 3.2 kg m^{-3} (Agusti and Phlips, 1992), and 4.5 kg m^{-3} (Reynolds et al., 1981). These were computed from cellular volumes and chl-*a* concentrations presented in the references and fall within the upper range of accepted values for phytoplankton (e.g. Morel and Bricaud, 1986). Values for marine pico-cyanobacteria are typically less than this around 1.15–1.78 kg m^{-3} (*ibid.*). The lowest c_i value of 2.1 kg m^{-3} was selected after analysing results produced by the different values, as discussed in section 4.3.4.

The experimental mean absorption efficiency factor, $\bar{Q}_a$, for *M. aeruginosa* was then calculated between 360 and 850 nm using the estimated chl-*a* specific PSD and a^*_φ (Morel and Bricaud, 1986). n' was then calculated by fitting the experimental $\bar{Q}_a$ to that modelled using the ADA. Δn, was determined as a Hilbert transform of n' according to the Kramers-Kronig theory of anomalous dispersion (Bernard et al., 2001). An initial value for $1+\varepsilon$ was then determined by convergence of the modelled efficiency factors for attenuation (Q_c) and for the non-absorbing equivalent (Q_c^{NAE}). The $1+\varepsilon$ value was selected at wavelength where n' was smallest. This technique was used given the absence of further scattering or attenuation data. A range of plausible $1+\varepsilon$ chromatoplasm values were also determined as described in section 4.2.5.

4.2.3 COMPLEX REFRACTIVE INDICES OF GAS VACUOLES

Using interference microscopy Fuhs (1969) estimated n=0.80 for vacuole and n=1.028 for the surrounding cytoplasm relative to water. Fuhs's (1969) calculations included the volumes of air, protein membrane and interstitial cytoplasmic material. The spectral refractive index for a hypothetical gas vacuole was calculated using a volume equivalent approach (Gladstone-Dale). Calculations were performed using the mean geometries for *Microcystis* vesicles given by Jost and Jones (1970) (length = 360 nm, diameter = 70 nm, wall thickness = 1.8 nm) and an assumed packing efficiency of 15% (Walsby, 1994). Using these geometries, the relative volume for interstitial cytoplasm (water), air and proteins was calculated as 0.15, 0.76 and 0.09 respectively. The spectral real and imaginary refractive indices for the lipid-free protein Ovalbumin (Arakawa et al., 2001) were used for the protein membrane. These data are similar to values reported elsewhere for proteins (n=1.20 and n'=1×10^{-5} Aas, 1996) and are generally representative of lipid-free proteins. Detailed spectral refractive index data for water and air were taken from Ciddor (1996) and Hale and Querry (1973), respectively.

4.2.4 PARAMETERISATION OF THE TWO-LAYERED SPHERE MODEL

A two-layered sphere model using the Aden and Kerker (1951) formulation and the code of Toon and Ackerman (1981) were used to calculate the IOPs (after Bernard et al., 2009) in a Fortran/Matlab environment (The MathWorks^{TM}). Inputs to the model are the radius of the core and shell layers, m for the core and shell layers, the wave number (wavelength) and angular resolution (which is 0.1 degrees). The output is the dimensionless angular intensity parameters (i_1 and i_2) and the efficiency factors for attenuation and scattering (Q_b) from which the phase function (β), the backscattering probability ($\tilde{b}_b$), and the absorption and backscattering efficiencies (Q_a, Q_{bb}) can be calculated (see Morel and Bricaud, 1986, for calculations). Using the PSD and m for shell and core layers, the bulk IOPs (a, b, and b_b) for the cell population were calculated at a 5 nm wavelength resolution.

The core and shell layers were assigned to the vacuole and chromatoplasm, respectively. By assigning the layer with the higher refractive index to be the outer layer, the effect of the cell wall membrane which is known to have a great impact on scattering (Quinby-Hunt et al., 1989, Svensen et al., 2007) is more adequately simulated. Furthermore, in cyanobacteria the photosynthetic thylakoids are most often arranged in concentric anastomosing shells parallel to the cell wall (Golecki and Drews, 1982), and this kind of arrangement with some additional irregularity is observed in *M. aeruginosa* (Šmarda, 2009). The sometimes peripheral arrangement of gas vacuoles are not without enclosure by the layered cell wall membrane, and a random arrangement within the centroplasm is more frequently observed in *M. aeruginosa*. This favors a core assignment for the vacuole which may even be surrounded by the photosynthetic lamella (Smith and Peat, 1967).

The effects of altering the relative volume occupied by the gas vacuole, V_g, on the IOPs is investigated. The relative volumes of the core, $V_c(=V_g)$, and shell, V_s, layers were adjusted according to $V_c = 1 - V_s$. The core radius, r_c, may be calculated using the shell radius, r_s, and V_c by $r_c = r_s V_c^{1/3}$. Considering relative gas vacuole volumes in the range 1 to 50%, and a population of cells with diameters between 3.2 and 8.0 μm, the diameters of the spherical core vacuole would range between 0.68 and 6.34 μm. This represents a particle with a minimum diameter comparable to the wavelength of visible light (680 nm), and in the anomalous diffraction domain.

It has been shown that the cell volume remains unchanged when gas vesicles are collapsed by pressurisation (Dubelaar et al., 1987, Porter and Jost, 1976). The synthesis of vesicles within the cell therefore decreases the relative volume occupied by the chromatoplasm, leading to a concentration effect on the absorbing material, assuming that the amount of absorbing material in the cell (c_i) remains constant. This effect must be accounted for in calculations when altering the relative volumes of core and shell layers. The equation relevant to a two-layered geometry relating n' to c_i and the relative shell volume, V_s, is given by (Bernard et al., 2009):

$$n'_{chrom}(675) = \frac{675}{n_{media}} \frac{c_i a^*_{sol}(675)}{\pi 4 V_s} \tag{4.1}$$

where $n_{media} = 1.334$ and $a^*_{sol}(675)$ is the theoretical maximum absorption by unpackaged chl-*a*.

This scales the n' at 675 nm by the maximum theoretical absorption of unpackaged chl-*a*, keeping the amount of absorbing material in the cell constant. The value for $a^*_{sol}(675)$ is given by Johnsen et al. (1994) as 0.027 mg^{-1} m^{-2} which is applicable to cyanobacteria (Bidigare et al., 1989).

4.2.5 Optical closure for *M. aeruginosa* using the two-layered model

The availability of the suite of *in situ* optical/biogeochemical data from the high biomass monospecific natural *M. aeruginosa* blooms in Hartbeespoort provides an opportunity to perform a detailed investigation of the optical properties of *M. aeruginosa*. For the data set used here, a_φ composed a mean of 85% (up to 98%) of the total absorption, and 96% (up to 99%) of the particulate absorption at 442 nm (see fig. 3.3.18 in Chapter 3. $a_\varphi(442)$ had a mean value of 18 m^{-1} while the corresponding mean values for a_{tr} and a_g were 0.3 and 1.1 m^{-1}. Therefore from an optical perspective *M. aeruginosa* is the overwhelmingly dominant contributor to the total absorption and scattering, with negligible or small contributions from tripton (non-phytoplankton) and dissolved components.

Neglecting the contribution of viruses, bubbles and other small particles (Stramski et al., 2001), a four component bio-optical model consisting of phytoplankton, tripton, *gelbstoff* and water, was used to forward model the R_{rs} using a direct solution of the equation of radiative transfer in Ecolight-S (V1.0 ©Sequoia Scientific). The input to Ecolight-S are the total IOPs (a_t, b_t, b_{bt}) and the downwelling irradiance. As a_t is known (or measured), the only unknowns in the forward model are (back)scattering for phytoplankton and tripton, assuming *gelbstoff* is non-scattering. Given the negligible contribution of tripton to particulate absorption and scattering, the only optically significant unknowns are the (back)scattering from *M. aeruginosa*, which in this case are estimated using the two-layered model. The data therefore provide an opportunity to investigate optical closure with regards *M. aeruginosa* using (back)scattering as determined by the two-layered model.

With regards to the two-layered model, assuming that the core vacuole layer m value is constant with a volume of 50%, and the n' value for the chromatoplasm is adequately determined, the only unknowns in the two-layered configuration are the shell layer $1+\varepsilon$ value and in this case the estimated PSD. Tests showed that variations in the PSD had small effects on the two-layer determined IOPs and resulting R_{rs}. Decreasing D_{min} or increasing D_{max} while holding V_{eff} constant had negligible effects. Increasing V_{eff} to 0.1 while simultaneously decreasing D_{min} to 1 μm or increasing D_{max} to 15 μm had small but noticeable effects resulting in a max. change in R_{rs} at chl-*a* of 100 mg m^{-3} of approx. 12%. Therefore there is a relatively small sensitivity to the width and size range of the PSD in R_{rs}.

Assuming the estimated PSD is acceptable, the only remaining unknown is the shell layer $1+\varepsilon$ value. At the high biomass observed in this study, the R_{rs} was found to be very sensitive to the chromatoplasm $1+\varepsilon$ value. Comparing values of 1.08 and 1.15 for the chromatoplasm, the corresponding $b^*_{b\varphi}$ increased over 370% which resulted in a 300% increase in R_{rs} for a constant chl-*a* value of 100 mg m^{-3}. Therefore, for the high biomass conditions and model configuration used here, the magnitude of R_{rs} is found to be primarily controlled by the shell $1+\varepsilon$ value.

Initial tests using the $1+\varepsilon$ chromatoplasm value determined after Bernard et al. (2001) resulted in $b_{b\varphi}$ values substantially lower than literature values as well as underestimates of R_{rs} as determined by forward simulations using Ecolight-S. Thus optical closure could not be achieved using the initially determined $1+\varepsilon$ value, suggesting that a higher value might be more appropriate. Therefore, in order to achieve optical closure of the experiment, the chromatoplasm $1+\varepsilon$ value was allowed to vary in the range 1.04 to 1.15 at a 0.001 interval. This range of values is in agreement with values for eukaryotic chloroplasts (Bernard et al., 2009) which are likely equivalent to a prokaryotic chromatoplasm and therefore likely to be acceptable from an optical perspective. The resulting $b^*_{b\varphi}$ and b^*_{φ} generated by the two-layer model were added to a look-up table (LUT).

The forward model was then allowed to select appropriate values for $b^*_{b\varphi}$ and b^*_{φ} from the LUT in order to provide the best fit with the measured R_{rs} solved using a non-linear Nelder-Mead simplex algorithm. In this way a range of appropriate values for the chromatoplasm $1 + \varepsilon$ value was determined which provided appropriate optical closure for the R_{rs}. Eight R_{rs} spectra for which absorption coefficients (in duplicate), biogeochemical parameters (in triplicate) and atmospheric parameters were co-incidentally measured were used.

The bio-optical model for the forward model was configured as:

$$a_t = chla \times a_{\varphi}^* + TR \times a_{tr}^* + a_g + a_w$$

$$b_t = chla \times b_{\varphi}^* + TR \times b_{tr}^* + b_w$$

$$b_{bt} = chla \times b_{b\varphi}^* + TR \times b_{btr}^* + b_{bw}$$

where subscript w stands for water.

All components in the forward bio-optical model were calculated using measured values for chl-*a*, TR and a_g for each sample. a_w and b_w ($b_{bw} = 1/2b_w$) were taken from Rottgers et al. (2011). The mass-specific tripton absorption, a_{tr}^*, used was $0.037e^{-0.010(\lambda-442)}$ as determined in Chapter 3. The corresponding tripton mass-specific (back)scattering coefficients, b_{tr}^* and b_{btr}^*, were estimated using a Mie model and an inverse ADA model (see Bricaud and Morel, 1986, for calculations). The tripton mass-specific PSD was computed from a_{tr}^* and an estimate of $n' = 0.01exp(-0.007\lambda)$ (Stramski and Wozniak, 2005) (note that the original equation given in Stramski et al. (2001) is incorrect). The tripton PSD was assumed to obey a Jungian distribution with slope $\gamma = -4$ and diameters between 1 and 100 μm in log-spaced bins. Mie calculations of homogeneous spheres were then used to compute b_{tr}^* and b_{btr}^* with the mass-specific tripton PSD and n'. n for tripton particles was set to 1.05, assuming a 90% detrital component ($n = 1.04$) and a 10% mineral component ($n = 1.18$) (Stramski et al., 2001). The fit between the measured a_{tr}^* and that modeled by Mie calculations was very close ($R^2 = 0.98$). The following power-law fits were thus determined: $b_{tr}^* = 0.648\lambda^{-0.753}$ and $b_{btr}^* = 9.925e^{-4}\lambda^{-0.0816}$.

The resulting uncertainty to R_{rs} from the Mie model determined tripton (back)scattering is likely to be negligible given the very small mean contribution ($\pm$ 4%) of tripton particles to a_t. Assuming an $a_p(442)$ value of 10 m^{-1}, the corresponding values for $a_{\varphi}(442)$ and $a_{tr}(442)$ would be 9.6 m^{-1} and 0.4 m^{-1}, respectively. Using $a_{\varphi}^*(442) = 0.035$ m^{-1}, a reasonable value for *M. aeruginosa* (Zhang et al., 2012), and $a_{tr}^*(442)$ of 0.037 m^{-1}, the corresponding values for chl-*a* and TR are 274 mg m^{-3} and 10 g m^{-3}, respectively. Using an approximate value of $b_{b\varphi}^*(442)$ of 0.006 m^{-1} (Zhou et al., 2012) and a value of $b_{btr}^*(442)$ of 6e-4 calculated as above, the corresponding values for $b_{b\varphi}(442)$ and $b_{btr}(442)$ are 1.64 m^{-1} and 0.006 m^{-1}, respectively. This equates to a contribution of 0.4% by tripton to b_{bp}. Thus the influence of tripton at these high biomass values is negligible.

The downwelling irradiance was calculated using Radtran (Gregg and Carder, 1990) the default atmospheric model for Ecolight-S using parameters recorded at each station including the date, latitude, longitude, GMT, wind speed, aerosol optical thickness (AOT, Solar Light Microtops II sun photometer) and cloud cover (%). Horizontal visibility used by Ecolight-S was estimated by

$vis = 3.9449/(AOT500 - 0.08498)$ (Retalis et al., 2010). The air mass type was set to continental. Default values were used for atmospheric pressure (=29.92 inches mercury), relative humidity (=80%), water vapor (=1.5) and ozone. The vertical profile used was constant with depth, given the shallow optical depth caused by the very high cyanobacterial biomass. Ecolight-S was called as a subroutine in Python programming language (V. 2.7.1).

4.3 RESULTS AND DISCUSSION

4.3.1 COMPLEX REFRACTIVE INDICES

Fig. 4.3.1 shows the data and results of the determination of the complex refractive indices for *M. aeruginosa* and the gas vacuole. The a_φ^* value (Fig. 4.3.1 A) is well within the range presented in the literature for cyanobacteria (e.g. Dupouy et al., 2008), and is almost identical to that for *M. aeruginosa* determined by Zhang et al. (2012), and slightly higher than values obtained by Dekker (1993) for eutrophic blue-green dominant assemblages. The characteristic absorption maximum of phycocyanin is clearly visible near 620 nm. The a_φ^* values used to calculate m did not account for increased apparent absorption that could result from backscatter by gas vacuoles. No attempt was made to correct the measurements for this effect. However, tests showed that variable a_φ^* has little effect on the value of $1 + \varepsilon$ determined by the method. The significance of the variability in n' on the IOPs will be investigated further (section 4.3.4).

The log-normal normalised PSDs are shown in Fig. 4.3.1 B. The effects of varying V_{eff} is evident on the distribution shapes (r_{eff} is fixed at 2.58 μm). The narrow distributions are likely to be representative of the spring blooms in Hartbeespoort, and closely resemble those for monospecific cultures (e.g. Ahn et al., 1992, Bricaud and Morel, 1986). The value chosen for V_{eff} had a small influence on the values determined for Q_a and n' but caused more significant changes in $1 + \varepsilon$ (between 1.078 and 1.081 for $V_{eff} = 0.05$ and 0.01 respectively). The value for V_{eff} was set to 0.02 so as to give a spread of smaller and larger cells without incurring a bias towards small cells, as is visible for $V_{eff} = 0.05$.

The experimental Qa is shown in Fig. 4.3.1 C, and agrees well with literature derived values for phytoplankton (*ibid*). n' (Fig. 4.3.1 D) also compares well to the literature values for homogeneous and heterogeneous cells (Ahn et al., 1992, Bernard et al., 2009, Bricaud and Morel, 1986) and has a mean spectral value of $0.0012i$. n and n' for the vacuole (Fig. 4.3.1 D, E) have mean spectral values of $2.079 \times 10^{-5}i$ and 0.825 respectively. The value determined for n in air is 1.10, identical to that estimated by Fuhs (1969) to have the highest probability. These were estimated by power law functions in further modeling of the IOPs: $n' = 2.28 \times 10^7 \lambda^{-4.66} + 1.08 \times 10^{-5}$ and $n = 333\lambda^{-1.94} + 0.82$.

The value of $1 + \varepsilon$ for *M. aeruginosa* was determined as 1.080 (Fig. 4.3.1 F). This value was determined at a wavelength of 625 nm where $n' = 0.001$. This value represents the mean n_m of a

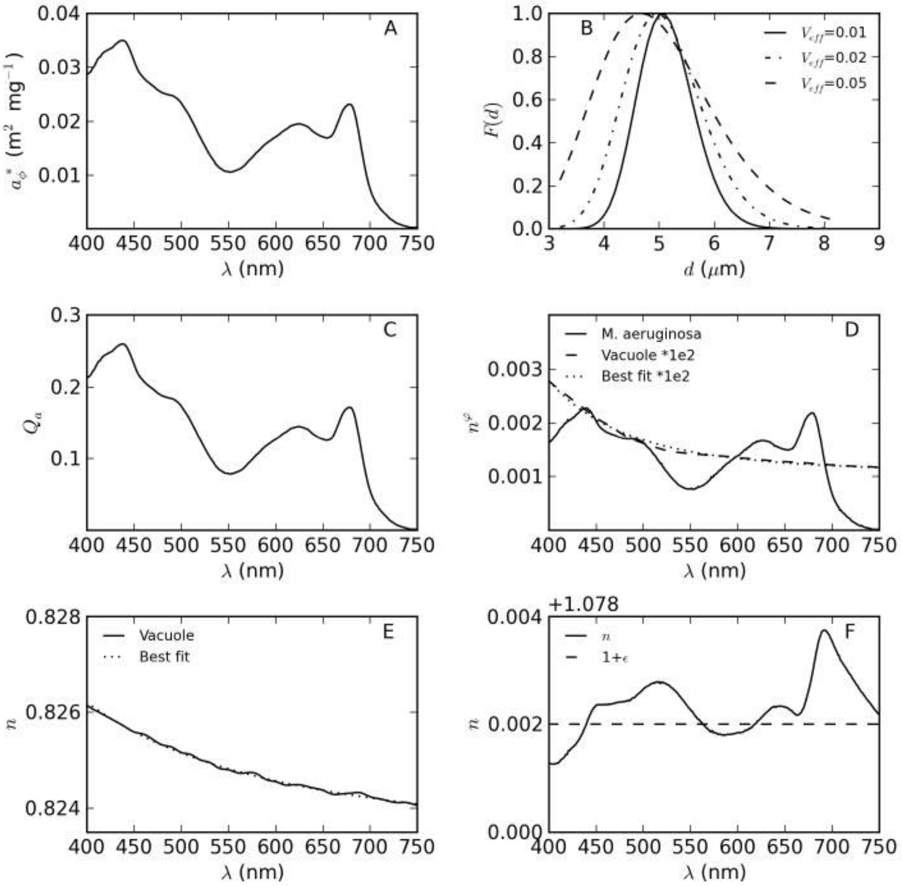

Figure 4.3.1: Optical and size parameters for *M. aeruginosa* and gas vacuole. A) Chl-*a* specific absorption, B) normalised log-normal size distribution function, $F(d)$, for V_{eff}=0.01, 0.02 and 0.05, C) experimental absorption efficiency factor, D) n' for *M. aeruginosa* and gas vacuole $\times 1e^2$, showing best fit line, E) n for gas vacuole showing best fit line, F) n for *M. aeruginosa* showing $1+\varepsilon$ value.

Microcystis cell which includes the cell wall, thylokoids, the cytoplasm and other refractive cytoplasmic inclusions such as polyphosphate granules. The value is within the range of those presented elsewhere for algal cells (Bricaud et al., 1988, Morel and Bricaud, 1986), however it seems quite high when compared with values used previously for modeling cyanobacteria or *M. aeruginosa* as a homogeneous cell (e.g. Volten et al., 1998, Zhou et al., 2012). However, the value of 1.04 used by Volten et al. (1998) is an estimate for generic phytoplankton from Morel and Bricaud (1986). A value of 1.036 was determined by Zhou et al. (2012) for cultured *M. aeruginosa* using similar methods to those presented here, however none of the absorption, size or attenuation data used to constrain the final choice of $1+\varepsilon$ was shown. More comparative values for $1+\varepsilon$ between 1.047–1.085 are given by natural populations of marine *Chlorella* (Spinrad and Brown, 1986) which have similar shape (spherical) and size (d=1.2–6.8μm) to *M. aeruginosa*. A m of $1.085+0.048i$ was derived for a homogenous cell of marine *Chlorella* (Quinby-Hunt et al., 1989). Therefore $m = 1.080 - 0.0012i$ for a homogeneous *M. aeruginosa* cell between 400 and 750 nm is not outside the range of values determined for algae. The final value for 1+ε for the shell layer of a vacuolate cell is determined using R_{rs} data (see section 4.2.5).

4.3.2 THE INFLUENCE OF GAS VACUOLATION ON EFFICIENCY FACTORS AND VOLUME COEFFICIENTS

The optical efficiency factors versus the Mie size parameter ($\alpha = \pi d n_w / \lambda$) for a single cell having variable gas vacuole content is shown in Fig. 4.3.2. The relative volume occupied by the gas vacuole is: 0%, corresponding to an essentially non-vacuolate homogeneous cell, 3% for an upwardly buoyant cell, 10 and 30% for an expected vacuole content in a buoyant surface bloom, and 50% for a heavily vacuolate over-buoyant cell. The non-vacuolate cell (V_g=0) demonstrates the expected interference patterns for Q_c and Q_b, tending towards theoretical expectations with increasing size. For cells with increasing vacuole content, there is significant perturbation in the phase, magnitude and shape of the efficiency factors. This is related to the internal gas vacuole, since the overall pigment content of the cell is constant. For a mean cell in the size range of *M. aeruginosa* Q_c and Q_b are slightly increased with increasing vacuolation, up to a point where they decreases dramatically with heavy vacuolation (V_g=50%). This is better observed by the spectral efficiency factors for the *M. aeruginosa* population shown in Fig. 4.3.3. The upward sloping Q_c and Q_b spectra are probably caused by the relatively high 1+ε value (Fig. 4.3.3 A, B). This value has the greatest influence on the slope and shape of Q_c and Q_b (see Bricaud and Morel, 1986), and its influence is investigated further in section 4.3.4. The value of $Q_c(510)$ ranges from 2.0–2.6 while that of $Q_b(510)$ ranges from 1.85–2.45 (table 4.3.1). Therefore according to the two-layered model, gas vacuoles can significantly alter the shape and magnitude of Qc and Qb through a shift in phase of the interference patterns of the efficiency factors (Fig. 4.3.2 A, B) . This finding is in agreement with Dubelaar et al. (1987) who found that gas vacuoles caused decreased overall spectral attenuation (see further analysis in section 4.3.4). The shift in the position of the red chl-*a* absorption induced attenuation feature near 685 nm towards shorter wavelengths is also visible with increasing vacuolation (Fig. 4.3.3 A), as observed by Dubelaar et al. (1987). This confirms that gas vacuoles are responsible for this phenomenon.

In accordance with theoretical expectations, Q_a is rather undisturbed by gas vacuolation, except for a very slight decrease with large heavily vacuolate cells (figs. 4.3.2 and 4.3.3 C). The agreement between the experimental and modelled Q_a is very close using a value of 0.022 for $a^*_{sol}(675)$. However, for gas vacuolation >50% there is a small departure from experimental values of Q_a (not shown). This effect is probably caused by a breakdown of the assumption of volume-equivalence (eq. 4.1) rather than from light shielding or other effects. Therefore a maximum gas vacuole volume of 50% was used for modeling, in order to not violate the volume equivalence assumption. It is apparent that gas vacuolation has very little implication for absorption according to the two-

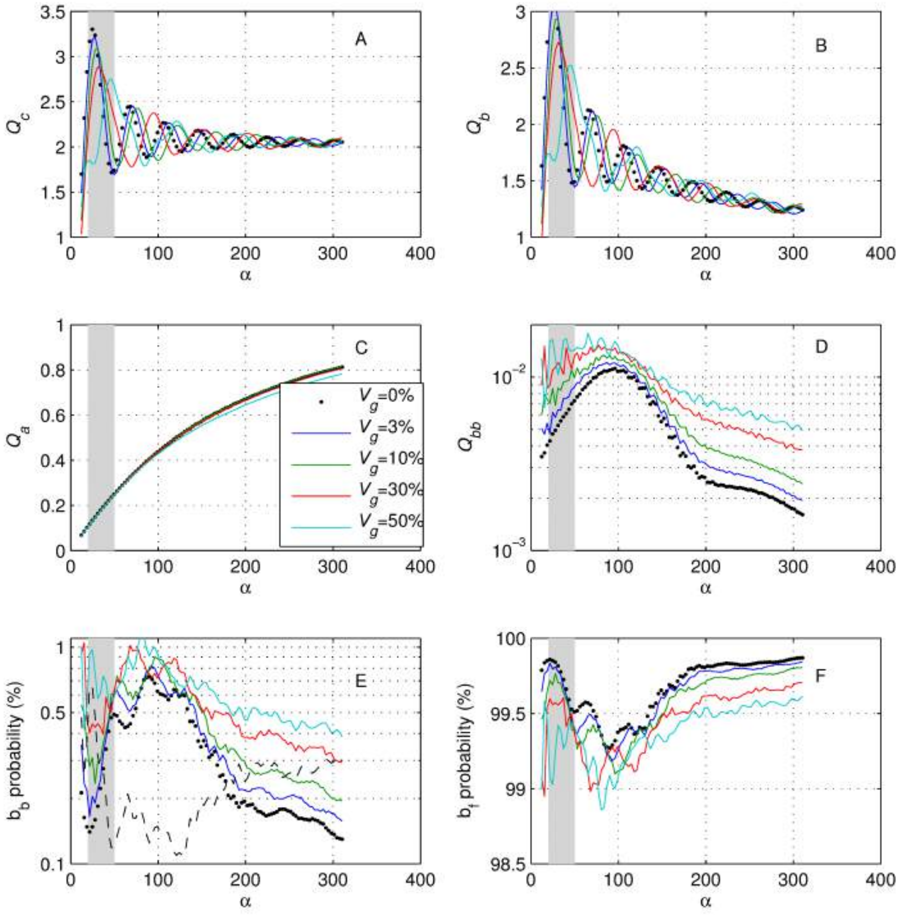

Figure 4.3.2: Optical efficiency factors and the backward and forward scattering ratios of *M. aeruginosa* versus the Mie size parameter, α, modelled as two-layered spheres with variable gas vacuolation (0–50% cell volume). Plotted for cell diameters from 1–50 μm at $\lambda = 675$ nm. The shading indicates the size range applicable to *M. aeruginosa*. The dotted line in E is the ratio of backscattering probability where $V_g = 50\%$ to that where $V_g = 0\% \times 10^{-1}$.

layered model, and therefore the model does not support a significant light shielding role for gas vacuoles in agreement with Ogawa et al. (1979).

The greatest effect of the gas vacuole is on Q_{bb} and the backward and forward scattering ratios (figs. 4.3.2 and 4.3.3 D, E, F). $Q_{bb}(510)$ for a non-vacuolate cell (=7.3×10^{-3}) falls in the range of algal species modelled with relatively high refractive indices (see Ahn et al., 1992, Bricaud et al., 1988). Vacuolation increases Q_{bb} markedly in a relatively spectrally invariant and linear fashion and especially for smaller cell sizes in the range of *M. aeruginosa* (table 4.3.1). $Q_{bb}(510)$ for a heavily vacuolate cell (=0.0156) is twice that of its homogeneous equivalent. $\tilde{b}_b$ may be up to 5 times larger in a heavily vacuolate cell than for a homogeneous equivalent in the size range of *M. aeruginosa* (Fig. 4.3.2 E). This effect is associated with decreased $\tilde{b}_f$ by up to 0.5% (Fig. 4.3.2 F), as was observed experimentally by Dubelaar et al. (1987). However, the spectral slope of $\tilde{b}_b$ indicates enhanced backscattering with higher vacuole content towards the red relative to the blue (Fig. 4.3.3 E). These curves closely resemble those determined experimentally (e.g. Zhou et al., 2012). The opposite is

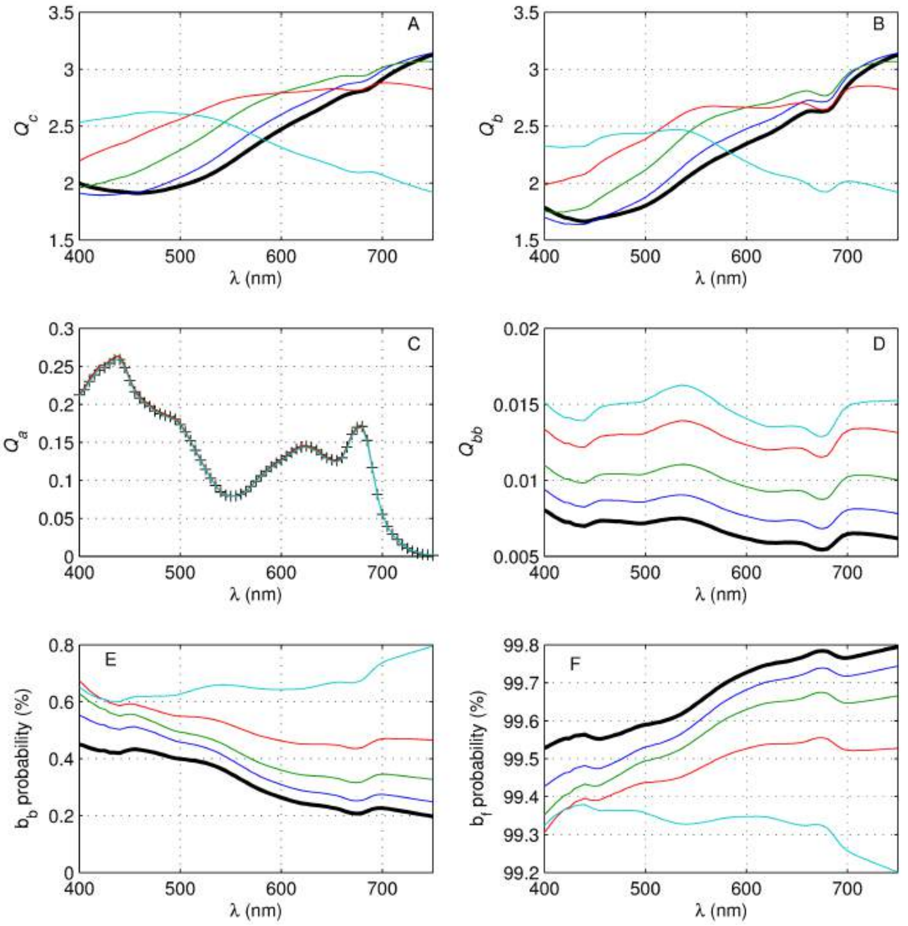

Figure 4.3.3: Optical efficiency factors and forward and backward scattering ratios of a population of *M. aeruginosa* modelled as two-layered spheres with variable gas vacuolation (0–50% cell volume). Legend is the same as Fig 4.3.2. The measured absorption efficiency factor is drawn for comparison in C (+).

observed for forward scattering probability (Fig. 4.3.3 F). Therefore the following can be said in relation to the effect of gas vacuoles on backscattering: firstly it appears that gas vacuolation has large implications for small cells of which *M. aeruginosa* is an example; secondly, Q_{bb} increases roughly linearly with increasing vacuole content; and lastly, $\tilde{b_b}$ seems to be enhanced in the red relative to the blue for cells with a high gas vacuole content.

The chl-*a* specific volume coefficients for variable gas vacuolation are shown in Fig. 4.3.4 A–D. The shapes of the attenuation and scattering spectra are identical to the efficiency factors in Fig. 4.3.3. The range of values for $b^*_\varphi(510)$ from 0.25–0.33 m² mg^{-1} are towards the upper range of values observed for cyanophyta and phytoplankton in modelling studies (Bricaud et al., 1988, Morel and Bricaud, 1986). The downward–sloping attenuation curves for V_g=50% resemble those previously measured for *M. aeruginosa* (Dubelaar et al., 1987). The modelled chl-*a* specific absorption is almost identical to the measured value (see Fig. 4.3.1). $b^*_{b\varphi}(510)$ is 1.0×10^{-3} m² mg^{-1} for a non-vacuolate cell, and 2.1×10^{-3} m² mg^{-1} for a heavily vacuolate cell. This amounts to a two–fold

Table 4.3.1: Chl-*a* specific volume coefficients (m² mg^{-1}), efficiency factors and scattering ratios (%) at 510 nm for a population of *M. aeruginosa* modelled as two-layered spheres with variable gas vacuole content (%) for shell layers $1+\varepsilon = 1.080$ and $1+\varepsilon = 1.036$.

V_g	c^*_φ	b^*_φ	$b^*_{b\varphi}\times10^3$	Q_c	Q_b	Q_{bb}	$\tilde{b}_{b\varphi}$	$\tilde{b}_{f\varphi}$
$1+\varepsilon$=1.080								
0	0.27	0.25	1.0	2.00	1.85	0.0073	0.39	99.59
3	0.28	0.26	1.2	2.09	1.94	0.0087	0.45	99.54
10	0.32	0.30	1.4	2.34	2.18	0.0106	0.49	99.50
30	0.35	0.33	1.8	2.60	2.44	0.0134	0.55	99.44
50	0.35	0.33	2.1	2.60	2.45	0.0156	0.64	99.35
$1+\varepsilon$=1.036								
0	0.38	0.36	0.1	2.77	2.62	0.0004	0.02	99.96
3	0.35	0.33	0.2	2.59	2.44	0.0015	0.06	99.92
10	0.33	0.31	0.4	2.42	2.28	0.0029	0.13	99.85
30	0.25	0.23	0.8	1.84	1.70	0.0055	0.32	99.66
50	0.24	0.22	1.0	1.73	1.59	0.0077	0.48	99.51

increase in $b^*_{b\varphi}$ due to the presence of the gas vacuole. The values are within experimental values for phytoplankton (e.g. Whitmire et al., 2010) but are lower than those observed for *M. aeruginosa* by Zhou et al. (2012) (= 5.727×10^{-3} m² mg^{-1}) and the vacuolate marine cyanophyte *Trichodesmium* (= 11×10^{-3} m² mg^{-1}) (Dupouy et al., 2008). $b^*_{b\varphi}$ is slightly negatively sloped but becomes more positively sloped towards the red >700 nm with increasing vacuolation. Previous measurements of $b^*_{b\varphi}$ for *M. aeruginosa* show a downward sloping spectral shape (Zhou et al., 2012). The change in n' and n due to vacuolation for the shell chromatoplasm layer is shown in Fig. 4.3.4 E and F. The space occupied by the gas vacuole causes the absorbing material to be concentrated thereby increasing the value of n' which leads to associated changes in Δn. This assumes that the size of the cell remains unchanged by vesicle synthesis.

4.3.3 The influence of gas vacuolation on the VSF

There have been limited attempts to measure and model the volume scattering function of *M. aeruginosa* both with and without gas vacuoles. Schreurs (1996) performed measurements presented in Volten et al. (1998) at 633 nm using an Helium-Neon laser to measure the VSF of vacuolate and pressurised (non-vacuolate) *M. aeruginosa* and another vacuolate *Microcystis* species. The presence of gas vacuoles was observed to cause unusual features in the VSF, specifically, an increase in magnitude between 20°–70°, and a decline towards the forward direction <40°. Similar to other studies citing the importance of intracellular structure on the scattering matrix (e.g. Quinby-Hunt et al., 1989, Svensen et al., 2007, Witkowski et al., 1998), these features have been speculatively attributed to gas vacuoles. The same studies used a population of homogeneous spheres using Lorenz-Mie theory to attempt to fit the measurements (n=1.04, n'=0.000). However, the homogeneous sphere

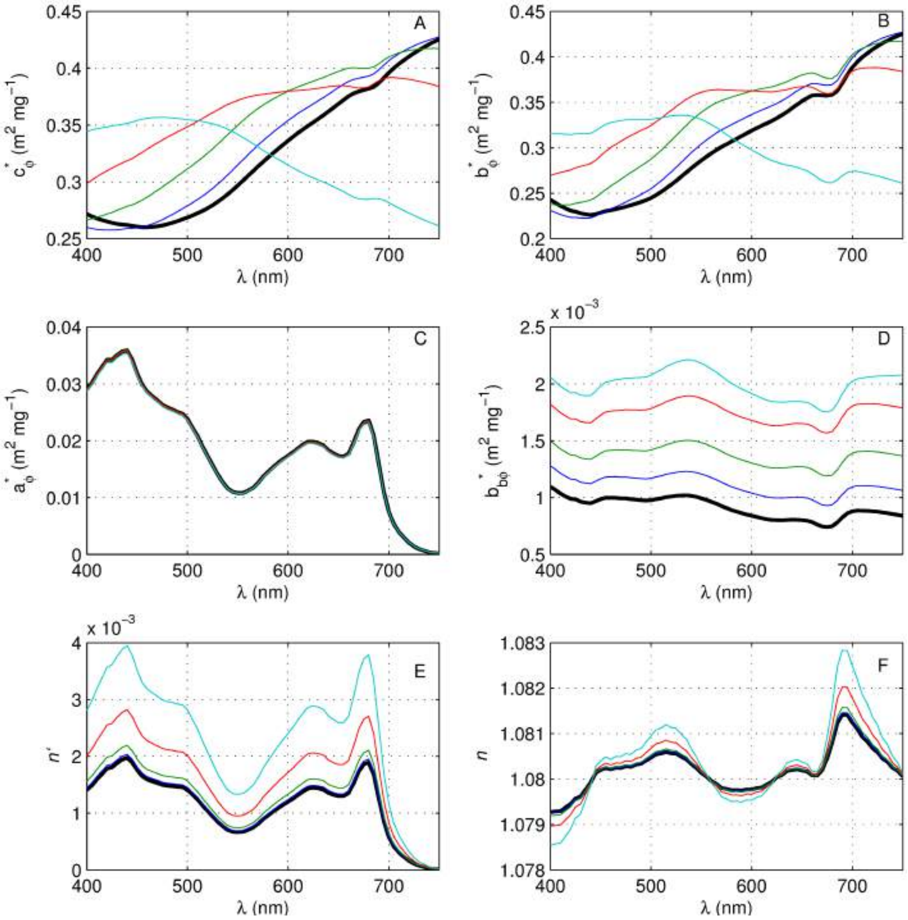

Figure 4.3.4: Chl-*a* specific volume coefficients for a population of *M. aeruginosa* modelled as two-layered spheres with variable gas vacuolation (A–D). Legend same as Fig 4.3.2. The influence of gas vacuolation on the n' and n of the shell layer are also shown (E and F).

model produced poor comparisons with measurements of both vacuolate and non-vacuolate cells. The flattening towards forward angle was only reproduced with a cell of significantly reduced n = 0.4 (Schreurs, 1996). The influence that gas vacuoles might have on the VSF in the extreme forward and backward directions remains unknown for the present. Although recently developed instruments have the capability to measure the VSF between 0.6°–177° (e.g. Zhang et al., 2002), no such measurements on vacuolate and non-vacuolate cells appear to have yet been made.

Fig. 4.3.5 A–D shows the VSFs at four wavelengths. Three features attributable to the gas vacuole are immediately apparent: an enlargement between 20°–70°, a flattening towards the forward direction <45° , and a steady enhancement and flattening of the VSF in the backward direction >90° for increasing vacuole content. The results are compared to those of Volten et al. (1998) in Fig. 4.3.5 E, and normalised to the San Diego Harbour VSF at 90° (Petzold, 1972). The two-layer model for a vacuolate cell containing V_g=10% accurately reproduces the enhanced scattering between 20°–70°, as well as the flattening in the forward direction < 45° observed for vacuolate cells.

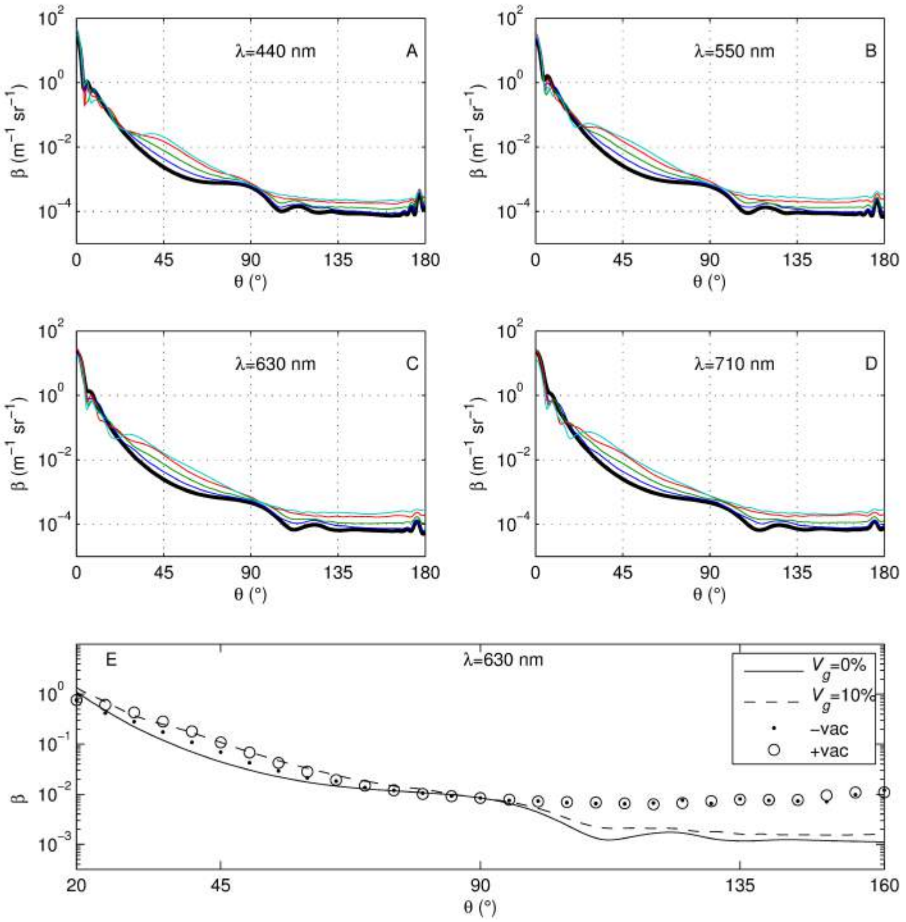

Figure 4.3.5: Volume scattering functions for a population of *M. aeruginosa* at various wavelengths modelled as two-layered spheres with variable gas vacuolation (0–50% cell volume). Legend same as fig 4.3.2. E shows comparison of these results with measurements of vacuolate (+vac) and non-vacuolate (-vac) *M. aeruginosa* made by Volten et al. (1998) at 633 nm (scaled to San Diego Harbor measurements of Petzold (1972) at 90°).

The fit between the modelled homogeneous cell and the measured non-vacuolate cell is also good in the forward direction (<90°). The enhancement in the backward direction from vacuoles is not observable in the measurements of Volten et al. (1998), and the magnitude of the measured VSF in the backward direction is substantially greater than that from the model. This is most likely caused by the assumption of sphericity, since the VSF in the backward direction is heavily influenced by non-sphericity (Clavano et al., 2007). Tests varying some of the model's parameters and using those presented in Volten et al. (1998) (n=1.04, n'=0.000, V_{eff}=0.92, R_{eff}=6.83) did not produce an improved fit. Nevertheless, the two-layered vacuole model accurately reproduces observations of the normalised VSF in the forward direction.

4.3.4 INFLUENCE OF THE CHOICE OF $1+\varepsilon$ AND c_i ON THE IOPs

The value for $1+\varepsilon$=1.036 chosen by Zhou et al. (2012) was also used to calculate the IOPs for comparison with section 4.3.1 (Fig. 4.3.6, Table 4.3.1). The resulting attenuation spectra compare more closely with the findings of Dubelaar et al. (1987) (Fig. 4.3.6A): the curves slope downwards towards the red; lower vacuole content results in gradually increased attenuation; and the shift of the attenuation peak caused by the absorption maximum of chl-*a* towards shorter wavelengths with increasing vacuolation is clearly observed (681 nm for V_g=50%, 685 nm for V_g=0%). Therefore, gas vacuolation is likely the cause of these changes in attenuation. Spectral scattering is also decreased with increasing vacuolation in a manner similar to attenuation (absorption was constant) (Fig. 4.3.6 B). The lower $1+\varepsilon$ value results in substantially lower backscattering relative to the higher refractive index value (Fig. 4.3.6 C, D). The heavily vacuolate cell (V_g=50%) scatters approximately the same as a non-vacuolate cell with the higher refractive index. The lower refractive index cell responds in much the same way as the cell with the higher refractive index to vacuolation with backscatter increasing in a roughly linear manner for increasing percentage vacuolation. The probability of backscatter for the lower refractive index cell is however more sloped, indicating a bias for light scatter in the red rather than in the blue. The VSF for the lower refractive index cell is generally smaller than for the higher refractive index cell, but less sloped in the backward direction (Fig. 4.3.6 E, F). The comparison with Volten et al.'s (1998) measured scattering function is poorer in the forward direction ($< \pi/2$) but slightly improved in the backward direction ($> \pi/2$). The distinctive features causing an enhancement and flattening in the VSF at forward angles is reproduced by the model.

The lower and higher refractive index cells respond in very similar ways to increasing gas vacuolation, and reproduce experimental observations in c and b, and in the VSF. The $1+\varepsilon$ value controls both the shape of c and b, and the magnitude of b_b; therefore it is one of the primary causal variables, along with the vacuole itself, influencing the IOPs. Although the shape of spectral attenuation may be used to constrain the choice of $1+\varepsilon$ (Bricaud and Morel, 1986) favouring a lower $1+\varepsilon$ value, the higher $1+\varepsilon$ value agrees better with measurements of the VSF and IOPs (Table 4.3.2). The final value for $1+\varepsilon$ however is determined in section 4.3.5 below.

The influence of c_i on the IOPs was also investigated using the values from Zhou et al. (2012) = 2.1 kg m^{-3}, Agusti and Phlips (1992) = 3.2 kg m^{-3} and Reynolds et al. (1981) = 4.5 kg m^{-3} (Table 4.3.2). The c_i value is directly linked to Q_a and causes changes in the values of n' and n due to the method used to determine m (section 4.2.2). Higher c_i values give higher values for Q_a and therefore n', however the value determined for n is relatively unchanged (Table 4.3.2). The variable Q_a and n' values result in changes in the (back)scattering efficiencies and in the chl-*a* specific IOPs produced by the two-layer model: higher c_i values are associated with lower Q_b and Q_{bb} values, and much smaller values for b^*_φ and $b^*_{b\varphi}$ (Table 4.3.2). The changes in the chl-*a* specific IOPs are primarily caused by normalising the PSD by chlorophyll. Therefore c_i has a large controlling influ-

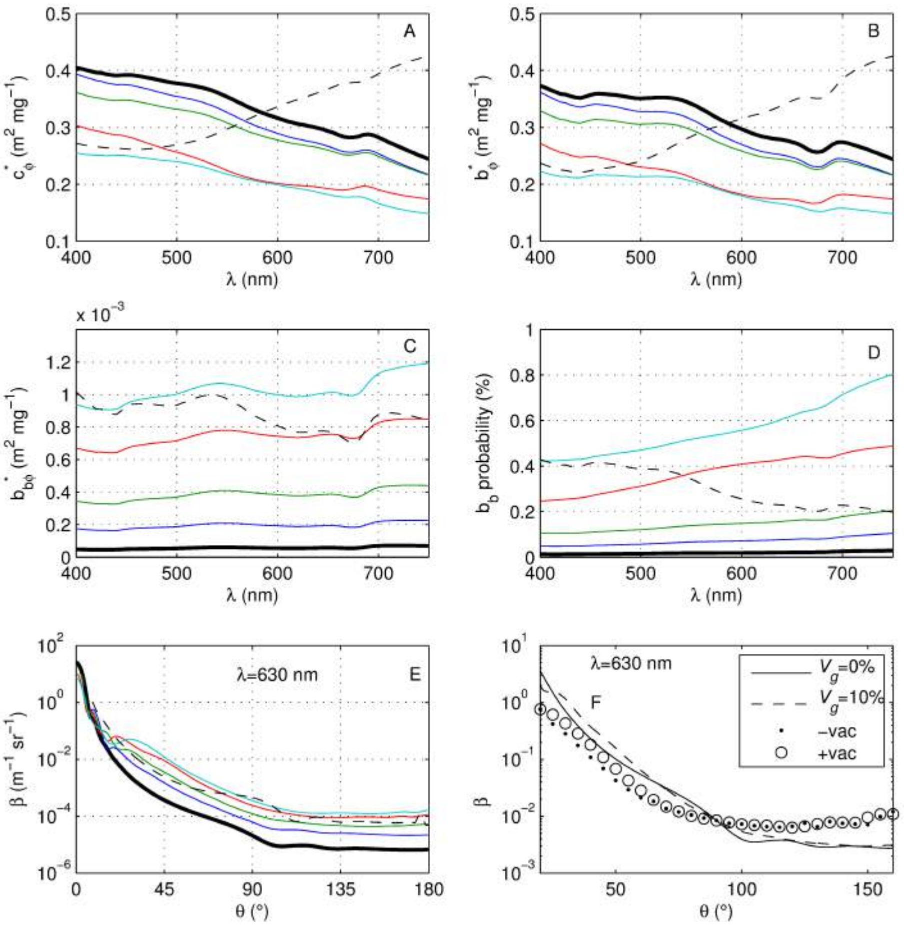

Figure 4.3.6: Chl-*a* specific IOPs and VSFs for a population of *M. aeruginosa* modelled as two-layered spheres with variable gas vacuolation (0–50% cell volume) and $1 + \varepsilon$=1.036. The dotted line in A–E is for a cell with V_g=0% and $1 + \varepsilon$=1.080. Legend same as Fig 4.3.2. F shows comparison with measurements of Volten et al. (1998) (see fig 4.3.5 for details).

ence on the two-layered model. The choice of c_i in this case was determined by the closeness to literature values of Zhou et al. (2012): the lowest c_i value = 2.1 kg m^{-3} most closely reproduced Zhou et al.'s (2012) $Q_b = 2.26$ and $Q_{bb} = 0.02$ values. A second reason for choosing the low c_i value is that higher c_i values were unable to reproduce the high values for $b^*_{b\varphi}$ observed in buoyant *M. aeruginosa* blooms. The higher c_i values had a dampening effect on scattering probably due to the concentration of absorbing material in the shell layer. For these reasons the lower c_i value was used.

4.3.5 Variable chromatoplasm $1 + \varepsilon$ values determined using R_{rs}

The measured and modelled R_{rs} spectra estimated using variable values of $1 + \varepsilon$ for the chromatoplasm are shown in fig. 6.3.5A,B. The spectral shapes of R_{rs} produced by the bio-optical model and Ecolight-S are in good agreement with those measured. The difference between 400 and 750 nm

Table 4.3.2: Effect of variable c_i on m and IOPs (510 nm) of a population of vacuolate cells ($V_g = 50\%$).

c_i (kg m^{-3})	2.096	3.16	4.525
$\bar{Q}_a(675)$	0.145	0.219	0.313
$n'(675)$	0.0017	0.0026	0.0041
$1 + \varepsilon$	1.0801	1.0801	1.0805
Q_b	2.45	2.36	2.27
Q_{bb}	0.016	0.015	0.014
b^*_φ (m^2 mg^{-1})	0.33	0.21	0.14
$b^*_{b\varphi}$ (m^2 mg^{-1})	0.0021	0.0013	0.0008
$\tilde{b}_{b\varphi}$ (m^2 mg^{-1})	0.0064	0.0062	0.0060

is on average less than 0.005 sr^{-1}, which is likely to be satisfactory given the high R_{rs} values (fig. 6.3.5C). There are a good spread of over and underestimates for R_{rs} with no apparent consistent bias for wavelengths < 700 nm (fig. 6.3.5D). The wavelength-specific coefficient of determination (fig. 6.3.5E) has troughs in the regions corresponding to the fluorescence bands of phycobilipigments (550 to 650 nm) and chl-*a* (near 685 nm). This is expected since the model does not account for fluorescence effects. The poor performance $<$500 and $>$700 nm is most likely related to uncertainties in $b^*_{b\varphi}$ towards the blue and NIR, respectively. The small sample size (n=8) must also be taken to account in the R^2 calculations. However, the correlation is sufficiently good in the regions 500 to 700 nm given that errors in R_{rs} determined *in situ* may be $>$10% depending on the wavelength and measurement conditions (Doxaran et al., 2004).

The mean value of $b^*_{b\varphi}(510)$ is 5.48×10^{-3} m^2 mg^{-1} with a range of 3.89 to 7.19×10^{-3} m^2 mg^{-1}. These values agree closely with that determined for cultured vacuolate *M. aeruginosa* by Zhou et al. (2012) = 5.7 $\times 10^{-3}$ m^2 mg^{-1} (fig. 6.3.5F). They are also within the range of values measured for *Microcystis* dominated assemblages in Spanish lake Rosarito (= 3.6 to 5.3 $\times 10^{-3}$ m^2 mg^{-1} at 412 nm) (Ruiz-Verdu, 2013). The b_{bp} profiles for Hartbeespoort measured *in situ* are shown in (Fig. 4.3.8 A, B). The estimated chl-*a* specific particulate backscattering at z = 0.8 m and 440 nm ranged from 0.37 to 1.5 $\times 10^{-3}$ m^2 mg^{-1}, and at 700 nm from 1.9 to 7.8 $\times 10^{-3}$ m^2 mg^{-1}. This is in the same order of magnitude as those estimated from R_{rs}. The b^*_{bp} values are likely underestimates since chl-*a* was measured at the surface, and the blooms were floating. There is some disagreement in the spectral shape between Zhou et al. (2012) (chl-*a* approx. 5 mg m^{-3}) and the two-layered sphere estimates (fig. 6.3.5F). Interestingly, b_{bp} is positively sloped towards the red near the surface and negatively sloped at depth (Fig. 4.3.8 B). Therefore there is some evidence for an upward sloping $b_{b\varphi}$ for *M. aeruginosa* in contrast to Zhou et al. (2012) which are downward sloping. The explanation for the depth-variable slope is not known, but seems to be related to biomass; if biomass affects the spectral slope then this finding has has important implications for b_{bp} measured using cultures. In summary, the $b^*_{b\varphi}$ values are typically larger or in the upper range of those determined

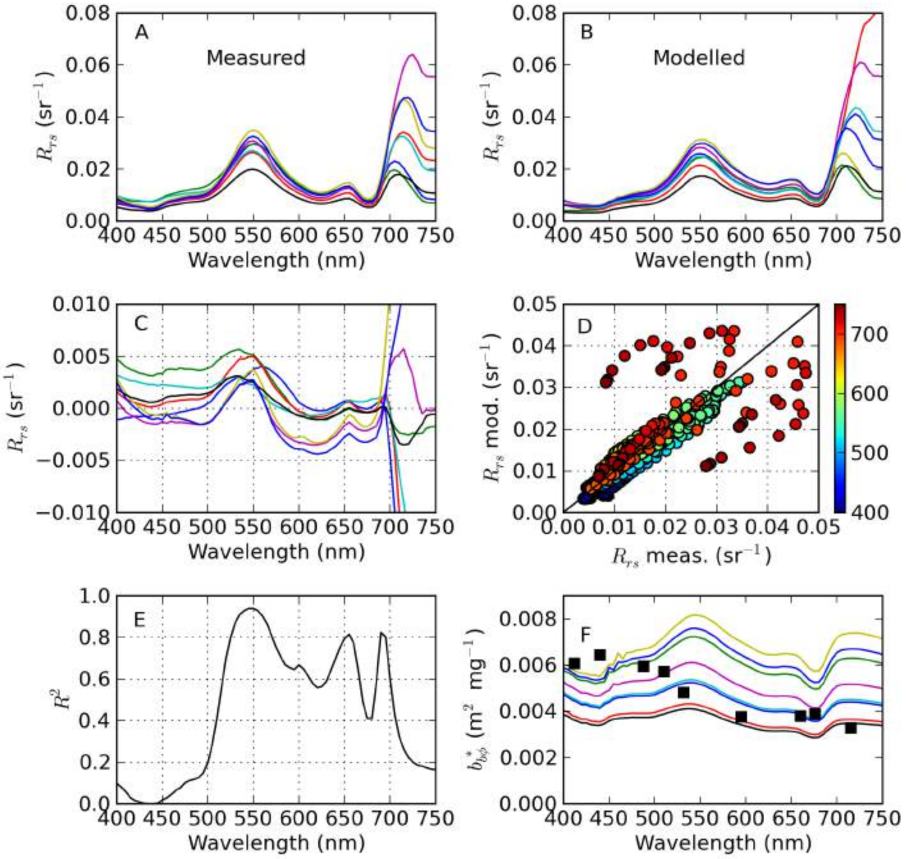

Figure 4.3.7: Tuning of the two-layered sphere model using measured R_{rs}. A) Measured and B) modelled R_{rs} and C) the The difference between the measured and modelled R_{rs}. D) Scatterplot of measured and modelled reflectance colored by wavelength. E) Wavelength-specific R^2 between measured and modelled R_{rs} (N=8). F) $b^*_{b\varphi}$ corresponding to various shell layer $1+\varepsilon$ values determined by fitting the measured and modelled R_{rs}, and that measured by Zhou et al. (2012) (squares). Colors in A B C and F represent different samples.

experimentally for cultured algae (e.g. Vaillancourt et al., 2004, Whitmire et al., 2010), and are in good agreement with the limited measurements made on vacuolate *M. aeruginosa*.

The modelled R_{rs} spectra correspond to chromatoplasm $1+\varepsilon$ values varying between 1.104 and 1.138 with a mean value of 1.12. The $1+\varepsilon$ values estimated using R_{rs} are likely to be justified for the following reasons: the overwhelming optical dominance of phytoplankton relative to other water components meaning that from an optical perspective the measurements were effectively performed on "cultures"; aside from V_g and some small uncertainty related to the estimated PSD, the primary factor controlling phytoplankton backscatter is the chromatoplasm $1+\varepsilon$ value which was the only variable parameter used to determine appropriate values for R_{rs}; the range of $1+\varepsilon$ values fall in the expected range of eukaryotic chloroplasts of 1.09 to 1.19, mean of 1.14 (Bernard et al., 2009), and result in an overall homogeneous n of 0.97 by volume equivalence; finally, the resulting values determined for $b^*_{b\varphi}$ are in close agreement with measurements made on vacuolate

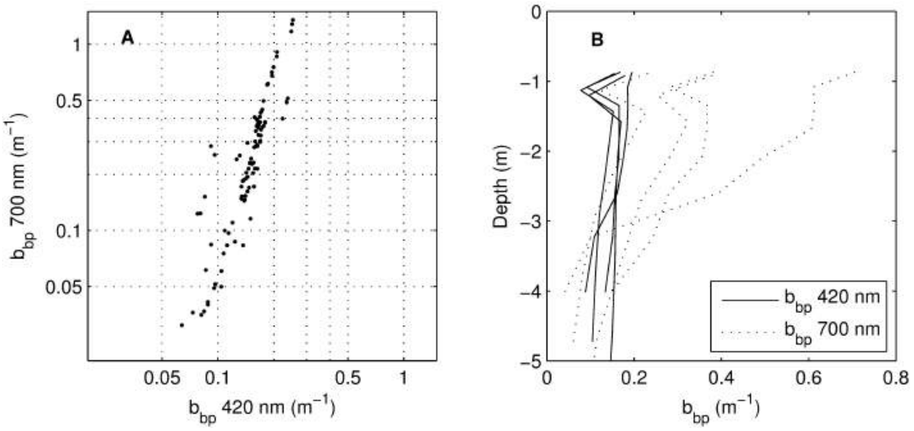

Figure 4.3.8: A) $b_{bp}(700)$ versus $b_{bp}(420)$ from 11 profiles. Note exponential relationship with log-scaled axes. B) Five selected depth profiles with minimum depth of 0.8 m. Note that $b_{bp}(420) > b_{bp}(700)$ at depth.

cultures and natural blooms of *M. aeruginosa*.

Furthermore, the chromatoplasm $1+\varepsilon$ values accord with previous two-layered modelling efforts: Quinby-Hunt et al. (1989) used a shell layer n=1.13 and core n=1.08 to best reproduced the scattering matrix of *Chlorella*, a species with similar morphology to *M. aeruginosa*; the typical $1+\varepsilon$ value for a shell layer proxy for the cell wall is 1.2 (e.g. Svensen et al., 2007). Given these considerations the resulting $1+\varepsilon$ values as determined by R_{rs} are likely to be appropriate albeit that assumptions are made regarding several components affecting the R_{rs} (e.g. the VSF for the tripton particles estimated using a Mie model).

Q factors and chl-*a* specific volume coefficients determined using the two-layered sphere with the mean chromatoplasm $1+\varepsilon$ value of 1.12 are shown in comparison to those measured by Zhou et al. (2012) in table 4.3.3. The values for $Q_b(510)$ and $Q_{bb}(510)$ compare well, but measured b^*_φ values are substantially higher than those from the two-layered sphere. It appears that the two-layered model has a lower total scattering due to the slightly lower value of Q_b. The backscattering probability is also elevated for the two-layered model, although $b^*_{b\varphi}(510)$ is very close.

Table 4.3.3: Optical efficiency factors and chl-*a* specific volume coefficients (m^2 mg^{-1}) at 510 nm for a population of *M. aeruginosa* modelled as a population of two-layered spheres with shell layer 1+ε=1.12 and V_g=50%.

	Q_c	Q_b	Q_{bb}	c^*_φ	b^*_φ	$b^*_{b\varphi}\times 10^3$	$\tilde{b}_{bb}$ (%)
Two layered spheres	2.35	2.20	0.040	0.321	0.30	5.5	1.8
Zhou et al. (2012)	-	2.26	0.020	-	0.6326	5.7	0.91

In comparison with eukaryotic species Q_{bb} is in the upper range of values measured on cultures: from 0.0018–0.064 at 510 nm (Vaillancourt et al., 2004, Zhou et al., 2012) and from 0.006–0.061 at

442 nm (Whitmire et al., 2010). Surprisingly, the largest of Q_{bb} values are from large dinoflagellates containing high intracellular carbon concentrations and unusual chromosome morphology and internal structures. This internal structire is used as an explanation for the higher than expected Q_{bb}. Using similar reasoning, intracellular gas vacuoles in *M. aeruginosa* are responsible for the high Q_{bb} values.

4.4 APPLICATIONS

4.4.1 INFLUENCE OF GAS VACUOLES ON REFLECTANCE

The large magnitude of R_{rs} and scattering in buoyant surface cyanobacterial blooms has been tentatively attributed to the presence of gas vacuoles (e.g. Ganf et al., 1989). The potential effect that intracellular gas vacuoles might have on the magnitude of R_{rs} was investigated through simulations for populations of vacuolate versus non-vacuolate cells. Vacuolate cells were modelled with a chromatoplasm $1+\varepsilon$ value of 1.12 and V_g=50% while homogeneous cells had $1+\varepsilon$ of 1.08, inside the plausible range for phytoplankton cells (Aas, 1996). In the simulations, $a_{tr}(440)$ and $a_g(440)$ were set to constant values typical of Hartbeespoort of 0.5 and 1.5 m^{-1}, respectively. Ecolight-S was run using a solar zenith angle of 30°, a wind speed of 2 m s^{-1}, and default atmospheric parameters.

R_{rs} for vacuolate and non-vacuolate *M. aeruginosa* populations was computed for chl-*a* between 1 and 1000 mg m^{-3}, a plausible range for Hartbeespoort (Fig. 4.4.1 A, B). The magnitude of R_{rs} for the vacuolate population is in the range observed in buoyant surface cyanobacterial blooms and those measured in this study (see Matthews et al., 2010, Randolph et al., 2008, Wang et al., 2010, Zimba and Gitelson, 2006). A large difference in the magnitude of R_{RS} between the vacuolate and non-vacuolate populations is apparent, which becomes increasingly pronounced as the concentration of chl-*a* increases. This effect is due solely to the increase in $b^*_{b\varphi}$ associated with vacuolate cells. The peak near 710 nm becomes apparent around chl-*a* = 30 mg m^{-3} (note the model does not include fluorescence effects at 685 nm). For chl-*a* $>$ 500 mg m^{-3}, R_{rs} is enlarged significantly towards the NIR ($>$ 700 nm). This is typical of surface *M. aeruginosa* blooms allowing them to be distinguished from other species of algae, e.g. dinoflagellates (Matthews et al., 2012). Therefore algorithms for detection/discrimination of vacuolate cyanophyte blooms might be targeted at the enlarged signal at these wavelengths. The results demonstrate the large influence variable phytoplankton backscatter resulting from gas vacuoles may have on the magnitude of R_{rs} and provide an explanation for the high values observed in hypertrophic cyanobacteria-dominant waters.

4.4.2 SENSITIVITY STUDY OF EXISTING EMPIRICAL MODELS FOR ESTIMATING CHL-*a*

While semi-analytical algorithms based on bio-optical models and solved using a variety of optimisation procedures are often used for deriving water constituents, forward modelled R_{rs} from bio-optical models also allow empirical relationships for water constituents to be validated (e.g.

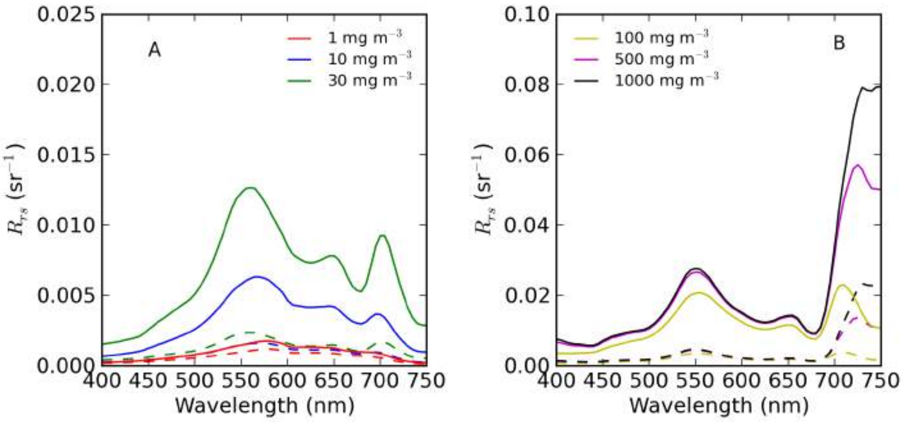

Figure 4.4.1: R_{rs} modelled at various concentrations of chl-*a* showing difference between vacuolate (solid lines) and non-vacuolate (dotted lines) populations of *M. aeruginosa*. Vacuolate cells were modelled with shell 1+ε of 1.12 and V_g=50%. Non-vacuolate cells were homogeneous cells with 1+ε of 1.080. The values for $a_{tr}(440)$ and $a_g(440)$ were constant at 0.5 m^{-1} and 1.5 m^{-1}, respectively. For more details see text.

Dekker et al., 2001, Matthews, 2011). In this example, the sensitivity of empirical relationships between chl-*a* and a 710:665 nm band ratio and the baseline subtraction maximum peak height (MPH) variable from Chapter 2, were tested using simulated R_{rs} for a population of vacuolate *M. aeruginosa*. Ecolight-S simulations were run for chl-*a* between 20 and 1000 mg m^{-3} for vacuolate cells (see section 4.4.1). $b^*_{b\varphi}$ was extended to 900 nm in order to facilitate computation of the MPH variable using the value at 750 nm. Noise was introduced by randomly varying the concentration of TR and $a_g(440)$ in the ranges 1 to 50 g m^{-3} and 0.5 to 5 m^{-1}, respectively, inside the natural variability expected for Hartbeespoort as determined in Chapter 3. This tested the sensitivity of the empirical relationships to variations in background constituent concentrations.

Fig. 4.4.2 shows the R_{rs} spectra and the resulting empirical relationships derived for the 710:665 ratio and the MPH variables. The best fit determined for the 710:665 ratio was:

$$chla = 7.294 \times exp^{1.2739 \times (R_{rs}(710)/R_{rs}(665))}, \quad R^2 = 0.99$$

while that for the MPH variable was:

$$chla = 222173mph^2 + 5231.9mph + 14.625, \quad R^2 = 1.0$$

The high correlation coefficients demonstrate the robustness of empirical-type algorithms for providing chl-*a* estimates in hypertrophic waters, as confirmed by the simulations. This confirms that empirical studies such as Schalles et al. (1998) and Matthews et al. (2012) have a strong bio-optical basis, provided that the dominant water constituent is phytoplankton (in this case the species tested is *M. aeruginosa*). The approach also demonstrates how empirical relationships derived from

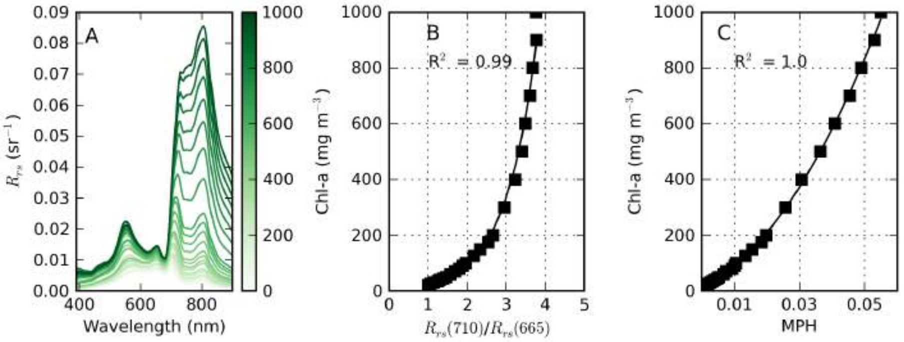

Figure 4.4.2: A) R_{rs} simulated for chl-*a* between 20 and 1000 mg m^{-3} for a vacuolate *M. aeruginosa* population with random perturbations in tripton concentration and $a_g(440)$. Empirical relationships between chl-*a* and B) the 710:665 band ratio and C) the MPH variable showing the best fit lines.

red/NIR optical signals might be species-specific since they are based on $b^*_{b\varphi}$. Therefore, empirically based algorithms are likely to be sensitive to species variability. The sensitivity study showed that the empirical relationships are stable despite variability in background concentrations of TR and *gelbstoff*.

4.5 CONCLUSION

The two-layered sphere model has facilitated in a simplified form the investigation of how a low refractive index particle (a gas vacuole) enclosed within a cell might impact the IOPs of *M. aeruginosa*. The two-layered model was capable of reproducing a number of features attributed to vacuoles: reduction in attenuation and the shift in the chl-*a* attenuation peak towards smaller wavelengths with increasing vacuolation; enlarged values for spectral backscattering particularly towards the red and NIR; decreased scattering in the forward direction noticeable as a dip towards smaller angles in the VSF; and an enlargement in the VSF between 30 and 60°. These findings confirm that gas vacuoles are responsible for these features and that the two-layer model is generally suitable as a first approximation for investigating the influence of gas vacuoles on IOPs in cyanobacteria. Sufficient closure between measured R_{rs} and that modelled using vacuolate two-layered spheres was obtained using chromatoplasm shell layer $1+\varepsilon$ values between 1.1 and 1.14. The corresponding $b^*_{b\varphi}(510)$ values between 3.8 and 7.2 $\times 10^{-3}$ m^2 mg^{-1} are in good agreement with those determined experimentally for *M. aeruginosa* (Zhou et al., 2012). The IOPs derived in this study are used in Chapter 5 to distinguish between vacuolate cyanobacteria and dinoflagellate speces using a radiative transfer inversion algorithm.

Simulations using Ecolight-S showed how gas vacuolate cells cause the R_{rs} to be greatly enlarged, relative to a population of cells modelled as homogeneous spheres. The changes in R_{rs} can be attributed to variable phytoplankton backscatter caused by intracellular structure (the gas vacuole).

Empirical relationships for estimating chl-*a* in eutrophic/hypertrophic waters are robust even under variable tripton and *gelbstoff* concentrations, and are likely to be sensitive to species variability, confirming the findings related to the MPH algorithm in Chapter 2. In conclusion, gas vacuoles are one of the most important bio-optical sub-structures profoundly affecting the IOPs of cyanobacteria and leading to increased backscatter in particular towards the red/NIR, which may be distinctive to the genera.

5

Distinguishing cyanobacteria from algae in optically-complex inland waters using a radiative transfer inversion algorithm

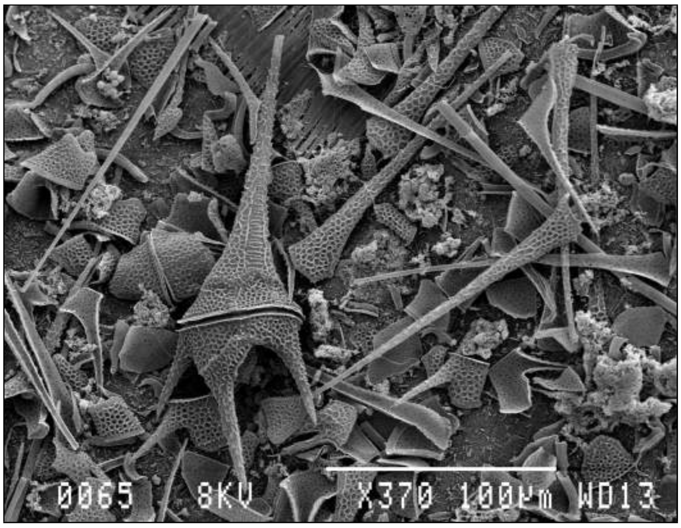

SEM of Ceratium hirundinella sampled at Loskop Dam in August 2011. Credit: Dr. Paul Oberholster.

Abstract

A hyperspectral radiative transfer based inversion algorithm was used to test the sensitivity of the inverse problem to phytoplankton assemblage size and species composition (type) in optically-complex inland waters. The algorithm was sensitive to high biomass blooms of the small celled *Microcystis aeruginosa* and the large celled *Ceratium hirundinella* through retrieval of assemblage size parameterised in terms of the effective diameter (D_{eff}) and type, determined as percentage cyanobacteria (cyano) composition. The inversion algorithm directly solves the radiative transfer equation (RTE) through using Ecolight-S (E-S) radiative transfer model (RTM) coupled with a bio-optical model solving for the IOPs, and a non-linear simplex optimisation algorithm solving for six unknowns to match the measured remote sensing reflectance (R_{rs}). Size variable chlorophyll-*a* (chl-*a*) specific phytoplankton absorption and (back)scattering coefficients (a_φ, b_φ, $b_{b\varphi}$) for cyano and dinoflagellate (dino) populations for input to the bio-optical model were calculated using a two-layered sphere model. Estimates of the complex refractive index (m) of the cyano/dino populations were derived using estimated/measured particle size distributions (PSD) and a_φ data and the anomalous diffraction approximation (ADA) technique. The algorithm provides estimates of D_{eff}, cyano/dino species composition in %, chl-*a*, and the spectral a_φ and combined *gelbstoff*/tripton absorption (a_{gtr}) and non-phytoplankton particulate backscattering (b_{bnpp}) coefficients in the range 400 to 800 nm. Estimates of size and type were significant in hypertrophic waters ($r>0.8$) but was expectedly poorer in mixed mesotrophic and oligotrophic waters. Chl-*a* and $a_\varphi(440)$ were retrieved with $r > 0.8$, while $a_{gtr}(440)$ was retrieved with $r > 0.7$ in oligo/mesotrophic waters. Good optical closure for R_{rs} was achieved over the considerable trophic range of optically-complex water types measured in the study. Type detection was optimised through using an empirical expression for cyano detection in eutrophic waters. The study demonstrates the feasibility of an inversion approach for differentiating cyano blooms from eukaryotic species in optically-complex inland waters.

5.1 INTRODUCTION

5.1.1 THE INVERSE PROBLEM OF WATER REMOTE SENSING IN OPTICALLY-COMPLEX WATERS

THE INVERSE PROBLEM FOR OPTICAL water remote sensing entails retrieval of the inherent optical properties (IOPs) and associated biogeochemical parameters of the water from the apparent optical properties (AOPs), most commonly the water remotely sensed reflectance (R_{rs}), using so-called inversion algorithms. The IOPs typically refer to the absorption coefficient (a) and the volume scattering function (β, VSF) which when integrated over the backward hemisphere gives the backscattering (b_b) coefficient and when integrated over both hemispheres gives the scattering (b) coefficient. The total absorption and (back)scattering coefficients of the water can be calculated as the sum of the respective coefficients of each of the optically significant constituents. These, for the purposes of this study, are partitioned into living phytoplankton (φ), chromophoric dissolved organic matter here referred to as *gelbstoff* (g), and non-phytoplankton particles (NPP) or tripton (tr), which includes minerals and detritus, not neglecting water itself (w). The IOPs of other water constituents such as bubbles, viruses, bacteria and very small particles e.g. colloids, are not explicitly determined for this study, but may also be significant contributors to the total IOPs (e.g. Stramski et al., 2004, 2001). The IOPs are independent of the ambient light field and therefore can be accurately measured and characterised in the laboratory or the field. This has been the subject of recent studies where the aim has been to characterise the IOPs in optically-complex inland waters, whose optical properties are generally poorly described in comparison to marine waters (see Chapter 3 and references therein). A detailed description of the IOPs for waters relevant to this study can be found in Chapter 3.

In contrast to the IOPs, the AOPs which include the remote sensing reflectance or R_{rs} defined as L_w/E_d where (L_w) is the water leaving radiance and E_d is the downwelling irradiance, are dependent on the IOPs and the ambient light field which is affected by multiple factors including viewing geometry, atmospheric properties and could cover. In addition AOPs must exhibit enough stability to be useful for describing the water. The quantity of most interest as far as the inverse problem is concerned is typically the R_{rs} useful because of its measurement by satellite-based remote sensing platforms, and its ease of measurement *in situ* using various instrumentation (Mobley, 1999). Therefore the inverse problem is most often framed in terms of the retrieval of IOPs from the R_{rs}. The inverse problem is most easily understood in relation to the 'forward problem', which is solving for the AOPs using known IOPs and the radiative transfer equation (RTE) in water. The forward problem can be accurately solved through various mathematical solutions of the RTE using radiative transfer models such as Hydrolight (Sequoia Scientific) (Mobley, 1994). A detailed knowledge of the IOPs of the water constituents is required to provide suitable optical closure with modelled and measured AOPs, which has recently been the subject of various studies in optically-complex coastal and inland waters (e.g. Effler et al., 2012, Gallegos et al., 2008, Tzortziou et al., 2006). The forward problem and its accurate calculation through radiative transfer modelling using suitably characterised IOPs in the form of a bio-optical model is the basis of many inversion algorithms, which are now discussed.

Detailed reviews of the theory and application of inversion algorithms have been performed by Gordon (2002), IOCCG (2006), Twardowski et al. (2005). Inversion algorithms typically fall into two categories. The first is the semi-analytical approach which use various algebraic equations expressing the AOPs in terms of the IOPs to solve for constituent IOPs and biogeochemical parameters (e.g. Lee et al., 2002, Roesler and Boss, 2003). The most often used equation expressing this relationship is the so-called reflectance approximation (REFA) (Gordon et al., 1975, Morel and Prieur, 1977), defined by:

$$R_{rs} \approx \frac{f}{Q} \frac{b_b}{a + b_b}$$

where f and Q are a dimensionless coefficient and the bidirectional function, respectively, dependent on the angular configuration, illuminations conditions, the IOPs and VSF of the water, and environmental factors such as wind (Morel et al., 2002). The REFA is therefore subject to the assumptions and uncertainties associated with the $\frac{f}{Q}$ factor which up to the present has not been adequately characterised in high-biomass, turbid and optically-complex waters (Chami et al., 2006, Lee et al., 2011). Furthermore, the single scattering approximation breaks down in highly scattering waters as a result of multiple scattering events which causes large changes in the radiance distribution and therefore f/Q and the REFA (Piskozub and McKee, 2011).

The second approach uses various optimisation procedures to match the spectral signatures of measured AOPs with those forward modelled using a RTM (e.g. Mobley et al., 2005, Schiller and Doerffer, 2005). The use of a RTM avoids the assumptions and uncertainties associated with the REFA and the associated f/Q factor, although some assumptions are made regarding the VSF. Various non-linear optimisation procedures are used in an iterative manner to reconstruct the observed reflectance spectrum. These algorithms may require large simulated data sets of reflectance spectra contained in spectral libraries or look-up tables which may be used to train or parameterise the algorithm, for example a neural network (Doerffer and Schiller, 2007). These approaches require assumptions regarding the characteristics and distributions of IOPs and constituent concentrations to be made. These two approaches have been broadly described as *explicit* and *implicit*, respectively (Gordon, 2002), and there exist numerous variants of both kinds of algorithms that have been developed, mainly for use in marine waters (see reviews). For the purposes of this study, algorithms and concerns relevant to the inverse problem in optically-complex inland and near-coastal waters are briefly reviewed.

Inversion procedures applied in inland or near-coastal waters with significant optical contributions from constituents other than phytoplankton including *gelbstoff*, minerals and tripton pose a very challenging case for remote sensing. Several water constituents each with value ranges potentially varying over several orders of magnitude must be solved for simultaneously. The main concern arises from the ambiguity, or non-unique nature of the solution owing to the additive nature of the IOPs due to various confounding constituents (Defoin-Platel and Chami, 2007). This is further exacerbated when using approximations for describing the relationship between R_{rs} and the IOPs, e.g. the REFA, which are subject to various assumptions (*ibid.*); and from the inherent noise present in hyperspectral resolution radiometric data (Gillis et al., 2013, Moses et al., 2012). Thus there is significant ambiguity in the retrieval of IOPs in optically-complex waters. The solution becomes plausible only through prior parameterisation of constituent IOPs constrained within certain value ranges and distributions that are representative of the natural waters under investigation (Defoin-Platel and Chami, 2007).

Despite these challenges and limitations, the development of inversion algorithms for optically-complex waters is desirable mainly because of their potential to maximise the information that can be retrieved from the remotely sensed signal through the estimation of the IOPs, and because of the limited applicability of approaches used in the open-ocean environment to optically-complex waters (IOCCG, 2006). Inversion procedures differ from empirically derived algorithms which derive biogeochemical parameters directly from reflectance variables (for reviews and details see Matthews, 2011, Odermatt et al., 2012). The empirical approach has been criticised as minimising the information that might be derived from the remotely sensed signal since it does not usually solve for the IOPs (IOCCG, 2006). However the inverse approach does not necessitate a significant improvement in reliability or accuracy of variable estimates (Matthews, 2011).

There are several examples of recent studies in optically-complex inland and coastal waters using the semi-analytical approach (e.g. Aurin and Dierssen, 2012, Mishra et al., 2014, Salama et al., 2009) and spectral matching type approaches (e.g. Doerffer and Schiller, 2007, Pozdnyakov et al., 2005, Santini et al., 2010, Vanderwoerd and Pasterkamp, 2008). While these studies do make good progress in modifying these procedures for complex and turbid waters, they are limited however in that they typically focus on one or other water type or trophic range, and are focused primarily on retrieval of chl-*a* and the absorption coefficients at a single wavelength or a few wavelengths and thereby provide little useful information on the spectral characteristics of the IOPs. In this regard they are limited in so far as providing information on the phytoplankton assemblage species composition or size, which can be retrieved from the IOPs and which has not yet been achieved for optically-complex waters. Studies investigating type detection have mainly been limited to detection of diagnostic spectral features associated with cyano species such as *Microcystis* or the marine *Trichodesmium* spp. resulting in flagging of pixels (e.g. Dupouy et al., 2011, Hu et al., 2010a, Matthews et al., 2012, Stumpf et al., 2012), or the retrieval of accessory pigmentation such as cyanobacterial phycocyanin (PC) using semi-analytical algorithms which are subject to large uncertainties and assumptions dependent on the phytoplankton assemblage composition (Hunter et al., 2010, Simis et al., 2005). The pixel flagging type approaches are limited in that they provide only a qualitative information on type without detailed information regarding the IOPs, other water constituents or size of the phytopankton assemblage. Therefore there exists a paucity of detailed inversion studies in optically-complex waters investigating the retrieval of spectral IOPs which simultaneously provide information on the phytoplankton assemblage species composition and size. Such a problem is the focus of this study, the rational, design and approach of which are now discussed with regard to the retrieval of type and size from R_{rs} data.

5.1.2 RATIONALE FOR TYPE AND SIZE DETECTION IN OPTICALLY-COMPLEX AND HYPERTROPHIC WATERS

The primary factors governing the IOPs of phytoplankton are the cell size (diameter=d), real refractive index (n) and internal structure, and pigmentation (Matthews and Bernard, 2013b, Morel and Bricaud, 1986, Whitmire et al., 2010). These vary considerably between species leading to considerable variation in the IOPs. Therefore, given the large influence of these variables on the IOPs, it is feasible to invert for the absorption coefficients (and indirectly species composition and size) from radiometric data (e.g. Bernard, 2005, Ciotti and Bricaud, 2006, Lee, 2004). While size is typically not directly retrieved, it can be determined through its effect on a_φ through the package effect (e.g. Hirata et al., 2008). As shown in Chapter 4, n for the shell layer of *M. aeruginosa* modelled by a two-layered sphere was retrieved by a constrained inversion. The feasibility for the inversion of size and species composition is now discussed with reference to various types of inland waters.

Harmful algal blooms often occur at high biomass in eutrophic waters, and are often dominated by one or a few species. Such conditions are typified by the *M. aeruginosa* and *C. hirundinella* blooms frequently occurring in South African inland waters, which have been already described in Chapter 3. Hyper-eutrophic inland waters frequently experience blooms with chl-a in excess of 20 mg m^{-3}, which even might exceed 1000 mg m^{-3}. In these conditions phytoplankton is typically the water constituent with the greatest contribution to the bulk absorption and scattering budgets, meaning that these can from an optical perspective be treated as case I type waters (Morel and Prieur, 1977). However the green waters that Morel and Prieur (1977) measured are likely to be significantly different from these, which nevertheless have a strong background contributions from tripton and dissolved components (including minerals, bacteria, etc.), meaning they are complex from an optical perspective. Therefore, although these waters can be treated as phytoplankton dominant, they nevertheless require an approach that takes account of the background constituents within appropriate ranges. However, the overwhelmingly large phytoplankton signal provides an opportunity to resolve the spectral features of R_{rs} associated with various species-specific pigments as postulated by Richardson (1996), and other diagnostic features including assemblage size and internal structure (Matthews and Bernard, 2013b). The latter features are known to have a primary controlling influence on the shape and magnitude of the absorption and (back)scattering of phytoplankton (Bricaud et al., 2004, Svensen et al., 2007), and are therefore likely detectable using remote sensing (e.g. Ciotti et al., 1999, 2002, Hirata et al., 2008). However, until the present study there is no comprehensive radiative transfer treatment aimed at retrieving assemblage size and type from R_{rs} in hypertrophic inland waters.

In comparison with hyper-eutrophic blooms, mesotrophic waters containing mixed assemblages of phytoplankton of variable size and type and relatively larger contributions to the bulk IOPs from NPP matter and *gelbstoff* present a more challenging case. These are water types that are typically encountered in medium biomass conditions in optically-complex coastal and inland waters. The R_{rs} signal is likely to be less sensitive to type and size owing to the smaller relative phytoplankton signal and spectrally variable and confounding optical signals. Conversely, there is likely to be more sensitivity to the dissolved and NPP matter components given the relatively larger signal contributions. The same may be said for oligotrophic waters (chl-$a < 10$ mg m^{-3}) which often have small signals from phytoplankton relative to the high average contributions from *gelbstoff* and tripton. For this reason the phytoplankton size and type is unlikely to be resolved with much sensitivity, with assessment perhaps limited to biomass (chl-a) only.

5.1.3 Study design, aims and objectives

An inversion algorithm using the full RTE to retrieval the IOPs from the AOPs has so far not been achieved (IOCCG, 2006). However, given the recent availability of radiative transfer models, such as E-S, capable of solving the RTE with very fast computational times, inverse models directly solving for the RTE have become feasible. In this study, a hyperspectral inversion algorithm is developed in which E-S is used to directly solve the RTE and calculate R_{rs} from the IOPs in combination with a spectral matching approach based on a non-linear downhill simplex optimisation. The use of E-S avoids the assumptions and some uncertainties associated with the REFA and $\frac{f}{Q}$ factor. Hyperspectral R_{rs} measurements together with two-layered sphere model derived phytoplankton chl-a specific IOPs (SIOPs) parameterised for assemblage size and species, are used to assess the sensitivity to phytoplankton type and size in inland waters. The study tests the hypothesis that blooms of cyanobacteria can be differentiated from eukaryotic phytoplankton from remotely sensed and bio-optical data on the basis of unique spectral pigment-related absorption features and diagnostic backscattering related to internal structure, i.e. gas vacuoles (see Chapter 4). The development of a technique for distinguishing blooms of cyanobacterial species from those of eukaryote species (see Chapter 2) is of considerable importance due to the large effect that toxin producing species have on ecosystem and human health.

The study uses an *in situ* dataset of simultaneously measured R_{rs}, IOPs, biogeochemical and environmental parameters from diverse South African inland waters. This includes data from hypertrophic high biomass blooms of *M. aeruginosa* and *C. hirundinella* in which phytoplankton is the overwhelmingly optical dominant constituent, as well as from meso/oligotrophic waters containing mixed assemblages of phytoplankton of variable size and type and significant contributions by *gelbstoff* and tripton. These data are used to test the study's hypothesis and assumptions regarding the resolution of phytoplankton assemblage size and type in high biomass, mixed meso/trophic and oligotrophic waters. The aims of the study are therefore to evaluate the ability of a radiative-transfer based inversion algorithm for differentiating small-celled *M. aeruginosa* cyanobacteria from large celled dino *C. hirundinella* high biomass blooms, and to determine the feasibility of determining species composition in mixed dino/cyano assemblages. The aims of the study are achieved through the following objectives:

1. derive plausible spectral m values for natural dino and cyano blooms using measured a_φ and

estimated/measured PSDs;

2. using m, determine size-based SIOPs of dino and cyano populations using a two-layered sphere model; and
3. develop an algorithm based on a radiative transfer inversion of R_{rs} and a bio-optical model using the two-layer model determined phytoplankton SIOPs for size and species composition retrieval.

The SIOPs used by the algorithm are derived from data from selected samples from high biomass *M. aeruginosa* and *C. hirundinella* blooms. However, the data on which the algorithm performance is tested esp. the mixed oligo/mesotrophic waters is independent. The study begins with a detailed description of the data and methods used to determine phytoplankton m and size-based SIOPs using the two layered model. These are discussed in the results section. The inversion algorithm is then discussed and its evaluation is presented in the applications section.

5.2 METHODS

5.2.1 REMOTE SENSING REFLECTANCE

R_{rs} was measured using an ASD FieldSpec® 3 Portable Spectroradiometer (ASD Inc., Bolder, CO) using the protocols outlined in Mueller et al. (2003). The ASD has a spectral range of 350 to 2500 nm, with a spectral resolution of 3 nm at 700 nm and a noise equivalent radiance of 1.1×10^{-9} W cm^{-2} nm^{-1} sr^{-1} at 700 nm. Measurements were only performed under mostly clear sky conditions (cloud cover$<$20%) since cloud cover is known to impart large errors from shadows and other effects (Doxaran et al., 2004, Mobley, 1999).

Ten radiance spectra were collected in sequence for Spectralon™ plaque, sky and water targets in order to minimise the effects of wind and waves and temporal variability in surface reflectance. Measurements were performed between 9 am and 12 pm using a viewing zenith angle of $\theta = 40°$ away from the sun azimuthally at $\varphi = 135°$. Care was taken to ensure that the plaque was free from shadow or reflectance effects from any source. Sky radiance was measured using the same viewing angle to the zenith. The measurement procedure was performed three times in sequence with dark readings taken between each sequence. The mean of the radiance spectra for each target was then computed, taking care to exclude contaminated or outlying spectra. R_{rs} was then calculated using the mean spectrum for each target according to Mobley (1999):

$$R_{rs} = (L_t - \rho L_s)/(\frac{\pi}{R_g} L_g) \tag{5.1}$$

where L_t is the water surface radiance, L_s is the sky radiance, ρ is the proportionality factor for the sky radiance to the reflected sky radiance on the water surface, L_g is the radiance measured from the Spectralon™ plate, and R_g is the Spectralon bidirectional reflectance function. The Spectralon™ plate was assumed to be Lambertian and a perfect reflector (R_g =0.99). The value of ρ is affected by the wind speed, viewing geometry and cloud cover (Mobley, 1999). Since the wind speed of all measurements was less than 5 m s^{-1} a value for ρ of 0.025 was used (see fig. 9 in Mobley (1999)).

5.2.2 ABSORPTION, BIOGEOCHEMICAL PARAMETERS AND PARTICLE SIZE DISTRIBUTIONS

The details of the sampling areas, strategy and methods for the determination of the biogeochemical parameters and absorption coefficients are provided in detail in Chapter 3. Therefore, only a brief overview is provided here and readers are referred to the aforementioned study for details. The concentration of chl-*a* was determined spectrophotometrically following the method of Sartory and Grobbelaar (1984). Seston (total suspended solids), and minerals (ashed dry weight) was determined using the gravimetric technique (Environmental Protection Agency, 1983). Tripton (non-living particulate matter) was determined from the seston, minerals and chl-*a* concentrations using the method described in Chapter 3. The quantitative filter technique was used to determine the absorption coefficients of pigmented (phytoplankton), non-pigmented (tripton) and *gelbstoff* following the protocols outlined in Mitchell et al. (2003).

Particle size distributions were determined using a Multisizer-4™ particle analyzer (Beckman-Coulter®) fitted with a 140 μm aperture. The 140 μm aperture allows accurate estimations for particles with diameters between 2.8 and 84 μm (2 to 60% aperture size), which is in the size range of typical natural phytoplankton assemblages. Samples were kept cool and in the dark until analysis which was performed on the same day as collection. Fresh water samples were diluted using Isoflow epics sheath fluid (azide free non-fluorescent balanced electrolyte solution) obtained from BeckmanCoulter® to ensure conductivity. After dilution, 20 ml of sample was counted maintaining a concentration of between 2.5 and 10% with correction for particle coincidence. Blank particle counts were measured using freshly 0.2 μm filtered lake water which was diluted with electrolyte solution identical to that of the samples. Further data processing was performed using scripts written in Python programming language. PSDs were corrected by subtracting the mean blank particle counts which were scaled for dilution. PSDs in cells per liter were median filtered to reduce spiking and interpolated onto linear spaced bins of 1 μm diameter through calculation of the spectral density. PSDs were partitioned into algal and non-algal components using a numerical technique (Bernard et al., 2001). The detrital distribution was estimated as a Jungian distribution with slope of -4 and scaled to the minimum volume of the PSD between 1 and 7 μm. The detrital distribution was then subtracted from the PSD to give the estimated phytoplankton size distribution. The effective radius (R_{eff}) and variance (V_{eff}) of the phytoplankton size distributions were calculated by (Hansen and Travis, 1974):

$$r_{eff} = \frac{\int \pi r^3 F(r) d(r)}{\int \pi r^2 F(r) d(r)} = \frac{1}{G} \int \pi r^3 F(r) d(r)$$

$$v_{eff} = \frac{1}{Gr_{eff}^2} \int (r - r_{eff})^2 \pi r^2 F(r) d(r)$$

where r is the particle radius in m, $F(r)$ is the number of particles per unit volume (cells per m^3), and $d(r)$ is the difference between the size bins in m. R_{eff} (or $D_{eff} = 2 \times R_{eff}$) is used to describe a 'mean' particle size for the distribution from an optical perspective while V_{eff} describes the width of the distribution. For comparative purposes, the equivalent spherical diameter (ESD) was estimated from microscope species counts using literature derived estimates of cell volumes for individual species mainly from Reynolds (2006).

5.2.3 COMPLEX REFRACTIVE INDICES OF PHYTOPLANKTON

The complex refractive index is composed of real (n) and imaginary (n') parts according to $m = n - in'$ and is the primary factor along with cell size governing light scattering of small particles including phytoplankton (Morel and Bricaud, 1986). In this study it is required for use with a two-layered sphere model which is used to derive the VSF and (back)scattering volume coefficients for natural phytoplankton populations. Since phytoplankton are modelled as two-layered spheres and not homogeneous spheres, values of m are required for both the inner sphere layer (core) and the outer layer (shell). For simulations of prokaryotic gas-vacuolate cyano cells the two layers are assigned to an internal gas vacuole surrounded by a chromatoplasm as in Chapter 4 using a relative volume for the gas vacuole core layer, V_c, of 50%. For simulating eukaryotic cells the core and shell layers are assigned to a cytoplasm and chloroplast, respectively after Bernard et al. (2009) using a chloroplast relative volume shell layer, V_s, of 30%. Analysis of the effects of varying the relative core:shell volumes for the vacuole/chromatoplasm configuration can be found in Chapter 4 and are assessed here for the eukaryotic chloroplast/cytoplasm assignment.

IMAGINARY REFRACTIVE INDICES

The homogeneous imaginary refractive index, n'_{hom}, was determined for natural cyano and dino phytoplankton blooms using the inverse anomalous diffraction approximation (ADA) method of Bricaud and Morel (1986) as described in Chapter 4. A mean *M. aeruginosa* dominant sample from Hartbeespoort was used for gas-vacuolate cyanos, while two discrete samples from a high biomass *C. hirundinella* bloom obtained from Loskop at the same sampling location on two different days at similar times, were used for dinos. The experimental mean absorption efficiency factors, $\bar{Q}_a$, were computed from measured a_φ phytoplankton PSDs. n'_{hom} was computed through fitting the absorption efficiency factor, Q_a, modelled using the ADA to $\bar{Q}_a$. The PSD for *M. aeruiginosa* was not measured due to difficulties associated with the colonial arrangement of the cells and their existence at extremely high biomass in a surface scum layer. Therefore the PSD was estimated using a log-normal distribution with $R_{eff} = 2.5$ and $V_{eff} = 0.02$ (see Chapter 4 for further details). For

C. hirundinella the PSDs were measured using the Multisizer-4™. The two discrete *C. hirundinella* samples allowed for a comparative assessment of the method used to determine n'_{hom}.

Using n'_{hom}, corresponding values of n' for the cyano chromatoplasm (n'_{chrom}) and dino chloroplast (n'_{chloro}) were derived using volume equivalence (Bernard et al., 2009). The volume equivalence approach scales n'_{hom} by the volume occupied by the absorbing layer according to: $n'_s = (n'_{hom} - n'_c V_s)/(1 - V_s)$, where n'_s is the value determined for the absorption shell layer (chromatoplasm/chloroplast) and n'_c is the imaginary refractive index of the core vacuole/cytoplasm layer. The vacuole n' was set to $2.28 \times 10^7 \lambda^{-4.66}$ while that for the cytoplasm was set to $0.0005 \times exp(-0.01(\lambda - 400))$ (Bernard et al., 2009). In addition to the volume equivalence determinations, an inverse solution using the two-layered sphere model was also used to determine n'_{chloro} for the dino (Bernard et al., 2009). The method solves for n'_{chloro} through fitting Q_a determined directly by the two-layer model to $\bar{Q}_a$ using the measured phytoplankton absorption and PSD, and assumed values for n for the chloroplast and cytoplasm (see below). The volume equivalence and two-layer determined n'_{chloro} were then compared.

REAL REFRACTIVE INDICES

In terms of the theory of anomalous dispersion (van de Hulst, 1957), the spectral variation in n denoted Δn in the vicinity of absorption bands is said to vary around a central value denoted $1 + \varepsilon$ according to $n = 1 + \varepsilon + \Delta n$ (Morel and Bricaud, 1986). Δn predicted by the Kramers-Kronig or Ketteler–Helmholtz theories can be determined as a Hilbert transform of n' (Bernard et al., 2001), while a plausible value of $1+\varepsilon$ for a homogeneous spherical cell can be determined provided the attenuation efficiency factor, Q_c, is measured to constrain the selection (Ahn et al., 1992, Bricaud and Morel, 1986). Given that no Q_c data were available to this study, and that phytoplankton are modelled as inhomogeneous two-layered spheres, values for n were not determined using this method. Alternative methods for determining the value of $1 + \varepsilon$ based on convergence of modelled Q_c and the non-absorption equivalent, Q_c^{NAE} after Bernard et al. (2001) are likely sub-optimal. Therefore estimates of the chromatoplasm $1 + \varepsilon$ value for cyano were determined as described in Chapter 4 through providing optical closure for measured R_{rs} and R_{rs} estimated using IOP data and E-S.

There is significant justification for this method as discussed in the aforementioned study. However, this method was not used for *C. hirundinella* for the following reasons: there were background concentrations of other phytoplankton species present; tripton and *gelbstoff* were significant contributors to the absorption and scattering budgets meaning that the blooms cannot from an optical perspective be treated as mono-specific“cultures” (see fig. 3.3.18 in Chapter 3). Given the larger uncertainties that would arise from these sources of variability, the method was determined infeasible for estimating the dino chloroplast $1 + \varepsilon$ value. Test simulations confirmed that the method was unsound given the optical complexity of the water.

Therefore, literature derived values were used to estimate the dino chloroplast $1+\varepsilon$ value (Bernard et al., 2009). Experimental data suggests that large dinos may have substantially higher $b_{b\varphi}$ than

Mie theory predicts for large cells, and has been attributed to unusual internal structure from chromosome morphology, unique nucleus arrangements and higher intracellular carbon concentrations (Vaillancourt et al., 2004, Whitmire et al., 2010). These findings encourage an elevated overall homogeneous n for large dinoflagellates such as *C. hirundinella* which would increase spectral backscattering. Therefore, a range of chloroplast $1+\varepsilon$ values varying from 1.10 to 1.14 were tested while varying the chloroplast volume between 20 and 30%. Following analysis the $1+\varepsilon$ value was set to 1.12, equivalent to the value of the cyano chromatoplasm, with V_s=30%. The corresponding overall homogeneous dino n is 1.05, within the accepted range for homogeneous phytoplankton cells (Aas, 1996).

The values of n for the core layer cyano gas vacuole was set to $n = 333\lambda^{-1.94} + 0.82$ while $1+\varepsilon$ for the dino cytoplasm was set to 1.02 (Bernard et al., 2009). Δn was computed as a hilbert transform of n'.

5.2.4 Phytoplankton IOPs derived from a two-layered sphere

The two-layered sphere model is likely the simplest geometry capable of simulating phytoplankton IOPs, given that Mie models are generally known to be unsatisfactory (Whitmire et al., 2010, Zhou et al., 2012). The two-layered sphere model was used to derive the VSF and volume coefficients for the *M. aeruginosa* and *C. hirundinella* samples. Details of the model are provided in Chapter 4 and in Bernard et al. (2009).

The intracellular chlorophyll concentration (c_i) is used in the model to scale the chromatoplasm/chloroplast n' according to V_s and the theoretical unpackaged chl-*a* absorption maximum at 675 nm, $a^*_{sol}(675)$, set to 0.027 $\text{mg}^{-1}\,\text{m}^{-2}$ (Johnsen et al., 1994):

$$n'_{chrom/chloro}(675) = \frac{675}{n_{media}} \frac{c_i a^*_{sol}(675)}{\pi 4 V_s}$$

c_i is also used to normalise the PSD and volume coefficients to produce chl-*a* specific PSDs and IOPs. Thus its value has a large impact on the model through effectively varying the number of particles absorbing/scattering light. The value of c_i for *M. aeruginosa* was set to 2.1 $\text{kg}\,\text{m}^{-3}$ (Zhou et al., 2012). For *C. hirundinella* c_i was computed using the measured absorption and PSD data according to:

$$c_i = C\left[\frac{\pi}{6}\int_0^{\infty} F(d)d^3 d(d)\right]^{-1} \tag{5.2}$$

where C is the chl-*a* concentration in $\text{mg}\,\text{m}^{-3}$.

The c_i values were used to derive the SIOPs for *M. aeruginosa* and *C. hirundinella*.

In addition to modelling the IOPs of the discrete samples, the two-layered model was used to determine hypothetical size-variant SIOPs for populations of cyanos and dinos. The size-specific SIOPs were derived using the aforementioned values of m for core/shell layers which are assumed to be representative of generic cyano and dino species. The expected size variability of common freshwater nano-micro cyanophytes ranges from d approx. 2.5 μm (*Aphanizomenon*) to d approx. 44 μm (per 1 mm filament *Planktothrix*) (Reynolds, 2006). The size range overlaps that of common filamentous gas-vacuolate cyanophytes such as *Dolichospermum* and *Oscillatoria* which are generally better modelled using infinite cylinders than homogeneous spheres (Schagen, 1997). However, it is not known how the two-layered sphere might perform in comparison to the infinite cylinder configuration for filamentous gas-vacuolate cyanophytes. Nevertheless the size-variable simulations aim to capture in a simplified form the expected optical variability resulting from assemblages with diverse gas-vacuolate cyanophyte species (such as occurs in Theewaterskloof). For freshwater dinoflagellates a similar size variability is expected in nature with d ranging from approx. 8 μm for *Gymnodinium* spp. to 44 μm for *C. hirundinella* (Reynolds, 2006).

It has been shown that single size distributions parameterised by D_{eff} and V_{eff} are suitable for representing mixed phytoplankton assemblages in optical modelling (Bernard et al., 2007). Accordingly, PSDs with D_{eff} ranging from 1 to 50 μm at a 1 μm resolution were used to simulate the size variability of polydispersed cyano/dino populations. The population of cells had diameters ranging from 1 to 100 μm at a 1 μm interval, in the range of nano-micro plankton. The standard size distribution expressed in terms of R_{eff} and V_{eff} was used according to (Bernard et al., 2001):

$$F(r) = r^{[(1-3V_{eff})/V_{eff}]} exp(r/(R_{eff}V_{eff}))$$

V_{eff} was set to a constant value of 0.6 determined as the mean of measured PSDs in Loskop and Theewaterskloof. This is near to the value of 0.63 suggested for use by Bernard et al. (2001). The PSDs were scaled to determine the number of particles corresponding to 1 mg chl-*a* m^{-3} using the aforementioned estimates for c_i.

5.2.5 INVERSE METHODS USING E-S RADIATIVE TRANSFER MODEL

The schematic for inversion algorithm showing the bio-optical model, use of E-S and optimisation procedure is shown in fig. 5.2.1. The algorithm is based on that of Bernard (2005) but is modified for freshwater cyano and dino types and to use E-S to solve the RTE.

E-S is a version of the Hydrolight radiative transfer model that solves the azimuthally averaged RTE with fast run times. Quick computational time is essential as E-S is called iteratively to calculate the R_{rs} using variable IOP inputs. For this study a spectrally variant Fournier-Forand phase function dependent on the value of b_b:b was used (Fournier and Forand, 1994). This approach was found to provide improved optical closure in optically-complex waters than alternative phase function definitions in Hydrolight (Gallegos et al., 2008, Mobley et al., 2002, Tzortziou et al., 2006). The Radtran Sky irradiance model (Gregg and Carder, 1990) in E-S was used to compute the downwelling irradiance (E_d). *In situ* measurements of atmospheric pressure, total precipitable water vapour column in cm (WV), and aerosol optical thickness (AOT) made using a Microtops II

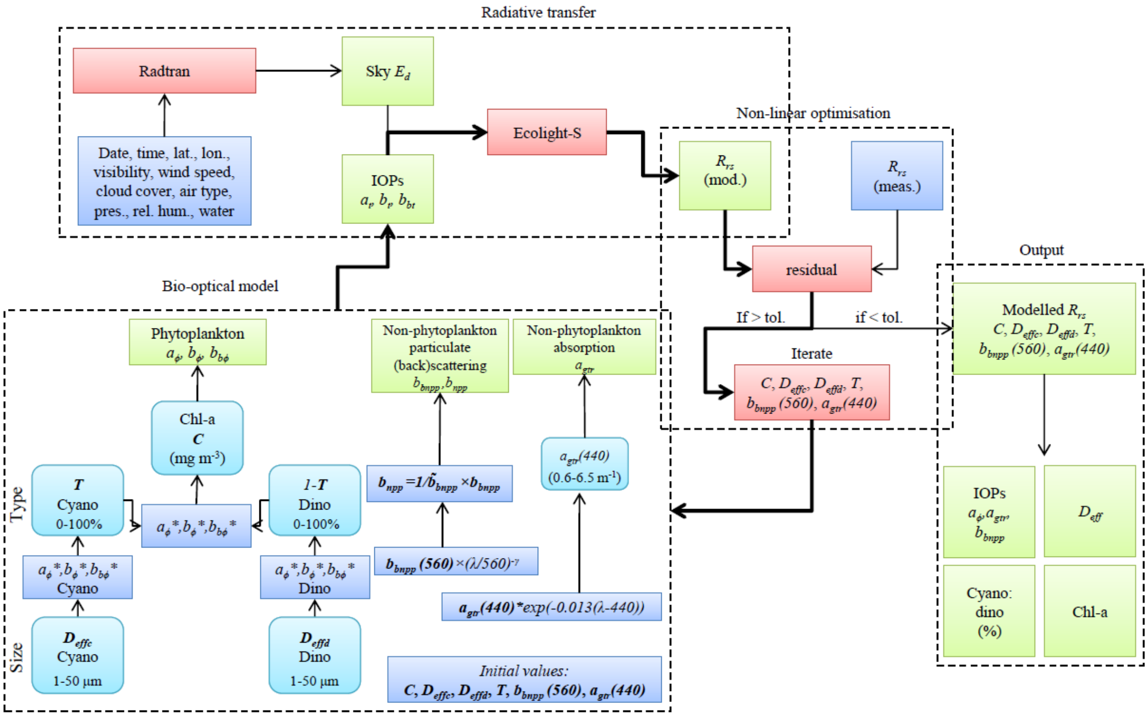

Figure 5.2.1: Schematic diagram for the radiative transfer inversion algorithm. Blue represents measured or estimated inputs, cyan represents variables solved for iteratively, red represents calculations and green represents outputs. The 2 pt. arrows represent the iterative process followed by the algorithm. tol. = tolerance, for other variables, see text.

sun photometer (Solar Light Co.) corresponding to each R_{rs} spectrum were used (where available). Horizontal visibility was calculated from AOT at 550 nm according to $3.9449/(AOT550 - 0.08498)$ (Retalis et al., 2010). Relative humidity was estimated from WV according to $18WV + 40$ (calculated using data in Raj et al., 2004). Cloud cover was estimated in % and a continental aerosol model was used.

The inputs to E-S are the total absorption, scattering and backscattering (a_t, b_t, b_{bt}) of the water as well as the incident downwelling irradiance (E_d) assuming the water is optically deep (no bottom effects). In E-S the IOPs are assumed to be constant with depth within homogeneous layers. Although it has been shown that the vertical profile of the IOPs has a significant effect on the observed R_{rs} signal (e.g. Kutser et al., 2008, Stramska and Stramski, 2005, Zaneveld et al., 2005) the turbid waters investigated in this study typically have very large optical depths, with chl-a $>$ 10 mg m^{-3} and Secchi disk depths less than 2 m (maximum of approx. 8 m for a few clear water samples). Therefore it is assumed that the bulk optical signal is derived from the upper 2 m of the water column, which is well represented by IOPs measured at the water surface.

The phytoplanton IOPs were calculated as an admixture of cyano and dino populations from the size-based SIOPs generated for D_{eff} between 1 and 50 μm. The value of D_{eff} is independent for cyano and dino populations in order to simulate assemblages composed of a mix of small cyano (e.g. *M. aeruginosa*) and large dino (e.g. *C. hirundinella*) species, as occurred in this study. The assemblage species composition is computed using T, the phytoplankton admixture coefficient varying between 0 and 1. This enables simulation of assemblages dominated either by cyano or dino species or a mixture of both. C, the concentration of chl-a in mg m^{-3}, calculates the total phytoplankton IOPs from the SIOP admixture. The phytoplankton volume coefficients were therefore calculated as:

$$i_{\varphi} = C \times [T i^{*}_{\varphi c}(D_{effc}) + (1 - T) i^{*}_{\varphi d}(D_{effd})]$$

where i can be replaced by either a, b or b_b, and subscripts c and d stand for cyanos and dinos, respectively.

It is possible to directly determine the TR (or NPP) component as a parameter in the inversion scheme using the mass-specific tripton absorption, scattering and backscattering coefficients which are then scaled using the TR concentration. Such an algorithm was built and tested but was not used for the following reasons: firstly the absorption signals from *gelbstoff* and TR (only differing in the slope coefficient, S) are hard to resolve due to their similarity; secondly, the approach cannot account for potential contributions to backscattering by non-tripton non-phytoplankton particles (e.g. very small particles, bubbles, bacteria); the variability in the mass-specific tripton volume coefficient was significant between the study areas owing to variable mineral:detrital ratios (Matthews and Bernard, 2013a) and therefore could not be sufficiently described by a set of mean coefficients. Improved optical closure was obtained using a coupled absorption term for *gelbstoff* and TR, termed a_{gtr}, and a separate term accounting for NPP (back)scattering, termed b_{npp} and b_{bnpp}.

a_{gtr} was calculated using an exponential function as:

$$a_{gtr} = a_{gtr}(442) e^{-S(\lambda - 442)}$$

where S is the slope coefficient equal to the mean value of 0.013 determined in the study areas (see Chapter 3). $a_{gtr}(442)$ was constrained to vary inside a range of 0.2 to 6.0 m^{-1}, appropriate to the study areas.

The power-law function has been determined to provide a close fit with measurements of the particulate backscattering (b_{bp}) in coastal and inland waters (e.g. Snyder et al., 2008, Sun et al., 2009). Thus b_{bnpp} was calculated by the power-law function:

$$b_{bnpp} = b_{bnpp}(560) \times (\lambda/560)^{\gamma}$$

where γ is the slope coefficient.

The value of γ typically ranges from 0 to -2 nm^{-1} with a mean value near -1 (*ibid.*). A range of values for $b_{bnpp}(560)$ and γ were tested to provide the best optical closure. In order to facilitate calculation of b_{npp} without the introduction of another variable in the optimisation procedure, b_{npp} was calculated as:

$$b_{npp} = \frac{1}{\tilde{b}_{bnpp}} \times b_{bnpp}$$

where $\tilde{b}_{bnpp}$ is the ratio b_{bnpp}:b_{npp}.

Based on a review of studies performed in complex waters, from sediment-dominated coastal waters to turbid eutrophic lakes, the value of $\tilde{b}_{bp}$ ranges from approx. 0.5 to 7% (McKee et al., 2009, Neukermans et al., 2012, O'Donnell et al., 2010, Snyder et al., 2008, Sun et al., 2009) (these studies refer to the bulk particulate matter (back)scattering, and not NPP as used here). A spectral dependency of $\tilde{b}_{bp}$ has been noted by some authors (McKee et al., 2009, Snyder et al., 2008) although this is somewhat disputed (Whitmire et al., 2007). In turbid productive waters $\tilde{b}_{bp}$ has been reported as being inversely proportional to the inorganic or mineral component of suspended matter and has little correlation with chl-*a* (Sun et al., 2009), typically varying between 1 and 2%. As phytoplankton typically scatter relatively little in comparison with hard mineral particles, b_{npp} is likely to differ only slightly from b_p, except in high biomass waters. It is also probable that b_{npp} has less spectral dependence than b_p which includes phytoplankton. Therefore a spectrally flat $\tilde{b}_{bp}$ with values ranging from 1 to 5% were assessed in the calculation of b_{npp}.

A four component bio-optical model was used to calculate the total volume coefficients for E-S according to:

$$a_t = a_\varphi + a_{gtr} + a_w$$

$$b_t = b_\varphi + b_{npp} + b_w$$

$$b_{bt} = b_{b\varphi} + b_{bnpp} + b_{bw}$$

where *w* stands for water.

The bio-optical model contains six variables, namely C, T, D_{effc}, D_{effd}, $b_{bnpp}(560)$ and $a_{gtr}(442)$, constrained in various value ranges. These are solved for using a Nelder-Mead downhill simplex non-linear optimisation algorithm by fitting R_{rs} calculated using E-S to the measured R_{rs} spectrum between 400 and 800 nm. The fit between the measured and modelled R_{rs} is calculated using the Euclidian distance and a wavelength weighting function, $f(\lambda)$:

$$d(x, y) = \sum_{i=1}^{N} f(\lambda_i) \times (|x_i - y_i|)^2$$

where x and y are the measured and modelled spectra, respectively. $f(\lambda)$ is used to assign a weight of 1% in the fitting procedure to wavelengths in the chl-*a* fluorescence domain from 680 to 695 nm as fluorescence is not accounted for by E-S.

The simplex algorithm iterates until the estimated variables change by less than the tolerance level which was $1 \times 10 - 6$. The algorithm performance was evaluated by comparing the modelled and measured values of the absorption coefficients, chl-*a*, D_{eff} and ESDs using a non-parametric correlation, as the variables were non-normally distributed. Phytoplankton species counts corresponding to each spectrum were used as an indication of species composition. The estimated mean assemblage D_{eff} was calculated as $TD_{effc} + (1 - T)D_{effd}$. The inversion algorithm was implemented in Python programming language and E-S was called as a subroutine.

5.3 RESULTS AND DISCUSSION

5.3.1 VARIABILITY IN PHYTOPLANKTON, R_{rs} AND ABSORPTION

The measured R_{rs} spectra for the three reservoirs are shown in fig. 5.3.1 alongside histograms corresponding to the measured chl-*a* and absorption coefficients at 442 nm. The spectra from Loskop (LK) are from waters primarily dominated by the large celled dino *C. hirundinella* which vary from oligotrophic to hypertrophic states (chl-*a* of 0.5 to 500 mg m^{-3}). Those from Hartbeespoort (HB) were measured during a hypertrophic mono-specific vacuolate *M. aeruginosa* bloom which had chl-*a* ranging from 70 to 13 000 mg m^{-3}. The *M. aeruginosa* bloom existed as dense aggregated surface accumulations (or scum) which was mixed into the water column depending on the prevailing wind conditions. Theewaterskloof (TW) waters were meso/eutrophic (chl-*a* from 5 to 35 mg m^{-2}) with a mixed phytoplankton population dominated by the large dino *Sphaerodinium fimbriatum* (*ESD*=± 40 μm), the filamentous vacuolate cyanophyte *Anabaena ucrainica* (*ESD*=± 16 μm) and various diatom species (see Chapter 3 for details). TW waters also had a higher mean mineral content of tripton (65% non-phytoplankton dry mass). Therefore, the LK and HB data represent cases of dominance by a large dino and a small vacuolate cyano, respectively, whereas the TW spectra present a case of a mixed population of a large dino and a small/intermediate vacuolate cyano species and higher mineral content. The variability in phytoplankton and water constituent composition is the cause of the observed differences in magnitude and shape of R_{rs}, which are now discussed.

R_{rs} from HB and TW have significantly higher magnitudes between 400 and 700 nm than those from LK (see fig. 5.3.1C). $R_{rs}(560)$ ranged from 0.018 to 0.048 sr^{-1} for HB, from 0.013 to 0.026 sr^{-1} for TW and from 0.003 to 0.011 sr^{-1} for LK. Since the waters in HB had insignificant contributions from constituents other than *M. aeruginosa*, this observation might be explained by the small cells which contained intracellular gas vacuoles which cause elevated spectral backscattering (Matthews and Bernard, 2013b). In the case of TW, the elevated backscattering may also result from a higher mineral content of suspended matter in addition to vacuolate *A. ucrainica*. The reduced magnitude of R_{rs} for LK is in accord with Mie theory which predicts reduced backscattering from larger cells (van de Hulst, 1957). Another noticeable feature is the non-negligible signal at wavelengths > 750 nm typical of turbid waters. The HB spectra with NIR signals > 0.1 sr^{-1} were measured over dense surface scum. These spectra resemble those of dry vegetation as a result of negligible absorption by

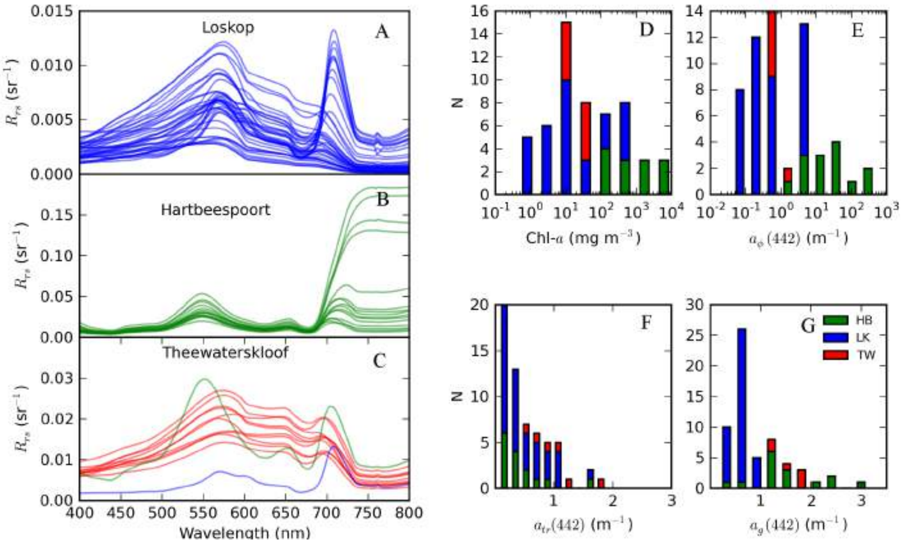

Figure 5.3.1: R_{rs} for A) Loskop, B) Hartbeespoort and C) Theewaterskloof with histograms for corresponding D) chl-a, E) $a_\varphi(442)$, F) $a_{tr}(442)$ and G) $a_g(442)$. Spectra from all three reservoirs are overlaid in C for comparison of shape and magnitude.

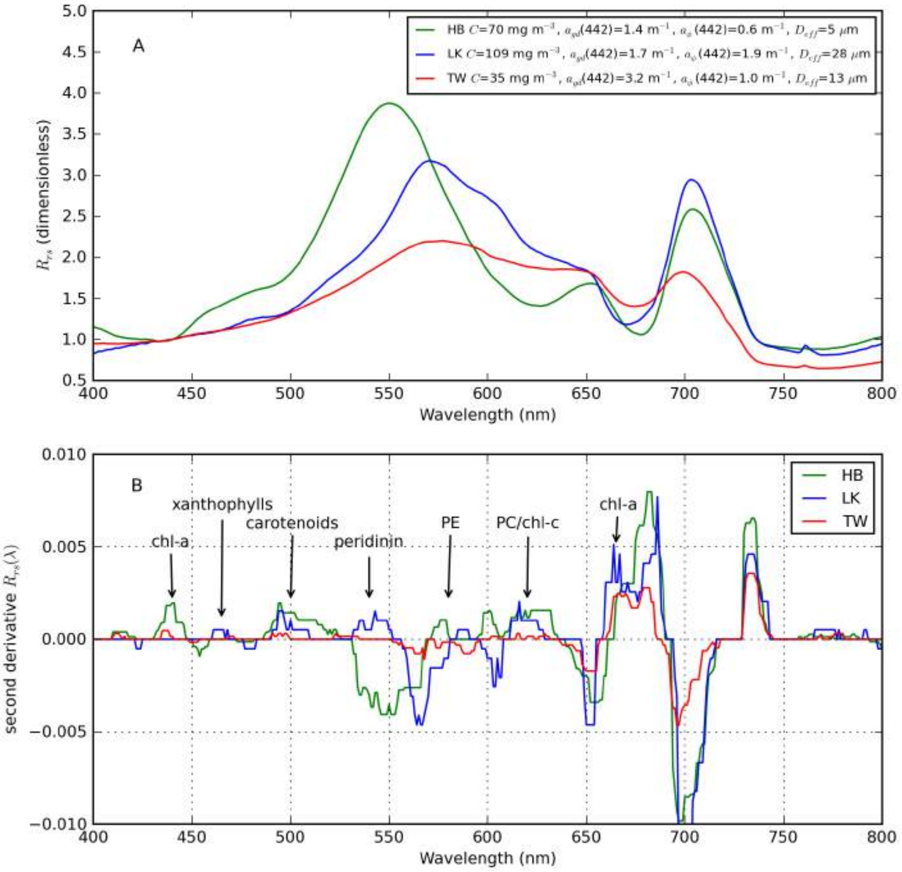

Figure 5.3.2: A) R_{rs} normalised at 440 nm from a small celled *M. aeruginosa* bloom (HB), a large celled *C. hirundinella* bloom (LK), and a mixed bloom of small-celled cyano and large-celled dino species (TW). Legend provides details about water constituents. B) Corresponding second derivatives for R_{rs} including labels identifying various pigment absorption features.

water (e.g. Kutser et al., 2008, Tebbs et al., 2013). Therefore the NIR signal in these turbid waters are significant which has important implications for atmospheric correction of remotely sensed radiances (e.g. Shi and Wang, 2009).

Selected spectra representative of the different species at similar biomass were normalised at 440 nm (soret chl-*a* absorption peak) for investigation of the variability in spectral shape (fig. 5.3.2A). In addition the second derivative of the spectra were calculated and smoothed using a median filter with a 9 nm window size in order to identify the pigment absorption features after Maldonado (2008) (fig. 5.3.2B). Absorption of light by different phytoplankton pigments can be determined as the primary cause of the observed differences in spectral shapes. *M. aeruginosa* posses distinctive phycobiliproteins phycocyanin (PC) and phycoerethrin (PE) absorbing strongly in the range 550 to 650 nm and are devoid of chlorophyllous pigments besides chl-*a*. *C. hirundinella* possess pigments chl-*c*, carotenoids peridian and fucoxanthin and xanthophylls diadinoxanthin and diatoxanthin which absorb light in the region 440 to 550 nm (Richardson, 1996, Schluter et al., 2006).

A number of distinctive features in the R_{rs} arise as a consequence of this unique pigmentation (see fig. 5.3.2A). Firstly, cyano-dominant waters (HB) possess a marked trough in the region 600 to 650 nm as a result of absorption by PE and PC. Correspondingly these spectra also have a marked peak near 650 nm resulting from proximal PC and chl-*a* absorption bands at 620 and 665 nm, respectively, and potential phycobiliprotein fluorescence as speculated by Matthews et al. (2012). This peak might be used to distinguish cyanobacteria from algae as shown in Chapter 2 of this thesis. Furthermore, there is a shift in the green peak < 550 nm as a result of PE absorption. For dino-dominant waters (LK), strong absorption by accessory pigments results in reduced R_{rs} in the region 440 to 550 nm. The absence of PC and PE mean that R_{rs} is enhanced in the region 550 to 650 nm and the green peak is situated further towards the red near 560 nm. In addition to pigment absorption, sun-induced pigment fluorescence is likely to be an additional process leading to differences in R_{rs}. In particular, cyanobacteria are known to possess reduced chl-*a* fluorescence as a result of various photophysiological processes (Seppälä et al., 2007). This is evident by a trough in R_{rs} near 685 nm, which has also been used as a marker for cyanos (Matthews et al., 2012, Wynne et al., 2008). In summary, changes in the position of the peak near 560 nm, the presence or absence of a peak near 650 nm, and features related to chl-*a* fluorescence are the primary spectral differences in waters dominated by cyanos versus dinos. The TW spectra have features corresponding to both cyano and dino pigmentation although these are less apparent (fig. 5.3.2B). The green peak located near 560 nm is indicative of strong accessory pigment absorption in the region 450 to 550 nm, and the presence of a small peak at 650 nm is evidence of PC absorption near 620 nm. The sensitivity of the inverse problem to resolve distinctive pigment features is assessed in section 5.4.2.

The histograms in fig. 5.3.1 indicate the expected range of variability that might be encountered for chl-*a*, $a_{\varphi}(442)$, $a_{tr}(442)$ and $a_g(442)$ in the waters under investigation. This information is essential for constraining the inverse retrieval of parameters. Chl-*a* and $a_{\varphi}(442)$ vary widely over 5 orders of magnitude. The distributions are bimodal with peaks near chl-*a* of 10 and > 100 mg

m^{-3}, the latter of which represents the high biomass blooms in HB and LK. The widest range of values is encountered in LK, while those of TW and HB are in the mid and upper ranges, respectively. $a_{tr}(442)$ varies inside the range 0.1 to 2.3 m^{-1} with the highest probability value near 0.5 m^{-1}. $a_{tr}(442)$ for TW occupies the upper range of values while that for HB occupies the lower range, with LK having the widest variability. For $a_g(442)$ the highest probability value is near 1 m^{-1} within a range of 0.4 to 3 m^{-1}, with LK occupying the lower range and TW and HB the upper range of values. These ranges we used to constrain the parameter estimates during the non-linear optimisation procedure.

5.3.2 COMPLEX REFRACTIVE INDICES OF *C. HIRUNDINELLA* AND *M. AERUGINOSA*

The measured SIOPs for *C. hirundinella* and *M. aeruginosa* are shown in fig. 5.3.3A. The reduced pigment packaging from the small cells size of *M. aeruginosa* results in a higher value for $a^*_\varphi(675)$ of 0.023, more than double than that for the large celled *C. hirundinella* samples of 0.0089 m^2 mg^{-1}. The large difference in cell size is visible in the estimated and measured phytoplankton volume distributions in fig. 5.3.3B. D_{eff} for *M. aeruginosa* is 5.2 μm based on measurements by Robarts (1984), while that measured for the two *C. hirundinella* samples are 29.6 and 30.9 μm. The *ESD* of *C. hirundinella* however is between 35 and 50 μm. The unimodal volume distributions show the overwhelming dominance of *C. hirundinella*, with relatively insignificant contributions by small cells. The significant differences in pigmentation, discussed above with respect to R_{rs}, are also apparent in the a^*_φ spectra. The calculated experimental $\bar{Q}_a$ demonstrate the considerably different optical behavior of the two species. *C. hirundinella* has considerably larger absorption efficiency relative to *M. aeruginosa*, resulting from the larger geometrical cross-section. There is very close agreement in $\bar{Q}_a$ between the two independent *C. hirundinella* samples.

The ADA estimated n'_{hom} and fitted Q_a (+) spectra are shown in figs. 5.3.3 C and D. The magnitudes of n'_{hom} compare closely with those estimated by Zhou et al. (2012) for freshwater species using the same methodology. The volume equivalence determined chloroplast and chromatoplasm n' are shown in fig. 5.3.3E. The difference in values for dino chloroplast and cyano chromatoplasm arise from the use of different shell volumes and differences in n' for the dino/cyano core layers. $n'_{chloro}(440)$ determined using the two-layered model approach are close to those calculated by volume equivalence, with small differences in the blue. The spectral n for the dino chloroplast and cyano chromatoplasm layers are shown in fig. 5.3.3F.

5.3.3 SIOPs OF *C. HIRUNDINELLA* AND *M. AERUGINOSA*

Fig. 5.3.4 shows the SIOPs determined by the two-layered sphere using the data in fig. 5.3.3. The coefficients for the two independent *C. hirundinella* samples are close, suggesting good reproducibility of the method used here. Spectral attenuation for *M. aeruginosa* is considerably larger than that for *C. hirundinella* as a result from larger (back)scattering. $c^*_\varphi(510)$ is 0.32 m^{-1} for *M.*

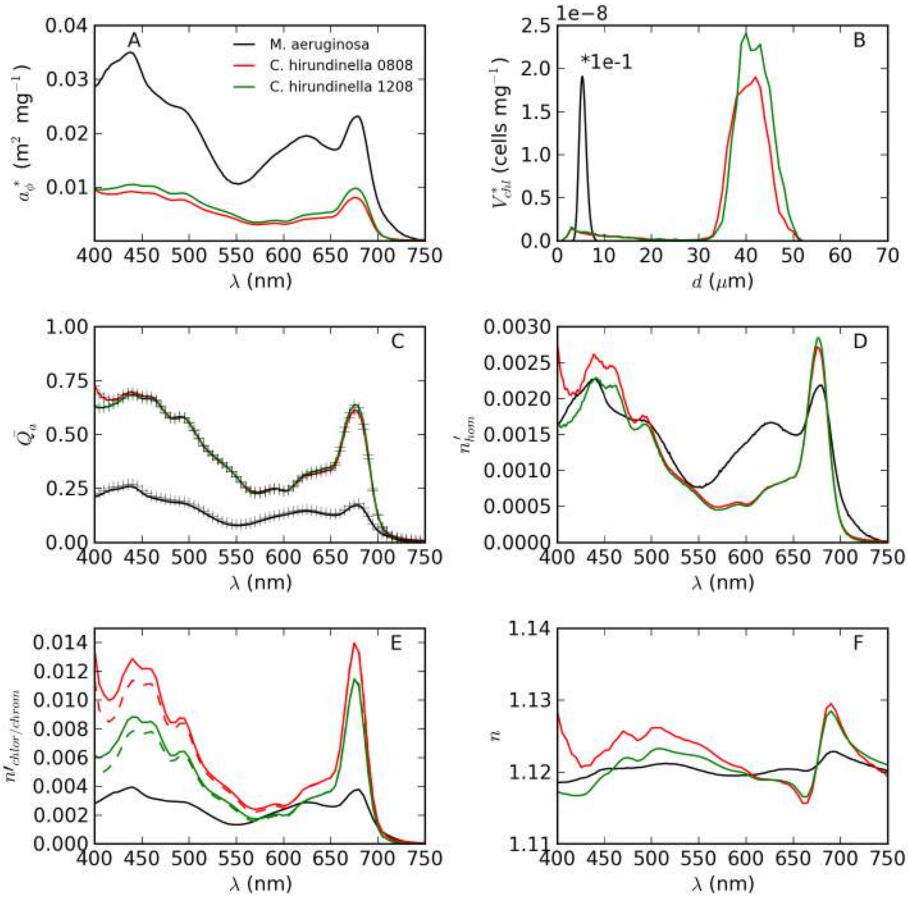

Figure 5.3.3: Derivation of complex refractive indices for *M. aeruginosa* and two *C. hirundinella* samples. A) Chl-*a* specific absorption, B) chl-*a* specific phytoplankton volume distribution, C) measured versus modelled (+) Q_a, D) n'_{hom}, E) n' for *M. aeruginosa* chromatoplasm for cell with 50% gas vacuole volume and for *C. hirundinella* chloroplast with 30% cell volume derived using volume equivalence (solid) and two-layer model (dashed) methods, F) n showing Δn for cyano chromatoplasm and dino chloroplast layers.

aeruginosa an order of magnitude higher than *C. hirundinella* which is 0.028 and 0.034 m^{-1}. Similarly, $b^*_\varphi(510)$ is 0.3 versus 0.02 m^{-1} while $b^*_{b\varphi}(510)$ is 0.0055 versus approx. 8 $\times 10^{-5}$ m^{-1}, respectively. Therefore $b^*_{b\varphi}$ is more than 2 orders of magnitude higher for *M. aeruginosa* resulting from the small cell size and internal vacuole structure (Matthews and Bernard, 2013b). The *C. hirundinella* $b^*_{b\varphi}$ spectra have more spectral shape with enhanced values in the NIR, as has been determined for other large celled species (Dierssen et al., 2006). There is a close match between the measured and modelled a^*_φ (fig. 5.3.3C).

The effects of varying the dino V_s and chloroplast $1+\varepsilon$ values on the efficiency factors and specific volume coefficients for (back)scattering are shown in fig. 5.3.5. Q_b in the expected range between 1 and 2 (there were insignificant effects on Q_a, not shown). There is no clearly discernible effect of chloroplast volume (V_s) on Q_b other than changes in spectral shape. For Q_{bb} and $b^*_{b\varphi}$ the changes are mostly related to magnitude with little change in spectral shape: Q_{bb} increases independently of

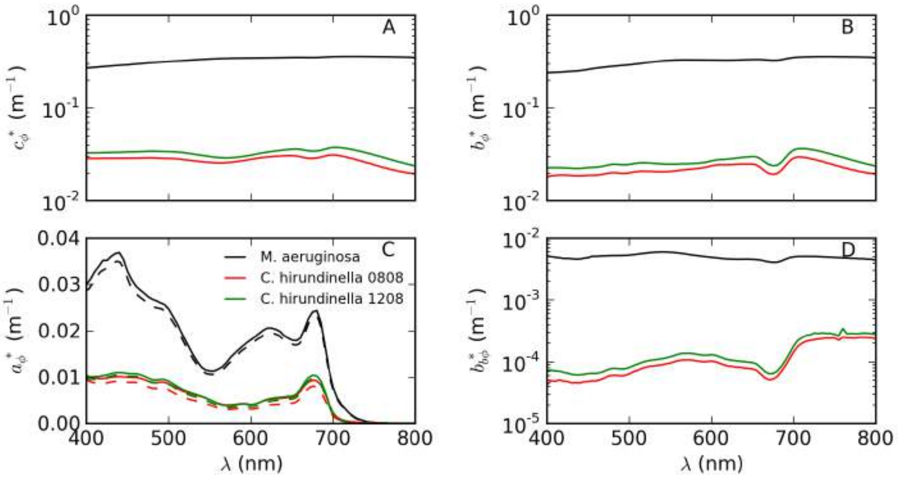

Figure 5.3.4: Chl-*a* specific volume coefficients for *M. aeruginosa* and *C. hirundinella* derived from the two-layered sphere model. The dinoflagellate was modelled with chloroplast $1+\varepsilon$ $= 1.12$ and $V_s = 30\%$ using the measured PSD in fig. 5.3.3. The cyano was modelled with a gas vacuole volume of 50% and chromatoplasm $1+\varepsilon = 1.12$ after Matthews and Bernard (2013b). Dotted lines in C are measured a^*_φ.

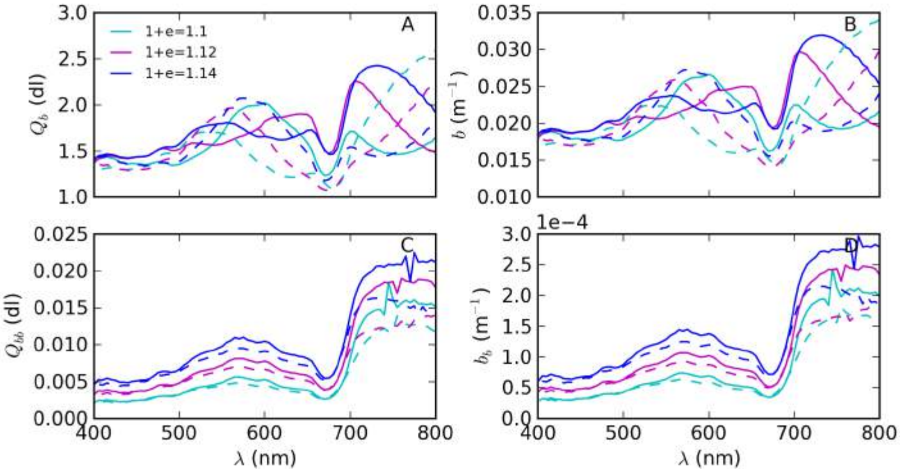

Figure 5.3.5: Effects of variable $1+\varepsilon$ and chloroplast volume on the efficiency factors and chl-*a* specific coefficients for scattering and backscattering for *C. hirundinella* 0808 sample derived from the two-layered sphere model using the measured size distribution. Dotted lines are for $V_s = 20\%$ and solid lines are for $V_s = 30\%$.

wavelength for larger $1+\varepsilon$ and V_s values, the latter effect being smaller than the former. Therefore the value of $1+\varepsilon$ of the shell layer has a larger effect on Q_{bb} than its volume. $b^*_{b\varphi}(510)$ for V_s = 30% increases from 4.86×10^{-5} m^{-1} for $1+\varepsilon$ of 1.1 to 9.95×10^{-5} m^{-1} for $1+\varepsilon$ of 1.14. The changes in Q_b can be explained by the sensitivity of the VSF in the forward direction to $1+\varepsilon$, the changes in spectral shape being caused by interference oscillations which are wavelength (and size) dependent (Morel and Bricaud, 1986). Conversely, there is less sensitivity to these effects in the backward direction resulting in little change is spectral shape.

The results from the two-layered model for *M. aeruginosa* are discussed in Chapter 4 and are therefore not discussed in detail here. The values of $Q_b(510) = 1.57$ and $Q_{bb}(510) = 0.0055$ derived for *C. hirundinella* do not agree with the high values of measurements made on the large dinoflagellate *C. longpipes* ($ESD = 55\ \mu$m) by Whitmire et al. (2010) which had values of 2.325 and 0.061, respectively. Similarly large values were determined by Vaillancourt et al. (2004) for *Alexandrium tamarense* ($ESD = 31\ \mu$m) which had $Q_{bb}(510)$ of 0.0148. The explanation for these enlarged values was provided as resulting from unusual internal structure and high cellular carbon content. However, if such high backscattering existed for *C. hirundinella* in the same order of magnitude as for *M. aeruginosa*, this would be reflected in similar R_{rs} magnitudes for blooms of similar biomass. However fig. 5.3.1 indicates that R_{rs} is substantially smaller for the *C. hirundinella* bloom than that for *M. aeruginosa*. This supports a smaller value of Q_{bb} and $b^*_{b\varphi}$ for *C. hirundinella*, in contrast to the results of Vaillancourt et al. (2004), Whitmire et al. (2010).

The results obtained here agree better with those of Zhou et al. (2012) who found $Q_b(510) = 1.68$ and $Q_{bb}(510) = 0.003$ for the small ($ESD = 5\ \mu$m) dinoflagellate *Amphidinium* spp. It could be possible that this species and *C. hirundinella* sampled in this study did not possess unusual internal structure or high intracellular carbon content. However the finding of Whitmire et al. (2010) that *C. longpipes* has a $b^*_{b\varphi}(510)$ of 0.0097 m^{-1}, larger than that of *M. aeruginosa* as measured by Zhou et al. (2012) is in the author's opinion, anomalous. Contrasting findings are present in the literature, for example, the large (d from 20 to 40 μm) HAB forming *K. Brevis* is known to possess low backscattering with a value of $b^*_{bp}(488)$ near 2×10^{-4} m^{-1} (calculated from data presented in Schofield et al., 2006); values for b^*_{bp} reported in a *C. balechi* bloom were near 1×10^{-4} m^{-1} (Matthews et al., 2012); and dinoflagellate bloom colour modelled by Dierssen et al. (2006) have a taxon b^*_{bp} near 3×10^{-4} m^{-1}, smaller than for other taxons. There is also a lack of accompanying evidence in the literature from natural dino blooms indicating that these species possess enlarged backscattering as a distinctive feature as reproduced in enhance R_{rs} (e.g, see measured spectra in Dierssen et al., 2006). The influence of contamination by highly scattering small non-algal particles, e.g. broken cellulose thecal plates, in cultures could be the source of the unusually observed high backscatter efficiency measured by Whitmire and others for dinoflagellates, as suggested in Whitmire et al. (2010).

5.3.4 Size variable phytoplankton SIOPs

The phytoplankton SIOPs for cyano and dino populations for variable D_{eff} determined by the two-layer model are shown in fig. 5.3.6. The expected variability related to size is demonstrated in the SIOPs, with reduced a^*_φ for a population of larger cells related to the package effect, and enlarged b^*_φ and $b^*_{b\varphi}$ for populations dominated by small cells. The coefficients for the cyanos are larger than those for dinos with equivalent D_{eff}. $a^*_\varphi(440)$ for cyanos with D_{eff} of 25 μm are 0.018 m^{-1} versus that of 0.013 m^{-1} for dinos. Similarly $b^*_\varphi(560)$ and $b^*_{b\varphi}(560)$ are 0.052 and 0.036 m^{-1}, and 7.8×10^{-4} and 2.2×10^{-4} m^{-1}, for cyanos and dinos respectively. Therefore a cyano population has roughly four times the backscattering of the size equivalent dino population. This is expected since the intracellular gas vacuole structure enlarges the spectral (back)scattering (Matthews and Bernard, 2013b). The size-variable SIOPs were used in the inversion algorithm to assess the sensitivity to size and type in mono-specific and mixed populations of dinos and cyanos.

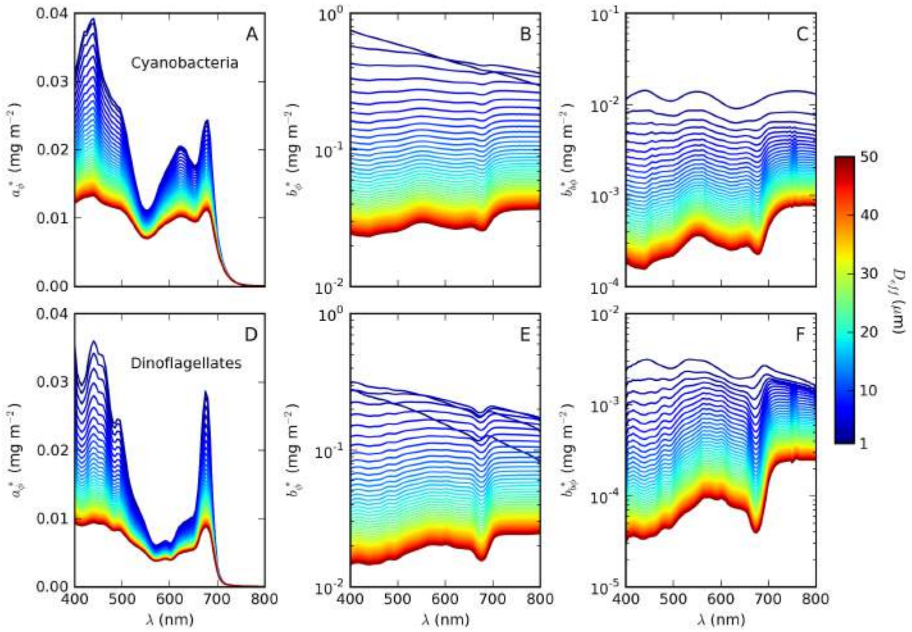

Figure 5.3.6: Chl-a specific volume coefficients for cyano and dinoflagellates for D_{eff} from 1 to 50 μm modelled using a two-layered sphere. The cyano had a gas vacuole volume of 50%, chromatoplasm $1+\varepsilon = 1.12$, and standard size distributions with $V_{eff} = 0.5$. The dino had a chloroplast $1+\varepsilon = 1.12$, $V_s = 30\%$ and standard size distribution with $V_{eff} = 0.5$. The value of c_i was constant for the cyanos and dinos at 2.1 and 3.2 kg m^{-3}, respectively.

5.4 APPLICATIONS

5.4.1 SENSITIVITY OF SIZE AND TYPE DETECTION TO INITIAL CONDITIONS

The spectral region from 500 to 650 nm typically contains the most information for type (and possibly size) detection, since the diagnostic pigment absorption features are most apparent at these wavelengths (see fig. 5.3.2). Therefore successful type (and size) detection was largely determined by whether the algorithm was able to resolve (provide a good match of) spectral features at these wavelengths. The initial values for D_{effc} and D_{effd} were fixed at 5 and 31 μm appropriate for *M. aeruginosa* and *C. hirundinella* dominant waters, respectively. The convergence of the measured and modelled R_{rs} and the retrieval of type and size was highly sensitive to the initial values of the six variables solved for by the algorithm. This illustrates that the inverse problem and its solution through the inversion model was ambiguous. Initial conditions providing good optical closure and acceptable phytoplankton size and type detection across the diverse water types were therefore determined after testing a range of plausible initial values (table 5.4.1). The table illustrates the sensitivity of the algorithm in terms of size and type detection to variations in a single initial condition while holding all other initial conditions constant at their default values (first row).

Table 5.4.1: Sensitivity of the inversion algorithm to initial conditions for resolving size and type. High sensitivity indicates a significant change (better or worse) in the retrieval of size and type from the default values used in the first row. Bold text indicates the variable being tested while others are held constant. emp = empirical, norm=normal wavelength weighting. See text for discussion.

C mg m^{-3}	T	$b_{bnpp}(560)$ m^{-1}	γ	$1/\tilde{b}_{bnpp}$	$a_{gtr}(440)$ m^{-1}	$f(x)$	Sensitivity
emp	0.5	0.1	0	50	2.5	norm	Default
10	0.5	0.1	0	50	2.5	norm	High
100	0.5	0.1	0	50	2.5	norm	Low
emp	**0.95**	0.1	0	50	2.5	norm	High
emp	**0.05**	0.1	0	50	2.5	norm	High
emp	0.5	**0.001**	0	50	2.5	norm	High
emp	0.5	**0.01**	0	50	2.5	norm	High
emp	0.5	**0.5**	0	50	2.5	norm	High
emp	0.5	0.1	**-0.5**	50	2.5	norm	High
emp	0.5	0.1	**-1.2**	50	2.5	norm	High
emp	0.5	0.1	0	**10**	2.5	norm	Medium
emp	0.5	0.1	0	**100**	2.5	norm	Low
emp	0.5	0.1	0	50	**0.5**	norm	Medium
emp	0.5	0.1	0	50	**4**	norm	Medium
emp	0.5	0.1	0	50	2.5	**500-650**	Low
emp	**0.6**	**0.1**	**0**	**50**	**2.5**	**norm**	Optimal

The algorithm was highly sensitive to the initial value of T, which was varied between 0.05 and 0.95 simulating both dino and cyano dominance, and mixed populations. A bias towards cyano-dominance provided excellent resolution of *M. aeruginosa* bloom spectra, and *vise versa*. Using a single value of 0.6 for T representative of a mixed assemblage provided acceptable differentiation between dino and cyano-dominant spectra (see discussion in section 5.4.2). Variations in the initial value used for C also had a large affect on the algorithm type and size estimates. An empirical algorithm using the reflectance ratio $R1 = R_{rs}(710){:}R_{rs}(665)$ derived from the dataset of form $C = -6.1R1^2 + 91.3R1 - 47.7$ constrained to a lower limit of 1 mg m^{-3}, was tested against constant values, and found to be more optimal. The empirical first guess for C enabled the algorithm to converge more rapidly towards a solution.

The slope and magnitude of NPP (back)scattering significantly affected the algorithms ability to resolve spectral features in the 500 to 650 nm region. More sloped spectral gradients resulted in significantly poorer type detection presumably through the introduction of additional spectral shape and noise. A spectrally invariant (flat) spectrum resulted in much improved spectral resolution and greater sensitivity to type and size. Higher initial values for $b_{bnpp}(560)$ near 0.1 m^{-1} resulted in better spectral matching, particularly for the hypertrophic *C. hurindinella* bloom waters. Therefore these waters are presumably affected by high NPP backscattering. The algorithm was less sensitive to the value of $\tilde{b}_{bnpp}$ used in the calculation of b_{npp}. A value of 2% was therefore used. There was little sensitivity to the initial value for $a_g(440)$. A value of 2.5 m^{-1} was used. A wavelength weighting function $f(\lambda)$ with more sensitivity in the spectral region 500 to 650 nm was found not to improve type/size detection. This means that the red-NIR and blue spectral regions are important for resolving type and size in complex waters.

The optimal initial conditions yielding satisfactory estimates for type and size were therefore determined through the sensitivity analysis (indicated in the last row of table 5.4.1). These were used to test the sensitivity of an inversion model run with a single set of initial conditions, and to assess the ambiguity of the solution. Further optimisation of the initial conditions for water types is performed in section 5.4.3.

5.4.2 Algorithm performance in diverse waters: sensitivity and ambiguity of the inverse problem

The performance of the inversion algorithm across the various trophic ranges and water types in shown in fig. 5.4.1 and table 5.4.2. As the variables were non-normally distributed a non-parametric measure of correlation was used. There are significant correlations for chl-*a* (r=0.95), a_φ (r=0.96), ESD (r=0.68) and D_{eff} (r=0.82). The retrieval of chl-*a* and $a_\varphi(440)$ for LK (r=0.93 and r=0.91, respectively) over the wide trophic range (chl-$a \pm 0.5$ to 500 mg m^{-3}) illustrates the robustness of the biomass estimates. The determination of $a_{gtr}(440)$ in meso/oligotroiphic waters ($\mathrm{r} > 0.7$) was significantly better than for hypertrophic waters as expected because of the relative magnitudes of the signals from non-phytoplankton components. Retrieval in the mixed high mineral composition waters of TW was the most challenging case, likely owing to greater ambiguity of the inverse problem. With regard to type, the *M. aeruginosa* and *C. hirundinella* blooms can be differentiated, and mixed water types are determined as such, while, as expected, there is little sensitivity to type in oligotrophic waters.

Mixed mesotrophic and oligotrophic waters

Retrieval of type and size in mixed mesotrophic and oligotrophic (chl-$a < 10$ mg m^{-3}) waters with large signals from both dissolved and NPP matter was more challenging than for the hypertrophic blooms (see below). Size was poorly retrieved with positive r values ≈ 0.3. A few reasonable comparisons were determined for the mesotrophic mixed assemblage in TW, which was a combination of large dino and intermediate cyano species, but there was a noticeable insensitivity to the larger assemblage size in LK waters which was generally underestimated by the algorithm. For oligotrophic waters, type was biased towards the cyano-dominant initial condition with typically $> 60\%$ cyano composition. This confirms the relative insensitivity for type detection in oligotrophic waters, since

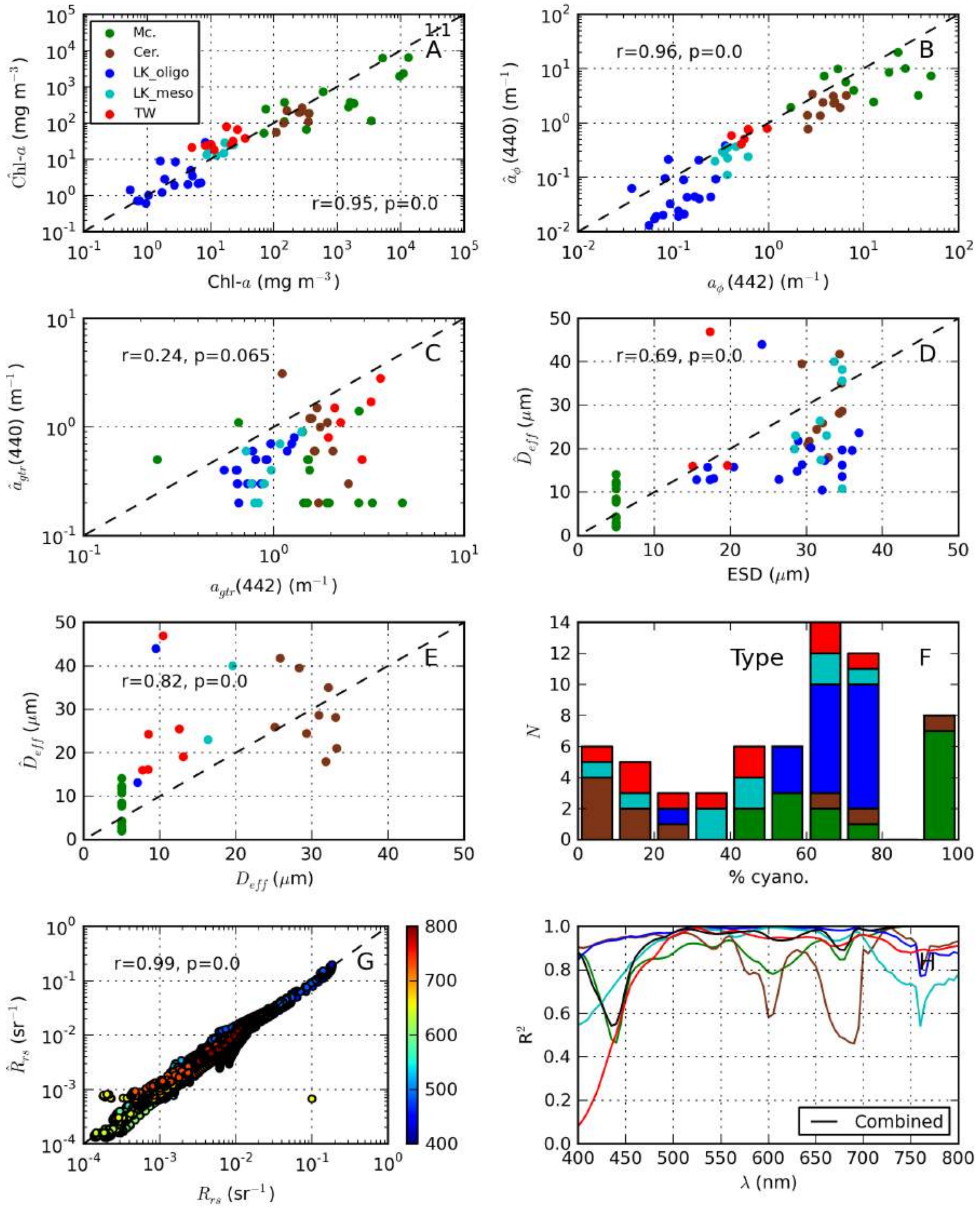

Figure 5.4.1: Measured versus modelled variables and retrieval of type and size for all water types. Estimated variables denoted ˆ are on the y axis. The 1:1 line is indicated by the dashed lines. Note log-log scales (A-C). Type is indicated in F by number of spectra (N) with a given cyano composition in %. R_{rs} is coloured by wavelength (nm) in G.

these waters were dominated at low biomass by dino/diatom assemblages. For each of the water types, the retrieval of chl-*a* and $a_\varphi(440)$ was performed satisfactorily with significant positive correlations with r values > 0.6 with some scatter around the 1:1 line. In general chl-*a* tended to be

Table 5.4.2: Spearman rank correlation coefficient (r) and number of samples (bracketed) for measured variables and those estimated using the inversion algorithm. Italics indicate correlations not significant at the 95% confidence interval. Note ESD and D_{eff} for HB were set to a constant assumed value of 5 μ m and therefore do not have a r value.

Water type/Reservoir	Chl-*a*	$a_{\varphi}(440)$	$a_{gtr}(440)$	ESD	D_{eff}	$R_{rs}(440)$
Combined	0.95 (56)	0.96 (59)	0.24 (59)	0.68 (55)	0.82 (34)	0.9 (63)
Mixed waters	0.88 (33)	0.87 (34)	0.74 (34)	*0.28 (30)*	*0.56 (10)*	0.81 (38)
Mixed meso/eutrophic	0.57 (14)	0.83 (12)	0.77 (12)	*0.32 (10)*	*0.37 (6)*	0.82 (16)
Mixed oligotrophic	0.77 (19)	0.67 (22)	0.73 (22)	*0.31 (20)*	*0.8 (4)*	0.70 (22)
Hypertrophic *Mc.* & *Cer.* blooms	0.69 (23)	0.81 (25)	*-0.27 (25)*	0.84 (25)	0.79 (24)	0.94 (25)
HB	0.77 (15)	0.71 (15)	*-0.38 (15)*	-	-	0.80 (15)
LK	0.93 (31)	0.91 (38)	0.55 (28)	0.32 (37)	*-0.15 (13)*	0.63 (38)
TW	0.73 (10)	*0.77 (6)*	*0.60 (6)*	*0.50 (3)*	*0.6 (6)*	*-0.05 (10)*

overestimated in mesotrophic waters, and $a_{\varphi}(440)$ tended to be underestimated in oligotrophic waters. This can relate to the determined assemblage composition which affects the magnitude of b_b through $b_{\varphi b}$, the latter which is typically larger for cyano dominated assemblages (see fig. 5.3.6). The improved sensitivity to and retrieval of $a_{gtr}(440)$ is apparent by r values > 0.7 (table 5.4.2). An explanation for the consistent underestimation of $a_{gtr}(440)$ is not clear. It may be related to the vertical structure of the IOPs, methodological errors in the determination of a_{gtr}, or other unknown sources. Nevertheless the significant positive correlation provides encouragement that $a_{gtr}(440)$ may be determined by inversion in mixed meso/oligotrophic waters. These findings confirm the hypothesis related to size and type detection, and that related to enhanced sensitivity to dissolved and tripton components, in mixed low biomass waters.

Selected examples illustrate the fits between the measured and modelled R_{rs} (fig. 5.4.2). The mineral rich waters in TW presented the most challenging case with poor agreement in the blue (fig. 5.4.2A). This effect, also visible in fig. 5.4.1G-H, could be related to optical variability of tripton particles or *gelbstoff*, or due to the assumed spectrally flat b_{bnpp} leading to generally underestimated NPP (back)scattering in the blue. This can also be used as an alternative explanation for the generally underestimated values for $a_{gtr}(440)$ for all waters. However a spectrally sloped b_{bnpp} interfered with type and size detection which was the primary aim of this study. Examples from mesotrophic and clear oligotrophic waters in LK showed a close match between measured and modelled R_{rs} (fig. 5.4.2B,C). For the clearest waters (chl-$a < 0.5$ mg m^{-3}) however, the algorithm struggled to reproduce the typical higher reflectance in the blue (fig. 5.4.2D), presumably as a result of underestimated non-phytoplankton (back)scattering.

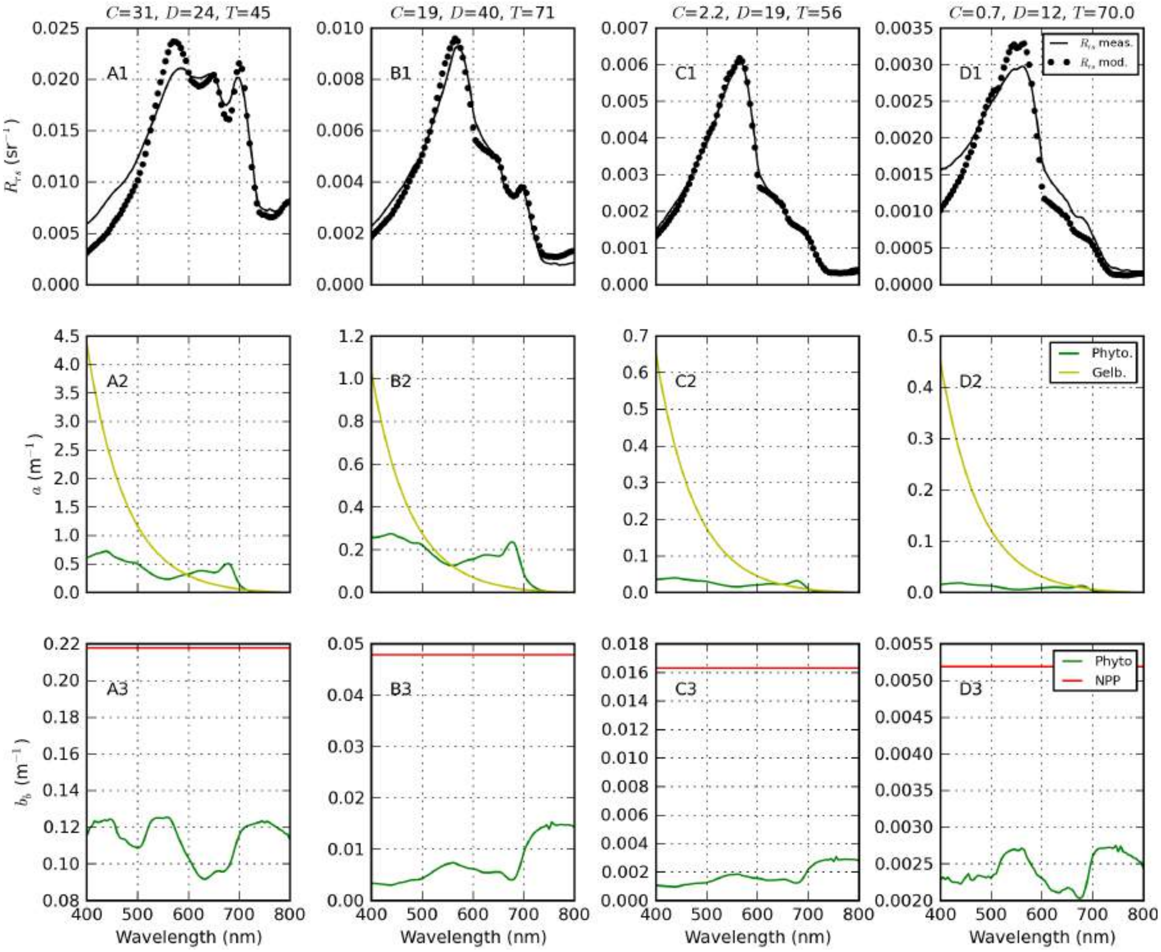

Figure 5.4.2: Examples of algorithm fitting in A) TW mixed, B) Loskop mesotrophic, and C-D) Loskop oligotrophic waters. Measured versus modelled R_{rs} are shown in the first row and a and b_b coefficients are in the second and third rows, respectively. The titles show the concentration of chl-a (mg m^{-3}), D_{eff} (μm), and type as % cyano estimated by the algorithm.

Hypertrophic waters: differentiating between cyanobacteria and dinoflagellates

Examples in fig. 5.4.3 show the measured and modelled R_{rs} and the IOPs determined by the algorithm in high biomass mono-specific blooms of *M. aeruginosa* and *C. hirundinella*. For most of the spectra, the algorithm closely matched the spectral features in the 500 to 650 nm range, thereby providing good separation of type between the blooms (see fig. 5.4.3A,B). This is reflected in fig. 5.4.1 which indicates the *C. hirundinella* bloom mode $>$ 80% dino composition, and the mode of the *M. aeruginosa* bloom spectra $>$ 90% cyano composition. Three of the *C. hirundinella* spectra were incorrectly determined as cyano-dominant resulting in poor spectral matching (example shown in fig. 5.4.3D). This affected the correlations in fig. 5.4.1H that illustrate the poor spectral matching in the 550 to 650 nm range for *Ceratium* dominant waters. Similarly the sensitivity for type detection for eight of the cyano-dominant spectra was relatively poor with values between 40 and 80% cyano composition. There was good distinction between the large and small celled populations (fig. 5.4.1D,E). Since size was not measured in the *M. aeruginosa* bloom, its value was estimated as 5 μm and was constant. This affected the r values for the hypertrophic waters which were 0.84 and 0.79 for ESD and D_{eff}, respectively. The population D_{eff} of the *C. hirundinella* bloom was determined as between 20 and 42 μm, close to its actual value from 25 to 35 μm. In general, the measured values for ESD were slightly higher than those measured for D_{eff}, which is expected since the Coulter Counter includes small particles. Similarly for the *M. aeruginosa* bloom, D_{eff} was determined as between 2 and 15 μm, which is close to its actual value.

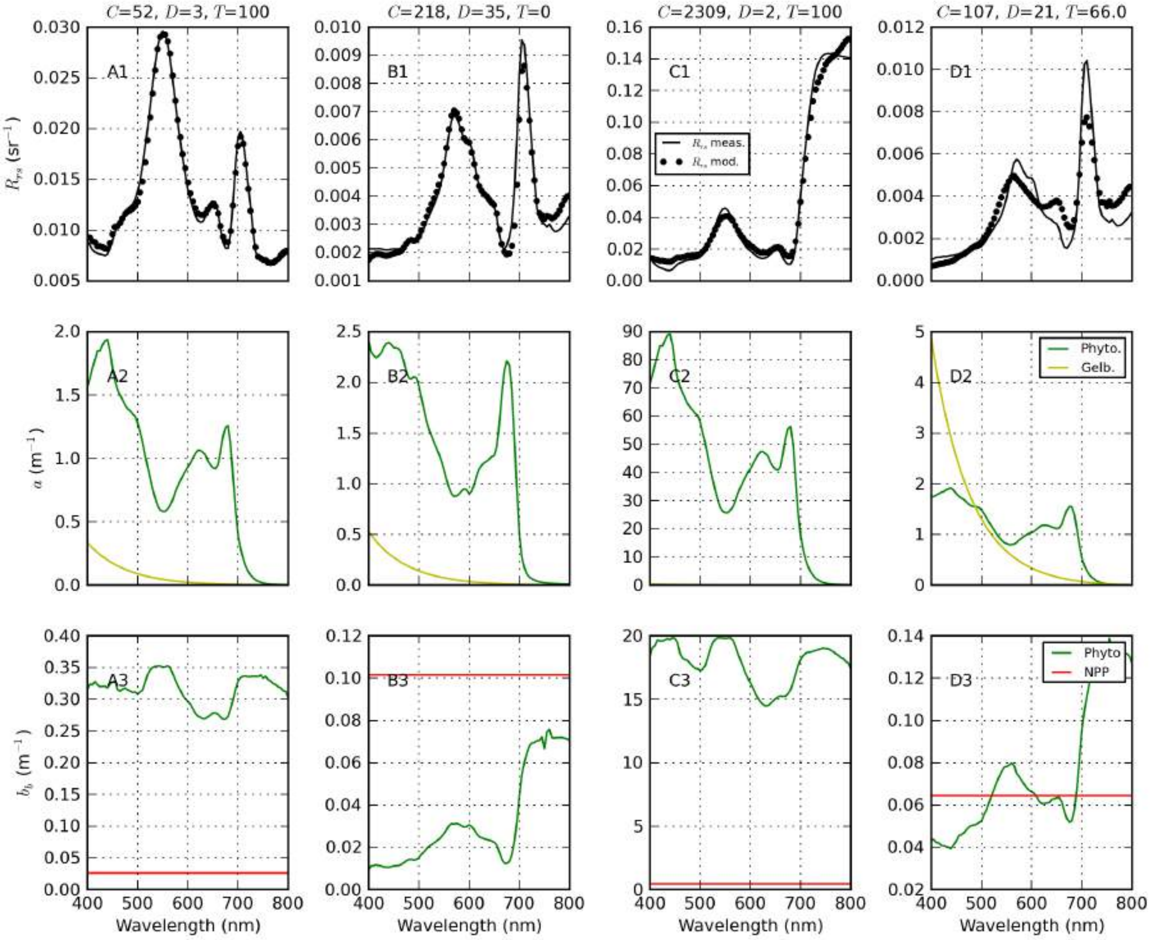

Figure 5.4.3: As for fig. 5.4.2 except for A) *M. aeruginosa* bloom in HB, B) *C. hirundinella* bloom in LK, C) *M. aeruginosa* surface scum in HB, and D) non-fitting example of *C. hirundinella* bloom in LK.

The retrieval of chl-*a* and $a_\varphi(440)$ was satisfactory with r > 0.7 considering the range of values over more than 3 orders of magnitude. The extremely high chl-*a* values in HB were measured in surface scum conditions. These were surprisingly resolved with closely matching R_{rs} spectra (see fig. 5.4.3C), although the values for chl-*a* and $a_\varphi(440)$ have substantially larger uncertainties. For the *C. hirundinella* blooms $a_\varphi(440)$ was generally underestimated relative to the measured values. The sensitivity to $a_{gtr}(440)$ in hypertrophic waters was poor, in agreement with previous discussion, with the measured values typically underestimated for HB. Overall the R_{rs} spectra were closely matched by the inversion scheme (fig. 5.4.1G,H). There was some wavelength dependence of the fitting, with poorer fits in the chl-*a* fluorescence band near 680 nm, in the region near 560 nm (associated with the position of the accessory pigment induced peak) and the peak near 440 nm. The poor fitting of the soret peak is possibly a result of negligible signal caused by high absorption by phytoplankton, detritus and dissolved matter. The blue region is therefore typically not easily resolved in highly scattering and absorbing waters which has important implications for remote sensing algorithm targeting this region.

In summary, the inversion experiment has tested both the sensitivity to type and size detection across water types and demonstrated the significant ambiguity of the inverse problem in mixed turbid waters. The results demonstrate that type and size detection is likely only feasible (using an unconstrained approach) in high biomass bloom scenarios, while the detection of dissolved and NPP absorption is likely only feasible in meso/oligotrophic waters. The solution was ambiguous with respect to phytoplankton type and size in many cases, leading in some cases to poor spectral fitting of R_{rs}. In contrast, is was found that biomass (chl-*a* and a_φ) could be retrieved with a good degree of confidence across all of the water types.

5.4.3 AN OPTIMISED INVERSION ALGORITHM FOR TYPE AND SIZE DETECTION

The above analysis has demonstrated the sensitivity and ambiguity of the inverse problem for type and size detection. The initial conditions were not adjusted according to the water type or known phytoplankton assemblage types or size. It is however feasible to select initial conditions that are specific for each spectrum, thereby potentially improving type (and size) detection. This is done by incorporating an empirical expression for cyano-dominance derived in Chapter 2 into the algorithm structure, providing an automated and improved initial guess for type (T). The cyano-flag is applicable only in waters where chl-*a* $>$ approx. 20 mg m^{-3} where the spectral features associated with phycocyanin pigment become clearly visible. Therefore, for spectra determined as medium-high biomass (chl-*a* $>$ 20 mg m^{-3}) using the empirical chl-*a* algorithm, the cyano-flag is used to detect the presence of cyano-dominant waters. If cyanobacteria is detected T is set to 90%, i.e. cyano-dominant; if not T is set to 10%, i.e. 90% dino-dominant. In all cases the flag correctly identified high biomass cyano-dominant waters in HB and TW, while those of LK were correctly identified as non-cyano dominant. This provides empirical evidence that the flagging procedure is robust for use with both water leaving reflectance and top-of-atmosphere type reflectance, as shown in Chapter 2. For medium-low biomass assemblages it is not feasible to determined cyano-dominance, therefore the assemblage is assumed to be mixed and T is set to 50%. The optimised algorithm function can therefore be described using the following logical statements:

- If chl $>$ 20 mg m^{-3} and cyanoflag = True, $T = 90\%$
- If chl $>$ 20 mg m^{-3} and cyanoflag = False, $T = 10\%$

- If chl < 20 mg m^{-3}, $T = 50\%$

The results of the algorithm with cyano-flagging are presented in fig. 5.4.4 and table 5.4.3 and can be compared with those of fig. 5.4.1. The spectral matching is evidently improved especially for the high biomass *C. hirundinella* blooms as a result of the more appropriate initial condition for type, as is visible in fig. 5.4.4H. This is reflected in slightly improved correlation coefficients for $R_{rs}(440)$. The pre-classification of type therefore reduces the ambiguity in the inverse problem, improving the algorithms ability to resolve diagnostic spectral features at various wavelengths. The type result for high biomass blooms are now correctly clustered towards the respective cyano and dino types (fig. 5.4.4F). For medium-low biomass LK waters, there is a bias towards dino-dominance which agrees with the assemblage species composition. The oligotrophic waters are clearly less sensitive to type with the majority near the initial value of 50%. The TW waters are more broadly spread with regards to type which reflects the mixed dino/cyano assemblage. The estimates of size as compared to ESD are improved with a higher correlation coefficient for the combined dataset of 0.8, and significant correlations for mixed waters (r=0.57) and even oligotrophic waters (r=0.65) (fig 5.4.4D,E, table 5.4.3). This reflects the sensitivity of the algorithm to the initial conditions as discussed in section 5.4.1. The ability to have various initial conditions through pre-classification of the spectra with respect to type and biomass therefore results in improved estimates of size. There are no significant differences in the estimates of chl-*a*, a_φ or a_{gtr} between the two algorithm versions.

Table 5.4.3: Correlation coefficients between measured and modelled variables using the type optimised inversion algorithm. See table 5.4.2 for details.

Water type/Reservoir	Chl-*a*	$a_\varphi(440)$	$a_{gtr}(440)$	ESD	D_{eff}	$R_{rs}(440)$
Combined	0.94 (56)	0.96 (59)	0.35 (59)	0.80 (55)	0.74 (34)	0.9 (63)
Mixed waters	0.85 (33)	0.89 (34)	0.73 (34)	0.57 (30)	*0.12 (10)*	0.83 (38)
Mixed meso/eutrophic	0.46 (14)	0.78 (12)	0.82 (12)	*0.55 (10)*	*-0.1 (6)*	0.85 (16)
Mixed oligotrophic	0.74 (19)	0.76 (22)	0.59 (22)	0.65 (20)	*0.6 (4)*	0.72 (22)
Hypertrophic *Mc.* & *Cer.* blooms	0.63 (23)	0.77 (25)	*0.17 (25)*	0.80 (25)	0.76 (24)	0.94 (25)
HB	0.73 (15)	0.66 (15)	*0.13 (15)*	-	-	0.81 (15)
LK	0.93 (31)	0.92 (38)	0.51 (28)	0.53 (37)	*-0.28 (13)*	0.64 (38)
TW	0.80 (10)	0.94 (6)	*0.41 (6)*	*0.50 (3)*	*0.43 (6)*	*0.05 (10)*

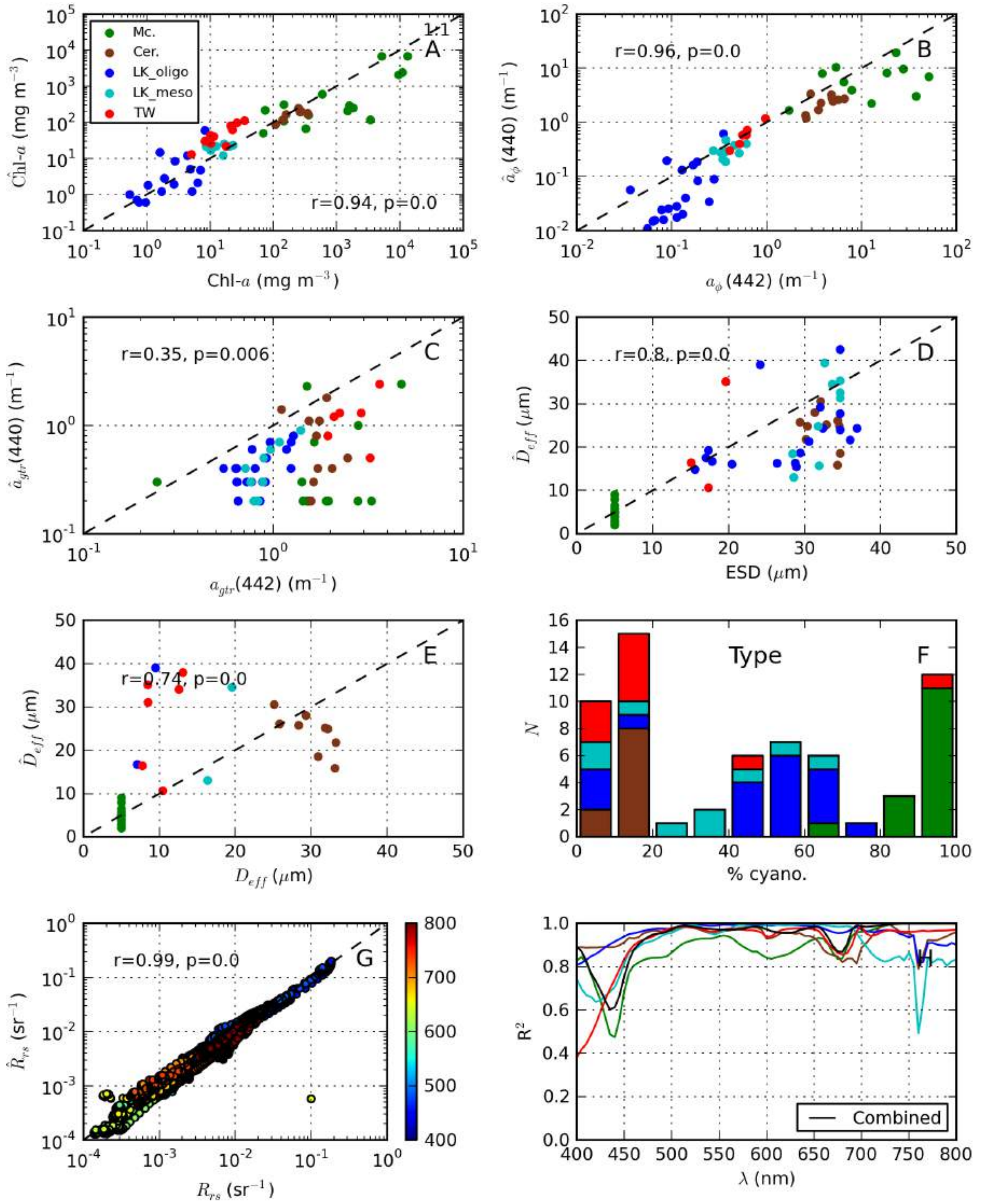

Figure 5.4.4: Measured versus modelled variables and retrieval of type and size for all water types. Estimated variables denoted ˆ are on the y axis. The 1:1 line is indicated by the dashed lines. Note log-log scales (A-C). Type is indicated in F by number of spectra (N) with a given cyano composition in %. R_{rs} is coloured by wavelength (nm) in G.

The retrieval of spectral a_φ allows for accessory pigment phycocyanin (PC) to be retrieved for cyano-dominant waters. $a_{pc}(620)$ was calculated as $a_\varphi(620) - 0.24 \times a_\varphi(665)$ after Simis et al. (2005). PC was then retrieved by $(a_{pc}(620)/0.0146)^{1.076}$ using the relationship determined in Chapter 3. The resulting PC concentrations were compared to those measured *in situ* (fig. 5.4.5). A statistically significant fit was determined for PC in both TW (r=0.94, n=5) and HB (r=0.59, n=15). Thus the retrieval of accessory pigments is achievable from the inversion scheme where the relationship between *a* and the pigment concentration is known. Importantly PC can only be accurately retrieved in high biomass cyano-dominant waters, and should not be preformed in lower biomass and mixed waters.

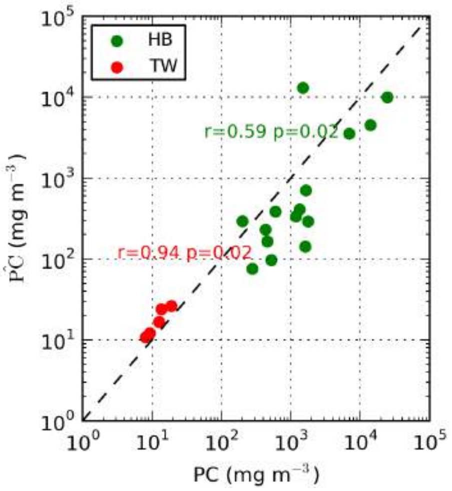

Figure 5.4.5: Measured versus modelled accessory pigment phycocyanin (PC) from the inversion algorithm.

5.5 CONCLUSION

The study has tested the feasibility for using a radiative transfer based inversion algorithm for differentiating between high biomass blooms of cyanobacteria and eukaryotic algae in hypertrophic inland waters. The results indicate that despite the considerable ambiguity of the inverse problem, and the considerable optical complexity of the waters under investigation, it is feasible to differentiate between blooms of small-celled *M. aeruginosa* cyanos from those of large celled *C. hirundinella* using an radiative transfer based inversion algorithm on the basis of unique spectral pigmentation and diagnostic phytoplankton absorption and (back)scattering. In this regard the phytoplankton assemblage size, parameterised in terms of D_{eff}, and the species percentage composition can be retrieved in hypertrophic waters with r approx. 0.8. In contrast, size and assemblage composition retrievals in mixed mesotrophic and oligotrophic waters with relatively large optical contributions from *gelbstoff* and tripton absorption was generally poor. In these cases, combined *gelbstoff* and tripton absorption was retrieved with higher certainty ($r > 0.7$), although was typically underestimated. The estimated chl-*a*, $a_\varphi(440)$ and cyanobacterial accessory pigment PC was highly correlated with measured values despite the exceptionally large value range for the waters investigated in this study. Therefore biomass estimates provided by the inversion algorithm are typically robust across water types with variable species composition. Optimisation of the initial conditions for type using a simple empirical flagging procedure improved type detection and optical closure of measured and modelled R_{rs}.

The study demonstrates one of the first uses of an inversion scheme using a coupled bio-optical model and RTM (see also (Rehm and Mobley, 2013)). This approach is likely to be used in future as computational abilities increase further for deriving IOPs directly from the R_{rs} in operational systems. The resolution of phytoplankton type and size from satellite-based multispectral sensors such as the Sentinel-3 Ocean and Land Colour Instrument (OLCI) and the Hyperspectral Imager for the Coastal Ocean (HICO) is likely to be achievable using the approach used in this study, which should be adapted for this purpose in future. However this is dependent on an atmospheric correction which provides accurate water leaving reflectance data which remains a challenge in optically-complex and turbid waters. The retrieval of various parameters can also likely be improved through a pre-classification of water types which select optimal initial conditions for use by the inversion algorithm. The algorithm structure can be used with alternative phytoplankton types (e.g. diatoms or chlorophytes) and ranges of constituents to enable more general application in coastal and inland waters.

6

Eutrophication, cyanobacterial blooms and surface scum in South African reservoirs: 10 years of MERIS observations

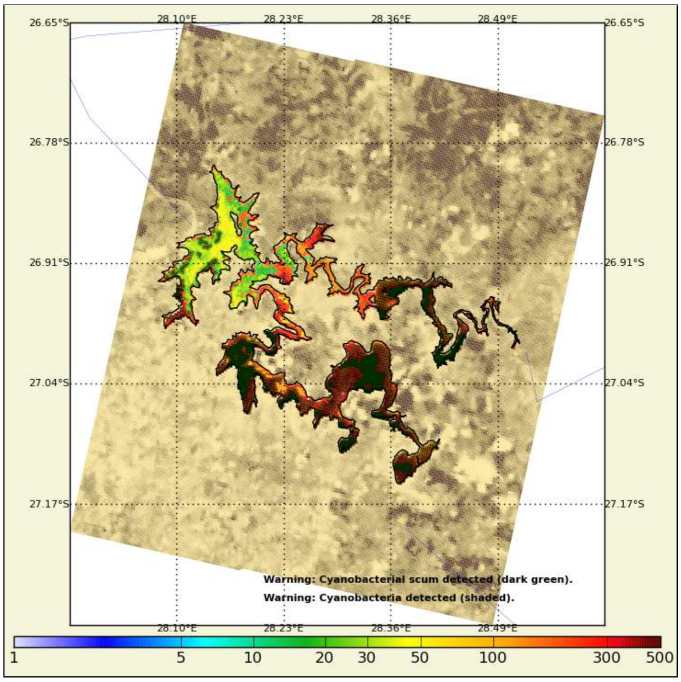

The MPH chlorophyll-a product for South Africa's second largest water supply reservoir, the Vaal Dam, on 20th March 2012 just days before MERIS stopped acquiring imagery.

Abstract

The medium resolution imaging spectrometer full resolution (MERIS FR) archive (2002 to 2012) over South Africa has been processed with the maximum peak height (MPH) algorithm for the 50 largest reservoirs in South Africa. The status, seasonality and trends of chlorophyll *a* (chl-*a*), cyanobacteria and surface scum area coverage are established for each of the reservoirs. The majority (60%) of the 50 reservoirs were hypertrophic (mean chlorophyll $a > 30$ mg m^{-3}), while 23 reservoirs had intermediate to extensive cyanobacteria coverage. Surface scum events occurred in at least 33 of the reservoirs, with intermediate to extensive coverage in seven of the reservoirs. Significant trends showed that reservoirs have both worsened and improved with regards to eutrophication, cyanobacteria and surface scum coverage between 2005 and 2012. A winter maximum in cyanobacteria coverage was observed against expectations for some of the reservoirs. An independent validation of the MPH algorithm demonstrates that gross trophic status can be determined with a high degree of confidence in both eukaryote and cyanobacteria waters ($r = 0.8$). However, chl-*a* estimation in oligo/mesotrophic waters remains challenging due to a wide range of potential sources of error. Cyanobacteria and surface scum identification is performed with a high degree of confidence as illustrated through selected case studies. The study is the first of its kind providing quantitative biogeochemical and phytoplankton species information in lakes from a time series of satellite remotely sensed data on a sub-continental scale, demonstrating how global analyses of biogeochemical properties in lakes might be performed in future. The study demonstrates the pivotal role that satellite remote sensing can play in supplementing *in situ* monitoring efforts, particularly in the developing world, and in contributing towards a better understanding of lakes in the earth's biogeochemical cycle.

6.1 INTRODUCTION

GLOBALLY, LAKES PLAY AN IMPORTANT ROLE in regulating earth's climate, acting as sentinels and regulators of climate change (Williamson et al., 2009), as well as being a crucial life-giving resource for humanity. Global observations of lakes using satellite remote sensing has rapidly progressed in the last two decades with global time series observations of surface water level (Crétaux et al., 2011) and wetland inundation having been obtained (Prigent et al., 2007). However, there exists a paucity of information regarding biogeochemical water quality information on a global scale for lakes, which constitutes a significant gap in understanding of the role of lakes in earth's biogeochemical cycle (nutrients and carbon) and their response to global change. Phytoplankton are an ideal indicator of responses to changes in biogeochemistry in lakes, with chl-*a* and cyanobacterial biomass estimates being robust measures of ecological integrity (Carvalho et al., 2012). Anthropogenic changes in nutrient cycles, hydrology and climate have led to an increased incidence of cyanobacterial algal blooms globally (Michalak et al., 2013, Paerl and Huisman, 2009). However currently there exists no analysis concerning the possible extent and magnitude of these changes on phytoplankton biomass (chl-*a*) and cyanobacterial blooms on global or continental scales.

Satellite remote sensing of biogeochemical parameters in water has been extensively applied to inland waters (for detailed reviews of studies and methods see Matthews, 2011, Odermatt et al., 2012). Time series observations of parameters related to phytoplankton and water clarity derived from various satellite instruments exist for several lakes (e.g. Hu et al., 2010b, Olmanson et al., 2008, Stumpf et al., 2012). However, these and other existing studies do not provide quantitative chl-*a* estimates, nor do they cover a large number of lakes on a sub-continental scale. Therefore their usefulness in contributing to global biogeochemical models is severely limited. Global, continuous estimates of biogeochemical parameters in lakes from satellite have been hindered by the absence of suitable products (i.e. algorithms) and by the lack of continuous satellite missions with the required spatial, spectral, temporal and radiometric resolutions. Recent South African studies demonstrate the medium resolution imaging spectrometer (MERIS) as the optimal past sensor for providing detailed water quality information products owing to its spectral, temporal, radiometric and spatial resolution (Matthews et al., 2012, 2010). Briefly, MERIS has a spatial resolution of 260 by 290 m depending on the altitude, an acquisition frequency of 2 to 3 days, and 15 spectral bands ideally positioned for water related applications. These sensor specifications allow for sufficient observational frequency and sensitivity to enable viable change detection on an approximately weekly time-scale, not offered by the many currently available high spatial resolution visible radiometers (e.g. Landsat or SPOT). Therefore, MERIS provided a unique opportunity for observing lakes on a global scale and high frequency, unparalleled by current *in situ* monitoring capabilities which may also be hindered by high costs or lack of capacity.

The maximum peak height (MPH) algorithm designed for operational use with MERIS is unique in that it provides quantitative chl-*a* estimates for cyanobacteria and eukaryote dominant waters, and robust cyanobacteria and surface scum detection, while also being applicable to various waters (see Chapter 2). The MPH also avoids error prone atmospheric correction schemes required for the use of most other products through utilising the signal at the top of atmosphere. The MPH can currently only be applied with the MERIS sensor or hyperspectral instruments, since other operational satellite-based instruments lack sufficient spectral resolution (including the moderate resolution imaging spectrometer or MODIS). However, its applicability to the forthcoming ESA Sentinel Ocean and Land Colour Instrument (OLCI) instrument should provide good product continuation for at least a further decade. This study presents results from the MPH algorithm applied to the full time series of MERIS observations (2002 to 2012) for the 50 largest South African inland water bodies. The study is unique with respect to both the quantitative time series products and its application to water bodies on a national/sub-continental scale (South Africa). This study is the first of its kind in aiming to provide quantitative biogeochemical products for a large number of lakes on a sub-continental scale from the MERIS full archive.

A great deal of information has been published on the occurrence and distribution of eutrophication and cyanobacteria in South African reservoirs (e.g. Harding and Paxton, 2001, Oberholster and Ashton, 2008, Oberholster et al., 2005, van Ginkel, 2012, 2011, van Ginkel et al., 2000). This includes recent reviews on eutrophication research (van Ginkel, 2012, 2011). In particular, monitoring efforts have been driven by the national eutrophication management plan (NEMP) by the Department of Water Affairs (DWA) (van Ginkel et al., 2000). The studies indicate that eutrophication and cyanobacterial blooms are widespread and extensive in South African reservoirs, and poisonings of domestic and wild animals by cyanobacterial toxins are a frequent occurrence (Oberholster et al., 2005, 2009). However, these studies are based on *in situ* point-based samples which are limited both spatially and temporally. Therefore, despite the great monitoring efforts, there remains much uncertainty regarding the overall status of eutrophication and cyanobacterial blooms in South African reservoirs both from a temporal and spatial perspective. This is exacerbated by the very large number of manmade impoundments (497 reservoirs with capacity larger than one million cubic meters) as a result of the aridity of the region and relative scarcity of water in South Africa, and almost complete absence of large natural lakes (Oberholster and Ashton, 2008).

Furthermore, for most South African reservoirs the phenology, seasonal variability and trends of production and phytoplankton species composition remain largely uncharacterised. The degree to which the occurrence of problem eukaryote species, for example the dinoflagellate *Ceratium hirundinella*, is increasing is also largely unknown (Hart and Wragg, 2009, Van Der Walt, 2011, van Ginkel et al., 2001). Information on the severity and occurrence of cyanobacterial scums (or mats) is also absent for South African reservoirs. Surface scums have significant negative ecological consequences on the diversity and functioning of the plankton community and higher order organisms, and associated toxin production is a health threat for potable and recreational water use (Chorus et al., 2000, Oberholster et al., 2009). Thus the lack of information on their occurrence and extent in South African reservoirs constitutes a risk to public health. Cyanobacterial surface scums also serve as an important ecological indicator of over-enrichment and meteorological warming and senescence (Michalak et al., 2013, Paerl and Huisman, 2009). Therefore, surface scum occurrence is likely to be a good indicator of regions subject to severe eutrophication or potential climate warming.

This paper aims to characterise phenological changes in eutrophication, cyanobacteria and surface scum in South African reservoirs using 10 years of data from the MERIS archive. The status, seasonality, and trends for each of the variables are determined for the reservoirs. In addition, the study seeks to validate the chl-*a* estimates from the MPH algorithm using an independently acquired *in situ* dataset. Case studies are used to demonstrate eukaryotic and cyanobacteria bloom detection, and surface scum mapping using the MPH algorithm. The provision of a satellite based dataset supplementing *in situ* monitoring data seeks to fill an information gap in the limnology of South African inland waters, as well as provide input into biogeochemical ecosystem models and regional climate change studies incorporating lakes, and to models predicting phytoplankton biomass and surface scum formation from meteorological and hydrological variables (e.g. Soranno, 1997).

6.2 METHODS

6.2.1 RESERVOIR SELECTION

The 50 largest reservoirs in South Africa by surface area were selected for the analysis (see table 6.3.1 for surface area and coordinates). The surface area of the reservoirs was obtained from high resolution shapefiles (RQS, 2004). Seasonal pans, estuaries and water bodies subject to tidal influence were not included. Weekly water level data available for most of the reservoirs between 2002 and 2012 was used to identify low-water periods (DWA, 2013a). Reservoirs with extended low-water (drought) periods or which were too narrow to be viewed without significant adjacency effects ($<$ 600 m wide) were excluded.

6.2.2 MPH ALGORITHM

The MPH algorithm was used to compute the concentration of surface chl-*a* as well as identify cyanobacteria-dominated water and surface scum conditions in the reservoirs (for detailed description see Chapter 2). The algorithm's main advantages are its ability to operate over a wide trophic range from oligotrophic to hypertrophic conditions and, its unique ability to distinguish between cyanobacteria-dominant and eukaryotic-dominant phytoplankton blooms. Derived using a match-up dataset of MERIS data and chl-*a* measured *in situ* from three South African inland waters and the Benguela marine system, it has an operating range of at least between 0.5 and 400 mg chl-*a* m^{-3}. Its limit of detection is less than 3.5 mg chl-*a* m^{-3}. The algorithm is based on the MERIS red/near infra-red bands between 664 and 850 nm taking advantage of the sun-induced chl-*a* fluorescence produced by algae near 685 nm and the particulate backscatter-induced peak near 710 nm visible in high biomass blooms (chl-*a* $>$ approx. 20 mg m^{-3}). Designed for implementation as an operational algorithm, its usage here is intended to 1) identify the trophic status of the water bodies through chl-*a* estimates, 2) identify cyanobacteria blooms and 3) identify cyanobacterial surface scum conditions (defined here as chl-*a* $>$ 500 mg m^{-3}). The MPH algorithm has the advantage of being easily implemented and is suitable for processing very large amounts of data. Chl-*a* estimates were limited to 1000 mg m^{-3} within an acceptable confidence range of the algorithm.

6.2.3 MERIS FR DATA PROCESSING

Archived MERIS full resolution (FR) level 1P data were obtained over South Africa between the years 2002 and 2012. The files contain 15 bands with uncorrected top-of-atmosphere (TOA) radiances. MERIS data were processed using open source processing tools in a Linux environment using Python programming language (V. 2.7.1). A schematic of the data processing chain is shown in figure 6.2.1. The accurate MERIS ortho-rectified geo-location operational software (AMORGOS, ACRI-ST) was used to ortho-rectify the data. AMORGOS provides accurate geo-location for MERIS imagery to within one pixel accuracy (<300 m) which is essential for extracting small targets such as the reservoirs in this study. The inputs are the MERIS FR files and the auxiliary orbit files corresponding to the specific scene (downloaded from ESA). AMORGOS uses a digital elevation model (DEM) to compute the latitude and longitude of a pixels first line of sight and intersection with the earth's surface. The outputs are geo-corrected latitude and longitude bands for the scene written into a new product file. Importantly, the data are not altered by the geo-correction process. A few scenes produced geo-location errors and therefore had to be removed manually after visual inspection of the data.

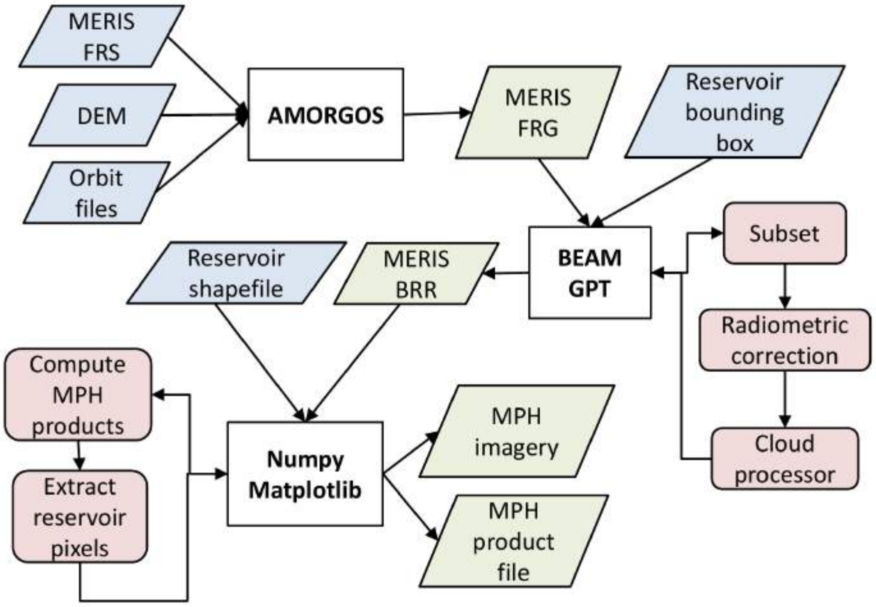

Figure 6.2.1: Schematic processing chain for MERIS data. Inputs are shaded in blue, outputs in green and processes in red. See text for details.

The files were processed after ortho-correction using the Basic ENVISAT Toolbox for (A)ATSR and MERIS (BEAM) V. 4.9.0.1. Within the graph processing framework in BEAM the files were subsetted according to a bounding box for each of the reservoirs, corrected for radiometric effects using the Radiometry Processor V. 1.0.1 (Bouvet and Ramoino, 2009), and corrected for gaseous absorption using the bottom-of-Rayleigh reflectance (BRR) processor V. 2.3 (ACRI, 2006, Santer et al., 1999) (see Chapter 2 for further details). The output is a subsetted BRR product for each reservoir in the scene. Clouds were detected using the Cloud Processor V. 1.5.203 (© ESA, FUB, and Brockmann Consult, 2004). The MERIS BRR subset files were then used to compute the MPH products using Numpy (V.1.5.1) in Python. The output products for each reservoir were plotted using matplotlib tools (V.1.0.1) and saved to a hierarchical data format (HDF) file for further processing.

Distinguishing between land and water pixels is challenging in hypertrophic conditions (Matthews et al., 2010) and in South African reservoirs with water levels that typically fluctuate widely both seasonally and with droughts. Conventional methods used to distinguish between land and water, such as empirically-based land-water separation algorithms, often fail due to the high reflectance values associated with cyanobacterial blooms and surface scums. Incorrect classification of land pixels as water will lead to erroneous results. In order to overcome these difficulties, water pixels were extracted using shapefiles drawn for each of the reservoirs from high resolution (30 m) archived Landsat data. Low water periods were identified with weekly water level data (DWA, 2013a). Shapefiles for the minimum and maximum water extents between 2002 and 2012 were drawn for each reservoir. In certain cases several shapefiles were needed due to fluctuating water levels. The shapefiles were then used to extract water pixels for each of the reservoirs from the MERIS data (see fig. 6.2.2). Where water level data were not available (only 5 natural lakes) the minimum water extent was determined by examining archived Landsat data between 2002 and 2012. This rigorous procedure ensured that land pixels were not included as water and that water pixels are not incorrectly classified as land.

6.2.4 TIME SERIES METHODS

Time series products for chl-*a* were computed for each of the water bodies. The lake-average chl-*a* value was determined for each image using the median chl-*a* value of all water pixels. The median was chosen as it is less sensitive to outliers than the arithmetic mean. Images in which $< 10\%$ of the lake area was visible due to cloud and/or position of the image swath were removed. The lake averaged chl-*a* value for each scene was used in subsequent time series analyses. The seasonal cycle for each water body was computed on a monthly basis using the mean of all observations acquired during that month for the entire time series (2002 to 2012). The phase, φ, and amplitude, A, of the seasonal cycle was determined for each of the lakes as the month with greatest chl-*a* value, and the difference between the months with the smallest and largest chl-*a* values, respectively. The seasonal anomalies in chl-*a*, denoted chl-a', were computed by subtracting monthly averages from the observations in that month. The trend of the seasonal anomalies was computed using linear regression analysis according to $y(t) = at + b$; the regression coefficient a was determined as the linear trend with respect to time t. The statistical significance of linear regressions was computed using the student-t test statistic according to:

$$t_r = \frac{r\sqrt{N-2}}{1-r^2}$$

where r, the correlation coefficient, is computed as:

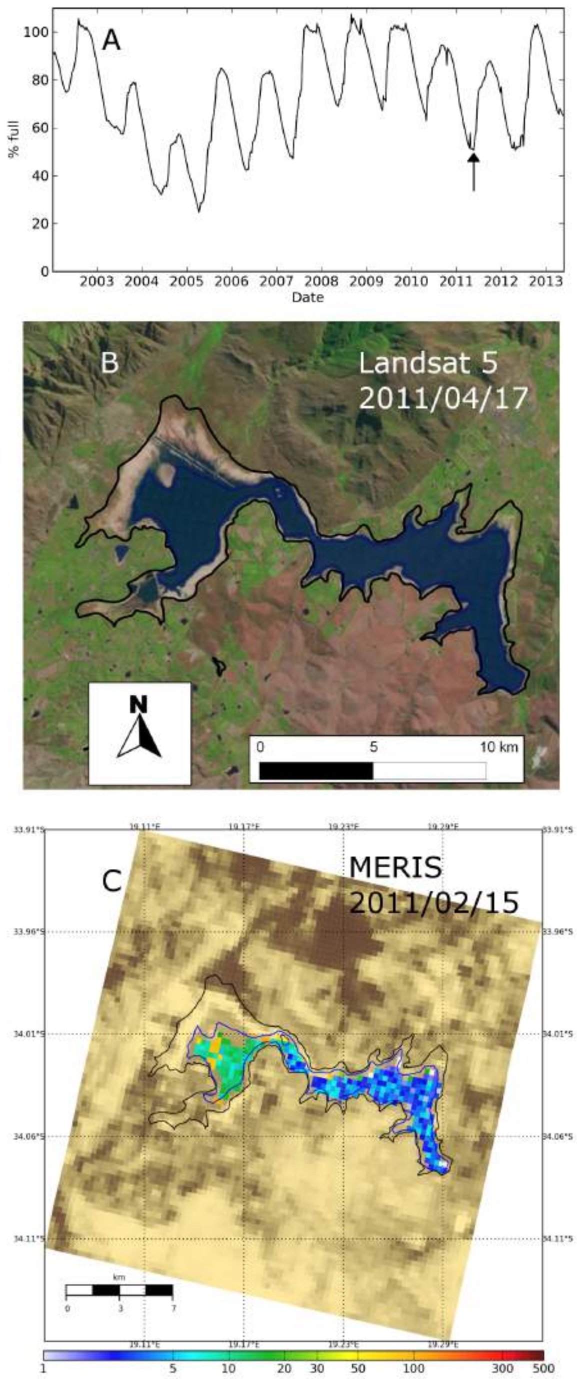

Figure 6.2.2: Example of extraction of water pixels using shapefiles for Theewaterskloof. A) Water level for Theewaterskloof between 2002 and 2012 in percent. B) High resolution Landsat RGB used to trace the low water shapefile (blue) and showing full water extent shapefile (black). The arrow in A shows the date at which the image was acquired. C) MERIS chl-a image showing extracted water pixels (colored). Units is mg m^{-3}.

$$r = \frac{1}{N-1} \sum_{t=1}^{N} \frac{x(t) - \bar{x}}{\sigma_x} \times \frac{t - \bar{t}}{\sigma_t}$$

where N is the number of observations, x is the variable of interest, t is time, and σ is the standard deviation.

Yearly chl-*a* averages were computed by calculating the mean of all observations within a given year. The trend of the yearly averages was computed using linear regression analysis as for the seasonal anomalies. Calculation of trends was limited to between 2005 and 2011 due to some missing data between 2002 and 2004 and excluding incomplete years, e.g. 2012. The mean value of all chl-*a* observations for the entire time series was used to determine the overall trophic state of the reservoir. Trophic status was defined using the Organisation for Economic Co-operation and Development chl-*a* thresholds applicable to inland waters: oligotrophic, 0 to 10 mg m^{-3}; mesotrophic, 10 to 20 mg m^{-3}; eutrophic, 20 to 30 mg m^{-3}; hypertrophic $>$ 30 mg m^{-3}. The water bodies were grouped according to the overall trophic status for comparison of the seasonal cycle.

The area coverage of cyanobacteria, A_{cy}, and surface scum, A_{sc}, in percent were computed as the number of pixels identified as cyanobacteria or surface scum normalised by the number of water pixels visible in the image. Surface scum is defined as pixels which are identified as cyanobacteria and have chl-*a* $>$ 500 mg m^{-3}. The overall mean area coverage in percent for cyanobacteria and surface scum were computed for the entire time series for each reservoir. The seasonality of cyanobacteria and surface scum area coverage was determined using monthly means, as for chl-*a*, and the phase (or timing) determined as the month with the greatest coverage. The trend of cyanobacteria and surface scum area coverage was determined, when appropriate, using the annual means between 2005 and 2011 as for chl-*a*.

6.2.5 In situ validation

Validation of the results obtained from the 50 reservoirs can be performed using case studies where sufficient data are available. A great deal of *in situ* chl-*a* data has been collected for South African reservoirs by the DWA through programs such as the NEMP (DWA, 2013b). The data exists as discreet-point samples collected most often near the reservoir wall but not from a single precise location (pers. comm. Michael Silberbauer, 2013). Thus samples are not necessarily representative of the reservoir surface. These data might be used to independently validate the MPH algorithm and provide error estimates for the satellite chl-*a* estimates. However, a direct comparison between such point data and the satellite derived lake median is complicated by the horizontal inhomogeneity of phytoplankton distribution within the reservoir. Reservoirs with strong trophic gradients, such as Loskop (Matthews and Bernard, 2013a), will lead to downward bias of *in situ* measurements compared to the true lake average. In contrast the integrated remote sensing measurement eliminates bias incurred by spatially limited point-based sampling. Therefore, a comparison of point-based measurements and integrated remotely sensed averages is sub-optimal.

Therefore, a matchup analysis was performed for each reservoir. The mean value for pixels contained in a small area (+- 10 pixels = 1km^2) corresponding to the approximate location of the *in situ* sample point was extracted from the time series of satellite data. The 'point-based' time series of satellite estimates was then compared to the time series of *in situ* data for date matches. The resulting matchups (same date) were compared using linear regression analysis. Reservoirs with very few matchups and poor correlations due to a mismatch between the location of the point and satellite observations were then excluded. Sufficiently good matchups were obtained for the following reservoirs: Albert Falls, Bronkhorstspruit, Hartbeespoort, Klipvoor, Midmar, Inanda and Vaalkop. The overall algorithm performance was evaluated for the combined matchup dataset, as well as for waters identified as cyanobacteria or eukaryote dominant. The comparison was limited to ch-*a* $< 350\,\mathrm{mg\,m^{-3}}$ because of the very high spatial patchiness associated with surface scums and extremely high biomass blooms. Five outliers were removed from the matchup dataset to improve the correlations. The goodness of fit was determined using the root mean square error (RMSE) which was calculated as:

$$\mathrm{RMSE} = \left(\frac{\sum(\text{chl-}a_{satellite} - \text{chl-}a_{insitu})^2}{N-2} \right)^{1/2}$$

The bias (average residual) was calculated as:

$$\mathrm{Bias} = \frac{\sum(\text{chl-}a_{satellite} - \text{chl-}a_{insitu})}{N}$$

The mean absolute percentage error (mape) was calculated by:

$$\mathrm{mape} = \frac{\sum((\text{chl-}a_{satellite} - \text{chl-}a_{insitu})/\text{chl-}a_{insitu})}{N}$$

where N is the number of observations.

6.2.6 ERROR ESTIMATES AND UNCERTAINTIES

Both *in situ* and satellite derived chl-*a* estimates are subject to uncertainties from a variety of sources. These include systematic and methodological errors, as well as those resulting from horizontal and vertical inhomogeneity in the water constituents distributions. The discreet-point sample error (Matthews et al., 2012) for *in situ* measurements results in large errors that increase with trophic state due to inhomogeneity in the horizontal and vertical distribution of phytoplankton. The discreet-point sampling error is particularly large for reservoirs with strong trophic gradients, which usually become clearer towards the reservoir wall: samples collected near the reservoir wall neglect the productivity occurring throughout the reservoir (e.g. methods in van Ginkel et al., 2000). It is expected that this error alone may result in large discrepancies between satellite and *in situ* estimates. The combined error from methodological and discreet-point sampling for spectrophotometrically determined chl-*a* typically range between 20 and 30% in South African inland waters (Matthews et al., 2012).

In contrast, the advantage of remote sensing is in its ability to provide a horizontally integrated surface estimate, while the vertical profile is not accounted for. Thus an integrated remote sensing estimate using the mean or median value for the visible lake surface provides a more holistic trophic estimate for the reservoir. The uncertainty in chl-*a* estimated using the MPH algorithm is 60% for eukaryote- and 30% for cyanobacteria-dominant waters with a range of 0.5 to 350 mg m^{-3} for data used to derive the algorithm (Matthews et al., 2012). In clear waters with chl-*a* = 1 mg m^{-3}, this equates to an associated uncertainty of ± 0.6 mg m^{-3}, while in highly turbid, cyanobacteria-dominant water, the error estimate for chl-*a* = 300 mg m^{-3} will be ± 90 mg m^{-3}. Thus the uncertainty from the MPH algorithm is only slightly higher than that for *in situ* measurements, with uncertainties for chl-*a* estimates $<$ approx. 5 mg m^{-3} becoming larger.

Satellite estimates are also prone to additional sources of error affecting individual pixels, such as bottom/shoreline effects (shallow clear water where the bottom is visible), contamination by atmospheric aerosols (such as smoke) leading to erroneous spectral shapes and resultant product estimates, cloud effects resulting from cloud shadows, fog and mist, and geo-location errors resulting in incorrect classification of land and water pixels. Contamination by these sources of error has been reduced by extracting water pixels away from the shoreline using shapefiles, by using cloud and aerosol flagging in data processing (already described), and by rigorous examination of the products for geo-location errors. Furthermore, MERIS scenes in which more than 30% of the scene was cloudy and in which $<$ 5% of the lake surface area was visible were not included in the time-series analysis. Therefore, it is likely that errors resulting from these sources have a small, or negligible effect on the results.

Therefore the satellite estimates can be expected to contain only slightly more uncertainty than *in situ* estimates. The satellite estimates are at least satisfactory for gross trophic status classification and cyanobacteria detection (Matthews et al., 2012). Ideally, the satellite estimates should be validated on a lake-by lake basis taking into account differences in the specific optical properties. However, such a validation is not feasible when considering the number of reservoirs examined in this study, or for large scale applications. Therefore, validation is performed only for selected reservoirs where sufficient data are available (section 6.3.5).

6.3 RESULTS AND DISCUSSION

6.3.1 TIME SERIES OF CHL-*a*, CYANOBACTERIA AND SURFACE SCUMS

Fig. 6.3.1 gives examples of the time series products derived from three reservoirs covering the diverse range of water conditions encountered in South African reservoirs. Each of these reservoirs represent different trophic states and algal blooms types. Hartbeespoort dam is representative of a hypertrophic system dominanted by frequent and persistent *Microcystis aeruginosa* cyanobacteria blooms and surface scum conditions. Loskop is a meso/eutrophic reservoir typically dominated by dinoflagellate *Ceratium hirundinella* blooms with occasional cyanobacteria blooms which occur seasonally and periodically (Oberholster et al., 2010). Sterkfontein is a high-altitude oligotrophic reservoir with seasonally timed increases in chl-*a* from low-biomass cyanobacterial blooms in the summer (van Ginkel et al., 2000). The time series products $\bar{chl}$, cyanobacteria and surface scum coverage, are a result of a large number of MERIS scenes: 775 for Hartbeespoort, 863 for Loskop and 566 for Sterkfontein. This equates to between approx. 90 to 60 scenes a year, or 4 to 8 scenes per month with less than 30% cloud cover. This observation frequency is suitable for drawing conclusions on a monthly or biweekly time-scale, and is therefore suitable for capturing the seasonal (monthly) phenology of bloom initiation and shorter bloom events occurring on the scale of weeks to months.

The results in fig. 6.3.1 demonstrate the interoperability of the MPH algorithm and remote sensing approach to reservoirs with known water types and trophic ranges. Presentation of the entire time series for each of the 50 reservoirs is not practical. However section 6.4 presents case studies from representative reservoirs where sufficient data are available to verify bloom events, types and duration, as well as surface scum occurrence. Further validation is difficult to perform since no *in situ* datasets are available with the time range, frequency and areal coverage comparable to those presented here. It may be feasible however to verify whether the satellite-based estimates are consistent with the range (rather than mean) of *in situ* chl-*a* measurements, and with data on cyanobacteria occurrence.

Examples showing the monthly seasonal cycle for chl-*a*, the associated anomalies (chl-a'), yearly averages, and the trends for the anomalies and yearly averages, are shown in fig. 6.3.2. These quantities are discussed with reference to all 50 reservoirs in the following section. The seasonal cycles for each of the reservoirs have different shapes, but are consistent in that they have an expected summer chl-*a* maximum. The greatest anomalies are typically observed during the peak bloom period in the summer months. Anomalous bloom events are also apparent (see Hartbeespoort 2003, Loskop 2007/2008 in fig. 6.3.2). The trends of the yearly averages and anomalies are also generally consistent, with Hartbeespoort having the largest positive trend between 8 and 10 mg chl-*a* year^{-1}. The magnitude and significance of the trends for all 50 reservoirs is discussed in the following section.

6.3.2 STATUS, SEASONALITY AND TRENDS OF EUTROPHICATION (CHL-*a*)

The findings of the analysis from 10 years of observations from the MERIS archive are presented in summarised form in table 6.3.1. The table contains the names, surface areas and geographical location of each of the reservoirs. The number of MERIS scenes with less than 30% cloud cover and in which more than 5% of the lake area is visible is indicated by N. These values are dictated by the coverage of the MERIS archive, which is severely biased towards the north eastern part of South Africa, resulting in far fewer observations for lakes in the south and south west. The mean values for chl-*a* ($\bar{chl}$), cyanobacteria ($\bar{A}_{cy}$) and surface scum ($\bar{A}_{sc}$) coverage estimated by the MPH algorithm are indicated along with the amplitude (A) and phase (φ) (timing) indicated by abbrevi-

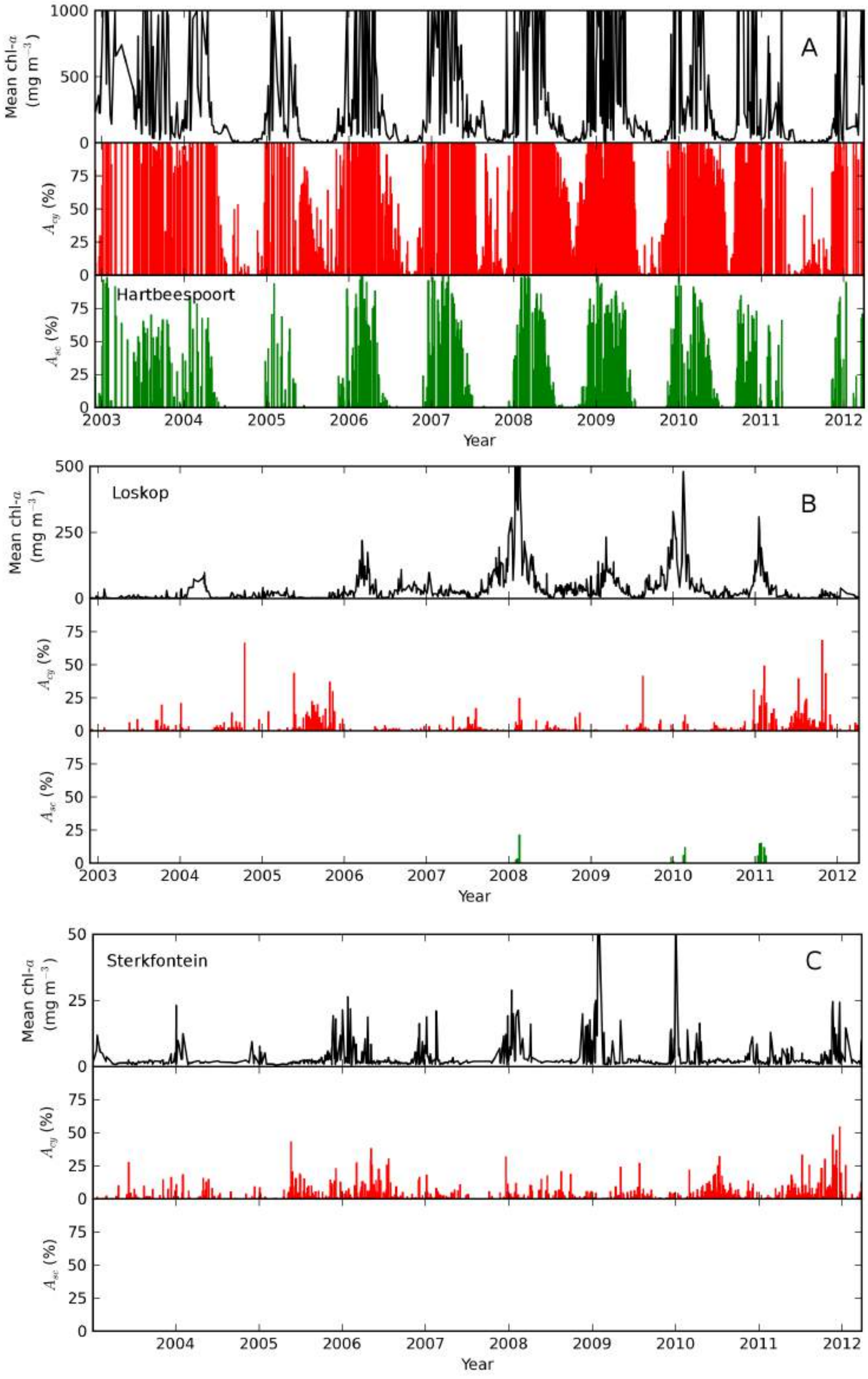

Figure 6.3.1: Timeseries for $\bar{\mathrm{chl}}$ and area coverage for cyanobacteria and surface scum for A) Hartbeespoort, B) Loskop and C) Sterkfontein. Note differences in scales for $\bar{\mathrm{chl}}$ and for years between the plots.

ated month of the year. The trends for both the yearly averages (a_{chl}) and the anomalies ($a_{\mathrm{chl}'}$) for chl-*a* are indicated as well as for cyanobacteria ($a_{A_{cy}}$) and surface scum ($a_{A_{sc}}$) area coverage (when applicable).

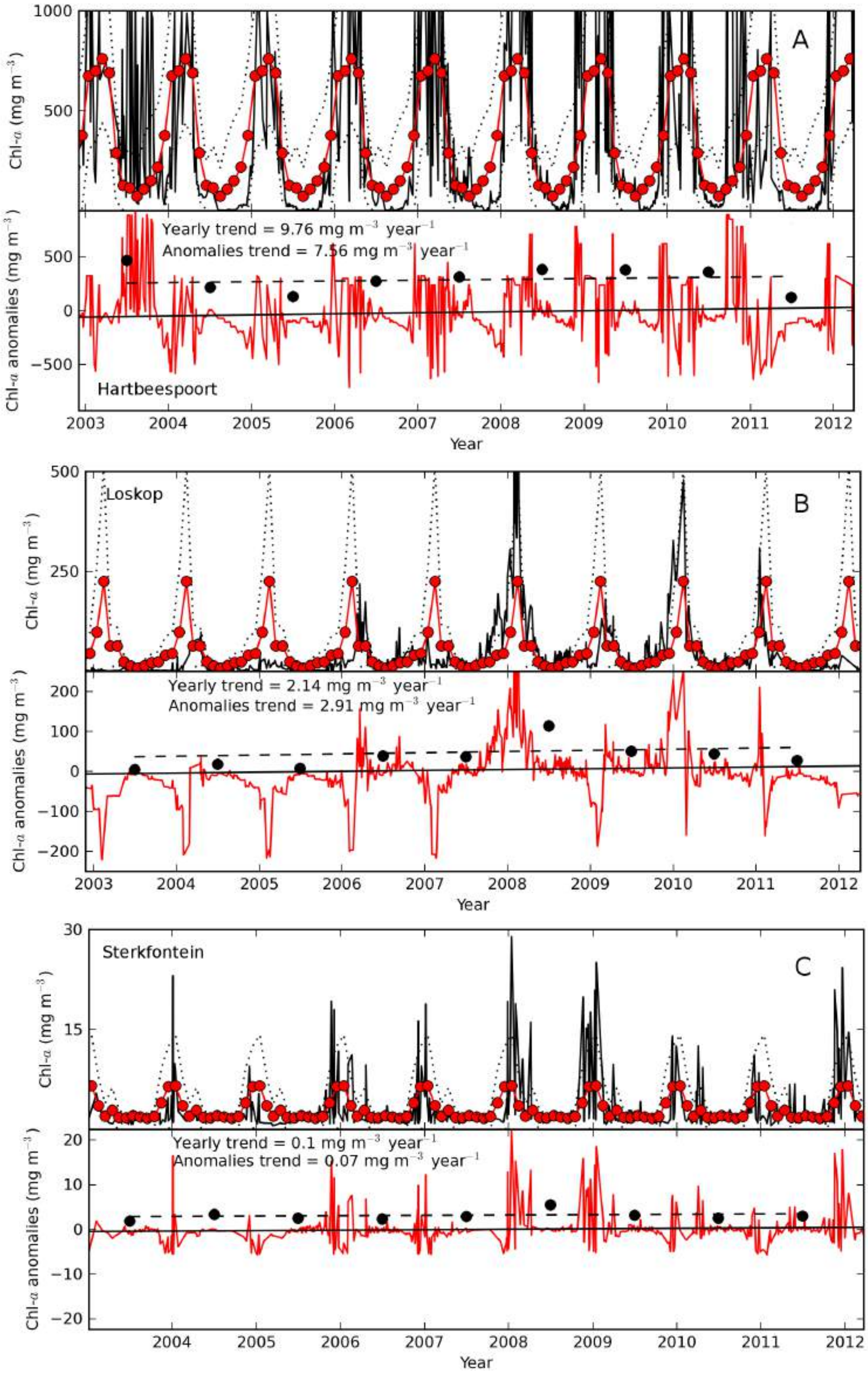

Figure 6.3.2: Upper panels: timeseries of chl-a (black line) overlaid with the seasonal signal (red dotted line) showing the standard deviation envelope (thin dashed line). Lower panels: chl-a anomalies (red line) and yearly averages (black dots) with fitted trend lines (solid and dashed, respectively). Shown for A) Hartbeespoort, B) Loskop and C) Sterkfontein. Note differences in y scales.

Table 6.3.1: Reservoir characteristics and statistics derived from 10 years of MERIS observations. Bold font indicates trends significant at the 95% confidence interval of the student-t distribution. For header abbreviations see text.

Name	Area	Lat.	Lon.	Alt.	N	$\bar{\text{chl}}$	A_{chl}	φ_{chl}	$a_{\text{chl}'}$	a_{chl}	$\bar{A_{cy}}$	$\varphi_{A_{cy}}$	$a_{A_{cy}}$	$\bar{A_{sc}}$	$\varphi_{A_{sc}}$	$a_{A_{sc}}$
	km^2			masl		mg m^{-3}	mg m^{-3}		$\text{mg m}^{-3}\text{ y}^{-1}$	$\text{mg m}^{-3}\text{y}^{-1}$	%		$\%\text{ y}^{-1}$	%		$\%\text{ y}^{-1}$
Gariep	346.6	-30.69	25.71	1260	652	186.5	384.5	Feb	**-21.5**	-12.3	9.7	Mar	**-1.7**	2.8	Feb	**-0.8**
Vaal	251.4	-26.90	28.14	1490	742	125.9	123.3	Dec	-0.7	1.4	24.6	Apr	-0.8	2.2	Apr	**0.2**
Bloemhof	186.5	-27.67	25.65	1235	519	201.4	310.4	Mar	-7.2	-0.8	29.3	Jan	-0.4	5.6	Mar	-0.9
Pongolapoort	113.4	-27.37	31.95	140	617	2.4	7.1	Jan	0.0	0.0	1.2	Jun	**0.2**	0.0	Feb	0.0
Vanderkloof	113.1	-30.15	24.88	1170	628	55.6	139.3	Feb	**14.2**	19.0	3.2	Mar	-0.5	0.2	Feb	**-0.1**
Sterkfontein	60.8	-28.43	29.02	1702	566	2.9	4.9	Jan	0.1	0.1	3.7	May	0.3	-	-	-
Lake Sibhayi	54.7	-27.37	32.69	20	646	5.4	6.5	Jan	-0.1	-0.1	3.9	Jan	**0.2**	0.0	Dec	-
Darlington	52.2	-33.15	25.15	239	412	696.8	579.4	Jan	**49.6**	**47.1**	56.1	Feb	**-4.7**	31.2	Feb	-1.6
Theewaterskloof	50.8	-34.03	19.20	307	175	25.5	22.1	May	**-4.6**	**-4.3**	15.3	Sep	-3.2	-	-	-
Heyshope	48.8	-27.03	30.50	1308	724	18.4	12.1	Aug	**2.5**	**2.7**	1.1	Jun	**0.1**	-	-	-
Kalkfontein	42.0	-29.52	25.26	1241	538	122.5	207.8	Feb	**-16.2**	-12.0	43.8	Jan	**-5.3**	6.2	Feb	-0.8
Grootdraai	32.7	-26.93	29.33	1549	730	73.9	116.2	Feb	-1.8	-0.7	20.1	Mar	0.8	0.5	Feb	0.0
Spitskop	31.7	-28.09	24.55	1045	526	379.2	667.8	Apr	-4.0	-12.0	49.7	Feb	-2.4	24.8	Apr	-2.5
Erfenis	29.9	-28.55	26.84	1331	533	402.6	469.0	Feb	**-46.8**	-44.1	13.9	Apr	-1.0	1.3	Mar	**0.5**
Kuhlange	28.3	-26.98	32.84	2	629	12.8	9.9	Nov	**-3.4**	**-3.7**	42.9	Jul	**-9.1**	-	-	-
Allemanskraal	26.4	-28.30	27.21	1371	572	349.1	456.9	Feb	**27.9**	32.2	27.0	Apr	**-6.5**	5.4	Apr	0.5
Woodstock	26.1	-28.72	29.21	1180	584	12.2	21.6	May	0.1	0.5	0.2	May	0.0	-	-	-
Loskop	23.0	-25.43	29.32	1006	863	42.4	216.7	Feb	2.1	2.9	1.6	Feb	0.3	0.1	Feb	**0.1**
AlbertFalls	21.8	-29.44	30.41	658	518	7.3	15.9	Nov	**-1.3**	**-1.4**	0.5	Sep	**0.1**	-	-	-
Brandvlei	18.7	-33.71	19.43	203	214	6.3	9.5	Oct	**-1.3**	**-2.9**	3.2	May	**-2.3**	-	-	-
Ntshingwayo	18.7	-27.99	29.91	1248	566	336.1	734.8	Mar	5.4	5.4	15.0	Dec	**2.2**	1.0	Jan	0.2
Tzaneen	16.8	-23.79	30.15	728	598	14.4	27.3	Dec	**-1.0**	-0.9	0.8	Jun	**-0.2**	-	-	-
Hartbeespoort	15.6	-25.75	27.86	1165	775	304.2	686.5	Mar	9.8	7.6	61.1	Apr	-0.1	24.3	Mar	0.8
Krugersdrift	15.3	-28.87	26.00	1252	538	434.7	518.2	Mar	-5.8	5.7	26.3	Dec	1.2	5.6	Feb	0.5
Umtata	15.2	-31.54	28.73	695	598	487.9	503.5	Jan	**-69.3**	**-67.4**	4.5	Dec	-0.2	2.5	Mar	-0.2
Voelvlei	14.5	-33.36	19.04	75	242	126.0	152.0	Nov	**-36.3**	**-51.1**	10.1	Mar	-1.5	0.4	Mar	0.1
Midmar	14.3	-29.51	30.19	1046	533	3.0	5.7	Jan	0.1	0.1	0.6	Jul	0.0	-	-	-
Xonxa	14.0	-31.82	27.14	939	624	57.9	144.9	Mar	**12.1**	16.6	1.8	Jan	-0.1	0.0	Jan	0.1
Spioenkop	13.9	-28.69	29.49	1091	576	61.0	174.5	Jan	1.4	6.0	0.6	Feb	0.2	-	-	-
Ncora	12.8	-31.78	27.65	1038	625	383.6	582.2	Dec	**-26.0**	**-23.9**	4.3	Mar	**0.9**	1.0	Mar	**0.3**

Continued on next page...

Name	Area km²	Lat.	Lon.	Alt. masl	N	$\bar{\text{chl}}$ mg m^{-3}	A_{chl} mg m^{-3}	φ_{chl}	$a_{\text{chl}'}$ mg m^{-3} y^{-1}	a_{chl} mg m^{-3}y^{-1}	$\bar{A}_{cy}$ %	$\varphi_{A_{cy}}$	$a_{A_{cy}}$ % y^{-1}	$\bar{A}_{sc}$ %	$\varphi_{A_{sc}}$	$a_{A_{sc}}$ % y^{-1}
Barberspan	12.7	-26.58	25.59	1354	637	52.9	41.7	Jan	**-8.2**	**-8.1**	67.2	Dec	-5.5	0.1	May	-
Klipvoor	12.6	-25.15	27.82	994	775	254.4	282.4	Dec	**-39.9**	**-36.6**	16.0	Dec	1.0	3.7	Dec	-0.4
Grassridge	12.5	-31.77	25.47	1055	646	427.0	641.1	Jan	**-34.5**	**-27.4**	25.1	Oct	-0.7	3.7	Dec	**-0.7**
Koppies	11.4	-27.23	27.69	1424	669	178.8	284.3	Mar	-3.6	0.8	60.0	Nov	-0.5	0.8	Dec	0.1
Zaaihoek	10.9	-27.43	30.09	1737	706	11.3	8.6	Jul	**-2.1**	**-2.1**	0.9	May	-0.1	-	-	-
Lubisi	10.7	-31.79	27.41	1020	668	82.4	235.4	Mar	**11.0**	15.3	2.6	Feb	0.0	0.0	Apr	-
Chrissiesmeer	10.4	-26.33	30.22	1676	723	128.4	101.2	Jan	1.6	2.1	44.1	Jun	-0.6	0.4	Mar	0.1
FlagBoshielo	10.4	-24.83	29.44	821	862	27.8	39.9	Jan	**1.8**	2.2	32.6	Aug	1.6	-	-	-
Goedertrou	10.1	-28.77	31.44	228	543	15.3	26.5	Jun	**-1.8**	-1.8	1.4	Dec	-0.5	-	-	-
Rustfontein	10.1	-29.30	26.63	1374	557	92.8	117.0	Jan	**15.4**	**17.4**	26.6	Apr	0.8	1.2	May	0.2
Fairview	9.8	-26.16	31.66	297	693	34.4	78.2	Apr	**-7.4**	-7.3	3.9	Apr	**-1.2**	0.1	May	-
Vaalkop	9.7	-25.31	27.47	987	752	85.4	139.4	Feb	**-7.9**	-9.2	16.4	Apr	**4.2**	0.0	Feb	0.1
Kwena	9.6	-25.37	30.37	1185	745	28.6	108.0	Feb	**-14.2**	**-15.3**	1.9	Dec	**-0.9**	0.0	Jan	-
Roodekoppies	8.9	-25.41	27.59	1018	749	192.1	474.4	Feb	-0.1	-0.4	18.0	Mar	2.2	3.5	Feb	**1.0**
Witbank	8.7	-25.90	29.31	1507	742	101.9	268.2	Feb	-3.0	-1.9	4.3	Jul	0.8	0.3	Jan	-0.1
Lake Msingazi	8.7	-28.76	32.10	5	554	5.1	6.5	Dec	0.2	**0.3**	6.0	Jun	-0.4	-	-	-
Bronkhorstspruit	7.7	-25.90	28.69	1435	748	118.9	182.6	Feb	**-11.9**	**-12.0**	2.9	Aug	**0.4**	-	-	-
Jericho	7.7	-26.64	30.48	1470	698	10.1	16.4	Dec	0.2	-0.1	3.1	Jun	0.1	-	-	-
Mokolo	7.3	-23.98	27.75	912	709	13.8	29.8	Dec	**0.6**	**1.0**	7.1	Sep	**0.6**	-	-	-
Inanda	6.7	-29.69	30.87	151	511	23.6	59.8	Mar	-1.1	0.8	7.7	Feb	**1.7**	0.7	Feb	0.1

Table 6.3.1 indicates the great variety in $\overline{\text{chl}}$ concentrations existing in South African reservoirs, which range between 2.4 mg m^{-3} for the clearest oligotrophic waters (Pongolapoort) to hypertrophic Darlington (696.8 mg m^{-3}). A histogram indicating the membership of the reservoirs to each of the trophic classes is shown in fig. 6.3.3A. A separate class is included for lakes with $\overline{\text{chl}}$ > 300 mg m^{-3}. The results indicate that of the 50 lakes observed, 14% are oligotrophic, 16% are mesotrophic, 8% are eutrophic, and 60% are hypertrophic of which 30% have $\overline{\text{chl}} > 300$ mg m^{-3}. Therefore the majority of South Africa's largest reservoirs might be classified as hypertrophic according to the data.

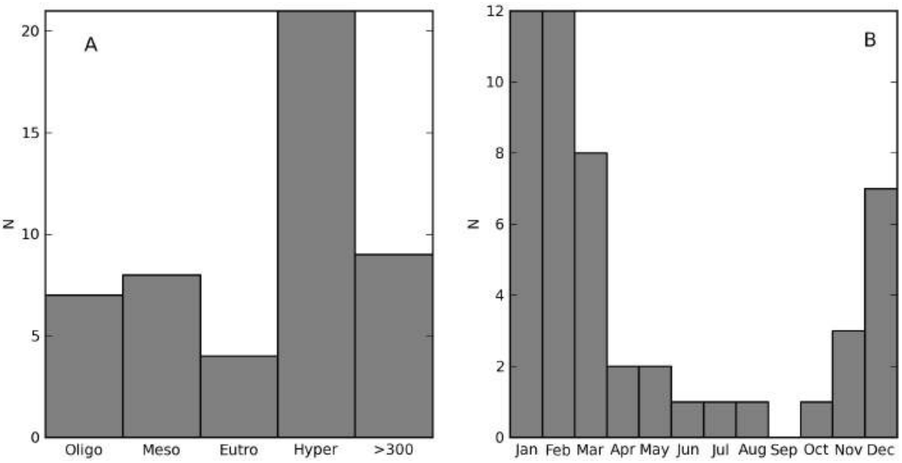

Figure 6.3.3: Histograms for (A) trophic status classes and (B) phase of the seasonal cycle of chl-*a* for 50 South African reservoirs. Oligo = oligotrophic, Meso = mesotrophic, Eutro = eutrophic, Hyper = hypertrophic. Lakes with $\overline{\text{chl}}$ greater than 300 mg m^{-3} are plotted in a separate category.

The seasonal cycles for each of the reservoirs are plotted together in fig. 6.3.4 grouped by various $\overline{\text{chl}}$ thresholds to facilitate comparison. The seasonal amplitude represents the range of variability present in any reservoir throughout the year. Lakes such as Sterkfontein, Pongolapoort, Sibayi and Midmar have small seasonal signals and little year round variability. The largest seasonal amplitude is associated with Hartbeespoort, Spioenkop, and Grassridge. These have very strong seasonal signals and display the greatest variability in productivity throughout the year. The phase of the seasonal cycle is also variable between the lakes (see fig. 6.3.3B). The late summer months January and February are the most productive: 62% of the lakes have their maximum chl-*a* production during summer, 24% are during autumn, 8% are during spring, and only 6% are during winter.

Fig. 6.3.5 shows the relationship between $\overline{\text{chl}}$ and the amplitude of the seasonal cycle. A_{chl} is significantly correlated with $\overline{\text{chl}}$ (r^2=0.8). Therefore lakes with the lowest $\overline{\text{chl}}$ values have the least seasonal variability or amplitude and those with the highest $\overline{\text{chl}}$ values typically having the greatest amplitudes. Various clustering of the reservoirs is visible in fig. 6.3.5. Towards the origin, a group is visible with $\overline{\text{chl}} < 50$ mg m^{-3} and $A_{chl} < 100$ mg m^{-3}. Within this group, Pongolapoort,

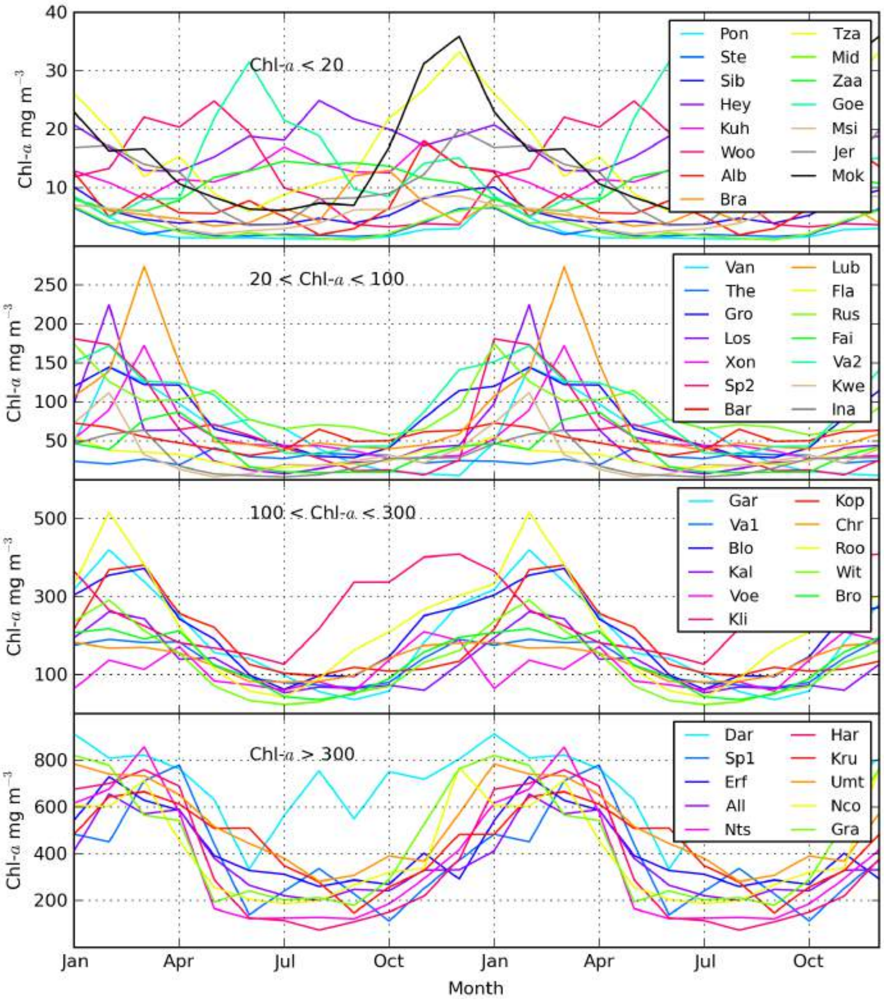

Figure 6.3.4: Seasonal cycle of chl-*a* for 50 South African reservoirs. The data are grouped in different panels by thresholds for mean chl-*a* to aid visibility. Reservoir names are abbreviated. Va1 = Vaal, Va2 = Vaalkop, Sp1 = Spioenkop, Sp2 = Spitskop. Note differing y-axes scales.

Sterkfontein, Midmar and Lakes Sibayhi and Msingazi are closely clustered together as the most oligotrophic reservoirs with the least seasonal variation. A second cluster is apparent with $\overline{chl}$ between 50 and 150 mg m^{-3} and A_{chl} between 100 and 300 mg m^{-3}. Loskop, Vaal and Chrissiesmeer belong to this grouping of eutrophic lakes, which may be subject to greater seasonal variability. A third cluster is apparent for $\overline{chl}$ between 150 and 300 mg m^{-3} and A_{chl} between 250 and 500 mg m^{-3}. Gariep, South Africa's largest reservoir, and Bloemhof belong to this cluster. Another cluster then exists for extremely hypertrophic lakes with $\overline{chl} > 300$ mg m^{-3} and $A_{chl} > 450$ mg m^{-3}. Hartbeespoort, Ntshingwayo, Allemanskraal and Krugersdrift belong to this cluster. This grouping represents reservoirs most severely affected by hypereutrophication and subject to extreme seasonal variability. It is not clear whether there is any ecological significance or cause to the apparent clustering. It does however indicate the presence of distinct states which might be used as an alternative classification scheme to the conventional trophic status classes. The four apparent classes, drawn in fig. 6.3.5 might be used to determine the level of impact by eutrophication. These are class 1, mildly impacted; class two, moderately impacted; class three, highly impacted; and class four, severely impacted. The classification might be used to establish reservoirs requiring high priority and urgent attention for eutrophication management.

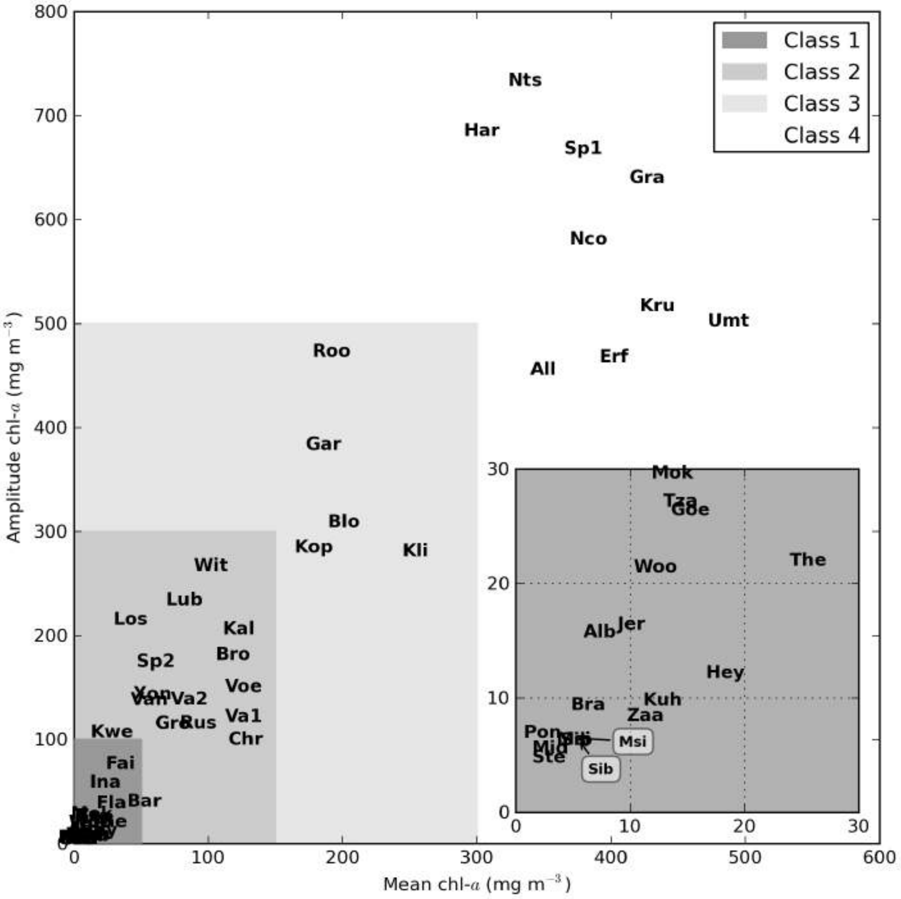

Figure 6.3.5: The mean versus the amplitude of chl-*a* for 50 South African reservoirs. Data are plotted using abbreviations of reservoir names. The insert shows a zoomed area towards the origin. Shading indicates various classes (see text for details). Reservoir names are abbreviated as in fig. 6.3.4.

The time-series trends for chl-*a* yearly averages and anomalies are plotted in fig. 6.3.6. The high correlation between the trend of the yearly averages and anomalies indicates the robustness of the trend calculations, since the high frequency anomaly signal is consistent with that of the the lowest frequency of observation (yearly). It is apparent that there are a greater number of negative anomaly trends than positive ones, 30 versus 20, of which 20 and 9 are significant, respectively. For instances in which the annual trend is significant there are 5 positive trends and 13 negative trends. Only significant trends may be used to draw conclusions regarding whether eutrophication is deteriorating or improving in a reservoir over the time period. The sum of significant anomaly trends is -220.5 mg m^{-3} year^{-1} while that for significant yearly trends is -187.7 mg m^{-3} year^{-1}. Therefore, based on the number of negative trends it would seem that within the 50 reservoirs eutrophication became less severe between the years 2005 and 2011. The trend estimates are limited with respect to the shortness of the time interval (seven years), the occurrence of anomalous bloom events/periods (resulting from e.g. water level fluctuations), and must be considered relative to the mean and seasonal variability (amplitude) of chl-*a* in the reservoir.

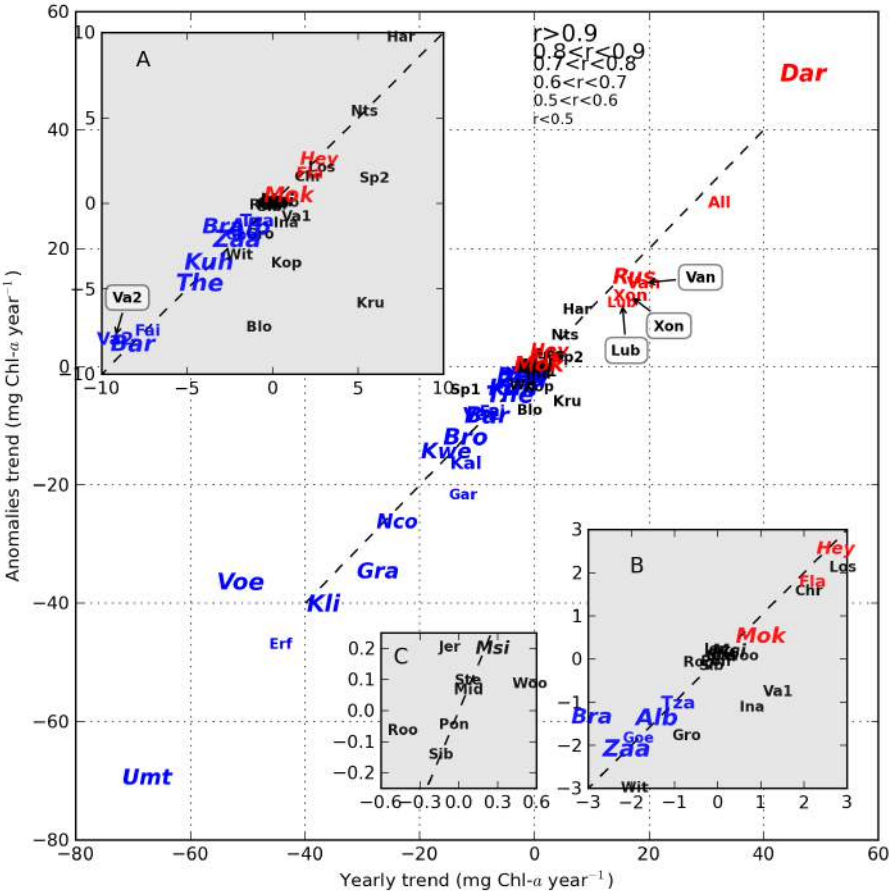

Figure 6.3.6: Trend coefficients of chl-*a* between 2005 and 2011 for yearly averages and anomalies for 50 South African reservoirs. Significant positive anomalies trends are indicated in red while significant negative anomalies trends are in blue. Italics indicates significant yearly trends. The font size indicates the value of the correlation coefficient, *r*. The inserts A, B and C are zoomed near the origin to ensure all data is visible (note scales). Reservoir names are abbreviated as in fig. 6.3.4.

An investigation of $\bar{\text{chl}}$ versus the trend might be used to identify which reservoirs are most affected by eutrophication (fig. 6.3.7). The plot indicates that within the different classes identified above, there exist reservoirs which are both improving and deteriorating in trophic status. Reservoirs in the severely impacted class require the most urgent attention: however Darlington and Allemanskrall appear to be worsening while Umtata and Erfenis appear to be improving despite the overall hypereutrophic conditions. The same conclusions can be drawn for reservoirs in the other classes from fig. 6.3.7. Vanderkloof, Rustfontein, Xonxa and Lubisi are also identified as requiring urgent attention in the moderately impacted class. The same data are redrawn in fig. 6.3.8

but the trend is normalised by the amplitude of the seasonal cycle. This indicates the percentage relative to the expected variability at which eutrophication is worsening or improving. The figure identifies that Heyshope although only mildly impacted by eutrophication, has the largest trend relative to the expected variability (>20 % per annum) , and therefore requires urgent management attention. The large trends for Darlington and Allemanskrall can be shown to be smaller relative to the expected seasonal variability (>10% per annum). Reservoirs which improved the most between 2005 and 2011 relative to the seasonal variability are Kuhlange (Kosi Lake), Zaaihoek, Voelvlei, Theewaterskloof and Barberspan (> 20% per annum). The results for $\overline{\mathrm{chl}}$ and the significant anomalies trends are plotted on a geographical map of South Africa in fig. 6.3.9. The status and trends of eutrophication with respect to water catchments are discussed in section 6.4.4 below.

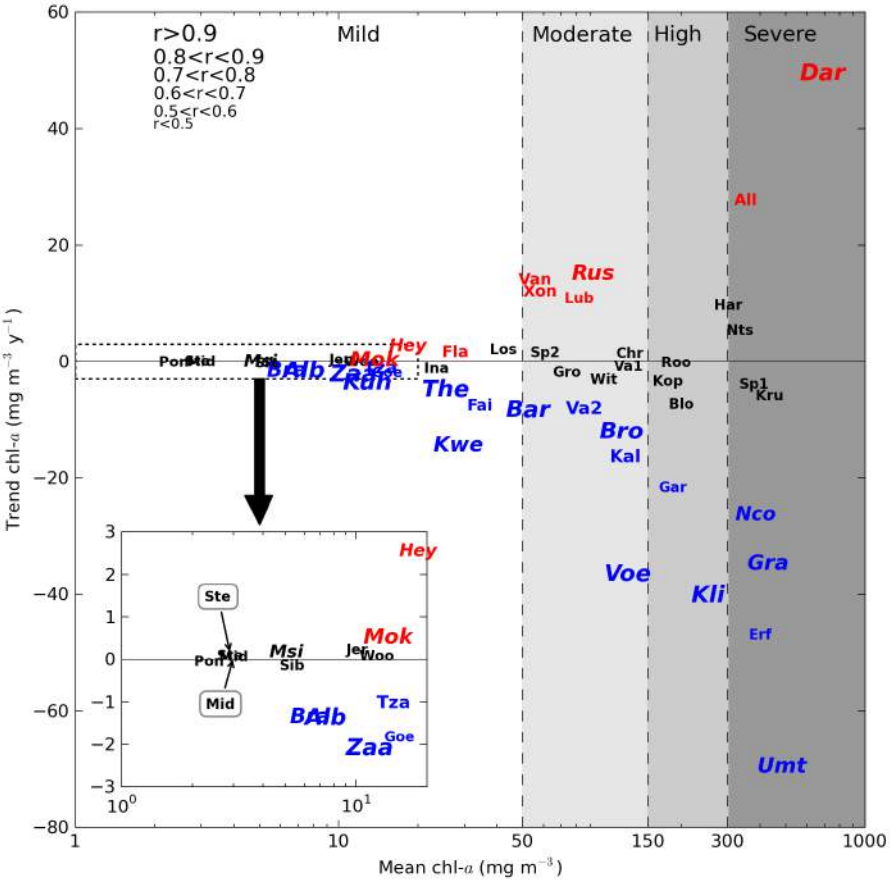

Figure 6.3.7: $\overline{\mathrm{chl}}$ versus the anomalies trend of chl-a for 50 South African reservoirs. Significant positive trends are red while significant negative trends are blue. Italics indicates significant yearly trends. The font size indicates the value of the correlation coefficient, r. The eutrophication classes are also designated. The insert shows a zoomed region towards the origin (note scale). Reservoir names are abbreviated as in fig. 6.3.4.

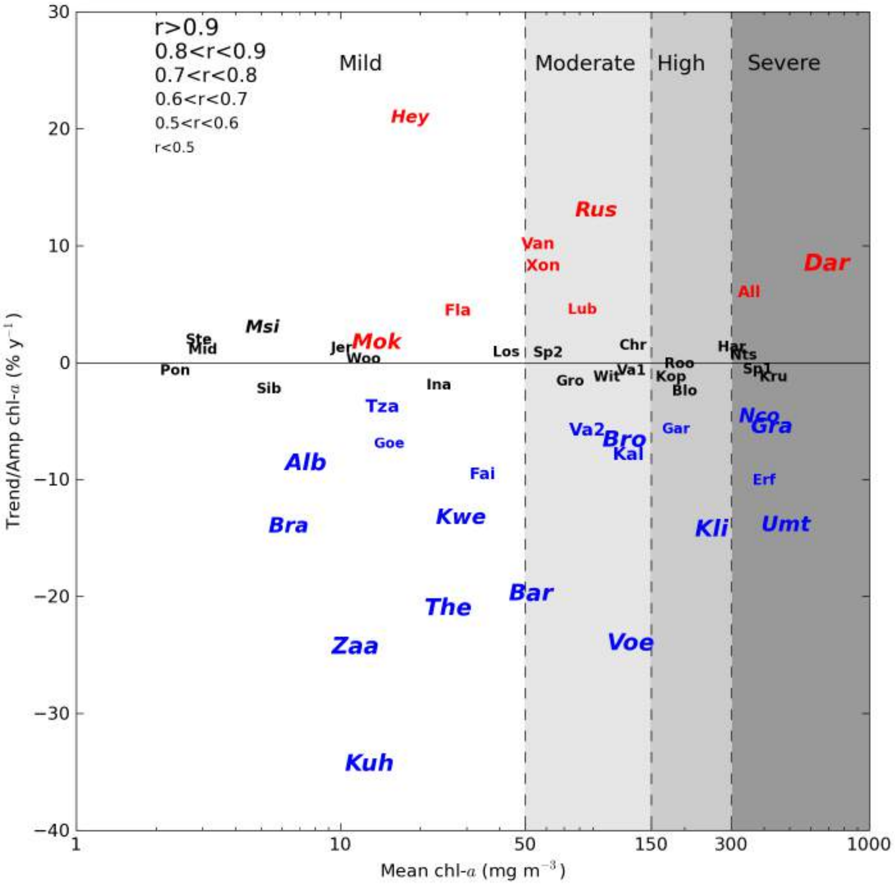

Figure 6.3.8: $\bar{\text{chl}}$ versus the anomalies trend normalised by the amplitude of chl-*a* for 50 South African reservoirs. Significant positive trends are red while significant negative trends are blue. Italics indicates significant yearly trends. The font size indicates the value of the correlation coefficient, *r*. Reservoir names are abbreviated as in fig. 6.3.4.

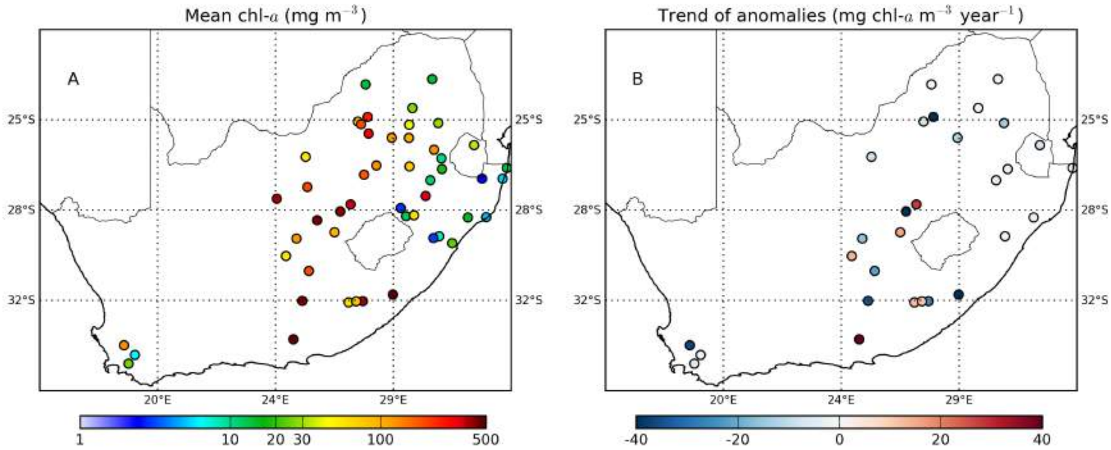

Figure 6.3.9: Status and trends of eutrophication (chl-*a*) in 50 South African reservoirs. A) The mean chl-*a* concentration. B) The trend coefficient of the anomalies (significant at the 95% confidence interval of student-t test).

6.3.3 STATUS, SEASONALITY AND TRENDS OF CYANOBACTERIAL BLOOMS

Fig. 6.3.10 shows histograms for the mean and phase of cyanobacterial blooms for the 50 reservoirs. Twenty seven (54%) of the reservoirs have <10% cyanobacteria coverage over the time series (of which 6 have less than 1%). These reservoirs can be said to have infrequent to occasional cyanobacterial blooms with insignificant or little area coverage. Examples of these reservoirs are Loskop and Sterkfontein (see fig. 6.3.1 for timeseries examples). Fourteen reservoirs have between 10 and 30% average cyanobacteria coverage. These reservoirs have common and regular cyanobacterial blooms with medium coverage and include South Africa's two largest reservoirs, Gariep and Vaal. Nine reservoirs have greater than 30% cyanobacteria area coverage. These reservoirs which include Hartbeespoort, Koppies, Barberspan and Darlington have frequent, persistent and extensive cyanobacterial blooms (see fig. 6.3.1 for Hartbeespoort example). The classes defined in terms of cyanobacteria coverage are drawn in fig. 6.3.10.

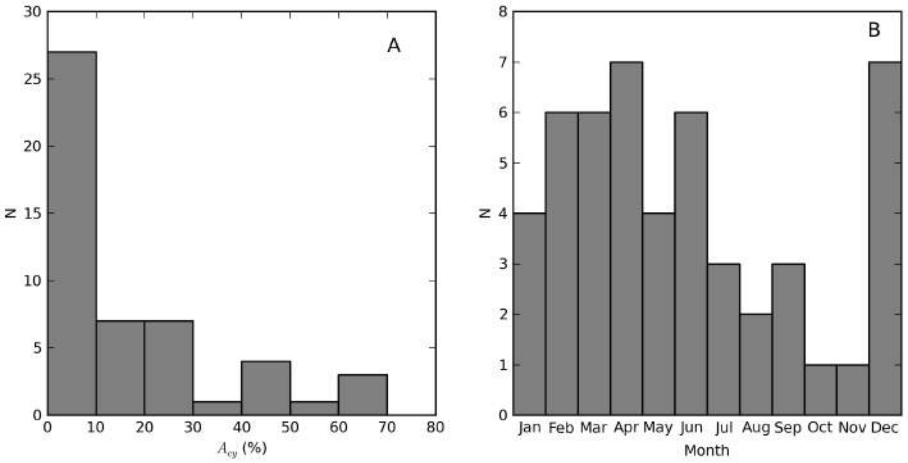

Figure 6.3.10: Histograms for (A) cyanobacteria area coverage and (B) phase of the seasonal cycle of cyanobacteria for 50 South African reservoirs.

The seasonal cycle of cyanobacterial blooms is shown in fig. 6.3.10B and fig 6.3.11. The majority of cyanobacterial blooms reach their maximum during summer and autumn months, with the peak occurrence being early summer (December) and mid autumn (April). Summer and autumn accounts for 34% (17) each of peak cyanobacterial occurrence, winter 26% (13) and spring only 10% (5) of reservoirs. The seasonal cycles for reservoirs with >5% $\bar{A}_{cy}$ are shown in fig, 6.3.11. The shapes of the cycles vary between reservoirs from distinct sinusoidal curves (e.g. Hartbeespoort and Chrissiesmeer) to bimodal curves (e.g. Barberspan and Theewaterskloof) which have two maximums at different times of the year. The occurrence of winter maximums is a surprising result, which has been observed previously by Oberholster and Botha (2007) for Midmar. The results obtained here confirm the winter maximum for Midmar which has a phase of July, although the overall coverage is low (0.6%) (table 6.3.1). This result is examined in detail in section 6.4.2. Distinct winter maximums are observed for Khulange (Kosi Lake), Chrissiesmeer and Flag Boshielo (fig. 6.3.11). What might be driving winter cyanobacterial blooms is uncertain however the results here suggest that it is a fairly common occurrence in South African reservoirs with 26% of the 50 reservoirs examined having winter maxima.

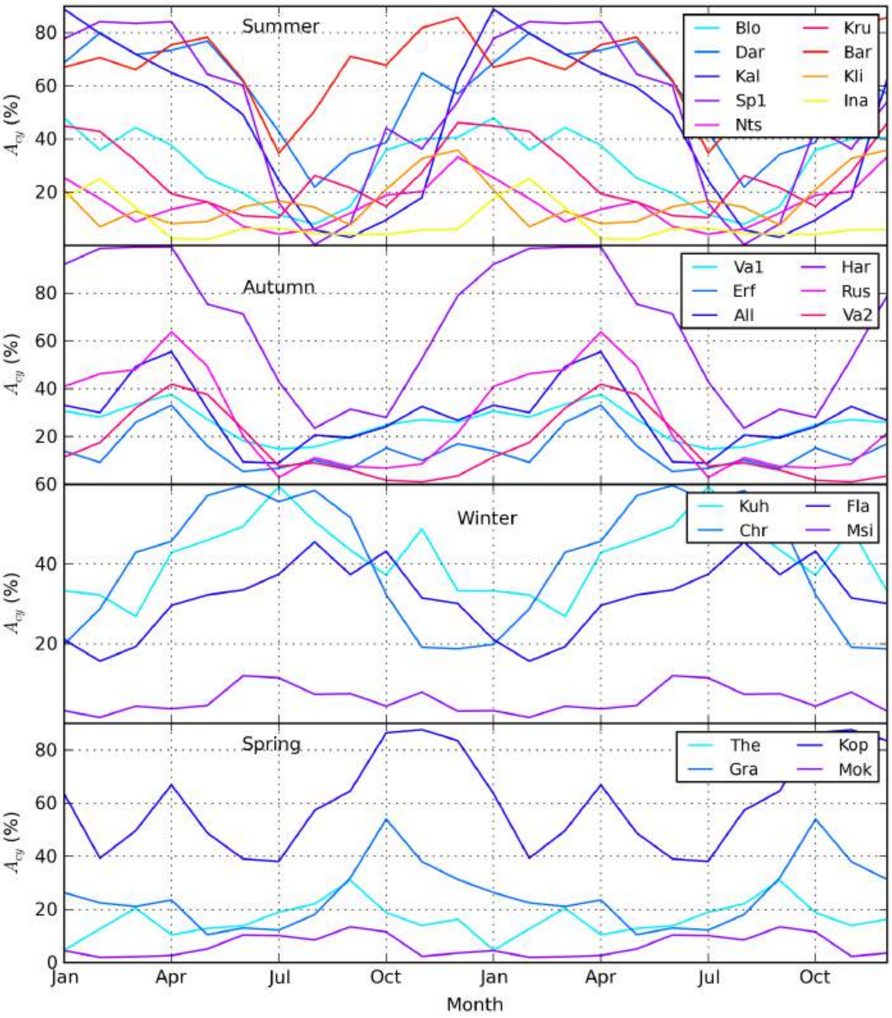

Figure 6.3.11: Seasonal cycle of cyanobacteria area coverage for South African reservoirs with $\bar{A_{cy}} > 5\%$. The data are grouped in different panels by season of the phase. Reservoir names are abbreviated as in fig. 6.3.4. Note differing y-axes scales.

Examining the trend of cyanobacteria occurrence between 2007 and 2011 reveals that cyanobacterial blooms are becoming more frequent in 10 reservoirs while also becoming less frequent in 9 others (fig. 6.3.12). The sum of significant negative trends is -31.8% y^{-1} whilst that for positive trends is 10.7% y^{-1}. The trends for most of the reservoirs (62%) are insignificant, indicating no significant changes over the time period for cyanobacterial bloom occurrence. The trend normalised by $\bar{A_{cy}}$ is plotted in fig. 6.3.13. The result indicates the trend relative to the mean cyanobacteria occurrence in a reservoir. The plot shows more clearly that eight reservoirs in the infrequent to occasional bloom category have relatively large significant positive trends, versus four negative trends. Therefore, reservoirs in this category are worsening with regard to more frequent cyanobacterial blooms over the time period. The large negative trends for reservoirs in the frequent category (e.g. Darlington, Kalkfontein) are shown to be smaller relative to $\bar{A_{cy}}$. The trends and mean A_{cy} are

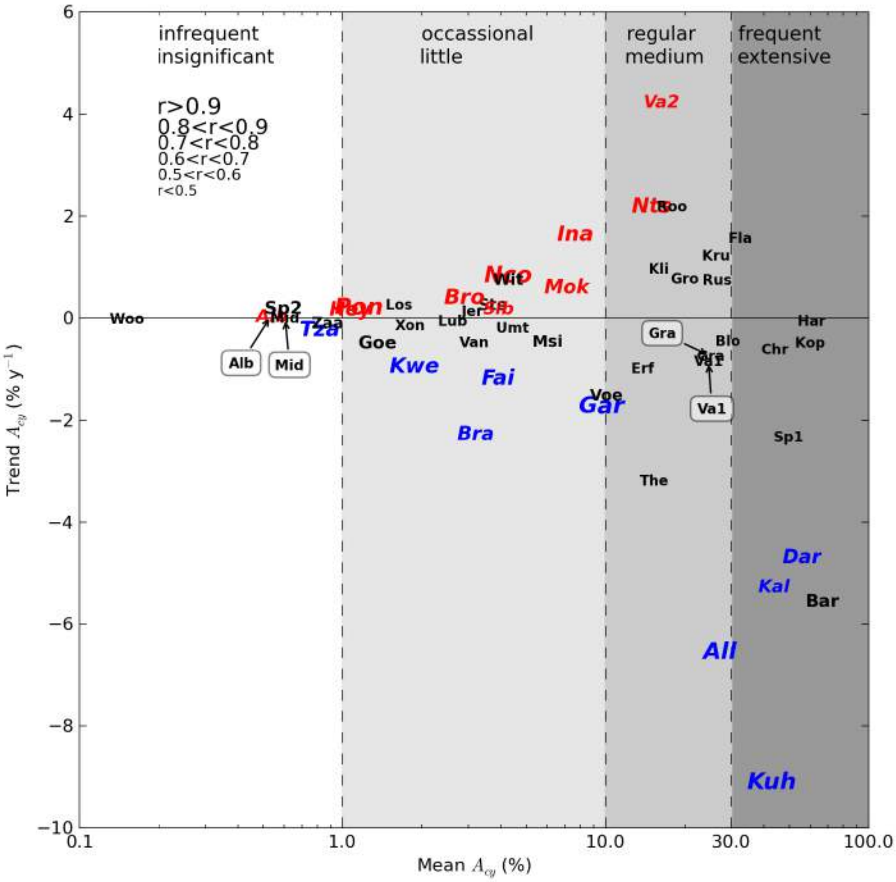

Figure 6.3.12: Mean versus the trend of cyanobacteria area coverage for 50 South African reservoirs. Significant positive trends are red while significant negative trends are blue (italics). The font size indicates the value of the correlation coefficient, r. Reservoir names are abbreviated as in fig. 6.3.4.

plotted geographically in fig. 6.3.14 and are analysed with respect to catchments in section 6.4.4.

6.3.4 Status, seasonality and trends of surface scums

Cyanobacterial surface scum conditions exist in at least 33 of the 50 (or 66%) reservoirs examined (fig. 6.3.15A). The majority have less than 1% mean area cover by scum (34%), 18% have between one and five percent cover, while just 8% and 6% have between five and 10% and >10% area coverage, respectively. Seventeen (34%) of the reservoirs have no occurrence of surface scums. Reservoirs with <1% $\bar{A_{sc}}$ have infrequent and insignificant surface scum coverage. These include Vanderkloof and Loskop (see fig. 6.3.1). Reservoirs with $\bar{A_{sc}}$ between 1 and 5% have occasional scum events with relatively little area coverage and includes Vaal and Roodepoort. Reservoirs with $\bar{A_{sc}}$ between 10 and 30% can be said to have regular scum events with intermediate area coverage, and include Bloemhof and Krugersdrif. Reservoirs with frequent and extensive scum coverage are Hartbeespoort (see fig. 6.3.1), Spioenkop and Darlington with $\bar{A_{sc}} > 30\%$. These classes are illus-

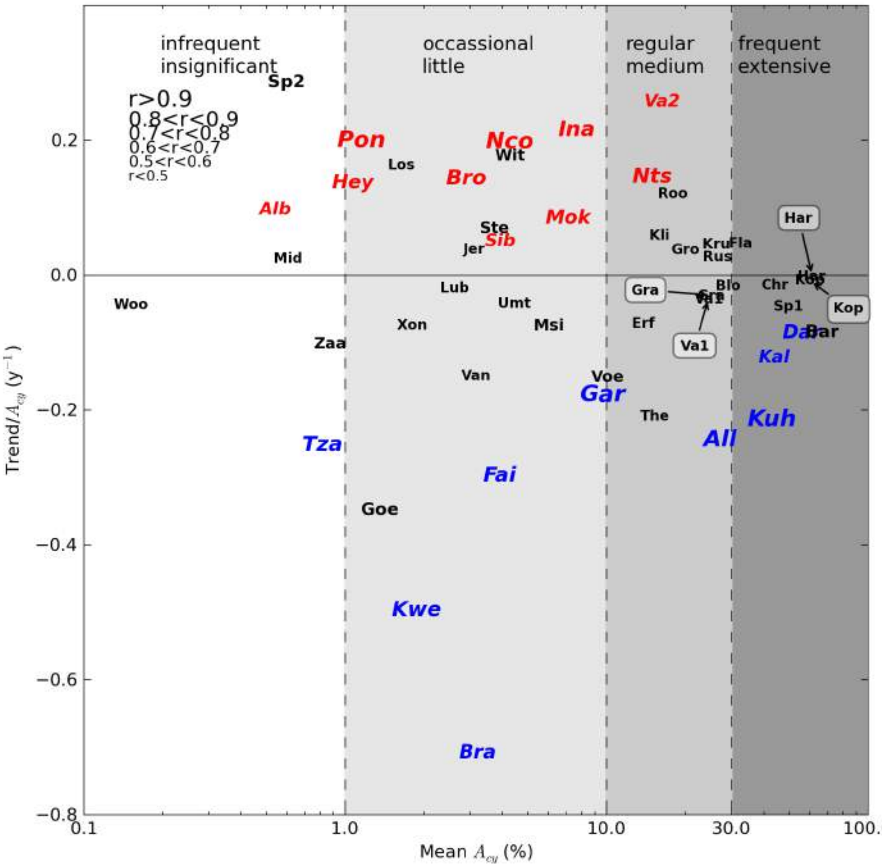

Figure 6.3.13: Mean area coverage of cyanobacteria versus the trend normalised by the mean for 50 South African reservoirs. Significant positive trends are red while significant negative trends are blue (italics). The font size indicates the value of the correlation coefficient, r. Reservoir names are abbreviated as in fig. 6.3.4.

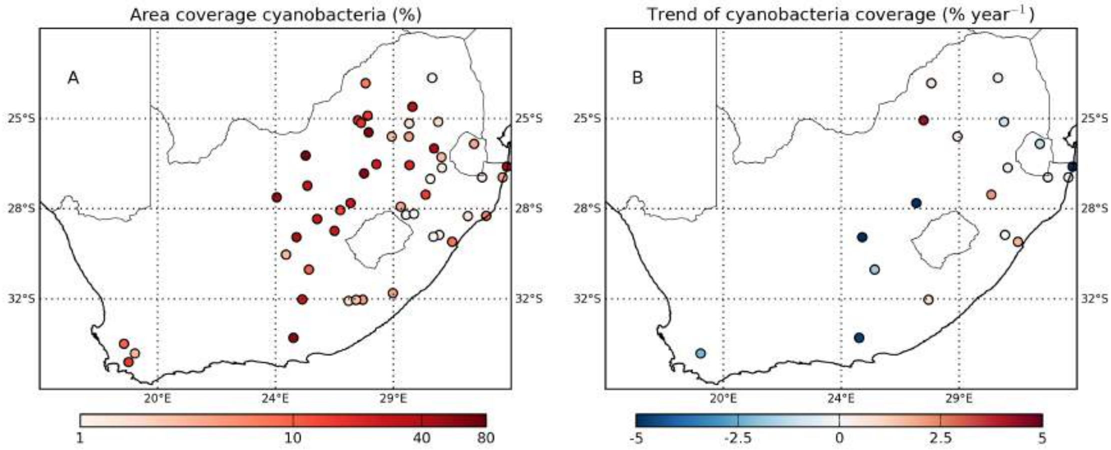

Figure 6.3.14: Status and trends of cyanobacterial blooms in 50 South African reservoirs. A) The mean cyanobacteria area coverage (%). B) trend coefficients of cyanobacterial area coverage (significant at the 95% confidence interval of student-t test).

trated in fig 6.3.16.

The seasonal timing of surface scum occurrence is strongly biased towards summer and autumn

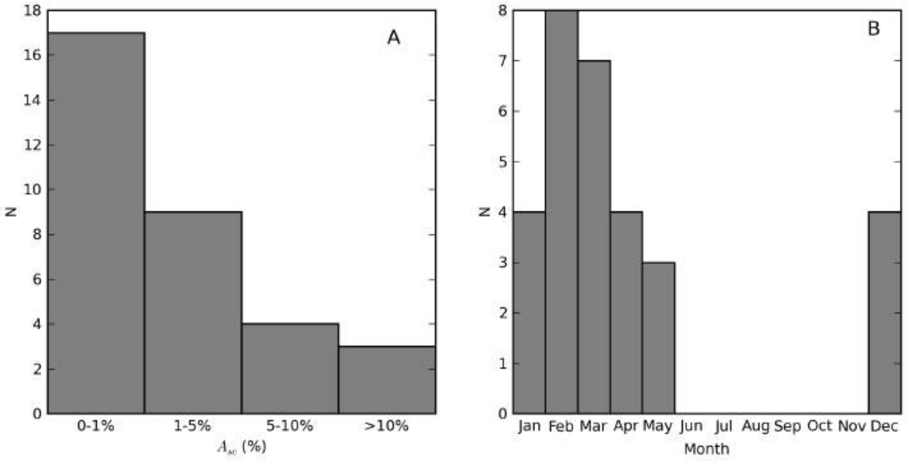

Figure 6.3.15: Histograms for (A) $\bar{A_{sc}}$ and (B) φ_{sc} for 50 South African reservoirs.

months with the maximum occurring during late summer (February) (fig. 6.3.15B). There are no cases with winter or spring scum maxima. The mean versus the trend of surface scum are shown in fig. 6.3.16. Five reservoirs, namely Loskop, Ncora, Erfenis, Vaal and Roodepoort, have significant positive trends (sum of 2.1% y^{-1}), while three Vanderkloof, Gariep and Grassridge have significant negative trends (sum of -1.6% y^{-1}) over the time period. Positive trends amount to 17 reservoirs, while only 11 have negative trends. Therefore overall it appears that surface scum events became slightly more frequent over the time period in the 50 reservoirs. However, little can be said of the change in surface scum occurrence in reservoirs where the trend is not significant. The trends and mean A_{sc} are plotted geographically in fig. 6.3.14 and are analysed with respect to catchments in section 6.4.4. A detailed investigation of the identification and classification of scums is presented in section 6.4.3.

6.3.5 Comparison with *in situ* measurements

The results for the matchup data are presented in table 6.3.2 and plotted in figs. 6.3.18 and 6.3.19. A comparison of the mean, median and standard deviation of *in situ* versus satellite estimates reveals that the MPH algorithm provides a good measure of gross trophic status. For hypertrophic Hartbeespoort, the mean *in situ* estimate is 53. 7 mg m^{-3} versus 60.1 mg m^{-3} from satellite estimates. For oligotrophic Midmar, the *in situ* estimate is 5.9 mg m^{-3} versus 7.2 mg m^{-3} estimated from satellite. Similar results are obtained for the other reservoirs. For all cyanobacteria-dominant waters the comparison is very close at 93.4 mg m^{-3} versus 110.8 mg m^{-3}, respectively. Similarly, for eukaryote-dominant waters the comparison is 33.5 mg m^{-3} versus 52.2 mg m^{-3}, respectively (see also the close median and std. dev. comparisons). The close comparisons serve to independently

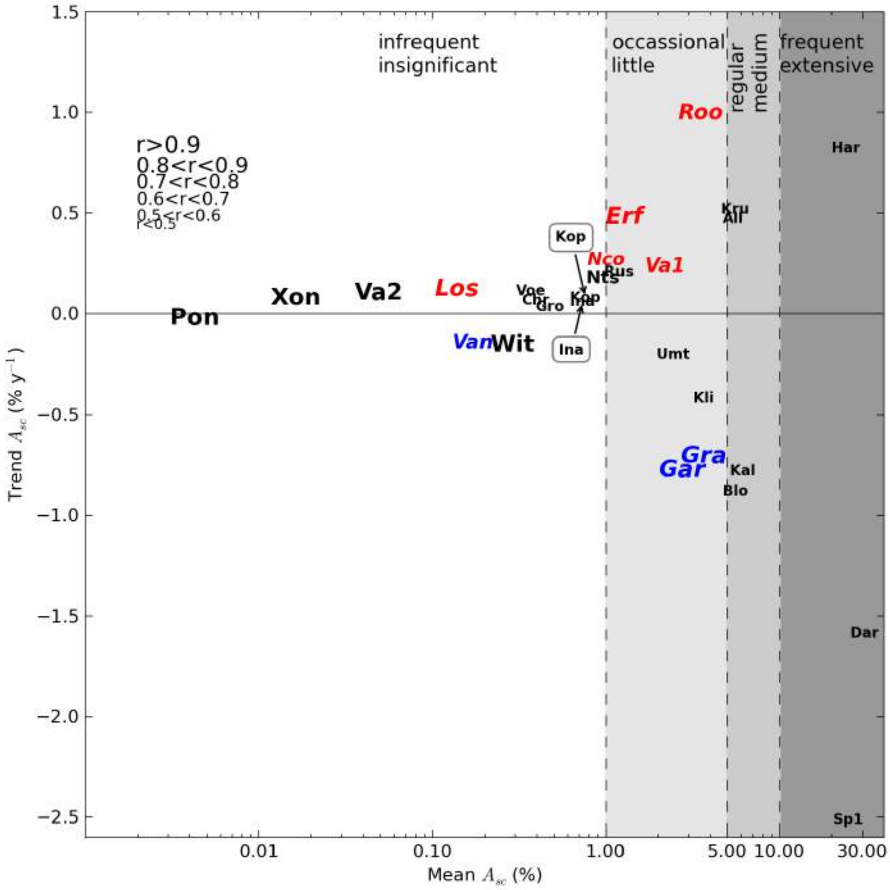

Figure 6.3.16: Surface scum area coverage mean versus the trend for 50 South African reservoirs. Significant positive trends are red while significant negative trends are blue (italics). The font size indicates the value of the correlation coefficient, r. Reservoir names are abbreviated as in fig. 6.3.4.

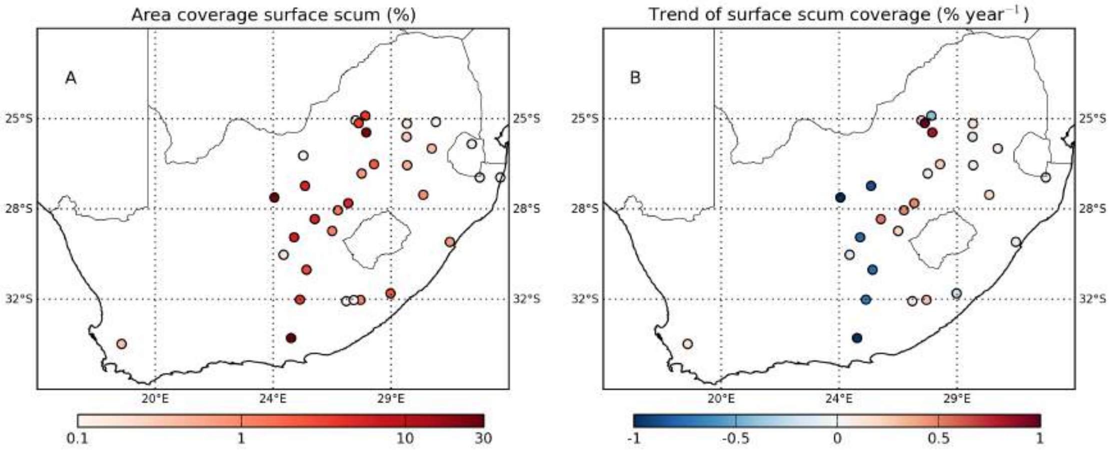

Figure 6.3.17: Status and trends of surface scum area coverage in 50 South African reservoirs. A) The mean surface scum area coverage. B) The trend coefficient of surface scum area coverage (significant at the 95% confidence interval of student-t test).

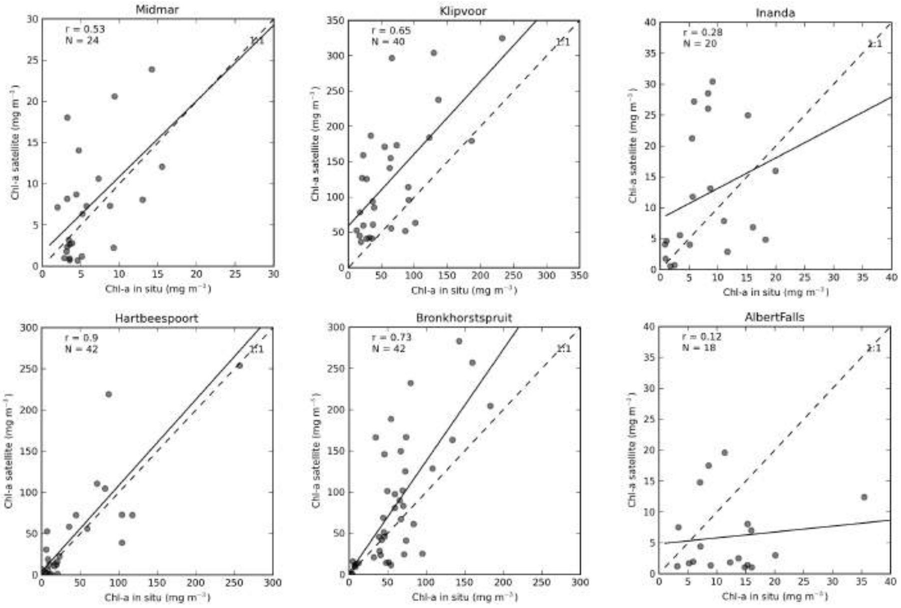

Figure 6.3.18: Scatter plots of *in situ* versus satellite estimated chl-*a* for six reservoirs. Solid line shows linear regression fits, while dotted line is 1:1 fit. *In situ* chl-*a* greater than 350 mg m^{-3} were not included due to large horizontal gradients in extremely high biomass conditions.

Table 6.3.2: Linear regression statistics for matchup *in situ* and satellite chl-*a* estimates. The mean, median and std. dev of satellite estimates are presented in brackets. Slope=m, intercept=c, p-value=p. Units for RMSE and bias are mg m^{-3}, MAPE is %.

Reservoir	Mean	Median	St. Dev.	r	m	c	n	p	RMSE	Bias	MAPE
AlbertFalls	12.2 (6.0)	11.8 (2.7)	7.4 (5.9)	0.12	0.10	4.85	18	0.64	11.51	-6.19	79.19
Bronkhorstspruit	59.9 (83.3)	54.4 (61.2)	40.4 (75.0)	0.73	1.36	2.08	41	0.00	59.56	23.37	73.20
Hartbeespoort	53.7 (60.1)	20.5 (26.7)	68.3 (79.7)	0.90	1.04	4.00	26	0.00	37.70	6.36	101.70
Inanda	8.0 (12.1)	7.1 (7.4)	5.7 (10.2)	0.28	0.49	8.23	20	0.24	11.63	4.20	141.48
Klipvoor	65.6 (126.1)	47.1 (104.9)	52.2 (81.6)	0.65	1.02	59.07	30	0.00	89.48	60.51	160.15
Midmar	5.9 (7.2)	4.5 (6.7)	3.7 (6.4)	0.53	0.92	1.69	24	0.01	5.84	1.21	88.01
Vaalkop	17.7 (37.0)	14.6 (31.6)	15.4 (32.4)	0.69	1.45	11.33	7	0.09	36.88	19.31	236.86
All	39.0 (57.5)	17.5 (23.7)	47.8 (74.7)	0.80	1.26	8.49	166	0.00	49.93	18.53	111.29
Cyanobacteria	93.4 (110.8)	72.0 (55.6)	83.9 (104.2)	0.89	1.11	7.10	15	0.00	54.37	17.38	101.68
Eukaryotes	33.5 (52.2)	16.0 (18.0)	38.6 (68.9)	0.78	1.39	5.64	151	0.00	49.86	18.64	112.25

validate the performance of the MPH for gross trophic status determination.

This result is also reflected in the regression analysis: the overall correlation for the combined dataset has a r value of 0.8 (p = 0.00, RMSE = 49.3). However, the slope of 1.26, intercept of 8.49 and bias = 18.53 mg m^{-3} indicate that the MPH algorithm has a tendency to overestimate chl-*a* relative to *in situ* measurements. However the scatter in fig. 6.3.19 shows that satellite estimates also have a strong tendency to underestimate at chl-*a* < 20 mg m^{-3}. Interestinly, the data < 20 mg m^{-3} have almost no correlation, being roughly flat. This could be related to the sensitivity of the MPH algorithm at low chl-*a* values, which is limited to ± 3.5 mg chl-*a* m^{-3} in eukaryote dominant waters (Matthews et al., 2012). Alternatively it could be a result of the limit of detection for *in situ* measurements which is typically between 1 and 2.5 mg m^{-3} (0.6 mg m^{-3} for Inanda, Albert Falls

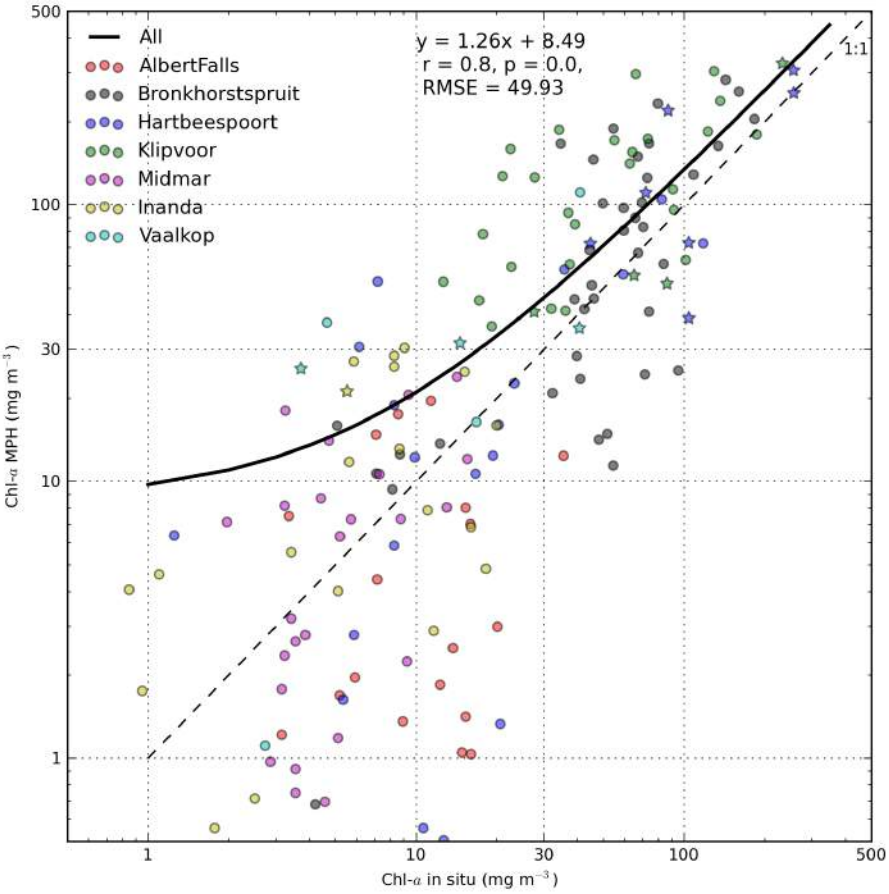

Figure 6.3.19: Log-log *in situ* versus satellite estimated chl-*a*. Starred data points are cyanobacteria dominant. Solid line shows linear fit for all data. *In situ* chl-*a* greater than 350 mg m^{-3} were not included due to large horizontal gradients in extremely high biomass conditions.

and Midmar).

For waters dominated by cyanobacteria, the fit is improved to r = 0.89 (N=15, RMSE=54.4 mg m^{-3}). This correlation (r=0.76, N=17, RMSE=46.6 mg m^{-3}) is better than the original data from which the algorithm was derived in Chapter 2. This provides independent verification that the MPH algorithm operates robustly for chl-*a* estimation in cyanobacteria dominant waters (most of these data are from Hartbeespoort). Therefore, chl-*a* detection for eutrophic cyanobacteria blooms is achieved with high degree of confidence, although with a positive bias (slope coefficient of 1.11 and bias = 17.4 mg m^{-3}).

For eukaryote-dominant waters, the fit is r = 0.78 (p=0.00, N=151, RMSE=49.9 mg m^{-3}). This is also comparable to the original derivation of the MPH algorithm in Chapter 2 which had a r value of 0.84. However, the algorithms tendency to overestimate for eukaryotes is slightly higher with m = 1.39, and bias of 18.7 mg m^{-3}. Detection of chl-*a* for low biomass waters ($<$ 20 mg m^{-3}) remains the most challenging case, and cannot in absolute terms be achieved with high confidence. Possible sources of error include the limit of detection of spectrophotometric methods used to determine chl-*a in situ*, algorithm sensitivity, and possible variable fluorescence quantum yeild at 681 nm on which the algorithm is based caused by variability in species, seasonality or physiological factors.

The strength of the correlation coefficient is highly variable among the reservoirs. The best fits are determined for hypertrophic/eutrophic reservoirs Hartbeespoort (r=0.9), Bronkhorstspruit (r=0.73), Vaalkop (r=0.69) and Klipvoor (r=0.65). $m > 1$ (positive bias) exists for these reservoirs (1.02 to 1.45) showing a tendency to overestimate chl-*a*. A mismatch between the satellite and *in situ* sample locations (which are not precisely know) might explain some of the poorer correlations. For oligo/mesotrophic waters (e.g. Albert Falls, Inanda and Midmar) the r value is much poorer (0.12 to 0.53). This is in agreement with the lack of correlation for chl-*a* $< 20\,\mathrm{mg\,m^{-3}}$ in fig. 6.3.19, for which possible explanations have already been given. For these reservoirs, $m < 1$, ranging from 0.1 to 0.92, indicating a tendency of the MPH to underestimate chl-*a* (see Albert Falls negative bias). Despite the poor correlations it is apparent that the MPH does provide close comparisons for the mean and median chl-*a* values in these reservoirs. However, the sensitivity for detecting small changes in chl-*a* is complicated by a range of possible sources of error, making comparison of *in situ* and satellite results in this range more complex.

6.4 APPLICATIONS

This section contains three case studies to verify the identification of eukaryotic, cyanobacterial and surface scum by the MPH algorithm: firstly the detection of eukaryote algae is validated through a case study of *C. hirundinella* blooms in Albert Falls; second, cyanobacteria detection is demonstrated through observations of winter cyanobacteria blooms in Midmar; and lastly, surface scum detection is verified with high resolution satellite imagery from Hartbeespoort dam.

6.4.1 CASE STUDY: OBSERVATIONS OF *C. HIRUNDINELLA* BLOOMS IN ALBERT FALLS

Hart and Wragg (2009) first reported on the occurrence of *C. hirundinella* blooms at Albert Falls in 2006. The study included a detailed survey of the lake in October 2006 and January 2007 for which maps of the spatial distribution of chl-*a* were produced (see fig. 3 in Hart and Wragg (2009)). The study also presented time series of mid-lake chl-*a* data and observed and predicted *Ceratium* abundance. These data serve as an ideal reference to verify the performance of satellite estimates to estimate the spatial distribution and phenology of *Ceratium* blooms.

Fig. 6.4.1 shows a comparison of satellite and *in situ* chl-*a* estimates as well as imagery coincident with the surveys performed by Hart and Wragg (2009). The time series graph shows a general correlation between the satellite and *in situ* observations. In particular, the *Ceratium* bloom events that occurred in spring/summer 2004 and winter 2006 as shown in Hart and Wragg (2009) are well represented. Note that cyanobacteria area coverage timed with these blooms is close to zero, indicating that the blooms are eukaryote dominant. This is also shown in the satellite imagery, where no pixels have been identified as cyanobacteria. Satellite lake averages from 2009 onwards show a consistent summer time eukaryote bloom of biomass around 20 to 50 mg m^{-3} presumably of *Ceratium*. The seasonal signal of chl-*a* reaches a maximum in January and a minimum in August (fig.6.3.4). The *in situ* data post July 2009 demonstrated no correlation, most likely due to a change in sample point location, and is therefore not shown. The satellite data could be used to further verify the rule-based model of Hart and Wragg (2009) for predicting *Ceratium* in Albert Falls.

The satellite imagery shows nearly identical patterns to fig. 3 in Hart and Wragg (2009) as regards the spatial distribution of the bloom, which increased exponentially towards the inflow in the south west corner. Image B1 was acquired on the same date as the survey while the other imagery is within one day of survey work. The clearer conditions that existed in January 2007 towards the main basin of the reservoir are vividly reproduced in the satellite observations. The actual values of the satellite observations are very close to those measured *in situ* with a maximum value towards the inflow $>$ 200 mg m^{-3} and satellite lake averages between 7.4 and 19.5 mg m^{-3} compared to *in situ* lake averages for October and January of 11.7 and 16.4 mg m^{-3}, respectively. This demonstrated how MERIS can be used to detect eukaryote blooms in spatially-constrained reservoirs.

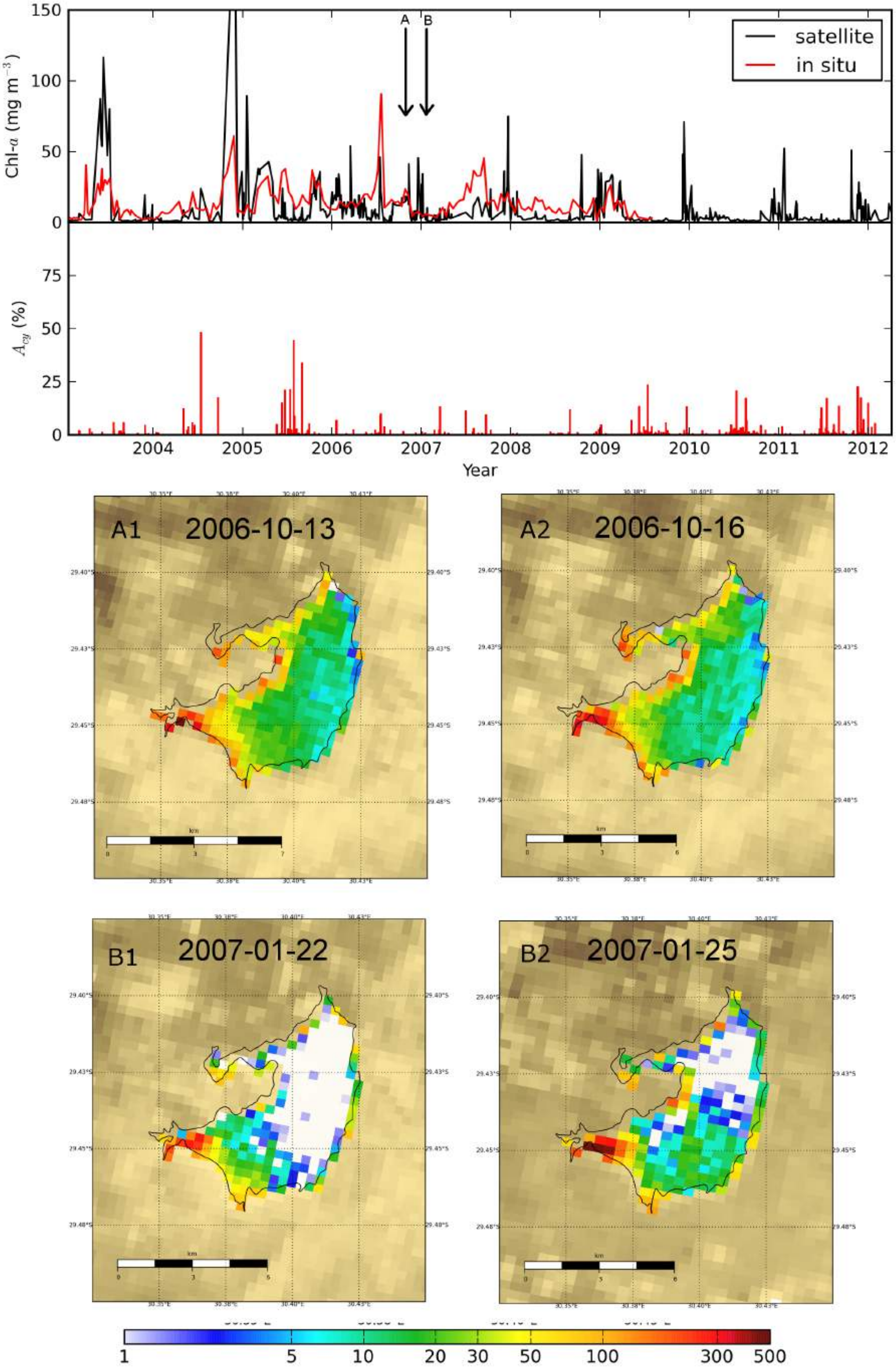

Figure 6.4.1: Albert Falls case study showing time series of *in situ* versus satellite chl-a and scenes acquired near or simultaneous to measurements made by Hart and Wragg (2009). A1-A2 are near first survey in October 2006 while B1-B2 are near the second survey in January 2007.

6.4.2 Case study: Verification of winter cyanobacteria blooms in Midmar

Winter cyanobacteria blooms that occurred in Midmar in 2005 were first reported by Oberholster and Botha (2007). Winter maxima of cyanobacteria are not expected since cyanobacteria are known to generally favour higher water temperatures ($> 20^\circ$C). However, fig. 6.3.11 shows that several South African reservoirs have winter cyanobacteria maxima including Chrissiesmeer, Kuhlange, Msingazi and Flag Boshielo. Interestingly, all but the latter of these waters are natural lakes. The explanation for winter cyano-blooms given by Oberholster and Botha (2007) related primarily to increased nutrient availability (nitrogen) tentatively attributed to large populations of waterfowl. It is possible that the same explanation might be given for the observation of winter cyanobacterial blooms in perennial lakes in the semi-arid eastern summer rainfall region of South Africa, which serve as a refuge for waterfowl during the dry winter months (e.g. Herremans, 1999, Petrie and Rogers, 1997).

Fig. 6.4.2 shows the time series of chl-*a* and cyanobacteria coverage and two satellite images from Midmar in July 2005. A general pattern of correlation is observed between the *in situ* and satellite chl-*a* estimates. More noticeably, a distinct increase in cyanobacteria coverage is detected during the winter of 2005, corresponding to the findings of Oberholster and Botha (2007). MERIS imagery from two dates during this period show cyanobacteria detected towards the shoreline (indicated by arrows) near the sample points in Oberholster and Botha (2007) (also indicated). The flag for cyanobacteria is raised for certain pixels (shown as green pixels - minimum cyanobacteria detection is 22 mg m^{-3}). The location of the cyanobacteria detection corresponds closely with the observations by Oberholster and Botha (2007). The record of cyanobacteria detection from 2003 to 2012 shows that the event is not an annual phenomenon, but appears more like an anomaly. The only other distinct winter cyanobacteria blooms in Midmar occurred during 2003, with much smaller events occurring during 2006, 2009 and 2010. Therefore, it appears that winter cyanobacteria blooms occurred infrequently and irregularly in Midmar between 2003 and 2012.

Therefore, cyanobacteria blooms are not a frequent nor persistent feature in Midmar, but rather occur on an event-scale. Furthermore, it appears that cyanobacteria are typically a minor component of the annual summer chl-*a* maximum in Midmar. The case study demonstrates the sensitivity and robustness of the MPH cyanobacteria flag to relatively low biomass cyanobacteria blooms, and how time series observations might be used for the detection of episodic cyanobacteria blooms.

6.4.3 Case study: Observation of surface scums in Hartbeespoort dam

Hartbeespoort serves as a ideal case study for surface scum detection since it is one of the most productive reservoirs in the world with exceptionally high biomass *M. aeruginosa* blooms (Matthews and Bernard, 2013a). High resolution Landsat imagery (30 m) acquired co-incident with MERIS is used here to verify the detection and classification of surface scum by the MPH algorithm. Fig. 6.4.3 shows two such examples, along with the time series for *in situ* and satellite chl-*a*. Surface

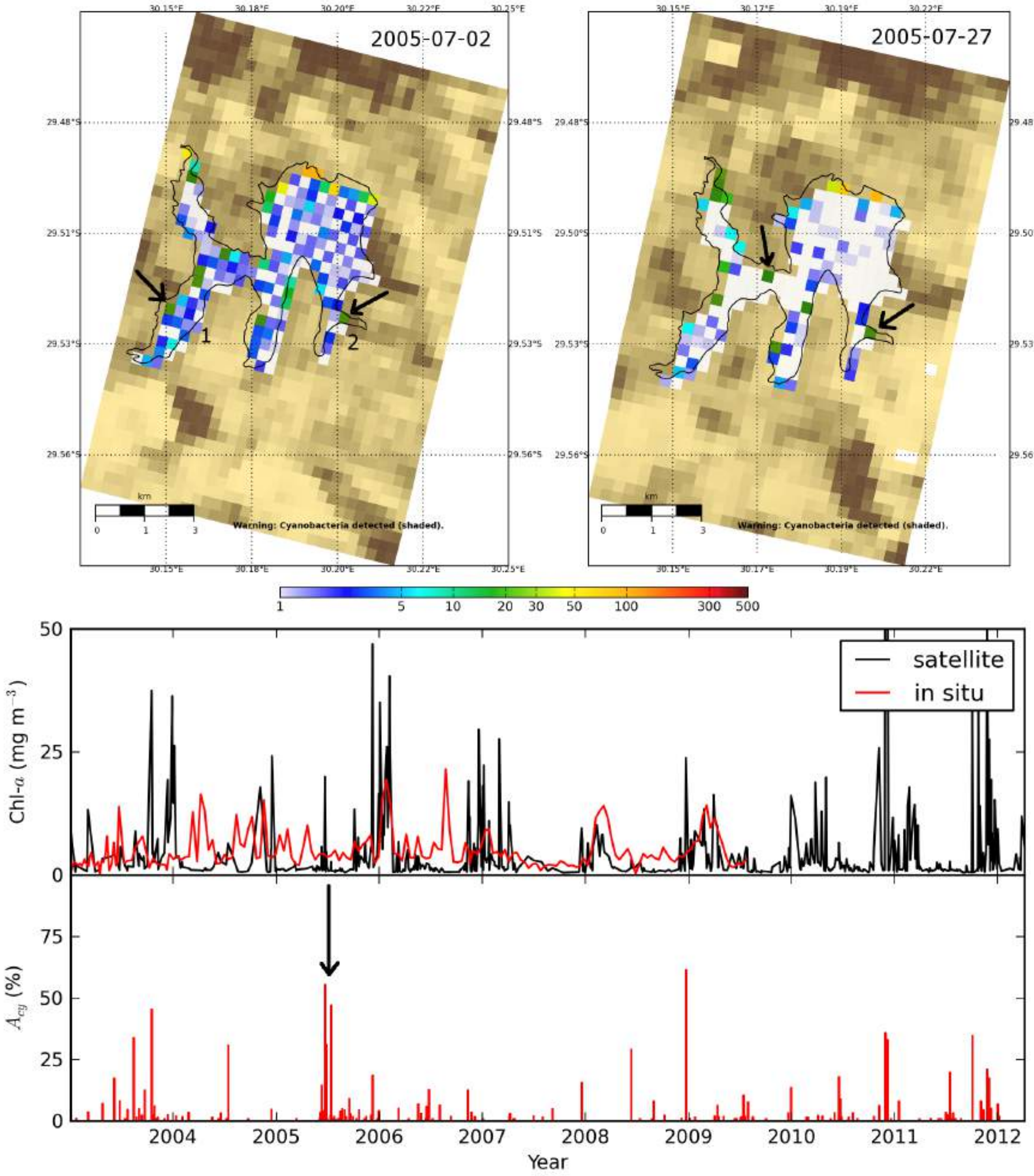

Figure 6.4.2: Midmar case study showing two scenes acquired near or simultaneous to measurements made by Oberholster and Botha (2007) illustrating winter cyanobacteria detection. The time series of *in situ* and satellite chl-a and cyanobacteria area coverage are also shown. The sample points in Oberholster and Botha (2007) are indicated at 1 and 2. The arrows indicate pixels identified as cyanobacteria, and bloom described by Oberholster and Botha (2007).

scums appear as bright green slicks on the water surface in the TM imagery, and as dark green pixels in the MERIS scenes (classified as chl-$a > 500$ mg m^{-3} and cyanobacteria flag raised). In the two examples, the Landsat and MERIS scenes were acquired less than 10 minutes apart. They show corresponding patterns in the spatial distribution of the surface scum. In these examples most of the reservoir surface is covered with scum, although small regions without scum visible in the TM scenes are correctly not classified as scum in the MERIS images. Thus the high resolution imagery verifies the identification of surface scums by the MPH algorithm and MERIS.

The chl-*a* time series shows a highly significant correlation over the time period, which is also reflected by the high correlation coefficient ($r = 0.9$, RMSE = 37.7 mg m^{-3}) for matchups. This is expected since the MPH algorithm is derived using data from Hartbeespoort and one other *Microcystis* dominant system. These results demonstrate the ability of the MPH algorithm for providing chl-*a* estimates and surface scum detection in hyper/eutrophic *Microcystis* dominant waters.

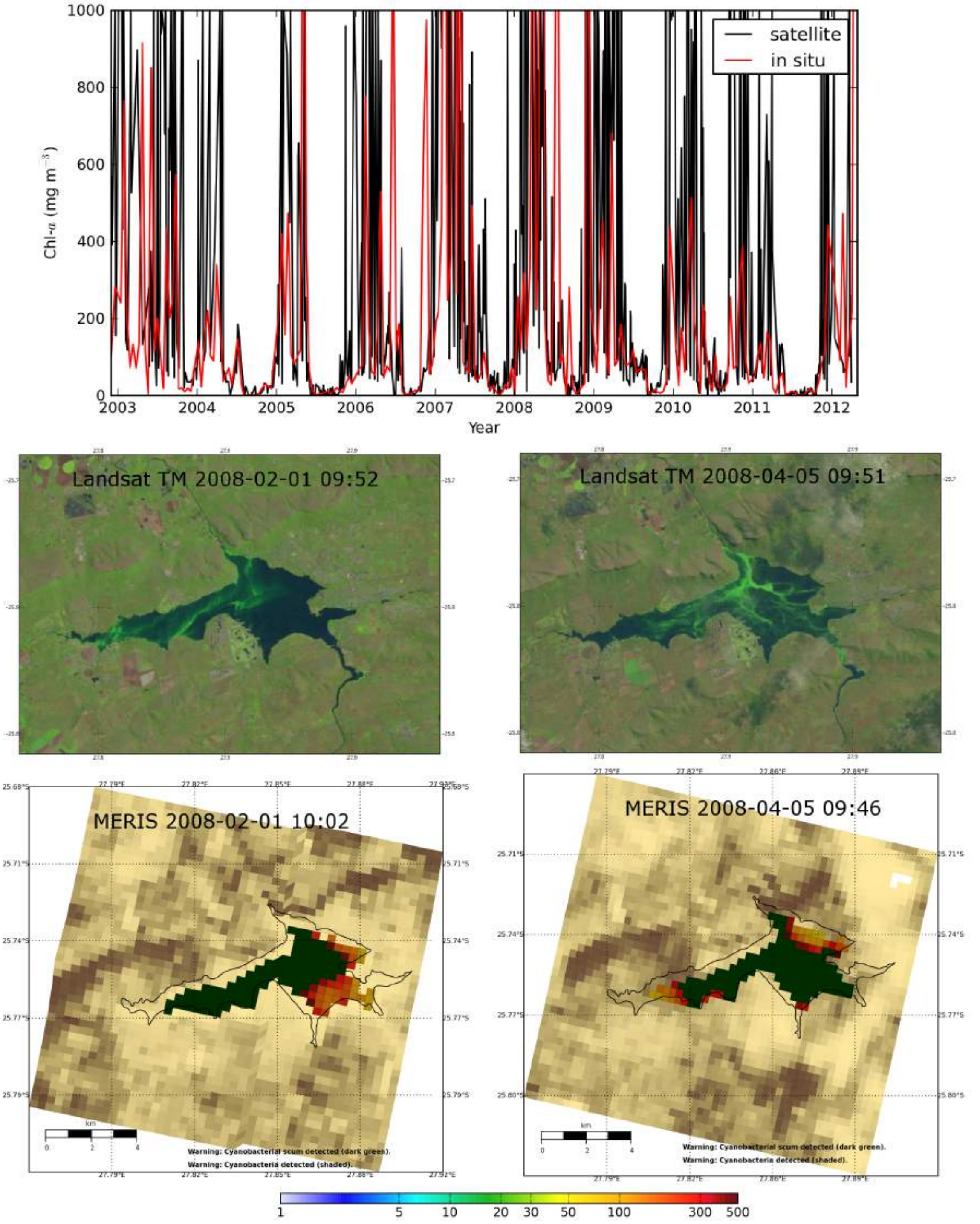

Figure 6.4.3: Hartbeespoort case study showing time series of *in situ* versus satellite chl-a and simultaneously acquired MERIS and Landsat imagery illustrating the detection of surface scum.

6.4.4 Reservoir classification and catchment scale analysis

The status with respect to eutrophication, cyanobacterial dominance and surface scum occurrence might be used to classify the condition of the reservoirs. The mean values determined for each of these variables are each plotted on each of the axes in fig. 6.4.4. The three dimensional plot shows the position of the reservoirs with respect to each other relative to the three variables. Using the classification ranges defined in preceding sections, an overall classification for each reservoir is presented in table 6.4.1. The range for each of the classes for chl-*a* are: < 50 mg m^{-3}, Mild; 50 to 150 mg m^{-3}, Moderate (Mod), 150 to 300 mg m^{-3}, High; and > 300 mg m^{-3}, Severe (Sev). For A_{cy} the classes are: $< 1\%$, insignificant; 1 to 10%, little; 10 to 30%, medium; and $> 30\%$, extensive. The classes for A_{sc} are: $< 1\%$, insignificant; 1 to 5%, little; 5 to 10%, medium; and $> 10\%$, extensive. Each of the classes are assigned a score from 1 (least impacted class) to 4 (most impacted class) or zero for none. The sum of the three scores gives the overall score for each reservoir (score column in table 6.4.1). In terms of the classification scheme the most severely impacted reservoirs are Darlington, Spitskop and Hartbeespoort, and the least impacted are Woodstock, Albert Falls, Tzaneen, Midmar and Zaaihoek. Note that the classification scheme is a combination of the three variables, so a low score does not necessarily mean the reservoir is the least eutrophic. The scoring might be used as as a scale for measuring priority for management of eutrophication and cyanobacterial blooms in the 50 largest South African reservoirs.

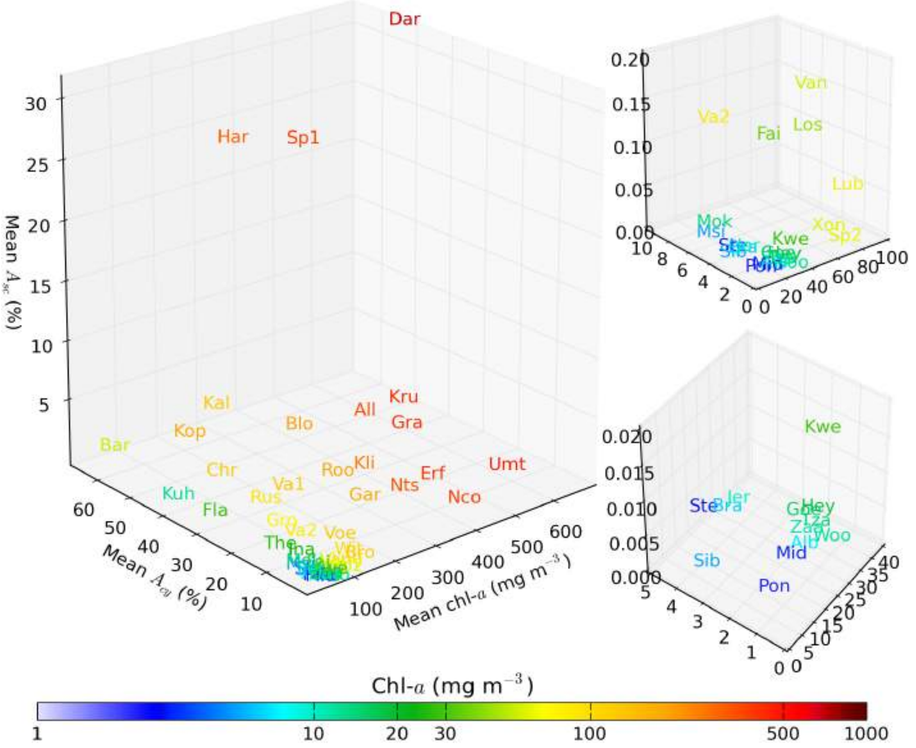

Figure 6.4.4: Three dimensional plot showing $\bar{\mathrm{chl}}$, $\bar{A_{cy}}$, and $\bar{A_{sc}}$ for 50 South African reservoirs. The inserts on the right hand side are zoomed in towards the origin for visibility. The color scale shows the values for $\bar{\mathrm{chl}}$. Reservoir names are abbreviated as in fig. 6.3.4.

Table 6.4.1: Overall classification of 50 South African reservoirs for 2003 to 2012 according to classes (see text).

Name	Chl-*a*	A_{cy}	A_{sc}	Score	Name	chl-*a*	A_{cy}	A_{sc}	Score
Gariep	High	little	little	7	Voelvlei	Mod	medium	insignificant	6
Vaal	Mod	medium	little	7	Midmar	Mild	insignificant	None	2
Bloemhof	High	medium	medium	9	Xonxa	Mod	little	insignificant	5
Pongolapoort	Mild	little	insignificant	4	Spioenkop	Mod	insignificant	None	3
Vanderkloof	Mod	little	insignificant	5	Ncora	Sev	little	little	8
Sterkfontein	Mild	little	None	3	Barberspan	Mod	extensive	insignificant	7
Lake Sibhayi	Mild	little	insignificant	4	Klipvoor	High	medium	little	8
Darlington	Sev	extensive	extensive	12	Grassridge	Sev	medium	little	9
Theewaterskloof	Mild	medium	None	4	Koppies	High	extensive	insignificant	8
Heyshope	Mild	little	None	3	Zaaihoek	Mild	insignificant	None	2
Kalkfontein	Mod	extensive	medium	9	Lubisi	Mod	little	insignificant	5
Grootdraai	Mod	medium	insignificant	6	Chrissiesmeer	Mod	extensive	insignificant	7
Spitskop	Sev	extensive	extensive	12	FlagBoshielo	Mild	extensive	None	5
Erfenis	Sev	medium	little	9	Goedertrou	Mild	little	None	3
Kuhlange	Mild	extensive	None	5	Rustfontein	Mod	medium	little	7
Allemanskraal	Sev	medium	medium	10	Fairview	Mild	little	insignificant	4
Woodstock	Mild	insignificant	None	2	Vaalkop	Mod	medium	insignificant	6
Loskop	Mild	little	insignificant	4	Kwena	Mild	little	insignificant	4
AlbertFalls	Mild	insignificant	None	2	Roodekoppies	High	medium	little	8
Brandvlei	Mild	little	None	3	Witbank	Mod	little	insignificant	5
Ntshingwayo	Sev	medium	little	9	Lake Msingazi	Mild	little	None	3
Tzaneen	Mild	insignificant	None	2	Bronkhorstspruit	Mod	little	None	4
Hartbeespoort	Sev	extensive	extensive	12	Jericho	Mild	little	None	3
Krugersdrift	Sev	medium	medium	10	Mokolo	Mild	little	None	3
Umtata	Sev	little	little	8	Inanda	Mild	little	insignificant	4

Reservoirs act as integrators and sentinels of change taking place in the broader catchment area in which they lie (Schindler, 2009). They are also sensitive to changes in climate related variables such as rainfall, and meteorology, which are captured through their physical, chemical and biological responses (Williamson et al., 2009). Therefore, through investigating the overall condition of the reservoirs located within specific catchments, clues may be provided to the overall condition of the catchment, specifically with respect to anthropogenic forcing of nutrient enrichment. A preliminary analysis of these effects is performed through integrating the statistics for the primary drainage basins (or catchment areas) within which the reservoirs lie. Table 6.4.2 shows the mean results for South African primary drainage basins, which are also displayed geographically for chl-*a* in fig. 6.4.5.

Importantly, the reservoirs are not evenly distributed among the drainage basins (see N in table 6.4.2) with some catchments having only one reservoir, or none. Other catchments such as Vaal and Phongolo have many reservoirs (13 and 8, respectively) meaning that assumptions of the catchment status can be made with more confidence. These two catchments might be used as contrasting examples. The reservoirs in the Vaal catchment have high chl-*a* (200 mg m^{-3}), cyanobacteria and surface scum coverage (34 and 5%, respectively). The Phongola catchment has on average low chl-*a* (just 13 mg m^{-3}), little cyanobacteria cover (8%) and almost no surface scum occurrence. Therefore the highly eutrophic Vaal catchment requires high priority as far as eutrophication man-

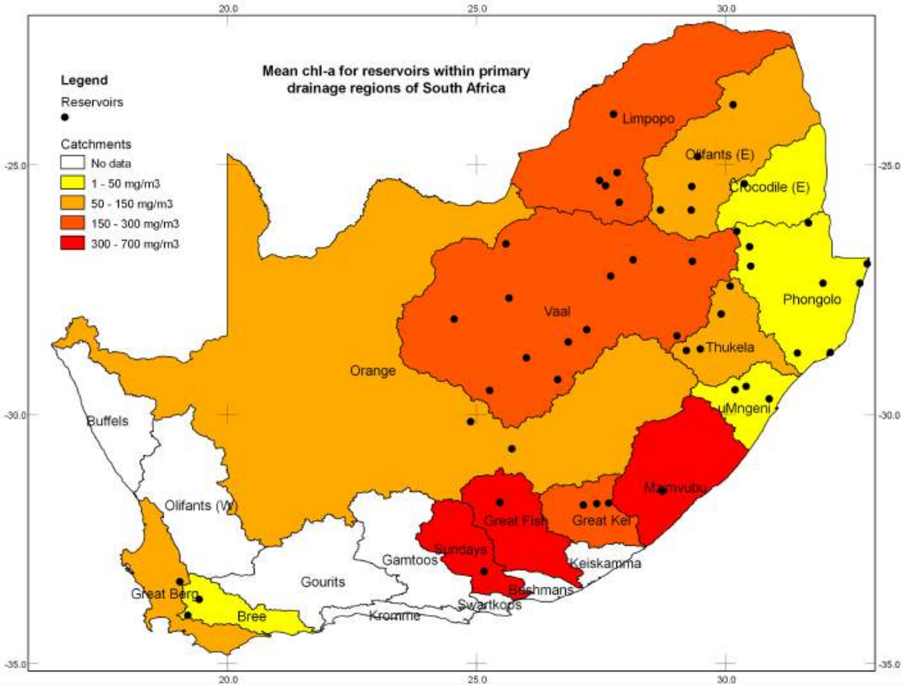

Figure 6.4.5: Map of South Africa showing primary drainage regions (catchments) in relation to the position of South Africa's 50 largest reservoirs (WRC, 1996). Catchments are colored according to the mean chl-*a* concentration for reservoirs located in that catchment (see legend). The catchments are labeled.

Table 6.4.2: Catchment integrated means and trends for chl-*a*, A_{cy} and A_{sc}. For trend columns the format is: mean (relative trend), mean significant trends only (no. significant trends).

Catchment	N	$\bar{\mathrm{chl}}$ mg m^{-3}	$\bar{A}_{cy}$ %	$\bar{A}_{sc}$ %	a_{chl} mg m^{-3} y^{-1}	$a_{A_{cy}}$ % y^{-1}	$a_{A_{sc}}$ % y^{-1}
Vaal	13	195.8	33.6	4.5	-1.36 (-0.01), 4.66 (2)	-1.54 (-0.05), -5.88(2)	-0.18 (-0.04), 0.37(2)
Phongolo	8	13	7.9	0	-1.26 (-0.10), -0.24(3)	-1.31 (-0.16), -1.93(5)	-0.01 (-0.35), -(-)
Limpopo	5	170	23.7	7.9	-7.55 (-0.04), -17.81(2)	1.59 (0.07), 2.43(2)	0.38 (0.05), 1.00(1)
Olifants (E)	5	61.1	8.4	0.2	-1.95 (-0.03), -12.02(1)	0.57(0.07), 0.11(2)	-0.01 (-0.04), 0.13(1)
Thukela	4	105.2	4.2	1	2.45 (0.02), -2.13(1)	0.57 (0.14), 2.22(1)	0.18 (0.19), -(-)
Great Kei	3	174.6	2.9	0.4	2.68 (0.02), -23.92(1)	0.22 (0.08), 0.85(1)	0.18 (0.51), 0.27(1)
uMngeni	3	11.3	2.9	0.7	-0.18 (-0.02), -1.43(1)	0.58 (0.20), 0.86(2)	0.06 (0.09), -(-)
Bree	2	15.9	9.2	0	-3.59 (-0.23), -3.59(2)	-2.72 (-0.29), -2.26(1)	- (-), -(-)
Orange	2	121	6.4	1.5	3.32 (0.03), -(-)	-1.09 (-0.17), -1.71(1)	-0.45 (-0.31), -0.45(2)
Crocodile (E)	1	28.6	1.9	0	-15.33 (-0.54), -15.33(1)	-0.93 (-0.49), -0.93(1)	- (-), -(-)
Great Berg	1	126	10.1	0.4	-51.14 (-0.41), -51.14(1)	-1.51 (-0.15), -(-)	0.12 (0.32), -(-)
Great Fish	1	427	25.1	3.7	-27.36 (-0.06), -27.36(1)	-0.74 (-0.03), -(-)	-0.7 (-0.19), -0.70(1)
Mzimvubu	1	487.9	4.5	2.5	-67.4 (-0.14), -67.40(1)	-0.18 (-0.04), -(-)	-0.2 (-0.08), -(-)
Sundays	1	696.8	56.1	31.2	47.08 (0.07), 47.08(1)	-4.67 (-0.08), -4.67(1)	-1.58 (-0.05), -(-)

agement is concerned, whilst the Phongolo catchment is substantially less impacted by eutrophication and cyanobacterial blooms. The impact of eutrophication on catchments in descending order is Vaal, Great Kei, Limpopo, Orange, Thukela, Olifants, Bree, Phongolo, and uMngeni (excluding catchments with only one observation). Assuming the reservoirs act as sentinels and integrators of the broader catchment, this information might be used to establish high priority catchments for eutrophication management.

As far as catchment trends are concerned, the results should be interpreted with caution, taking into account the number of reservoirs in the catchment, and the significance of the underlying trends. The overall catchment trend is calculated as the the mean of significant and non-significant annual trends (table 6.4.2). This value is normalised by the mean value for the catchment to calculate the relative trend. The mean of significant trends only and their number is also indicated for each catchment. The latter statistic might be used with more confidence, since the non-significant trends have higher uncertainty. However, given the very few number of trends significant at the 95% level, the mean of all trends can be used although with less certainty. The following discussion pertains only to catchments with more than 2 reservoirs, since it is difficult to make catchment-scale conclusions taking into account only one or two reservoirs.

For chl-*a* almost all the catchment-scale trends are negative (exception of Thukela and Great Kei). This is also reflected in the mean of significant only trends (however Vaal becomes positive). Therefore, it would seem that the drivers of hyper-nutrification decreased in most catchments over the time series (see section 6.3.2). Limpopo has the largest negative trend of -7.5 mg m^{-3} y^{-1}, relative 4% y^{-1}. The largest relevant trend is for Phongolo at -10% y^{-1}. Cyanobacteria cover however has positive trends in all these catchments with the exception of Vaal and Phongolo. uMngeni has the largest relative trend (20%) at 0.5% y^{-1}. The significant only trend calculations gives a similar result. Therefore overall it appears that cyanobacterial blooms became more common over the time series in most catchments. Similarly for surface scum, positive trends dominate the catchments (exception of Vaal and Phongolo). All the means of significant only trends are positive. Limpopo has the greatest positive trend at 0.38% y^{-1} (5% y^{-1} relative trend) but the largest relative trend is for Great Kei at 50% y^{-1}. As for chl-*a* the number of significant trends per catchment is very small (max.=2). It is therefore difficult to make confident assertions regarding the change in surface scum coverage (and other variables) over the time series, apart from the tentative conclusions drawn here.

6.5 CONCLUSIONS

The study presented time series of chl-*a*, cyanobacterial blooms and surface scums for the 50 largest South African reservoirs from 2003 to 2012 as observed by MERIS. The status, seasonality and trends of each of the variables has been presented for each of the reservoirs. The majority of the 50 reservoirs are hypertrophic (60%) with mean chl-*a* > 30 mg m^{-3}. The seasonality of chl-*a* production is strongly biased towards summer months, which peaks during January and February. Trends in chl-*a* suggest that overall eutrophication became less severe in the 50 reservoirs between 2005 and 2011. Cyanobacterial blooms were detected in all of the 50 reservoirs over the time period, but at insignificant/little coverage in 27 of the reservoirs. Persistent and extensive cyanobacteria coverage was determined for 9 reservoirs. Cyanobacteria blooms were strongly seasonal, with maximum coverage occurring during summer and autumn months. The detection of several reservoirs possessing winter cyanobacteria coverage maxima suggests this is a phenomenon occurring in South

African lakes, the cause of which is unknown. The overall trend in cyanobacteria coverage is uncertain, with an approximately equal number of significant positive and negative trends. Therefore the change in cyanobacteria occurrence in South African reservoirs remains uncertain.

Surface scum conditions existed in 33 of the 50 reservoirs over the time period. However, for most, the coverage was insignificant, with intermediate to extensive coverage occurring in only seven reservoirs. The seasonality of surface scum coverage was strongly biased towards summer and autumn months, reaching a maximum in February. Therefore, measures should be taken to reduce the risk of exposure to surface scums at these reservoirs. A new classification scheme for South African lakes combining the mean satellite estimates of chl-*a*, cyanobacteria and surface scum coverage identifies reservoirs most severely impacted by eutrophication and cyanobacterial blooms. This information can be used to prioritise management and mitigation strategies, in order to reduce health risks.

An independent validation of chl-*a* estimates from the MPH algorithm showed that gross trophic status can be determined with a high degree of confidence in both cyanobacteria and eukaryote-dominant waters. Oligotrophic and mesotrophic waters (chl-$a < 20\,\mathrm{mg\,m^{-3}}$) are more challenging, and further work is needed to elucidate and clarify the possible sources of error for estimating chl-*a* using the MPH approach. Detailed case studies showed that the spatial distribution and chl-*a* estimates in eukaryotic algal blooms can be determined with a high degree of certainty in small lakes. In addition cyanobacteria detection can be performed sufficiently, and surface scum detection with a high degree of confidence in eutrophic cyanobacteria-dominant waters.

The study has demonstrated both the power and efficiency of satellite based monitoring performed on a sub-continental scale. Time series of satellite-based chl-*a* estimates such as those derived here may be used in ecosystem models in order to establish the role played by lakes in global biogeochemical cycles. The study can also contribute to new avenues of research into catchment-scale climatological drivers of eutrophication and cyanobacterial blooms, as well as to models for predicting phytoplankton biomass and surface scum formation from meteorological and hydrological variables (e.g. Soranno, 1997). It has also demonstrated how satellite-based monitoring systems can play a vital role in supplementing traditional *in situ* monitoring networks to fill information gaps.

7

Conclusion

THE RESULTS OF THIS STUDY confirm the hypothesis that cyanobacteria can be differentiated from algae in optically-complex inland waters using the remote sensing techniques developed in this thesis. These include a simple empirically-based algorithm called the maximum-peak height or MPH algorithm (Chapter 2), as well as an advanced radiative transfer based algorithm which accounts for all of the inherent optical properties of the water constituents in waters ranging from oligotrophic to hypertrophic states (Chapter 5).

The MPH algorithm was found to successfully differentiate blooms of the cyanophyte *Microcystis aeruginosa* from those dominated by eukaryotic phytoplankton on the basis of enhanced backscattering in the red/near infra-red (NIR) region of the spectrum, as well as on the basis of unique reflectance features associated with absorption and fluorescence of cyanobacterial pigments. The algorithm also provides chl-*a* estimates across large trophic gradients, allowing for the effective characterisation of the severity of eutrophication in inland waters. In addition to providing a reliable index for the presence of cyanobacterial blooms, surface scum and floating vegetation, the MPH also provides quantitative estimates of cyanobacterial biomass, distinguishing it from previous efforts including the Floating Algal Index (Hu, 2009) and Maximum Chlorophyll Index (Gower et al., 2005) algorithms which provide only an index. Importantly, the MPH algorithm is applied to top-of-atmosphere data which effectively bypasses the need for an aerosol atmospheric correction which is typically prone to large errors over small and optically-complex inland water targets.

The absorption properties of the dominant water constituents of three reservoirs, namely Hartbeespoort, Loskop and Theewaterskloof, and their relationships with biogeochemical variables, have been characterised in detail in Chapter 3. This adds to the growing knowledge of the optical properties of optically-complex inland waters, particularly those that are hypertrophic. The occurrence of small-celled cyanobacteria species such as *M. aeruginosa* in inland waters caused a violation of the typical relationship between phytoplankton absorption, cell size and biomass usually observed in open-ocean waters as a result of the package effect.

The detailed investigation in Chapter 4 is one of the first studies that provide a full simulation of the effects of vacuole features on the optics of phytoplankton. The study has characterised the optical properties of *M. aeruginosa* and investigated the optical consequences of intracellular gas vacuoles using a two-layered sphere model. Gas vacuoles change the shape of the volume scattering function (VSF) and substantially increase spectral backscattering while simultaneously decreasing forward scattering. The study confirms that gas vacuoles lead to enhanced reflectance associated with cyanobacterial blooms and impart distinctive optical characteristics to vacuolate cyanobacteria. The two-layered model reproduced features in the spectral attenuation and the VSF that have previously been observed for vacuolate cyanobacteria, and therefore is a suitable model for investigating the effects of gas vacuole internal structure. These findings substantiate, from a bio-optical perspective, those of Chapter 2 that *M. aeruginosa* blooms might effectively be distinguished from dinoflagellate/diatom dominated assemblages on the basis of enhanced reflectance in the red and NIR.

An advanced radiative transfer based inversion algorithm for the detection of phytoplankton type and size, and IOPs, was successfully used to distinguish between high biomass blooms of *M. aeruginosa* and those of the large-celled dinoflagellate *Ceratium hirundinella*. The retrieval of size and type was more challenging in meso/oligotrophic conditions given the small contribution by phytoplankton to the bulk absorption/scattering budgets, and relatively larger contributions by dissolved and non-phytoplankton particulate matter. The absorption properties of the latter were retrieved more adequately in meso/oligotrophic waters. Chl-*a* and phytoplankton absorption was sufficiently retrieved over the entire trophic range of the data, however size and type detection is optimal when phytoplankton are significant or dominant optical contributors. The study confirms that robust detection of phytoplankton type and the discrimination of cyanobacteria from algae is best performed in higher biomass blooms (chl-$a > 20$ mg m^{-3}) because of the optically-complex nature of inland and near-coastal waters, as is the case for cyanobacteria accessory pigment phycocyanin (Kutser et al., 2006). A greater understanding of the ecology and population dynamics of cyanobacteria and algae in inland waters is required in order to fine-tune the optical models used by algorithms aimed at phytoplankton functional type detection. The full potential of the inversion algorithm will be seen through its application to satellite-based earth observation data; however this is dependent on a suitable atmospheric correction providing accurate water-leaving reflectance estimates for inland waters.

Finally, the status and trends of eutrophication, cyanbacterial blooms and surface scums were effectively characterised for the 50 largest South African reservoirs between 2002 and 2012 through application of the MPH algorithm to the MERIS Full Resolution data archive. Most of these reservoirs were determined as hypertrophic (60%), and cyanobacterial blooms occurred at least once in all 50 of the reservoirs over the time series. Cyanobacterial surface scum (chl-$a > 500$ mg m^{-3}) occurred in 33 of the 50 reservoirs and was timed with the onset of warmer temperatures during the summer months. Validation of the MPH algorithm using an independently acquired dataset indicated that the algorithm provided a reliable estimate of chl-*a* and trophic status, highlighting its potential for re-parameterisation using a dataset from lakes worldwide towards the development of a standard chl-*a* product for inland waters. The Chapter unequivocally shows the considerable contribution that systematic and near real-time earth observation can make towards both local monitoring efforts, and international initiatives such as the Group on Earth Observation water societal benefit area. This is one of the most comprehensive uses of earth observation data for eutrophication studies. Given that water quality is a critical issue in South Africa and around the world, the study demonstrates the considerable role that earth observation can make towards human health and environmental monitoring objectives (see `www.afro-sea.org.za/php/damSearch.php` for near real-time dissemination system for the MPH product, credit: Andy Rabagliati).

Several recommendations and areas of future research have been highlighted by the present study:

- Further research is required to enhance the cross-applicability of the MPH algorithm and the method used for cyanobacteria detection, which should be re-parameterised to provide the first global algorithm for quantitative eutrophication and cyanobacterial bloom detection. Furthermore the MPH should be adapted to the spectral characteristics of the planned Ocean and Land Colour Instrument (OLCI) on Sentinel-3 and other hyper/multispectral space-born instruments, including the South African EO-SAT 1 and Sentinel-2 high resolution visible sensors. The MPH should also be used to back-process the entire MERIS FR archive to provide the first global estimates of eutrophication and cyanobacteria occurrence for the world's freshwater systems.

- Despite the research conducted in this study, the precise (back)scattering properties of freshwater (vacuolate) cyanobacteria remain largely uncharacterised. Further research should be undertaken to measure the VSF over the full angular range to more adequately determine the magnitude and shape of cyanobacteria backscattering, and further validate the two-layer model output regarding the impact of gas vacuoles on the IOPs.

- The advanced radiative transfer inversion algorithm should be modified for retrievals of size and type from multi/hyperspectral satellite remote sensing instruments such as MERIS, the Hyperspectral Imager of the Coastal Ocean (HICO) and the planned OLCI. This however is dependent on the availability of an accurate water leaving reflectance product for inland and near-coastal waters, which should the subject of ongoing research. The optimal initial conditions for the inversion algorithm should be determined on a spectrum or per-pixel basis using a classification algorithm and/or a type-based pixel flagging procedure.

References

Aas, E. (1996). Refractive index of phytoplankton derived from its metabolite composition. *Journal of Plankton Research*, 18(12):2223–2249.

ACRI (2006). MERIS Level 2 Detailed Processing Model. Technical Report 7.

Aden, A. and Kerker, M. (1951). Scattering of electromagnetic waves from two concentric spheres. *Journal of Applied Physics*, 22:1242–1246.

Agusti, S. and Phlips, E. J. (1992). Light absorption by cyanobacteria: Implications of the colonial growth form. *Limnology and Oceanography*, 37(2):434–441.

Ahn, C. Y., Joung, S. H., Yoon, S. K., and Oh, H. M. (2007). Alternative Alert System for Cyanobacterial Bloom, Using Phycocyanin as a Level Determinant. *The Journal of Microbiology*, 45(2):98–104.

Ahn, Y. H., Bricaud, A., and Morel, A. (1992). Light backscattering efficiency and related properties of some phytoplankters. *Deep-Sea Research*, 39:1835–1855.

Arakawa, E. T., Tuminello, P. S., Khare, B. N., and Milham, M. E. (2001). Optical properties of ovalbumin in 0.130-2.50 microm spectral region. *Biopolymers*, 62(2):122–128.

Aurin, D. A. and Dierssen, H. M. (2012). Advantages and limitations of ocean color remote sensing in CDOM-dominated, mineral-rich coastal and estuarine waters. *Remote Sensing of Environment*, 125:181–197.

Babin, M. (1996). Remote sensing of sea surface Sun-induced chlorophyll fluorescence: consequences of natural variations in the optical characteristics of phytoplankton and the quantum yield of chlorophyll a fluorescence. *International Journal of Remote Sensing*, 17(12):2417–2448.

Babin, M. and Stramski, D. (2004). Variations in the mass-specific absorption coefficient of mineral particles suspended in water. *Limnology and Oceanography*, 49(3):756–767.

Babin, M., Stramski, D., Ferrari, G. M., Claustre, H., Bricaud, A., Obolensky, G., and Hoepffner, N. (2003). Variations in the light absorption coefficients of phytoplankton, nonalgal particles, and dissolved organic matter in coastal waters around Europe. *Journal of Geophysical Research-Oceans*, 108(C7)(3211):4.1–4.20.

Belzile, C., Vincent, W. F., Howard-Williams, C., Hawes, I., James, M. R., Kumagai, M., and Roesler, C. S. (2004). Relationships between spectral optical properties and optically active substances in a clear oligotrophic lake. *Water Resources Research*, 40(W12512):1–12.

Bennett, A. and Bogorad, L. (1973). Complementary chromatic adaptation in a filamentous blue-green alga. *The Journal of cell biology*, 58(2):419–435.

Berges, J. A. (1997). Ratios, regression statistics, and ”spurious” correlations. *Limnology and Oceanography*, 42(5):1006–1007.

Bernard, S. (2005). The bio-optical detection of harmful algal blooms.

Bernard, S., Probyn, T. A., and Barlow, R. G. (2001). Measured and modelled optical properties of particulate matter in the southern Benguela. *South African Journal of Science*, 97(9):410–420.

Bernard, S., Probyn, T. a., and Quirantes, A. (2009). Simulating the optical properties of phytoplankton cells using a two-layered spherical geometry. *Biogeosciences Discussions*, 6(1):1497–1563.

Bernard, S., Shillington, F. A., and Probyn, T. A. (2007). The use of equivalent size distributions of natural phytoplankton assemblages for optical modeling. *Optics Express*, 15(5):1995–2007.

Beutler, M. (2003). *Spectral fluorescence of chlorophyll and phycobilins as an in-situ tool of phytoplankton analysis - models, algorithms and instruments*. PhD thesis, Christian-Albrechts-Universität, Kiel, Germany.

Bidigare, R. R., Schofield, O., and Prezelin, B. B. (1989). Influence of zeaxanthin on quantum yield of photosynthesis of Synechococcus clone WH7803 (DC2)*. *Marine Ecology Progress Series*, 56:177–188.

Binding, C. and Greenberg, T. (2011). An assessment of MERIS algal products during an intense bloom in Lake of the Woods. *Journal of Plankton Research*, 33(5):793–806.

Binding, C., Jerome, J., Bukata, R., and Booty, W. (2008). Spectral absorption properties of dissolved and particulate matter in Lake Erie. *Remote Sensing of Environment*, 112(4):1702–1711.

Blank, C. E. and Sánchez-Baracaldo, P. (2010). Timing of morphological and ecological innovations in the cyanobacteria - a key to understanding the rise in atmospheric oxygen. *Geobiology*, 8(1):1–23.

Blondeau-Patissier, D., Brando, V. E., Oubelkheir, K., Dekker, A. G., Clementson, L. A., and Daniel, P. (2009). Bio-optical variability of the absorption and scattering properties of the Queensland inshore and reef waters, Australia. *Journal of Geophysical Research*, 114(C5):C05003.

Bogorad, L. (1975). Phycobiliproteins and complementary chromatic adaptation. *Annual review of plant physiology*, 26:369–401.

Bouvet, M. and Ramoino, F. (2009). Equalization of MERIS L1b products from the 2nd reprocessing. Technical Report 1, European Space Agency.

Bricaud, A., Babin, M., Claustre, H., Ras, J., and Tièche, F. (2010). Light absorption properties and absorption budget of Southeast Pacific waters. *Journal of Geophysical Research*, 115(C8):C08009.

Bricaud, A., Babin, M., Morel, A., and Claustre, H. (1995). Variability in the chlorophyll-specific absorption coefficients of natural phytoplankton: Analysis and parameterization. *Journal of Geophysical Research*, 100(C7):13321–13332.

Bricaud, A., Bedhomme, A. L., and Morel, A. (1988). Optical properties of diverse phytoplanktonic species: experimental results and theoretical interpretation. *Journal of Plankton Research*, 10(5):851–873.

Bricaud, A., Claustre, H., Ras, J., and Oubelkheir, K. (2004). Natural variability of phytoplanktonic absorption in oceanic waters: influence of the size structure of algal populations. *Journal of Geophysical Research*, 109(C11010):1–12.

Bricaud, A. and Morel, A. (1986). Light attenuation and scattering by phytoplanktonic cells: a theoretical modeling. *Applied Optics*, 25(4):571–580.

Bricaud, A., Morel, A., and Prieur, L. (1981). Absorption by dissolved organic matter of the sea (yellow substance) in the UV and visible domains. *Limnology and Oceanography*, 26(1):43–53.

Bricaud, A., Morel, A., and Prieur, L. (1983). Optical Efficiency Factors of Some Phytoplankters. *Limnology and Oceanography*, 28(5):816–832.

Campbell, G., Phinn, S. R., and Daniel, P. (2010). The specific inherent optical properties of three subtropical and tropical water reservoirs in Queensland, Australia. *Hydrobiologia*, 658(1):233–252.

Campbell, J. W. and Feng, H. (2005). The empirical chlorophyll algorithm for MODIS: Testing the OC3M algorithm using NOMAD data. In *Ocean Color Bio-optical Algorithm Mini-workshop, 27 - 29 September 2005*, pages 1–9, Durham, New Hampshire. NASA.

Carvalho, L., Poikane, S., Lyche Solheim, a., Phillips, G., Borics, G., Catalan, J., Hoyos, C., Drakare, S., Dudley, B. J., Järvinen, M., Laplace-Treyture, C., Maileht, K., McDonald, C., Mischke, U., Moe, J., Morabito, G., Nõges, P., Nõges, T., Ott, I., Pasztaleniec, a., Skjelbred, B., and Thackeray, S. J. (2012). Strength and uncertainty of phytoplankton metrics for assessing eutrophication impacts in lakes. *Hydrobiologia*, 704(1):127–140.

Cavalli, R. M., Laneve, G., Fusilli, L., Pignatti, S., and Santini, F. (2009). Remote sensing water observation for supporting Lake Victoria weed management. *Journal of environmental management*, 90(7):2199–2211.

Chami, M., McKee, D., Leymarie, E., and Khomenko, G. (2006). Influence of the angular shape of the volume-scattering function and multiple scattering on remote sensing reflectance. *Applied optics*, 45(36):9210–9220.

Chorus, I., Falconer, I. R., Salas, H. J., and Bartram, J. (2000). Health risks caused by freshwater cyanobacteria in recreational waters. *Journal of Toxicology and Environmental Health*, Part B(3):323–347.

Ciddor, P. E. (1996). Refractive index of air: new equations for the visible and near infrared. *Applied optics*, 35(9):1566–1573.

Ciotti, A. M. and Bricaud, A. (2006). Retrievals of a size parameter for phytoplankton and spectral light absorption by colored detrital matter from water-leaving radiances at SeaWiFS channels in a continental shelf region off Brazil. *Limnology and Oceanography: Methods*, 4:237–253.

Ciotti, A. M., Cullen, J. J., and Lewis, M. R. (1999). A semi-analytical model of the influence of phytoplankton community structure on the relationship between light attenuation and ocean color. *Journal of geophysical research*, 104(C1):1559–1578.

Ciotti, A. M., Lewis, M. R., and Cullen, J. J. (2002). Assessment of the relationships between dominant cell size in natural phytoplankton communities and the spectral shape of the absorption coefficient. *Limnology and Oceanography*, 47(2):404–417.

Clavano, W. R., Boss, E., and Karp-boss, L. (2007). Inherent optical properties of non-spherical marine-like particles - from theory to observation. *Oceanography and Marine Biology: An Annual Review*, 45:1–38.

Codd, G. A. (2000). Cyanobacterial toxins, the perception of water quality, and the prioritisation of eutrophication control. *Ecological Engineering*, 16(1):51–60.

Crétaux, J.-F., Jelinski, W., Calmant, S., Kouraev, A., Vuglinski, V., Bergé-Nguyen, M., Gennero, M.-C., Nino, F., Abarca Del Rio, R., Cazenave, A., and Maisongrande, P. (2011). SOLS: A lake database to monitor in the Near Real Time water level and storage variations from remote sensing data. *Advances in Space Research*, 47(9):1497–1507.

Dabrowski, J. (2012). *Water quality, metal bioaccumulation and parasite communities of Oreochromis mossambicus in Loskop Dam, Mpumalanga, South Africa.* M.sc., University of Pretoria, Pretoria.

Dall'Olmo, G. and Gitelson, A. a. (2005). Effect of bio-optical parameter variability on the remote estimation of chlorophyll-a concentration in turbid productive waters: experimental results. *Applied Optics*, 44(3):412–422.

de Figueiredo, D. R., Azeiteiro, U. M., Esteves, S. M., Gonçalves, F. J. M., and Pereira, M. J. (2004). Microcystin-producing blooms–a serious global public health issue. *Ecotoxicology and environmental safety*, 59(2):151–63.

Deblois, C. P., Marchand, A., and Juneau, P. (2013). Comparison of Photoacclimation in Twelve Freshwater Photoautotrophs (Chlorophyte, Bacillaryophyte, Cryptophyte and Cyanophyte) Isolated from a Natural Community. *PLOS ONE*, 8(3):1–14.

Defoin-Platel, M. and Chami, M. (2007). How ambiguous is the inverse problem of ocean color in coastal waters? *Journal of Geophysical Research*, 112(C03004):1–16.

Dekker, A. (1993). *Detection of optical water quality parameters for eutrophic waters by high resolution remote sensing*. PhD thesis, Free University, Netherlands.

Dekker, A. G., Vos, R. J., and Peters, S. W. M. (2001). Comparison of remote sensing data, model results and in situ data for total suspended matter (TSM) in the southern Frisian lakes. *Science of the Total Environment*, 268(1-3):197–214.

Desortová, B. (1981). Relationship between chlorophyll-a concentration and phytoplankton biomass in several reservoirs in Czechoslovakia. *Int. Revue ges. Hydrobiol.*, 66(2):153–169.

Dierberg, F. E. and Carriker, N. E. (1994). Field testing two instruments for remotely sensing water quality in the Tennessee Valley. *Environmental science & technology*, 28(1):16–25.

Dierssen, H. M., Kudela, R. M., Ryan, J. P., and Zimmerman, R. C. (2006). Red and black tides: Quantitative analysis of water-leaving radiance and perceived color for phytoplankton, colored dissolved organic matter, and suspended sediments. *Limnology and Oceanography*, 51(6):2646–2659.

Doerffer, R. and Schiller, H. (2007). The MERIS Case 2 water algorithm. *International Journal of Remote Sensing*, 28(3-4):517–535.

Downing, J. A., Watson, S. B., and McCauley, E. (2001). Predicting Cyanobacteria dominance in lakes. *Canadian Journal of Fisheries and Aquatic Sciences*, 58(10):1905–1908.

Doxaran, D., Cherukuru, N. C., Lavender, S. J., and Moore, G. F. (2004). Use of a Spectralon panel to measure the downwelling irradiance signal: case studies and recommendations. *Applied optics*, 43(32):5981–5986.

Dubelaar, G. B. and van der Reijden, C. S. (1995). Size distributions of Microcystis aeruginosa colonies: a flow cytometric approach. *Water Science and Technology*, 32(4):171–176.

Dubelaar, G. B., Visser, J. W., and Donze, M. (1987). Anomalous behaviour of forward and perpendicular light scattering of a cyanobacterium owing to intracellular gas vacuoles. *Cytometry*, 8(4):405–412.

Ducklow, H. and Dickson, A. (1994). Chapter 14. Measurement of Chlorophyll a and Paeopigments by Fluorometric Analysis. *JGOFS Protocols*, pages 119–122.

Dupouy, C., Benielli-Gary, D., Neveux, J., Dandonneau, Y., and Westberry, T. K. (2011). An algorithm for detecting Trichodesmium surface blooms in the South Western Tropical Pacific. *Biogeosciences*, 8(12):3631–3647.

Dupouy, C., Neveux, J., Dirberg, G., Röttgers, R., Barboza Tenório, M. M., and Ouillon, S. (2008). Bio-optical properties of the marine cyanobacteria Trichodesmium spp. *Journal of Applied Remote Sensing*, 2(023503):1–17.

DWA (2013a). Hydrological services data extracted between 1990-01-01 and 2013-01-01. Hydrological Services, Department of Water Affairs, Pretoria, http://www.dwaf.gov.za/hydrology/.

DWA (2013b). National Water Management System data extracted between 2002-01-01 and 2012-04-28. Department of Water Affairs, Pretoria, http://www.dwaf.gov.za/iwqs/report.aspx.

Effler, S. W., Strait, C. M., Perkins, M., and Donnell, D. M. O. (2012). Optical characterization and tests of closure for Oneida Lake, New York, USA. *Inland waters*, 2:211–228.

Environmental Protection Agency (1983). Methods for chemical analysis of water and wastes. Technical Report 600479020, United States Environmental Protection Agency, Cincinnati, Ohio.

Estapa, M. L., Boss, E., Mayer, L. M., and Roesler, C. S. (2012). Role of iron and organic carbon in mass-specific light absorption by particulate matter from Louisiana coastal waters. *Limnology and Oceanography*, 57(1):97–112.

Fawcett, A., Pitcher, G., Bernard, S., Cembella, A., and Kudela, R. (2007). Contrasting wind patterns and toxigenic phytoplankton in the southern Benguela upwelling system. *Marine Ecology Progress Series*, 348:19–31.

Ferrari, G. M. and Tassan, S. (1998). A method for the experimental determination of light absorption by aquatic heterotrophic bacteria. *Journal of Plankton Research*, 20(4):757–766.

Ferrari, G. M. and Tassan, S. (1999). A method using chemical oxidation to remove light absorption by phytoplankton pigments. *Journal of Phycology*, 35(5):1090–1098.

Fleming, L. E., Rivero, C., Burns, J., Williams, C., Bean, J. A., Shea, K. A., and Stinn, J. (2002). Blue green algal (cyanobacterial) toxins, surface drinking water, and liver cancer in Florida. *Harmful Algae*, 1(2):157–168.

Fogg, G. E., Stewart, W. D. P., Fay, P., and Walsby, A. E. (1973). Gas vacuoles. In *The blue-green algae*, pages 93–110. Academic Press, London.

Fournier, G. R. and Forand, L. J. (1994). Analytic phase function for ocean water. In Jaffe, J. F., editor, *Proc. SPIE 2258, Ocean Optics XII, 194 (October 26)*, pages 194–201, Bergen, Norway.

Fuhs, G. (1969). Interferenzmikroskopische beobachtungen an den Polyphosphatkoerpern und gasvacuolen von cyanophyceen. *Osterreichische botanische Zeitschrift*, 116:411–422.

Galat, D. and Verdin, J. (1989). Patchiness, collapse and succession of a cyanobacterial bloom evaluated by synoptic sampling and remote sensing. *Journal of Plankton Research*, 11(5):925–948.

Gallegos, C. L., Davies-Colley, R. J., and Gall, M. (2008). Optical closure in lakes with contrasting extremes of reflectance. *Limnology and Oceanography*, 53(5):2021–2034.

Ganf, G. G., Oliver, R. L., and Walsby, A. E. (1989). Optical properties of gas-vacuolate cells and colonies of Microcystis in relation to light attenuation in a turbid, stratified reservoir (Mount Bold Reservoir, South Australia). *Australian Journal of Marine and Freshwater Research*, 40(6):595–611.

Giardino, C., Brando, V. E., Dekker, A. G., Strömbeck, N., and Candiani, G. (2007). Assessment of water quality in Lake Garda (Italy) using Hyperion. *Remote Sensing of Environment*, 109(2):183–195.

Giardino, C., Candiani, G., and Zilioli, E. (2005). Detecting Chlorophyll-a in Lake Garda Using TOA MERIS Radiances. *Photogrammetric Engineering & Remote Sensing*, 71(9):1045–1051.

Gillis, D. B., Bowles, J. H., and Moses, W. J. (2013). Improving the retrieval of water inherent optical properties in noisy hyperspectral data through statistical modeling. *Optics express*, 21(18):21306–21316.

Gitelson, A. (1992). The peak near 700 nm on radiance spectra of algae and water: relationships of its magnitude and position with chlorophyll concentration. *International Journal of Remote Sensing*, 13(17):3367–3373.

Gitelson, A., Garbuzov, G., Szilagyi, F., Mittenzwey, K. H., Karnieli, A., and Kaiser, A. (1993). Quantitative remote sensing methods for real-time monitoring of inland waters quality. *International Journal of Remote Sensing*, 14(7):1269–1295.

Gitelson, A., Mayo, M., Yacobi, Y. Z., Parparov, A., and Berman, T. (1994). The use of high-spectral-resolution radiometer data for detection of low chlorophyll concentrations in Lake Kinneret. *Journal of Plankton Research*, 16(8):993–1002.

Gitelson, A. A., Dall'Olmo, G., Moses, W., Rundquist, D. C., Barrow, T., Fisher, T. R., Gurlin, D., and Holz, J. (2008). A simple semi-analytical model for remote estimation of chlorophyll-a in turbid waters: validation. *Remote Sensing of Environment*, 112(9):3582–3593.

Gitelson, A. A., Gurlin, D., Moses, W. J., and Barrow, T. (2009). A bio-optical algorithm for the remote estimation of the chlorophyll-a concentration in case 2 waters. *Environmental Research Letters*, 4:45003.

Golecki, J. R. and Drews, G. (1982). Supramolecular organization and composition of membranes. In Carr, N. G. and Whitton, B. A., editors, *The biology of cyanobacteria*, chapter 6, pages 125–142. Blackwell Scientific, Berkeley and Los Angeles.

Gons, H., Auer, M., and Effler, S. (2008). MERIS satellite chlorophyll mapping of oligotrophic and eutrophic waters in the Laurentian Great Lakes. *Remote Sensing of Environment*, 112(11):4098–4106.

Gons, H. J. (1999). Optical teledetection of chlorophyll a in turbid inland waters. *Environmental Science & Technology*, 33(7):1127–1132.

Gons, H. J. (2005). Effect of a waveband shift on chlorophyll retrieval from MERIS imagery of inland and coastal waters. *Journal of Plankton Research*, 27(1):125–127.

Gons, H. J., Burger-wiersma, T., Otten, J. H., and Rijkeboer, M. (1992). Coupling of phytoplankton and detritus in a shallow, eutrophic lake (Lake Loosdrecht, The Netherlands). *Hydrobiologia*, 233:51–59.

Gons, H. J., Rijkeboer, M., and Ruddick, K. G. (2002). A chlorophyll-retrieval algorithm for satellite imagery (Medium Resolution Imaging Spectrometer) of inland and coastal waters. *Journal of Plankton Research*, 24(9):947–951.

Gordon, H. R. (2002). Inverse methods in hydrologic optics. *Oceanologia*, 44(1):9–58.

Gordon, H. R., Brown, O. B., and Jacobs, M. M. (1975). Computed relationships between the inherent and apparent optical properties of a flat homogeneous ocean. *Applied optics*, 14(2):417–427.

Gower, J. and King, S. (2007). Validation of chlorophyll fluorescence derived from MERIS on the west coast of Canada. *International Journal of Remote Sensing*, 28(3):625–635.

Gower, J., King, S., Borstad, G., and Brown, L. (2005). Detection of intense plankton blooms using the 709 nm band of the MERIS imaging spectrometer. *International Journal of Remote Sensing*, 26(9):2005–2012.

Gower, J. F. R. (1980). Observations of in situ fluorescence of chlorophyll-a in Saanich Inlet. *Boundary-Layer Meteorology*, 18(3):235–245.

Gower, J. F. R., Doerffer, R., and Borstad, G. a. (1999). Interpretation of the 685nm peak in water-leaving radiance spectra in terms of fluorescence, absorption and scattering, and its observation by MERIS. *International Journal of Remote Sensing*, 20(9):1771–1786.

Gregg, W. W. and Carder, K. L. (1990). A simple spectral solar irradiance model for cloudless maritime atmospheres. *Limnology and Oceanography*, 35(8):1657–1675.

Guanter, L., Ruiz-Verdú, A., Odermatt, D., Giardino, C., Simis, S., Estellés, V., Heege, T., Domínguez-Gómez, J. A., and Moreno, J. (2010). Atmospheric correction of ENVISAT/MERIS data over inland waters: Validation for European lakes. *Remote Sensing of Environment*, 114(3):467–480.

Hale, G. M. and Querry, M. R. (1973). Optical Constants of Water in the 200-nm to 200-microm Wavelength Region. *Applied optics*, 12(3):555–563.

Hansen, J. and Travis, L. (1974). Light scattering in planetary atmospheres. *Space Science Reviews*, 16:527–610.

Harding, W. R. (1997). Phytoplankton primary production in a shallow, well-mixed, hypertrophic South African lake. *Hydrobiologia*, 344:87–102.

Harding, W. R. and Paxton, B. R. (2001). Cyanobacteria in South Africa: a review (TT 153/01). Technical report, Water Research Commission.

Hart, R. C. and Wragg, P. D. (2009). Recent blooms of the dinoflagellate Ceratium in Albert Falls Dam (KZN): History, causes, spatial features and impacts on a reservoir ecosystem and its zooplankton. *Water SA*, 35(4):455–468.

Herremans, M. (1999). Waterbird diversity, densities, communities and seasonality in the Kalahari Basin, Botswana. *Journal of Arid Environments*, 43(3):319–350.

Hirata, T., Aiken, J., Hardman-Mountford, N., Smyth, T., and Barlow, R. (2008). An absorption model to determine phytoplankton size classes from satellite ocean colour. *Remote Sensing of Environment*, 112(6):3153–3159.

Hoge, F. E., Lyon, P. E., Swift, R. N., Yungel, J. K., Abbott, M. R., Letelier, R. M., and Esaias, W. E. (2003). Validation of Terra-MODIS Phytoplankton Chlorophyll Fluorescence Line Height. I. Initial Airborne Lidar Results. *Applied Optics*, 42(15):2767.

Holm-Hansen, O., Lorenzen, C. J., Holmes, R. W., and Strickland, J. D. H. (1965). Fluorometric Determination of Chlorophyll. *Journal du Conseil*, 30(1):3.

Hoogenboom, H. J., Dekker, A. G., and Althuis, I. A. (1998). Simulation of AVIRIS Sensitivity for Detecting Chlorophyll over Coastal and Inland Waters. *Remote Sensing of Environment*, 65:333–340.

Hu, C. (2009). A novel ocean color index to detect floating algae in the global oceans. *Remote Sensing of Environment*, 113(10):2118–2129.

Hu, C., Cannizzaro, J., Carder, K. L., Muller-Karger, F. E., and Hardy, R. (2010a). Remote detection of Trichodesmium blooms in optically complex coastal waters: Examples with MODIS full-spectral data. *Remote Sensing of Environment*, 114(9):2048–2058.

Hu, C., Lee, Z., Ma, R., Yu, K., Li, D., and Shang, S. (2010b). Moderate Resolution Imaging Spectroradiometer (MODIS) observations of cyanobacteria blooms in Taihu Lake, China. *Journal of Geophysical Research*, 115(C4):1–20.

Hunter, P. D., Tyler, A. N., Carvalho, L., Codd, G. a., and Maberly, S. C. (2010). Hyperspectral remote sensing of cyanobacterial pigments as indicators for cell populations and toxins in eutrophic lakes. *Remote Sensing of Environment*, 114(11):2705–2718.

Ibelings, B. W., Kroon, B. M. A., and Mur, L. R. (1994). Acclimation of photosystem II in a cyanobacterium and a eukaryotic green alga to high and fluctuating photosynthetic photon flux densities, simulating light regimes induced by mixing in lakes. *New Phytologist*, 128(3):407–424.

IOCCG (2006). Remote sensing of inherent optical properties: Fundamentals, tests of algorithms, and applications. Technical Report Reports of the International Ocean-Colour Coordinating Group, No. 5, IOCCG, Dartmouth, Canada.

Johnk, K. D., Huisman, J., Sharples, J., Sommeijer, B., Visser, P. M., and Stroom, J. M. (2008). Summer heatwaves promote blooms of harmful cyanobacteria. *Global Change Biology*, 14(3):495–512.

Johnsen, G., Samset, O., Granskog, L., and Sakshaug, E. (1994). In vivo absorption characteristics in 10 classes of bloom-forming phytoplankton: taxonomic characteristics and responses to photoadaptation by means of discriminant and HPLC analysis. *Marine Ecology Progress Series*, 105:149–157.

Jost, M. and Jones, D. (1970). Morphological parameters and macro-molecular organization of gas vacuole membranes of Microcystis aeruginosa Kuetz. emend. Elenkin. *Canadian Journal of Microbiology*, 16:159–164.

Jost, M. and Zehnder, A. (1966). Die Gasvakuolen der Blaualge Microcystis aeruginosa. *Schweiz, Z. Hydrol.*, 28:1–3.

Jupp, D. L. B., Kirk, J. T. O., and Harris, G. P. (1994). Detection, identification and mapping of cyanobacteria: Using remote sensing to measure the optical quality of turbid inland waters. *Australian Journal of Marine and Freshwater Research*, 45(5):801–828.

Kirk, J. T. O. (1975). A Theoretical Analysis of the Contribution of Algal Cells to the Attenuation of Light Within Natural Waters. II. Spherical Cells. *New Phytologist*, 75(1):21–36.

Kirk, J. T. O. (1994). *Light and photosynthesis in aquatic ecosystems*. Cambridge University Press, Bristol.

Kitchen, J. C. and Zaneveld, J. R. V. (1992). A Three-Layered Sphere Model of the Optical Properties of Phytoplankton. *Limnology and Oceanography*, 37(8):1680–1690.

Kutser, T. (2004). Quantitative detection of chlorophyll in cyanobacterial blooms by satellite remote sensing. *Limnology and Oceanography*, 49(6):2179–2189.

Kutser, T. (2009). Passive optical remote sensing of cyanobacteria and other intense phytoplankton blooms in coastal and inland waters. *International Journal of Remote Sensing*, 30(17):4401–4425.

Kutser, T., Metsamaa, L., and Dekker, A. G. (2008). Influence of the vertical distribution of cyanobacteria in the water column on the remote sensing signal. *Estuarine, Coastal and Shelf Science*, 78:649–654.

Kutser, T., Metsamaa, L., Strömbeck, N., and Vahtmäe, E. (2006). Monitoring cyanobacterial blooms by satellite remote sensing. *Estuarine, Coastal and Shelf Science*, 67(1-2):303–312.

Kutser, T., Paavel, B., and Metsamaa, L. (2009). Mapping coloured dissolved organic matter concentration in coastal waters. *International Journal of Remote Sensing*, 30(22):5843–5849.

Laurion, I., Lami, a., and Sommaruga, R. (2002). Distribution of mycosporine-like amino acids and photoprotective carotenoids among freshwater phytoplankton assemblages. *Aquatic Microbial Ecology*, 26:283–294.

Le, C., Hu, C., English, D., Cannizzaro, J., Chen, Z., Kovach, C., Anastasiou, C. J., Zhao, J., and Carder, K. L. (2013). Inherent and apparent optical properties of the complex estuarine waters of Tampa Bay: What controls light? *Estuarine, Coastal and Shelf Science*, 117:54–69.

Le, C., Li, Y., Zha, Y., Sun, D., Huang, C., and Zhang, H. (2011). Remote estimation of chlorophyll a in optically complex waters based on optical classification. *Remote Sensing of Environment*, 115(2):725–737.

Lee, Z. (2004). Absorption spectrum of phytoplankton pigments derived from hyperspectral remote-sensing reflectance. *Remote Sensing of Environment*, 89(3):361–368.

Lee, Z., Carder, K. L., and Arnone, R. A. (2002). Deriving inherent optical properties from water color: a multiband quasi-analytical algorithm for optically deep waters. *Applied Optics*, 41:5755–5772.

Lee, Z., Du, K., Voss, K., Zibordi, G., Lubac, B., Amone, R., Weidemann, A., and Arnone, R. (2011). An inherent-optical-property-centred approach to correct the angular effects in water-leaving radiance. *Applied optics*, 50(19):3155–3167.

Lee, Z., Hu, C., Gray, D., Casey, B., Arnone, R., Weidemann, A., Ray, R., and Goode, W. (2007). Properties of coastal waters around the US: preliminary results using MERIS data. In *Proc. Envisat Symposium, 23–27 April 2007*, number c, Montreux, Switzerland. ESA SP-636.

Lehmann, H. and Jost, M. (1971). Kinetics of the assembly of gas vacuoles in the blue-green alga Microcystis aeruginosa Kuetz. emend. Elekin. *Archives of Microbiology*, 79:59–68.

Letelier, M. and Abbott, M. R. (1996). An analysis of chlorophyll fluorescence algorithms for the moderate resolution imaging spectrometer (MODIS). *Remote Sensing of Environment*, 58(2):215–223.

Lung'ayia, H. B. O., M'harzi, A., Tackx, M., Gichuki, J., and Symoens, J. J. (2000). Phytoplankton community structure and environment in the Kenyan waters of Lake Victoria. *Freshwater Biology*, 43:529–543.

Maffione, R. A. and Dana, D. R. (1997). Instruments and methods for measuring the backward-scattering coefficient of ocean waters. *Applied Optics*, 36(24):6057–6067.

Maldonado, D. J. C. (2008). *Spectral properties and population dynamics of the harmful dinoflagellate Cochlodinium polykrikoides (Margalef) in southwestern Puerto Rico*. Phd, University of Puerto Rico, Mayaguez.

Matthews, M. W. (2011). A current review of empirical procedures of remote sensing in inland and near-coastal transitional waters. *International Journal of Remote Sensing*, 32(21):6855–6899.

Matthews, M. W. and Bernard, S. (2013a). Characterizing the Absorption Properties for Remote Sensing of Three Small Optically-Diverse South African Reservoirs. *Remote Sensing*, 5:4370–4404.

Matthews, M. W. and Bernard, S. (2013b). Using a two-layered sphere model to investigate the impact of gas vacuoles on the inherent optical properties of Microcystis aeruginosa. *Biogeosciences*, 10(12):8139–8157.

Matthews, M. W., Bernard, S., and Robertson, L. (2012). An algorithm for detecting trophic status (chlorophyll-a), cyanobacterial-dominance, surface scums and floating vegetation in inland and coastal waters. *Remote Sensing of Environment*, 124:637–652.

Matthews, M. W., Bernard, S., and Winter, K. (2010). Remote sensing of cyanobacteria-dominant algal blooms and water quality parameters in Zeekoevlei, a small hypertrophic lake, using MERIS. *Remote Sensing of Environment*, 114(9):2070–2087.

McKee, D., Chami, M., Brown, I., Calzado, V. S., Doxaran, D., and Cunningham, A. (2009). Role of measurement uncertainties in observed variability in the spectral backscattering ratio: a case study in mineral-rich coastal waters. *Applied optics*, 48(24):4663–4675.

Mckee, D., Cunningham, A., Wright, D., and Hay, L. (2007). Potential impacts of nonalgal materials on water-leaving Sun induced chlorophyll fluorescence signals in coastal waters. *Applied Optics*, 46(31):7720–7729.

Meffert, M. E., Oberhäuser, R., and Overbeck, J. (1981). Morphology and taxonomy of Oscillatoria redekei (Cyanophyta). *British phycological journal*, 16(1):107–114.

Metsamaa, L., Kutser, T., and Stroembeck, N. (2006). Recognising cyanobacterial blooms based on their optical signature: a modelling study. *Boreal Environment Research*, 11(6):493–506.

Michalak, A. M., Anderson, E. J., Beletsky, D., Boland, S., Bosch, N. S., Bridgeman, T. B., Chaffin, J. D., Cho, K., Confesor, R., Daloglu, I., Depinto, J. V., Evans, M. A., Fahnenstiel, G. L., He, L., Ho, J. C., Jenkins, L., Johengen, T. H., Kuo, K. C., Laporte, E., Liu, X., McWilliams, M. R., Moore, M. R., Posselt, D. J., Richards, R. P., Scavia, D., Steiner, A. L., Verhamme, E., Wright, D. M., and Zagorski, M. a. (2013). Record-setting algal bloom in Lake Erie caused by agricultural and meteorological trends consistent with expected future conditions. *Proceedings of the National Academy of Sciences of the United States of America*, 110(16):6448–6452.

Mishra, S., Mishra, D. R., and Lee, Z. (2014). Bio-Optical Inversion in Highly Turbid and Cyanobacteria Dominated Waters. *IEEE Transactions on Geoscience and Remote Sensing*, 52(1):375–388.

Mitchell, B. G., Kahru, M., Wieland, J., and Stramska, M. (2003). Determination of spectral absorption coefficients of particles, dissolved material and phytoplankton for discrete water samples. In Mueller, J. L., Fargion, G. S., and McClain, C. R., editors, *Ocean Optics Protocols For Satellite Ocean Color Sensor Validation, Revision 4, Volume IV: Inherent Optical Properties: Instruments, Characterizations, Field Measurements and Data Analysis Protocols*, chapter 4. National Aeronautical and Space Administration, Greenbelt, Maryland.

Mobley, C. (1994). *Light and Water: radiative transfer in natural waters*. Academic Press, San Diego.

Mobley, C. (1999). Estimation of the remote-sensing reflectance from above-surface measurements. *Applied Optics*, 38(36):7442–7455.

Mobley, C. D., Sundman, L. K., and Boss, E. (2002). Phase function effects on oceanic light fields. *Applied optics*, 41(6):1035–1050.

Mobley, C. D., Sundman, L. K., Davis, C. O., Bowles, J. H., Downes, T. V., Leathers, R. a., Montes, M. J., Bissett, W. P., Kohler, D. D. R., Reid, R. P., Louchard, E. M., and Gleason, A. (2005). Interpretation of hyperspectral remote-sensing imagery by spectrum matching and look-up tables. *Applied optics*, 44(17):3576–92.

Morel, A., Ahn, Y.-H., Partensky, F., Vaulot, D., and Claustre, H. (1993). Prochlorococcus and Synechococcus: A comparative study of their optical properties in relation to their size and pigmentation. *Journal of Marine Research*, 51(3):617–649.

Morel, A. and Bricaud, A. (1986). Inherent optical properties of algal cells including picoplankton: theoretical and experimental results. *Can. Bull. Fish. Aquat. Sci*, 214:521–559.

Morel, A., David, A., and Gentili, B. (2002). Bidirectional reflectance of oceanic waters: accounting for Raman emission and varying particle scattering phase function. *Applied Optics*, 41(30):6289–6306.

Morel, A. and Prieur, L. (1977). Analysis of variations in ocean color. *Limnology and Oceanography*, 22(4):709–722.

Moses, W., Gitelson, A., Berdnikov, S., and Povazhnyy, V. (2009a). Satellite estimation of chlorophyll-a concentration using the red and NIR bands of MERIS—the Azov Sea case study. *IEEE Geoscience and Remote Sensing Letters*, 6(4):845–849.

Moses, W. J., Bowles, J. H., Lucke, R. L., and Corson, M. R. (2012). Impact of signal-to-noise ratio in a hyperspectral sensor on the accuracy of biophysical parameter estimation in case II waters. *Optics express*, 20(4):4309–4330.

Moses, W. J., Gitelson, A. A., Berdnikov, S., and Povazhnyy, V. (2009b). Estimation of chlorophyll-a concentration in case II waters using MODIS and MERIS data—successes and challenges. *Environmental Research Letters*, 4(4):45005.

Mueller, J. L., Morel, A., Frouin, R., Davis, C., Arnone, R., Carder, K., Lee, Z., Steward, R., Hooker, S., Mobley, C. D., McLean, S., Holben, B., Miller, M., Pietras, C., Knobelspiesse, K. D., Fargion, G. S., Porter, J., and Voss, K. (2003). Radiometric Measurements and Data Analysis Protocols. In Mueller, J. L., Fargion, G. S., and McClain, C. R., editors, *Ocean Optics Protocols For Satellite Ocean Color Sensor Validation, Revision 4, Volume III:*, volume III, page 78. NASA, Goddard Space Flight Space Center, Greenbelt, Maryland.

Neukermans, G., Loisel, H., Mériaux, X., Astoreca, R., and McKee, D. (2012). In situ variability of mass-specific beam attenuation and backscattering of marine particles with respect to particle size , density , and composition. *Limnology and Oceanography*, 57(1):124–144.

Neville, R. and Gower, J. F. R. (1977). Passive Remote Sensing of Phytoplankton via Chlorophyll *a* Fluorescence. *Journal of Geophysical Research*, 82(24):3487–3493.

Oberholster, P. J. and Ashton, P. J. (2008). State of the Nation Report: An Overview of the Current Status of Water Quality and Eutrophication in South African Rivers and Reservoirs. Technical report, Republic of South Africa, Pretoria.

Oberholster, P. J. and Botha, A. M. (2007). Use of PCR based technologies for risk assessment of a winter cyanobacterial bloom in Lake Midmar, South Africa. *African Journal of Biotechnology*, 6(15):1794–1805.

Oberholster, P. J., Botha, A. M., and Cloete, T. E. (2005). An overview of toxic freshwater cyanobacteria in South Africa with special reference to risk, impact and detection by molecular marker tools. *Biokemistri*, 17(2):57–71.

Oberholster, P. J., Cloete, T. E., Ginkel, C. E. V., Botha, A. M., and Ashton, P. J. (2009). The use of remote sensing and molecular markers as early-warning indicators of the development of cyanobacterial hyperscum crust and microcystin-producing genotypes in the hypertrophic Lake Hartebeespoort, South Africa.

Oberholster, P. J., Myburgh, J. G., Ashton, P. J., and Botha, A.-M. (2010). Responses of phytoplankton upon exposure to a mixture of acid mine drainage and high levels of nutrient pollution in Lake Loskop, South Africa. *Ecotoxicology and environmental safety*, 73(3):326–335.

Odermatt, D., Giardino, C., and Heege, T. (2010). Chlorophyll retrieval with MERIS Case-2-Regional in perialpine lakes. *Remote Sensing of Environment*, 114(3):607–617.

Odermatt, D., Gitelson, A., Brando, V. E., and Schaepman, M. (2012). Review of constituent retrieval in optically deep and complex waters from satellite imagery. *Remote Sensing of Environment*, 118:116–126.

Odermatt, D., Kiselev, S., Heege, T., Kneubühler, M., and Itten, K. I. (2008). Adjacency effect considerations and air/water constituent retrieval for Lake Constance. In ESA/ESRIN, editor, *Proceedings of the 2nd MERIS/(A)ATSR user workshop. Frascati, Italy*, number 1.

O'Donnell, D., Effler, S. W., Strait, C. M., and Leshkevich, G. A. (2010). Optical characterizations and pursuit of optical closure for the western basin of Lake Erie through in situ measurements. *Journal of Great Lakes Research*, 36:736–746.

Ogawa, T., Sekine, T., and Aiba, S. (1979). Reappraisal of the so-called light shielding of gas vacuoles in Microcystis Aeruginosa. *Archives of Microbiology*, 122:57–60.

Olmanson, L. G., Bauer, M. E., and Brezonik, P. L. (2008). A 20-year Landsat water clarity census of Minnesota's 10,000 lakes. *Remote Sensing of Environment*, 112(11):4086–4097.

O'Reilly, J. E., Maritorena, S., Mitchell, B. G., Siegel, D. A., Carder, K. L., Garver, S. A., Kahru, M., and McClain, C. (1998). Ocean color chlorophyll algorithms for SeaWiFS. *Journal of Geophysical Research*, 103(C11):24937–24953.

Paerl, H. W. and Huisman, J. (2009). Climate change: a catalyst for global expansion of harmful cyanobacterial blooms. *Environmental microbiology reports*, 1(1):27–37.

Perkins, M., Effler, S. W., Strait, C., and Zhang, L. (2009). Light absorbing components in the Finger Lakes of New York. *Archiv für Hydrobiologie*, 173(4):305–320.

Petrie, S. A. and Rogers, K. H. (1997). Satellite tracking of white-faced whistling ducks in a semiarid region of South Africa. *The Journal of Wildlife Management*, 61(4):1208–1213.

Petzold, T. J. (1972). Volume scattering functions for selected ocean waters. Technical report, Scripps Institution of Oceanography Visibility Laboratory, San Diego, California.

Piskozub, J. and McKee, D. (2011). Effective scattering phase functions for the multiple scattering regime. *Optics express*, 19(5):4786–4794.

Pitcher, G. C. and Calder, D. (2000). Harmful algal blooms of the southern Benguela Current: a review and appraisal of monitoring from 1989 to 1997. *South African Journal of Marine Science*, 22(1):255–271.

Pitcher, G. C. and Probyn, T. A. (2011). Anoxia in southern Benguela during the autumn of 2009 and its linkage to a bloom of the dinoflagellate Ceratium balechii. *Harmful Algae*, 11:23–32.

Pitcher, G. C. and Weeks, S. J. (2006). The variability and potential for prediction of harmful algal blooms in the southern Benguela ecosystem. *Large Marine Ecosystems*, 14:125–146.

Porter, J. and Jost, M. (1976). Physiological effects of the presence and absence of gas vacuoles in the blue-green alga, Microcystis aeruginosa Kuetz. emend. Elenkin. *Archives of Microbiology*, 110:225–231.

Pozdnyakov, D. V., Korosov, A., Grassl, H., and Pettersson, L. (2005). An advanced algorithm for operational retrieval of water quality from satellite data in the visible. *International Journal of Remote Sensing*, 26(12):2669–2687.

Prigent, C., Papa, F., Aires, F., Rossow, W. B., and Matthews, E. (2007). Global inundation dynamics inferred from multiple satellite observations, 1993–2000. *Journal of Geophysical Research*, 112(D12107):1–13.

Qin, B., Xu, P., Wu, Q., Luo, L., and Zhang, Y. (2007). Environmental issues of Lake Taihu, China. *Hydrobiologia*, 581(1):3–14.

Quinby-Hunt, M., Hunt, A., Lofftus, K., and Shapiro, D. (1989). Polarized-light scattering studies of marine chlorella. *Limnology and Oceanography*, 34(8):1587– 1600.

Quirantes, A. and Bernard, S. (2006). Light-scattering methods for modelling algal particles as a collection of coated and/or nonspherical scatterers. *Journal of Quantitative Spectroscopy and Radiative Transfer*, 100(1-3):315–324.

Raj, E. P., Devara, P. C. S., Maheskumar, R. S., Pandithurai, G., Dani, K. K., Saha, S. K., Sonbawne, S. M., and Tiwari, Y. K. (2004). Results of Sun Photometer–Derived Precipitable Water Content over a Tropical Indian Station. *Journal of Applied Meteorology*, 43(10):1452–1459.

Rajagopal, S., Sicora, C., Várkonyi, Z., Mustárdy, L., and Mohanty, P. (2005). Protective effect of supplemental low intensity white light on ultraviolet-B exposure-induced impairment in cyanobacterium Spirulina platensis: formation of air vacuoles as a possible protective measure. *Photosynthesis research*, 85(2):181–189.

Randolph, K., Wilson, J., Tedesco, L., Li, L., Pascual, D. L., and Soyeux, E. (2008). Hyperspectral remote sensing of cyanobacteria in turbid productive water using optically active pigments, chlorophyll a and phycocyanin. *Remote Sensing of Environment*, 112(11):4009–4019.

Raps, S., Kycia, J. H., Ledbetter, M. C., and Siegelman, H. W. (1985). Light Intensity Adaptation and Phycobilisome Composition of Microcystis aeruginosa. *Plant Physiol.*, 79:983–987.

Raven, J. A. (1987). The Role of Vacuoles. *New Phytologist*, 106(3):357–422.

Rehm, E. and Mobley, C. D. (2013). Estimation of hyperspectral inherent optical properties from in-water radiometry: error analysis and application to in situ data. *Applied optics*, 52(4):795–817.

Reinart, A. and Kutser, T. (2006). Comparison of different satellite sensors in detecting cyanobacterial bloom events in the Baltic Sea. *Remote Sensing of Environment*, 102(1-2):74–85.

Retalis, A., Hadjimitsis, D. G., Michaelides, S., Tymvios, F., Chrysoulakis, N., Clayton, C. R. I., and Themistocleous, K. (2010). Comparison of aerosol optical thickness with in situ visibility data over Cyprus. *Natural Hazards and Earth Systems Sciences*, 10:421–428.

Reynolds, C. S. (2006). *The Ecology of Phytoplankton*. Cambridge University Press, New York.

Reynolds, C. S., Jaworski, G. H. M., Cmiech, H. A., and Leedale, G. F. (1981). On the annual cycle of the blue-green alga microcystis aeruginosa kutz. Emend. Elenkin. *Philosophical transactions of the Royal Society of London. Series B, Biological sciences*, 293(1068):419–477.

Richardson, L. L. (1996). Remote Sensing of Algal Bloom Dynamics. *BioScience*, 46(7):492–501.

Robarts, R. (1984). Factors controlling primary production in a hypertrophic lake (Hartbeespoort Dam, South Africa). *Journal of plankton research*, 6(1):91–105.

Robarts, R. and Zohary, T. (1992). The influence of temperature and light on the upper limit of Microcystis aeruginosa production in a hypertrophic reservoir. *Journal of Plankton Research*, 14(2):235–247.

Roesler, C. (1998). Theoretical and experimental approaches to improve the accuracy of particulate absorption coefficients derived from the quantitative filter technique. *Limnology and Oceanography*, 43(7):1649–1660.

Roesler, C. S. and Boss, E. (2003). Spectral beam attenuation coefficient retrieved from ocean color inversion. *Geophysical Research Letters*, 30(9):1–4.

Rottgers, R., Doerffer, R., McKee, D., and Schonfeld, W. (2011). Algorithm Theoretical Basis Document: The Water Optical Properties Processor (WOPP). Technical report, Helmholtz-Zentrum Geesthacht, University of Strathclyde, Geesthacht.

RQS (2004). Dams and some lakes of South Africa. Resource Quality Services, Pretoria, http://www.dwa.gov.za/iwqs/gis_data/river/rivs500k.html.

Ruiz-Verdu, A. (2013). Personal communication.

Ruizverdu, A., Simis, S., Dehoyos, C., Gons, H., and Penamartinez, R. (2008). An evaluation of algorithms for the remote sensing of cyanobacterial biomass. *Remote Sensing of Environment*, 112(11):3996–4008.

Salama, M. S., Dekker, A. G., Su, Z., Mannaerts, C. M., and Verhoef, W. (2009). Deriving inherent optical properties and associated inversion-uncertainties in the Dutch Lakes. *Hydrol. Earth Syst. Sci*, 13:1113–1121.

Santer, R. (2010). ICOL+ Algorithm Theoretical Basis Document. Technical Report V1.0, Brockmann Consult.

Santer, R., Carrere, V., Dubuisson, P., and Roger, J. (1999). Atmospheric correction over land for MERIS. *International Journal of Remote Sensing*, 20(9):1819–1840.

Santer, R. and Schmechtig, C. (2000). Adjacency effects on water surfaces: primary scattering approximation and sensitivity study. *Applied Optics*, 39(3):361–375.

Santini, F., Alberotanza, L., Cavalli, R. M., and Pignatti, S. (2010). A two-step optimization procedure for assessing water constituent concentrations by hyperspectral remote sensing techniques: an application to the highly turbid Venice lagoon waters. *Remote Sensing of Environment*, 114(4):887–898.

Sarada, R., Pillai, M. G., and Ravishankar, G. (1999). Phycocyanin from Spirulina sp: influence of processing of biomass on phycocyanin yield, analysis of efficacy of extraction methods and stability studies on phycocyanin. *Process Biochemistry*, 34(8):795–801.

Sartory, D. P. and Grobbelaar, J. U. (1984). Extraction of chlorophyll a from freshwater phytoplankton for spectrophotometric analysis. *Hydrobiologia*, 114(3):177–187.

Schagen, M. (1997). *Numerical calculation of the scattering properties of cylindrical phytoplankton*. PhD thesis, Vrije University.

Schalles, J. F., Gitelson, A. A., Yacobi, Y. Z., and Kroenke, A. E. (1998). Estimation of chlorophyll a from time series measurements of high spectral resolution reflectance in an eutrophic lake. *Journal of Phycology*, 34(2):383–390.

Schiller, H. and Doerffer, R. (2005). Improved determination of coastal water constituent concentrations from MERIS data. *IEEE Transactions on Geoscience and Remote Sensing*, 43(7):1585–1591.

Schindler, D. W. (2009). Lakes as sentinels and integrators for the effects of climate change on watersheds, airsheds, and landscapes. *Limnology and Oceanography*, 54(6, part 2):2349–2358.

Schluter, L., Lauridsen, T. L., Krogh, G., and Jorgensen, T. (2006). Identification and quantification of phytoplankton groups in lakes using new pigment ratios - a comparison between pigment analysis by HPLC and microscopy. *Freshwater Biology*, 51(8):1474–1485.

Schofield, O., Kerfoot, J., Mahoney, K., Moline, M., Oliver, M., Lohrenz, S., and Kirkpatrick, G. (2006). Vertical migration of the toxic dinoflagellate Karenia brevis and the impact on ocean optical properties. *Journal of Geophysical Research: Oceans (1978-2012)*, 111(C6):C06009.

Schreurs, R. (1996). *Light scattering by algae: fitting experimental data using Lorenz-Mie theory*. PhD thesis, Vrije University, Amsterdam.

Schwarz, S. and Grossman, A. R. (1998). A response regulator of cyanobacteria integrates diverse environmental signals and is critical for survival under extreme conditions. *Proceedings of the National Academy of Sciences of the United States of America*, 95:11008–11013.

Scott, W., Seaman, M., Connell, A., Kohlmeyer, S., and Toerien, D. (1977). The limnology of some South African impoundments I. The physico-chemical limnology of Hartbeespoort Dam. *Journal of the Limnological Society of southern Africa*, 3(2):43–58.

Seppälä, J., Ylöstalo, P., Kaitala, S., Hällfors, S., Raateoja, M., and Maunula, P. (2007). Ship-of-opportunity based phycocyanin fluorescence monitoring of the filamentous cyanobacteria bloom dynamics in the Baltic Sea. *Estuarine, Coastal and Shelf Science*, 73(3-4):489–500.

Shear, H. and Walsby, A. E. (1975). An investigation into the possible light-shielding role of gas vacuoles in a planktonic blue-green alga. *European Journal of Phycology*, 10(3):241–251.

Shi, W. and Wang, M. (2009). An assessment of the black ocean pixel assumption for MODIS SWIR bands. *Remote Sensing of Environment*, 113(8):1587–1597.

Simis, S. G. and Kauko, H. M. (2012). In vivo mass-specific absorption spectra of phycobilipigments through selective bleaching. *Limnology and Oceanography: Methods*, 10(2):214–226.

Simis, S. G. H. (2013). Personal communication.

Simis, S. G. H., Peters, S. W. M., and Gons, H. J. (2005). Remote sensing of the cyanobacterial pigment phycocyanin in turbid inland water. *Limnology and Oceanography*, 50(1):237–245.

Simis, S. G. H., Ruiz-Verdu, A., Dominguez-Gomez, J. A., Pena-Martinez, R., Peters, S. W. M., and Gons, H. J. (2007). Influence of phytoplankton pigment composition on remote sensing of cyanobacterial biomass. *Remote Sensing of Environment*, 106(4):414–427.

Smith, R. V. and Peat, A. (1967). Comparative structure of the gas-vacuoles of blue-green algae. *Archives of Microbiology*, 57:111–122.

Smith, V. H., Tilman, G. D., and Nekola, J. C. (1999). Eutrophication: impacts of excess nutrient inputs on freshwater, marine, and terrestrial ecosystems. *Environmental Pollution*, 100(1-3):179–196.

Snyder, W. A., Arnone, R. A., Davis, C. O., Goode, W., Gould, R. W., Ladner, S., Lamela, G., Rhea, W. J., Stavn, R., Sydor, M., and Weidemann, A. (2008). Optical scattering and backscattering by organic and inorganic particulates in U.S. coastal waters. *Applied optics*, 47(5):666–677.

Sommaruga, R. and Robarts, R. D. (1997). The significance of autotrophic and heterotrophic picoplankton in hypertrophic ecosystems. *FEMS microbiology ecology*, 24:187–200.

Soranno, P. A. (1997). Factors affecting the timing of surface scums and epilimnetic blooms of blue-green algae in a eutrophic lake. *Canadian Journal of Fisheries and Aquatic Sciences*, 54:1965–1975.

Sotis, G. (2007). Envisat-1 Products Specifications Volume 11: MERIS Products Specifications. Technical Report 5 B.

Spinrad, R. W. and Brown, J. F. (1986). Relative real refractive index of marine microorganisms: a technique for flow cytometric estimation. *Applied optics*, 25(12):1930–1934.

Stewart, D. E. and Farmer, F. H. (1984). Extraction and quantitation of phycobiliprotein pigments from phototrophic plankton. *Limnology and Oceanography*, 29(2):392–397.

Stramska, M. and Stramski, D. (2005). Effects of a nonuniform vertical profile of chlorophyll concentration on remote-sensing reflectance of the ocean. *Applied optics*, 44(9):1735–1747.

Stramski, D., Babin, M., and Wozniak, S. B. (2007). Variations in the optical properties of terrigenous mineral-rich particulate matter suspended in seawater. *Limnology and Oceanography*, 52(6):2418–2433.

Stramski, D., Boss, E., Bogucki, D., and Voss, K. J. (2004). The role of seawater constituents in light backscattering in the ocean. *Progress in Oceanography*, 61(1):27–56.

Stramski, D., Bricaud, A., and Morel, A. (2001). Modeling the inherent optical properties of the ocean based on the detailed composition of the planktonic community. *Applied Optics*, 40(18):2929–2945.

Stramski, D. and Wozniak, S. B. (2005). On the role of colloidal particles in light scattering in the ocean. *Limnology and Oceanography*, 50(5):1581–1591.

Stumpf, R. P., Wynne, T. T., Baker, D. B., and Fahnenstiel, G. L. (2012). Interannual variability of cyanobacterial blooms in Lake Erie. *PLoS ONE*, 7(8):e42444.

Suggett, D., Moore, C., Hickman, A., and Geider, R. J. (2009). Interpretation of fast repetition rate(FRR) fluorescence: signatures of phytoplankton community structure versus physiological state. *Marine Ecology Progress Series*, 376:1–19.

Sun, D., Li, Y., Wang, Q., Gao, J., Lv, H., Le, C., and Huang, C. (2009). Light scattering properties and their relation to the biogeochemical composition of turbid productive waters: a case study of Lake Taihu. *Applied optics*, 48(11):1979–1989.

Svensen, O., Frette, O., and Erga, S. R. (2007). Scattering properties of microalgae: the effect of cell size and cell wall. *Applied Optics*, 46:5762–5769.

Tebbs, E., Remedios, J., and Harper, D. (2013). Remote sensing of chlorophyll-a as a measure of cyanobacterial biomass in Lake Bogoria, a hypertrophic, saline–alkaline, flamingo lake, using Landsat ETM+. *Remote Sensing of Environment*, 135:92–106.

Toon, O. B. and Ackerman, T. P. (1981). Algorithms for the calculation of scattering by stratified spheres. *Applied optics*, 20(20):3657–3660.

Twardowski, M. S., Lewis, M. R., Barnard, A., and Zaneveld, J. R. V. (2005). In-water instrumentation and platforms for ocean color remote sensing applications. In Miller, R. L., Castillo, C. E. D., and McKee, B. A., editors, *Remote sensing of coastal aquatic environments*, page 347. Springer, Dordrecht.

Tzortziou, M., Herman, J. R., Gallegos, C. L., Neale, P. J., Subramaniam, A., Harding, L. W., and Ahmad, Z. (2006). Bio-optics of the Chesapeake Bay from measurements and radiative transfer closure. *Estuarine, Coastal and Shelf Science*, 68(1-2):348–362.

Vaillancourt, R. D., Brown, C. W., Guillard, R. R. L., and Balch, W. M. (2004). Light backscattering properties of marine phytoplankton: relationships to cell size, chemical composition and taxonomy. *Journal of Plankton Research*, 26(2):191–212.

van Baalen, C. and Brown, R. M. (1969). The ultrastructure of the marine blue green alga, Trichodesmium erythraeum, with special reference to the cell wall, gas vacuoles, and cylindrical bodies. *Archiv Für Hydrobiologie*, 69(1):79–91.

van de Hulst, H. C. (1957). *Light scattering by small particles*. Wiley, New York.

Van Der Walt, N. (2011). *Investigation into the occurrence of the dinoflagellate, Ceratium hirundinella in source waters and the impact thereof on drinking water purification*. PhD thesis, North-West University, Potchefstroom.

van Ginkel, C. (2012). Algae, phytoplankton and eutrophication research and management in South Africa: past, present and future. *African Journal of Aquatic Science*, 37(1):17–25.

van Ginkel, C. and Silberbauer, M. (2007). Temporal trends in total phosphorus, temperature, oxygen, chlorophyll a and phytoplankton populations in Hartbeespoort Dam and Roodeplaat Dam, South Africa, between 1980 and 2000. *African Journal of Aquatic Science*, 32(1):63–70.

van Ginkel, C. E. (2011). Eutrophication : Present reality and future challenges for South Africa. *Water Sa*, 37(5):693–701.

van Ginkel, C. E., Hohls, B. C., and Vermaak, E. (2001). A Ceratium hirundinella (O.F. Müller) bloom in Hartbeespoort Dam , South Africa. *Water SA*, 27(2):269–276.

van Ginkel, C. E., Silberbauer, M. J., and Vermaak, E. (2000). The seasonal and spatial distribution of cyanobacteria in South African surface waters. *Verhandlungen Internationale Vereinigung für Theoretische und Angewandte Limnologie*, 27:871–878.

van Liere, L. and Walsby, A. E. (1982). Interactions of cyanobacteria with light. In Carr, N. G. and Whitton, B. A., editors, *The biology of cyanobacteria*, chapter 2, pages 9–46. Blackwell Scientific, Berkeley and Los Angeles.

Van Valkenburg, S., Jones, J. K., and Heinle, D. R. (1978). A comparison by size class and volume of detritus versus phytoplankton in Chesapeake Bay. *Estuarine and Coastal Marine Science*, 6:569–582.

van Wyk, E. and van Wilgen, B. W. (2002). The cost of water hyacinth control in South Africa: a case study of three options. *African Journal of Aquatic Science*, 27:141–149.

Vanderwoerd, H. and Pasterkamp, R. (2008). HYDROPT: A fast and flexible method to retrieve chlorophyll-a from multispectral satellite observations of optically complex coastal waters. *Remote Sensing of Environment*, 112(4):1795–1807.

Viskari, P. J. and Colyer, C. L. (2003). Rapid extraction of phycobiliproteins from cultured cyanobacteria samples. *Analytical Biochemistry*, 319(2):263–271.

Visser, P. M., Ibelings, B. W., Mur, L. R., and Walsby, A. E. (2005). *The ecophysiology of the harmful cyanobacterium microcystis*, pages 109–142. Harmful cyanobacteria. Springer, Netherlands.

Volten, A. H., Haan, J. F. D., Hovenier, J. W., Schreurs, R., Vassen, W., Dekker, A. G., Hoogenboom, J., Charlton, F., and Wouts, R. (1998). Laboratory Measurements of Angular Distributions of Light Scattered by Phytoplankton and Silt. *Limnology and Oceanography*, 43(6):1180–1197.

Šmarda, J. (2009). Cell ultrastructure changes accompanying the annual life cycle of the cyanobacterium Microcystis aeruginosa. *Algological Studies*, 130(1):27–38.

Waaland, J. R., Waaland, S. D., and Branton, D. (1971). Gas vacuoles: Light shielding in blue-green algae. *The Journal of cell biology*, 48(1):212–215.

Walmsley, R. and Bruwer, C. (1980). Water transparency characteristics of South African impoundments. *Journal of the Limnological Society of southern Africa*, 6(2):69–76.

Walsby, A. E. (1994). Gas vesicles. *Microbiological reviews*, 58(1):94–144.

Wang, Q., Sun, D., Li, Y., Le, C., and Huang, C. (2010). Mechanisms of Remote-Sensing Reflectance Variability and Its Relation to Bio-Optical Processes in a Highly Turbid Eutrophic Lake: Lake Taihu (China). *IEEE Transactions on Geoscience and Remote Sensing*, 48(1):575–584.

Wen, Y. H. (1992). Contribution of bacterioplankton, phytoplankon, zooplankton and detritus to organic sestin carbon load in a Changjian floodplain lake (China). *Arch. Hydrobiol.*, 126(2):213–238.

Whitmire, A. L., Boss, E., Cowles, T. J., and Pegau, W. S. (2007). Spectral variability of the particulate backscattering ratio. *Optics express*, 15:7019–7031.

Whitmire, A. L., Pegau, W. S., Karp-boss, L., Boss, E., and Cowles, T. J. (2010). Spectral backscattering properties of marine phytoplankton cultures. *Optics Express*, 18(14):1680–1690.

WHO (1999). *Toxic Cyanobacteria in Water: A guide to their public health consequences, monitoring and management*. E & FN Spon, London.

Williamson, C. E., Saros, J. E., Vincent, W. F., and Smol, J. P. (2009). Lakes and reservoirs as sentinels , integrators , and regulators of climate change. *Limnology and Oceanography*, 54(6, part 2):2273–2282.

Witkowski, K., Krol, T., Zielinski, A., and Kuten, E. (1998). A Light-Scattering Matrix for Unicellular Marine Phytoplankton. *Limnology and Oceanographyology*, 43(5):859–869.

WRC (1996). Catchments of South Africa - quaternary. Water Research Commission - with modifications by Resource Quality Services, Department of Water Affairs, http://www.dwaf.gov.za/.

Wyman, M. and Fay, P. (1986). Underwater Light Climate and the Growth and Pigmentation of Planktonic Blue-Green Algae (Cyanobacteria) II. The Influence of Light Quality. *Proceedings of the Royal Society B: Biological Sciences*, 227(1248):381–393.

Wynne, T. T., Stumpf, R. P., Tomlinson, M. C., Warner, R. A., Tester, P. A., Dyble, J., and Fahnenstiel, G. L. (2008). Relating spectral shape to cyanobacterial blooms in the Laurentian Great Lakes. *International Journal of Remote Sensing*, 29(12):3665–3672.

Yacobi, Y. Z., Gitelson, A., and Mayo, M. (1995). Remote sensing of chlorophyll in Lake Kinneret using high spectral-resolution radiometer and Landsat TM: spectral features of reflectance and algorithm development. *Journal of Plankton Research*, 17(11):2155–2173.

Zaneveld, J. R., Barnard, A., and Boss, E. (2005). Theoretical derivation of the depth average of remotely sensed optical parameters. *Optics express*, 13(22):9052–9061.

Zhang, X., Lewis, M., Lee, M., Johnson, B., and Korotaev, G. (2002). The volume scattering function of natural bubble populations. *Limnology and Oceanography*, 47(5):1273–1282.

Zhang, Y., Liu, M., Qin, B., van der Woerd, H. J., Li, J., and Y, L. (2009a). Modeling Remote-Sensing Reflectance and Retrieving Chlorophyll-a Concentration in Extremely Turbid Case-2 Waters (Lake Taihu, China). *IEEE Transactions on Geoscience and Remote Sensing*, 47(7):1937–1948.

Zhang, Y., Liu, M., van Dijk, M. a., Zhu, G., Gong, Z., Li, Y., and Qin, B. (2008). Measured and numerically partitioned phytoplankton spectral absorption coefficients in inland waters. *Journal of Plankton Research*, 31(3):311–323.

Zhang, Y., Liu, M. L., Wang, X., Zhu, G. W., and Chen, W. M. (2009b). Bio-optical properties and estimation of the optically active substances in Lake Tianmuhu in summer. *International Journal of Remote Sensing*, 30(11):2837–2857.

Zhang, Y., Yin, Y., Wang, M., and Liu, X. (2012). Effect of phytoplankton community composition and cell size on absorption properties in eutrophic shallow lakes : field and experimental evidence. *Optics express*, 20(11):11882–11898.

Zhao, J., Cao, W., Yang, Y., Wang, G., Zhou, W., and Sun, Z. (2008). Measuring natural phytoplankton fluorescence and biomass: A case study of algal bloom in the Pearl River estuary. *Marine pollution bulletin*, 56(10):1795–1801.

Zhou, W., Wang, G., Sun, Z., Cao, W., Xu, Z., Hu, S., and Zhao, J. (2012). Variations in the optical scattering properties of phytoplankton cultures. *Optics express*, 20(10):11189–11206.

Zhu, Y., Chen, X. B., Wang, K. B., Li, Y. X., Bai, K. Z., Kuang, T. Y., and Ji, H. B. (2007). A simple method for extracting C-phycocyanin from Spirulina platensis using Klebsiella pneumoniae. *Applied microbiology and biotechnology*, 74(1):244–248.

Zimba, P. V. and Gitelson, A. (2006). Remote estimation of chlorophyll concentration in hyper-eutrophic aquatic systems: Model tuning and accuracy optimization. *Aquaculture*, 256(1-4):272–286.

Zohary, T. (1985). Hyperscums of the cyanobacterium Microcystis aeruginosa in a hypertrophic lake (Hartbeespoort Dam, South Africa). *Journal of Plankton Research*, 7(3):399–409.

Zohary, T., Pais-Madeira, A., Robarts, R., and Hambright, K. (1996). Interannual phytoplankton dynamics of a hypertrophic African lake. *Archiv Fur Hydrobiologie*, 136(1):105–126.

Colophon

This thesis was typeset using LaTeX, originally developed by Leslie Lamport and based on Donald Knuth's TeX. The body text is set in 11 point Arno Pro, designed by Robert Slimbach in the style of book types from the Aldine Press in Venice, and issued by Adobe in 2007. A template, which can be used to format a PhD thesis with this look and feel, has been released under the permissive MIT (X11) license, and can be found online at github.com/suchow/ or from the author at suchow@post.harvard.edu.